UNIVERSITE PARIS 13 – INSTITUT GALILEE

N° attribué par la bibliothèque

THESE

Présentée pour obtenir le grade de

DOCTEUR DE L'UNIVERSITE PARIS 13

Discipline : Physique

Présentée et soutenue publiquement

par

Getachew-Tilahun AYENEW

Investigation of photonic properties of self-assembled nanoparticle monolayers: application to photonic crystal cavities and patterned organic light emitting diodes

Soutenue le 8 juillet 2014 devant le jury composé de :

M. Alexis FISCHER, LPL, Université Paris 13 Directeur de thèse
M. Azzedine BOUDRIOUA, LPL, Université Paris 13 Directeur de thèse
M. Chii-Chang CHEN, National Central University, Taïwan
M. François FLORY, IM2NP, Rapporteur
Mme Agnès MAITRE, INSP, UMPC, Rapporteur
Mme Céline Fiorini, Commissariat à l'Énergie Atomique.
M. Olivier GORCEIX, LPL, Université Paris 13

Acknowledgment

Table of Contents

Introduction

Chapter 1: Nanoparticles and Photonic Crystals

Chapter 2:Photonic properties of monolayer of periodically arrayed dielectric spheres

Chapter 3: Nanoparticle based two dimensional patterning of organic light emitting diodes (OLEDs)

Chapter 4: Conclusion and Perspective

Introduction

1. Introduction and context

The last few decades have seen the emergence of conducting and electroluminescent organic materials- polymers and small organic molecules [1]**.** There have been remarkable progresses in their synthesis and in their development for use in optoelectronic devices. Organic optoelectronic materials have novel semiconducting and optical properties which can be changed by chemical engineering. Moreover, they have simple fabrication process, easy shaping and flexibility properties which make them advantageous over their inorganic counterparts. At the same time that organic optoelectronics was flourishing, there has also been many progress in the rapidly developing fields of nanoscience and nanotechnology. In this aspect, the fundamental physics at the nanoscale level was scientifically studied and the technology to fabricate nanoscale structures, nanoparticles and the methods to characterize them have been improved. Thus it is tempting to combine the advancing technologies of organic optoelectronics and nanotechnologies for the design and fabrication of novel organic light sources.

One first potential application deals with using nano and micro-particles to make micro and nano-OLEDs. The patterning methods based on micro nano-particles offer interesting perspectives for high resolution near field microscopes and high resolution displays based on micro and nano OLED light source [2]..

A second type of application deals with light extraction that requires nanostructures at the interface of certain layers that constitutes the OLEDs so as to overcome the limit angle. Periodic nanostructures are interesting for enhancing light extraction and OLED external quantum efficiency. This has led to achievements in lighting OLEDs with higher efficiency.

A third type of applications deals with the organic diode lasers. The organic diode laser has not been demonstrated so far, and an abundant literature has identified the electrical and optical issues that prevent the electrically driven laser operation [3,4]. The main limitation remains the low carrier mobility of the organic films resulting in OLED current-densities in the range of 0.1 A/cm^2 to 1 A/cm^2 under DC excitation [5,6], and in the range of 1 A/cm^2 up to 1 kA/cm^2 under pulsed excitation [7,8]. One way to overcome this limitation is to design laser

structure with a laser threshold current density at a level compatible with the available organic light emitting diode (OLED) current density. Such low threshold laser architecture can be divided into several types for which micro and nano patterning play a crucial role.

- Distributed feedback (DFB) lasers are based on a periodic gratings that are used to provide feedback with a very high efficiency. One dimensional DFB structures offer low laser threshold that is even lowered with 2D gratings [9]. These 1D or 2D periodic gratings requires micro and nano-patterning.

- Photonic crystal laser: In micro- and nano-cavity organic lasers the organic emitter is embedded in a defect cavity in a photonic crystal. The Photonic crystal is designed such the light cannot propagate in the material and the light is confined in the defect. The photonic crystal substitutes the laser mirrors in conventional lasers. The literature presents several examples of L or H defect cavities in 2D photonic crystal slabs. These laser structures provides among the lowest threshold reported in the literature. 3D photonic crystal can potentially confined light in three dimensions which is expected to reduce the laser threshold even more, however they have rarely been investigated in the visible domain due to the difficulty of fabrication of 3D structures in the nanometer range. The self-assembling properties of nanoparticles offer an interesting and a unique perspective for the fabrication of 3D photonic crystal.

The conventional fabrication technique for the above mentioned structures relies on electron beam lithography or similar techniques. But fabrication techniques like electron beam lithography are costly, time taking, and not suitable for mass production. Recently, unconventional methods based on self-assembly of nanoparticles are helping to solve the limitations of conventional methods both technically and financially. These techniques usually don't need expensive machines; they can be used to make large area structures and are suitable for mass production. Self-assembled nanoparticles were used in a variety of ways to make periodic structures which can be combined with organic emitters [10]. People have made and used 2D spherical nanoparticles for light extraction from OLEDs [11,12]. In addition, nanoparticles were used as a route for fabrication 2D photonic crystals for organic DFB lasers, by the process called nanosphere lithography [13]. 3D array of nanoparticles based

structures, opal and inverse opals, were fabricated and used to make photonic crystal lasers, with the advantage towards 3D optical confinement.

Although micro and nanoparticles have been applied in the bottom-up approach to the realization of the different structures, a systematical theoretical studies of the optical properties of these objects is still lacking or incomplete. Among these objects one can distinguish opals and inverse opals as 3D objects and single layer of self-assembled nanoparticles or their inverse as quasi 2D objects. A systematical and unifying study of the photonic properties of these different objects will allow to list the different potential applications and define more precisely the construction parameters.

2. Objective of the thesis

The general context of this thesis is to combine the organic light emitting diodes and the photonic properties of nanostructures realized with nano-particles. In the framework of this thesis we consider nanostructures obtained by the bottom-up approach based on the self-organized micro and nanoparticles. More specifically, taking into account the photonic properties provided by the self-organized nanoparticles and any type of two-dimensional or three-dimensional photonic nanostructures realized with them, an important question addressed in this study is how these photonic properties can be used to improve OLED or organic lasers providing a better light extraction, or a lower laser threshold. More generally we aim at investigating the interest of self-assembled micro and nanoparticles and the bottom-up approach for the fabrication of organic opto-electronic devices.

3. Layout

To investigate these questions, we divided this work in 4 main chapters: the first chapter will be devoted to the nanoparticles and the photonic crystals. We will recall what nanoparticles are, how they are synthesized and how they self-assemble. The historical background of nanoparticles and their synthesis methods will be cited. We will then focus on the geometries of both the self-assembled nanoparticles in 3 dimensions as well as on the single layers. Knowing their geometries, lattice and structures is a prerequisite to consider next their photonic properties. In the second part, we will recall the main principles on photonic crystals and the theoretical background will be given. We will then consider how the photonic

properties can be investigated numerically. For this, we will introduce the Maxwell equations in periodic media and the Finite Difference Time Domain (FDTD) method as prerequisite to calculate numerically the band structure.

The second chapter will deal with the theoretical study of 2D periodic microspheres. We will apply the numerical results to investigate the existence of forbidden bandgaps in different slab geometries. More precisely we will consider a self-sustained single layer of nanoparticles, and first we will map the complete and partial photonic bandgaps for these nanoparticles self-assembled in 3 dimensions, before considering single layer of self-assembled nanoparticles. The in-plane transmission spectra of single layers of nanoparticles will then be studied. In addition, the possibility of using 2D nanoparticle based photonic crystals are discussed.

Chapter 3 is dedicated to the organic light emitting diodes and how nanoparticles can be used to pattern them. We will first recall what organic materials and how organic heterostructures are designed and fabricated. We will then discuss the experimental results on the application of nanoparticles with OLEDs. Nanoparticle based photolithography technique applied to make micro OLEDs will be presented and discussed.

Chapter 4: The last part will be the summery and perspectives of the thesis.

4. References

[1] Alan J. Heeger, “Semiconducting and Metallic Polymers: The Fourth Generation of Polymeric Materials (Nobel Lecture),” Angew. Chem. Int. Ed., Vol. 40, 2591- 2611(2001)

[2] Yu-Jung Lu , Hon-Way Lin , Hung-Ying Chen, Yu-Chen Yang and Shangjr Gwo, “Single InGaN nanodisk light emitting diodes as full-color subwavelength light sources, “ Applied Physics Letters, Vol. 98, 233101(2011)

[3] M. A. Baldo, D. F. O'Brien, M. E. Thompson, and S. R. Forrest, “Prospects for electrically pumped organic lasers,” Phys. Rev., Vol. 66, 1–16 (2002).

[4] E. J. W. List, C.-H. Kim, A. K. Naik, U. Scherf, G. Leising, W. Graupner, and J. Shinar, “Interaction of singlet excitons with polarons in wide band-gap organic semiconductors: A quantitative study,” Phys. Rev., Vol. 64, 1–11 (2001).

[5] M. Ichikawa, K. Nakamura, M. Inoue, H. Mishima, T. Haritani, R. Hibino, T. Koyama, and Y. Taniguchi, “Photopumped laser oscillation and charge-injected luminescence from organic semiconductor single crystals of a thiophene/phenylene co-oligomer,” Appl. Phys. Lett., Vol. 87, 221113–16 (2005).

[6] Y.-L. Liao, W.-Y. Hung, T.-H. Hou, C.-Y. Lin, and K.-T. Wong, “Hole mobilities of 2,7- and 2,2′-disubstituted 9,9′-spirobifluorene-based triaryldiamines and their application as hole transport materials in OLEDs,” Chem. Mater., Vol. 19, 6350–6357 (2007).

[7] H. Nakanotani, T. Oyamada, Y. Kawamura, H. Sasabe, and C. Adachi, “Injection and Transport of High Current Density over 1000 A/cm2 in Organic Light Emitting Diodes under Pulse Excitation,” J. Appl. Phys.,Vol. 44, 3659–3662 (2005).

[8] S. V. Frolov, M. Liess, P. A. Lane, W. Gellermann, Z. V. Vardeny, M. Ozaki, and K. Yoshino, “Exciton dynamics in soluble poly(p-phenylene-vinylene): Towards an ultrafast excitonic switch,” Phys. Rev. Lett. , Vol. 78, 4285–4288 (1997).

[9] Xin Liu, Sönke Klinkhammer, Kai Sudau, Norman Mechau, Christoph Vannahme, Johannes Kaschke, Timo Mappes, Martin Wegener and Uli Lemmer ,“Ink-Jet-Printed Organic Semiconductor Distributed Feedback Laser,” Appl. Phys. Express, Vol. 5, 072101(2012)

[10] F. Li, X. Li, J. Z. and B. Yang, “Enhanced light extraction from organic light-emitting devices by using microcontact printed silica colloidal crystals”, Organic Electronics, Vol. 8, 635–639(2003)

[11] Yu-Hsuan Ho, Kuan-YuChen, Kai-YuPeng, Ming-Chih Tsai, Wei-Cheng Tian, and Pei-Kuen Wei “Enhanced light out-coupling of organic light-emitting diode using metallic nanomesh electrodes and microlens array,” OPTICS EXPRESS, Vol. 21, (2013)

[12] Chung Sock Choi, Sung-Min Lee, Myung Sub Lim, Kyung Cheol Choi, Donghyuk Kim, DukYoung Jeon, Youngjo Yang, and O Ok Park “Improved light extraction efficiency in organic light emitting diodes with a perforated WO3 hole injection layer fabricated by use of colloidal lithography” OPTICS EXPRESS A309, Vol. 20, (2012)

[13] Sungmo Ahn, Hanbit Kim, Heonsu Jeon, , Jeong Rok Oh, Young Rag Do, and Hyo Jin Kim,“Two-Dimensional Hexagonal Lattice Photonic Crystal Band-Edge Laser Patterned by Nanosphere Lithography,” Applied Physics Express, Vol. 5, 042102 (2012)

Chapter 1 :

Nanoparticles and Photonic Crystals

1.1 General Introduction

The general context of this study deals with both the bottom-up approach of the nanostructures and with their photonic properties. More precisely, the aim of this chapter is to provide the basis for calculating the photonic properties of nanoparticle based nanostructures in order to figure out how they can be used to improve organic light sources or design new organic light sources. This is achieved in four steps: In the first section (1.2) the nano particles and their synthesis are introduced before their use to elaborate colloidal crystals is presented (section 1.3). In section 1.4, the theory of the photonic crystals as well as the different computational methods are presented. Finally, section 1.5 presents approaches of using photonic crystals as organic laser resonators.

1.2 Nanoparticles

1.2.1 Introduction

In recent years, there has been increasing interests and demands for nanoscale materials because nanometer size materials can exhibit novel and improved properties as compared to the bulk material [1]. Different interpretations of the dimensions that set the boundary between normal materials and nanomaterials have been proposed. A nanoobject should have at least one dimension smaller than 100 nm, although the term nano is interchangeably used for sizes of a few hundreds of nanometer [2]. Nanoparticles, nanofilms and nanowires are nanometric objects along three, two and one dimension, respectively. In the case of nanostructured materials, at least one of the components has a nanometric dimension. Because the nanosize materials are larger than individual atoms and molecules but are smaller than the bulk

material, they show a behavior that is intermediate between that of a macroscopic solid and that of an atomic or molecular system. These different properties are due to high surface-to-volume ratio, quantum size effect, and electrodynamic interactions [3, 4].

Nanoscience and nanotechnology are young fields which deal about the study, design and fabrication of nanoscale materials and can be used across all other science fields, such as chemistry, biology, physics, materials science, and engineering[5]. Although, nanotechnology is usually used for studies conducted at the nanoscale, the term has been increasingly used to refer to the conventional microfabrication techniques in the sub-micron range [6]. The concept of nanotechnology was first introduced in 1959 by Richard Feynman in his talk "There's Plenty of Room at the Bottom" when he imagined a day when things could be miniaturized, when huge amounts of information could be encoded onto increasingly small spaces, and when machinery could be made considerably smaller and more compact, in which he described the possibility of synthesis via direct manipulation of atoms. The term "nano-technology" was first used by Norio Taniguchi in 1974 and later by K. Eric Drexler, though it was not widely known [7].

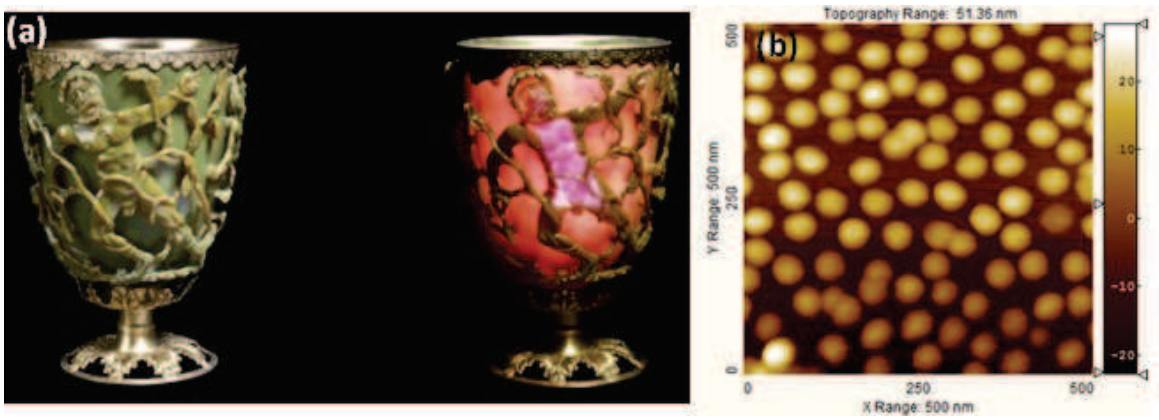

Figure 1: (a). The Lycurgus cup. (b). AFM image of gold nanoparticles [9].

Although nanotechnology is a recently used term, the application of nanoparticles dates back to the Bronze Age when people unknowingly used them to make colored glasses. The Lygurcus cup (400 AC) is a famous example of colored glass that used gold and silver nanoparticles [8]. The vessel appears dull green in reflected light, and turns bright translucent red in transmitted light (Figure 1(a) and 1(b)). The color effect arises from gold and silver nanoparticles (20-50 nm) present in the glass matrix [9]. Figure 1(b) shows atomic force microscope image of gold nanoparticles. Although the application of nanoparticles has old

history, the scientific research of nanotechnology and nanoparticles has relatively short history [10]. Michael Faraday had demonstrated the synthesis of gold nanoparticles in 1857 [11]. Later Gustavo Mie published his pioneer work explaining the fascinating optical properties of metallic colloids [12]. But in recent years, due to their novel optical, electrical, magnetic properties, structural nanoparticles have been subject of intensive scientific study. They can have applications which range from biomedicine to optoelectronics. Metallic nanoparticles like gold and silver and dielectric nanoparticles such as titanium dioxide (TiO2), silicon dioxide (SiO2), polsysterne (PS), Poly (methyl methacrylate) (PMMA), zinc oxide (ZnO) have been used for variety of applications making use of their optical and/or electronic properties. They can be used in printable inks to electronic chips, photovoltaics, sensory probes, drug delivery in biological and medical applications, and catalysis [13]. In this thesis we are interested in the study of spherical dielectric nanoparticles which can be applied to make colloidal crystals [14].

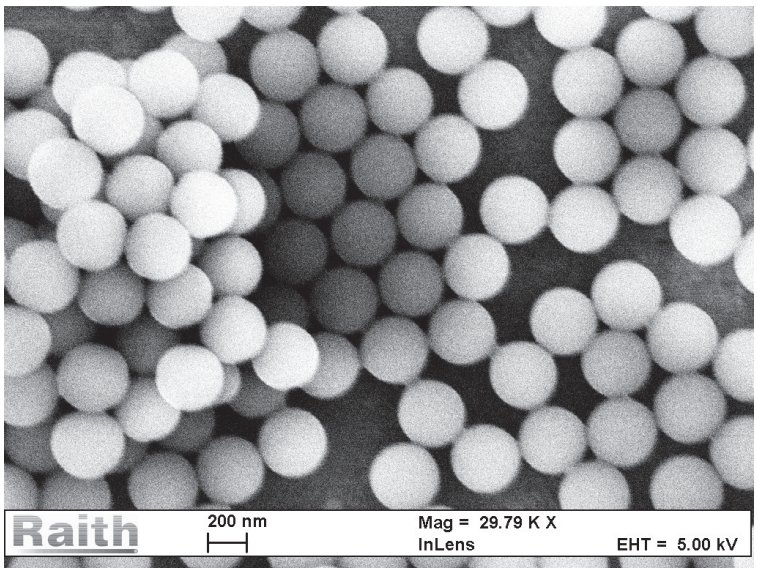

Figure 2: Polystyrene nanoparticles (Synthesized by Dr. Chia-hua Chan and Prof. Chii-Chang CHEN, National Central University (Taiwan).

1.2.2 Nano-Fabrication Process

There are two main approaches in the process of nanofabrication: the bottom-up and the top-down approaches ; The top-down approach is a conventional method of fabrication that consists in cutting small nanostructure elements from larger pieces, i.e. reducing the dimensions of the original material as shown in figure 3. Pattern transfer (lithography), deposition (or film growth), etching (or removal of material) are some of the process stepss used in thetop down approach [15].

The bottom up approach is assembling atomic or molecular building blocks in controllable fashions to form various desired structures (Figure 3). Methods of chemical vapor growth: vapor-solid-liquid (VSL) growth and self-assembly methods are examples of bottom up approaches.

The bottom-up approach has advantage of being used in large area pattering and is cost effective requiring only simple equipment. In addition, three-dimensional structures can be generated in a single step, which usually needs more steps in top-down approaches. However, the bottom up approaches have disadvantage in that they are not perfect concerning long-range pattern fidelity as compared to the top-down approach in which almost any patterns can be fabricated [16].

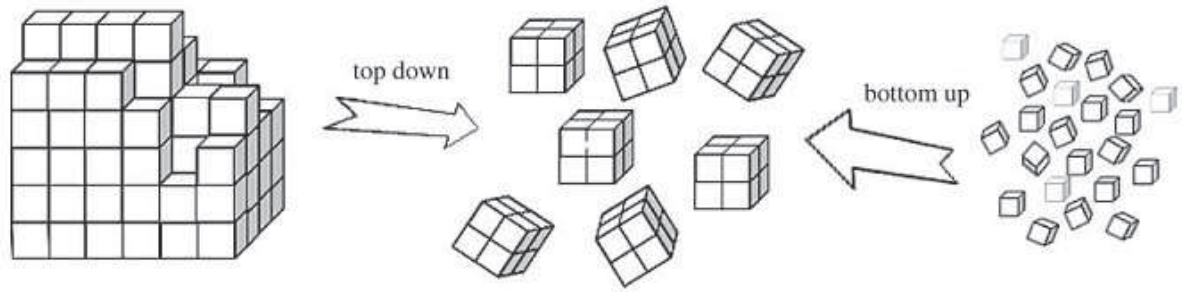

Figure 3: Bottom-up versuss top down fabrication approaches. Top down approach involves size reduction to nanoscale for assembly. Bottom up approach involves assembly from smaller units[15].

1.2.3 Synthesis of nanoparticles

Recently numerous synthesis methods were explored and successfully used to produce spherical nanoparticles. This included plasma synthesis, chemical vapor deposition, emulsion polymerization, dispersion polymerization, sol-gel processing and hydrothermal techniques [17]. The efforts in synthesis of nanoparticles include size control, shape control, morphology and surface reactivity which intern affect the optical, the electronic, and the catalytic properties of the nanoparticles.

Here we will give examples of some synthesis processes for the synthesis of dielectric TiO_2, SiO_2, and PS nanoparticles, as we are more involved in this type of nanoparticles. We will describe different approaches of synthesis of these nanoparticles.

1.2.3.1 Solgel method for the synthesis of silica and titania nanoparticles

Sol-gel technique is inexpensive low temperature wet synthetic method for the synthesis of inorganic polymeric materials [18]. The Solgel process involves the evolution of inorganic networks through the formation of a colloidal suspension (sol) and gelation of the sol to form a network in a continuous liquid phase (gel). This process can be used to synthesis silica (SiO_2) and titania(TiO_2) microspheres [19].

The solgel process involves two steps: hydrolysis (Eq. a) and polycondensation (Eq. b and c) as indicated below. Metal alkoxides (M(OR)x, where M = Si, B, Ti, Al, etc. and R is an alkyl-group, e.g. CH_3, C_2H_5, C_3H_7, etc.) are used as precursors, catalyzed by an acid or base, in alcoholic solutions (at temperatures < 100°C). The metal alkoxide is partially hydrolyzed and polymerized to form a 3-dimensional glass-like network in which multivalent metal atoms are linked together by difunctional bridging oxygen atoms[20].

$$\text{M-OR + HOH} \longrightarrow \text{M-OH + ROH} \quad \text{hydrolysis (a)}$$

$$\text{M-OH + HO-M} \longrightarrow \text{M-O-M + HOH} \quad \text{water Condensation (b)}$$

$$\text{M-OH + RO-M} \longrightarrow \text{M-O-M +ROH} \quad \text{alcohol Condensation (c)}$$

For the synthesis of SiO_2 nanoparticles , the alkoxide tetraethyl orthosilicate (TEOS) ($Si(OC_2H_5)_4$) (Si $(OEt)_4$) can be used as a precursur. The general reactions of TEOS that leads to the formation of silica particles in the sol-gel process can be written as:

$$Si(OC_2H_5)_4 + H_2O \xrightarrow{\text{hydrolysis}} Si(OC_2H_5)_3OH + C_2H_5OH$$

$$\equiv Si - O - H + H - O - Si \equiv \xrightarrow{\text{water condensation}} \equiv Si - O - Si \equiv + H_2O$$

$$\equiv Si - OC_2H_5 + H - O - Si \equiv \xrightarrow{\text{alcohol condensation}} \equiv Si - O - Si \equiv + C_2H_5OH$$

The hydrolysis of TEOS molecules forms silanol groups. The condensation/ polymerization between the silanol groups or between silanol groups and ethoxy groups creates siloxane bridges (Si–O–Si) that form entire silica structure [21]. Similarly TiO_2 nanoparticles can be synthesised by using titanium isopropoxide, $[Ti(OC_3H_7)_4]$, as a precursor [22].

1.2.3.2 Synthesis of polystrene (PS) nanoparticles by emulsion polymerization

Polsystirene (PS) latexes are microscopic polymeric dispersions in a liquids . In the synthesis process of PS latexes, latexes start out as monomer emulsions which are monomer droplets immiscibly dispersed in water. The emulsions are subsequently polymerized to form latexes. This polymerization process is known as emulsion polymerization and is a common chemical synthesis method of PS nanoparticles [23].The two main processes in the formation of nanoparticles in emulsion polymerization are: nucleation and growth. The typical reaction mixture in emulsion polymerization consists of water, of the monomer, and of a water-soluble initiator which are completed by an emulsifier [24].

1.3 Colloidal crystals: Nanoparticle based crystals

1.3.1 Introduction

Colloids consist of small, discrete particles dispersed in a continuous liquid media. Colloidal crystals are three-dimensional or two dimensional crystals which are made by the organization or crystallization of monodispersed spherical colloids. Colloidal crystalline

lattices diffract light in a similar fashion that atoms and molecular crystals diffract x-rays [16]. In recent years, colloidal crystals have received a great deal of attention because of their applications in the manipulation of light and of the photonic band gap properties. The gemstone opal is a good example of naturally occurring colloidal crystal which is formed by sedimentation of silicon dioxide in water [25]. The gemstone opal diffracts visible and near-infrared light as a result of the sub-micrometer diameters of the colloids which gives its natural astonishing color as in figure (4(a)) below. Colloidal crystals can also be fabricated artificially by a process called self-organization. Figure 4(b) shows thin film of artificial opal deposited on glass substrate, while figure 4(c) shows scanning electron microscope (SEM) image of regularly arranged spherical particles [25, 26, 27].

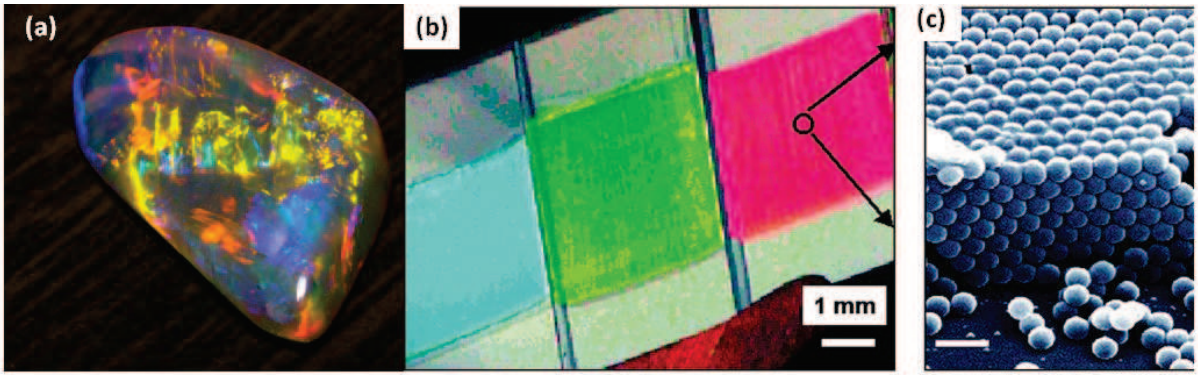

Figure 4: Artificial and natural opals. (a) Phototograph of natural opal. (b) Thin films of colloidal crystals (artificial opal). (c) A scanning electron micrograph of micrometer structure of these films (scale bar, 1 μm) [26].

By controlling the self-organization process two dimensional or three dimensional dielectric nanosphere based photonic crystals can be fabricated. When single-layers of dielectric spheres are made as in indicated in figure 5, they can be assumed as 2D photonic crystal slabs based on spheres, rather than cylinders, and hexagonal close packed arrangement is mainly obtained [28]. The other type of structure which is obtained by the self-organization is the multilayer of microspheres which can be assimilated to a 3D photonic crystal. If multilayer of microspheres are considered, the FCC crystal structure is considered. The entropy of the system is such that the minimum energy or more stable structure correspond to those of an FCC arrangement [21,29]. The figure 5(b) shows the schematic diagram of the opal structure which is 3D fcc lattice. The opal photonic crystal has connected air veins. By infiltration the opal with a dielectric materials and subsequent removal of the nanospheres, an inverse opal with connected dielectric veins can be obtained.

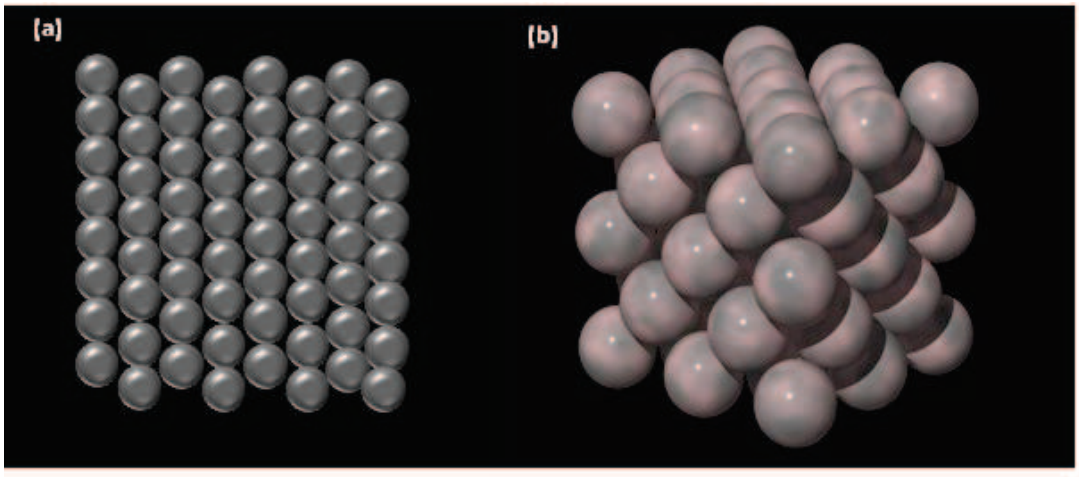

Figure 5: Schematic diagram of colloidal crystals which can be obtained by artificial self organization process. (a) ML of microspheres, which is 2D hexagonal structure. (b) An FCC Opal structure.

1.3.2 The self-organization method: towards colloidal crystals

Although traditional top-down microfabrication methods provide good control and more defect free photonic crystal structures, they are time consuming and expensive. The making of 3D periodic structures with such method is even more complicated and is stepwise [30].

But the availability of nanospheres which can be synthesized by relatively cheaper chemical process and the possibility of using them in a bottom-up approach opened a better alternative to the top-down approach fabrication method of photonic crystals [29]. In contrast to top-down fabrication approaches which use lithographic or other means to carve periodic structures, the bottom-up self-organization method is used to form colloidal crystals spontaneously under ambient conditions of pressure and temperature. The self-organization method is more advantageous over the top-down approaches in that it provides rapid,inexpensive, and easily controlled deposition on large areas [31,32,33,34].

The self-organization of nanoparticles can be made by different techniques like centrifugation [35], sedimentation [36], evaporation[37], dip coating[38], drop coating[33] or spin coating [39]. Although each method might be preferable over the other according to the required product, the main driving force for the final close-packed particle self-assembly is, in all cases, the same: attractive capillary forces between the particles and convective flow may contribute to transporting particles to the drying front [27].

In this thesis, we will give more emphasis on the fabrication of multilayer of nanoparticles by convective selfassembly method and the fabrication of monolayers of hexagonal closed packed spheres by drop coating and dip coating techniques.

1.3.2.1 Fabrication of opals: 3D periodical structures

To obtain the desired optical properties, making high quality opals without undesired defects is important. The number of defects depends on many parameters such as particle monodispersity and the size of particles. Larger monodispersity implies lesser number of defects. Also when particles are large in size, the probability to have misplacements in the particle settlement increases.

1.3.2.1.1 Self-assembly by sedimentation

Colloidal crystallization by sedimentation is one of the most commonly used techniques for making 3D colloidal crystals. Sedimentation by gravitational force provides a simple and efficient method to achieve multilayer assemblies of mesoscale particles. However, one major disadvantage of this method is the limited range of sizes that can be used to make photonic bandgap materials. Small particles (smaller than 300nm) take a very long time to deposit or don't deposit at all, and large particles (larger than 550nm) deposit too quickly, resulting in poor periodicity, and is not a convenient method [21, 29,36,40]. To solve this problem, sedimentation by centrifugal force can be used. During centrifugation, centrifugal force from the rotation and capillary force from solvent evaporation act together to assemble the spheres in a cubic close-packed arrangement [35].

1.3.2.1.2 Convective self-organization

The usual mechanism of self-organization of colloidal particle suspensions in thin evaporating films is know as "*convective self-organization*" or "*evaporation induced self-assembly*" [31,32,33,41]. In convective self-organization, a substrate is inserted in a solution of nanospheres as shown in figure 6(a) and the particle suspension is left to evaporate naturally depositing

high-quality thin colloidal crystal films on a vertical substrate via the meniscus of an evaporating solvent. The flow of water caused by solvent evaporation leads the particles to self-organize onto a substrate in an ordered way, the flux of the liquid compensating for evaporation from the crystal surface [42, 43].

The convective self-assembly method is fast, requires only small amount of suspension, without the need for any complex or expensive equipment [41]. The self-organization process starts from monodispersed spherical colloids, which are small spherical solid particles dispersed in a fluid [29].

To control the number of layers, it is important to control the rate of evaporation and the angle of inclination of substrate in this technique. When the substrates are inclined at different angles as in figure 6(b), the contact line shape at the air water glass substrate interface are varied as shown in figure 6(c) below. The contact line shape of the sample tilted to -10° is the steepest and gradually becomes smoother as the tilted angle increases. Thus, the thickness of ordered colloidal particles assembling in the vicinity of the air water glass substrate interface can be controlled by the tilted angle of the dipped glass substrate [34].

This method has two limitations: the long evaporation time and, more importantly the deposition is limited to smaller colloidal particles that sediment at a rate that is slower than the evaporation of the solvent. If the sedimentation rate is faster than the evaporation rate, colloidal particles depart from the meniscus, and the deposition process is terminated [29].

The acceleration or deceleration of the array formation and the quality of the film can be controlled by changing the environmental conditions, such as humidity, temperature, and particle volume fraction.

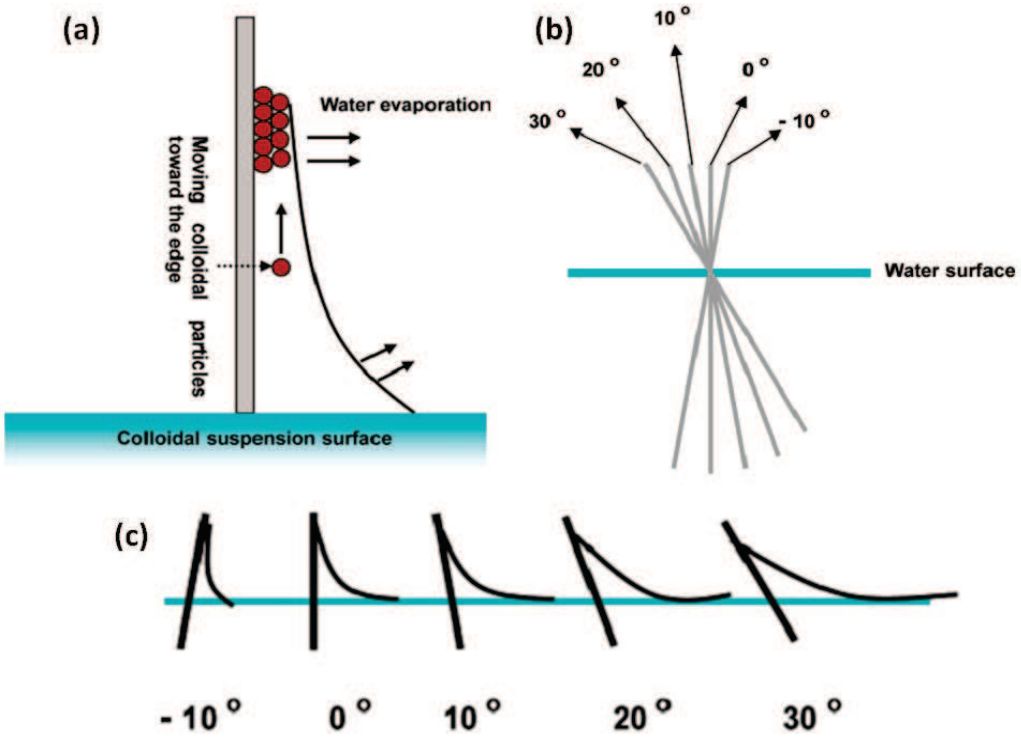

Figure 6: (a) Systematic illustration of convective self-assembly. (b) Substrate inclined at different angles. The normal to the water surface plane is 0° and established tilted angles are -10°, 0°, 10°, 20°,and 30°, respectively. (c) Contact line shapes with tilted angles.[30]

1.3.2.2 Fabrication of single layer of self-organized spheres :

Several techniques allow the fabrication of single layer of self-organized spheres. Among this are the dip coating technique and the drop coating techniques.

1.3.2.2.1 Drop coating:

To create single layer of nanoparticles, the technique of drop coating can be used. When a latex solution is dropped on a substrate surface, the drop spreads on the surface of the substrate as Denkov et al studied [33].The evaporation of water leads to a gradual decrease of the liquid layer thickness with time. Until the thickness is larger than the particle diameter, it decreases uniformly. The array formation starts when the thickness of water layer becomes

approximately equal to the particles diameter and the crystal growth takes place through a directional motion of particles towards the ordered region (figure 7(a)). Once the order regions are formed the thinning of the water layer inside them is slowed due to the hydrophilicity of the particles. The kinetic observations of the crystallization demonstrate two distinct processes: nucleation, preceded by thinning of the thin liquid film, and crystal growth. Figure 7(b) shows the process of ordering. The particles in the upper left part of the photograph are moving towards the ordered phase, building up the hexagonal array.

Particle concentration has a big impact on the quality of single-layer. Highly concentrated solution give bilayer or multilayer arrangement and low contractions result in formation of large area without the single layer, or many small groups of nanoparticles [33,44,45,46].

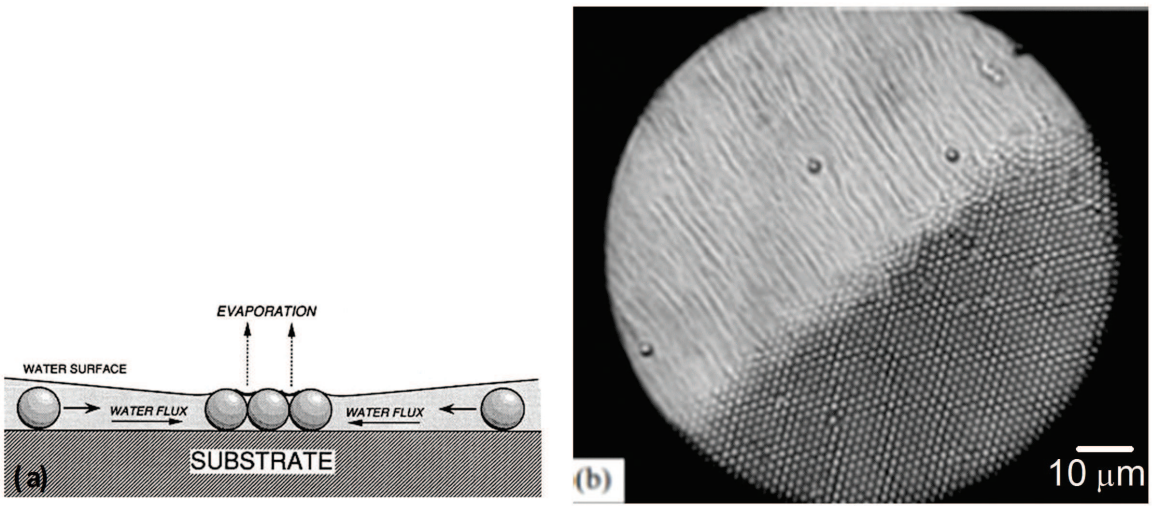

Figure 7: Principle of drop coating. (a) Convective flux toward the ordered phase due to the water evaporation from the menisci between the particles in the 2D array. (b) The process of ordering. The particles in the upper left part of the photograph are moving towards the ordered phase, building up the hexagonal array. [33]

1.3.2.2.2 Dip coating:

The basic principle of dip coating is that if a wetting vertical substrate is withdrawn from a solution of colloidal crystals at a particular rate, one may be able to deposit a single-layer of colloids on the substrate with the growth direction being opposite to the direction of drawing[27,38, 47].

Figure 8 shows schematic diagram of the principle of dip coating. A substrate is dipped vertically into a suspension of nanoparticles and is drawn up with a velocity of ν_w . When the substrate is drawn upwards, there is suspension influx from the bulk suspension toward the wetting suspension film. The upward influx consists of a water component, j_w, and of a particle flux component, j_p. The water flux j_w compensates for the water evaporated from the film j_e, and the particle flux j_p causes particles to accumulate in the film, thus forming dense structures [38]. The factors which affect film quality and thickness are temperature, withdrawing speed, sphere diameter and colloidal concentration [47].

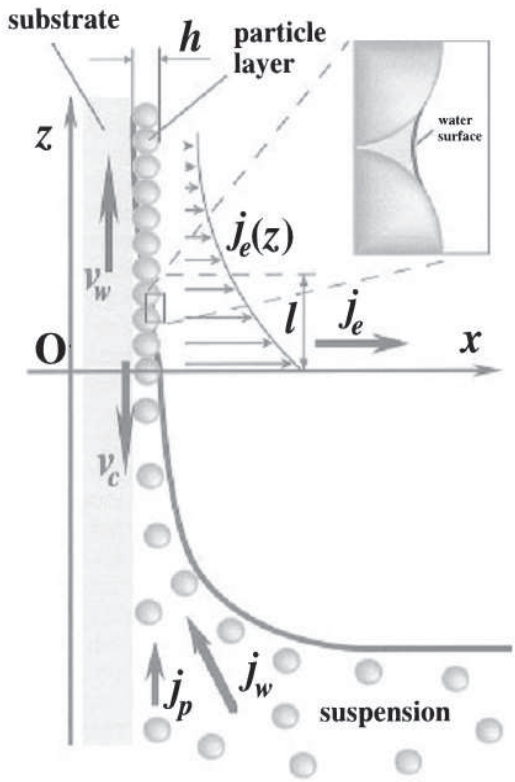

Figure 8: Sketch of the particle and water fluxes in the vicinity of monolayer particle arrays growing on a substrate plate that is being withdrawn from a suspension. The inset shows the menisci shape between neighboring particles. Here, v_w is the substrate withdrawal rate, v_c is the array growth rate, j_w is the water influx, j_p is the respective particle influx, j_e is the water evaporation flux, and h is the thickness of the array.[38]

1.3.2.3 Fabrication methods of inverse opals

Inverse opals are negative replicas of opals. Instead of consisting of a regular arrangement of uniform spherical dielectric spheres (as in opals), they consist of a regular arrangement of spherical voids surrounded by solid walls.

Inverse opals are fabricated in the following steps.

1. Self-assembly to make the template (opal)
2. Matrix infiltration

3. Template removal (etching or pyrolysis)

Inverse opals are usually fabricated by assembly of a colloidal crystal template (e.g., comprised of polymer latex spheres), infiltration and deposition of a matrix phase, or a precursor to a solid matrix phase for infiltration and subsequently removing the spheres by *pyrolysis* or etching methods. Here the colloidal crystals (opals) serve as templates, the voids of which are infiltrated by material that solidifies there. The original colloidal particles are subsequently removed, leaving behind a new material with pores [48].

The infiltration of the voids can be made by chemical vapor deposition[49], atomic layer deposition[50] or sol-gel wet chemical method. From the simplicity of the process, we will focus on the solgel method of infiltration. The removal of the templates can be done thermally for low melting point microspheres or by chemical attack.

1.3.2.3.1 Sol-gel infiltration:

The solgel method uses liquid precursors to infiltrate the opal template and is an easy and effective way of generating inverse opals. The liquid precursors infiltrate the space between the spheres by capillary forces. After curing the liquid precursor into a solid, the colloidal particles are selectively removed through a calcination (thermal removal) (for spheres like PMMA, PS...) or chemical etching according to the material of the templates [51, 52]. The final radius of the air spheres and the spacing between the spheres can be controlled by the radius of the original colloidal spheres [53]. The following diagram (figure 9) shows the process of making inverse opal photonic crystals. A template opal structure is infiltrated with the precursor solution and after template removal the inverse opal structure is obtained [54].

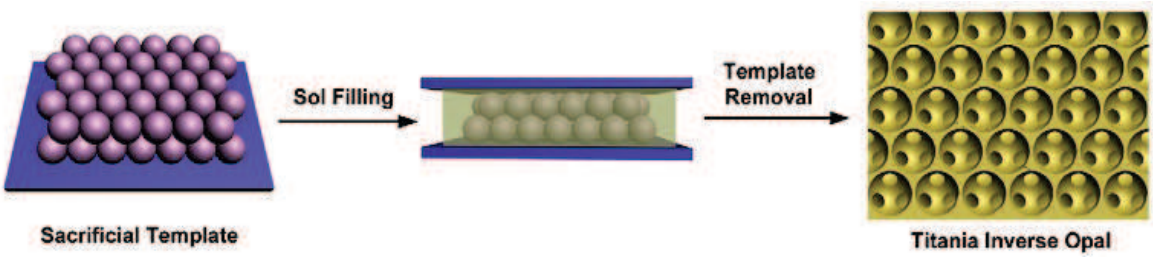

Figure 9: Schematic fabrication process for the formation of titania inverse opal by an optimized sol–gel opal infiltration.[20]

Titania has several solid polymorphs depending on the temperature to which it is heated. Rutile, the most stable phase (crystalline phase), is formed at temperatures beyond 600 °C. Rutile is an interesting structure for photonic crystals because it has a higher refractive index than anastase, which has intern higher refractive index than the amorphous phase of TiO2 [23,22].

1.3.2.4 Technological approach to the fabrication of nanoparticle based photonic crystal defects

Incorporating precise, controlled pre-engineered defects in photonic crystals using conventional lithography techniques like ebeam lithography is more straightforward. In conventional lithography the defects don't require any special processing aside from that needed to form the PhC it self. But other methods like colloidal self-organization need other external methods to make the defects. Although uncontrolled defects can appear in the self-organization of colloidal crystals, the controlled addition of well-defined defects has not been shown to be not compatible with the self-assembly process so far [55].

One method has been the nanorobotics for artificial assembly and making opal like crystals with better optical properties or to make target defects [21].

Recently electron beam lithography was used to make controlled defects in opals. For the inscription of single-site defects, electron beam is used with control of the penetration depth as well as the transverse extent of the cloud of scattered electrons inside individual beads. PMMA microspheres, which are sensitive to electron beam were used, and after exposure development is used for the removal of the selectively exposed beads as shown in figure 9(a) [56].

In addition, introducing physical templates on the substrate with the required pattern can be used before the assembly of microspheres is made so that the nanospheres will assemble to have a monolayer of sphere defined by the template. Figure 9(b) and 9(c) show a square lattice of monolayer of nanoparticles, and unique assembled of monolayers of spheres made by surface templating [57, 58]. The templates (eg. 2D array of holes) can be lithographically patterned on a the substrate.

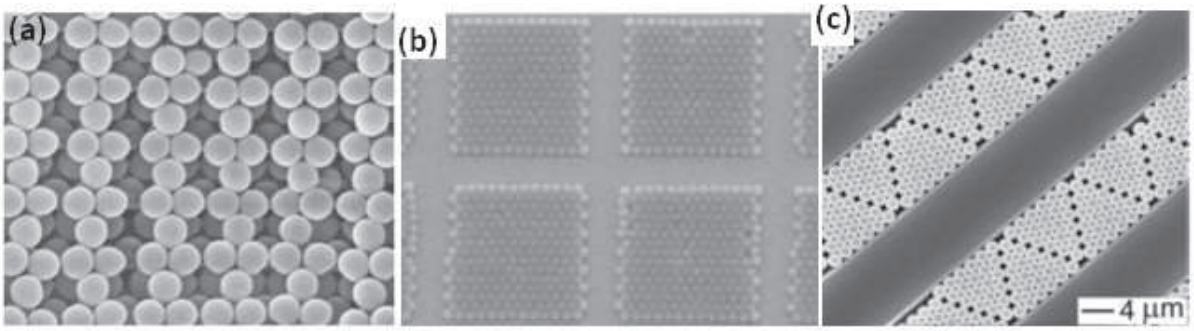

Figure 10: (a)Scanning electron microscope image of a gold-coated rectangular lattice of defects inscribed in the three-dimensional crystal of opal structure. The second layer of the face centered cubic lattice of beads is displayed in the sites of open defects [55] (b) Example of structures combining self-organization and top-down approach [57] (c) 2D colloidal crystal pattern made by surface templating against channels [58]

1.3.2.5 Fabrication of non-closed packed 2D colloidal crystals

2D colloidal crystals fabricated by the usual self-oganization methods are hexagonally arranged densely packed structures. This arrangement is the most thermodynamic stable arrangement with the minimum free energy. But for optical applications, the optimum optical design may not match with the closed packed arrangement of spheres. Various approaches have been tried to make such non-compact spheres. Among them is the etching of closed packed spheres**.** The nanospheres are etched down to the desired diameter while conserving their position. The distance between nanospheres can be controlled by choosing a good size of nanospheres to make the closed packed structure and the size of microspheres can be controlled by the etching amount.

Different etching methods like isotropic plasma etching, anisotropic reactive ion etching (RIE) and electron beam irradiation were used to achieve non compact hexagonal arrangement of spheres. Figures 11 (a)-(d) show the etching of different microspheres by plasma. The size of the spheres is reduced successively from figure (*a)* to (*d)* by increasing the etching time keeping the same distance between the center of the spheres [59]. Once defects are made in opals, subsequent processes of making the inverse-opals will also have the defects.

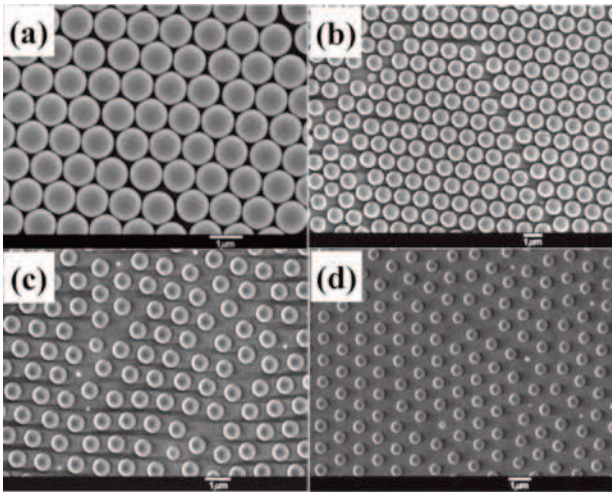

Figure 11: SEM images of 2D PS colloidal crystals. (a) Initial 1000 nm microspheres in closely packed arrays, (b-d) non-close-packed colloidal crystals by plasma etching 4, 6, 7 min, respectively.[59]

1.4 Photonic Crystals

1.4.1 Introduction

The quest for compact and low threshold lasers and the possibility of integrating them with waveguides, modulators, and detectors has led to an intensive technological and scientific research on the controlling and engineering of the optical properties of materials [60, 61]. One of these optical materials which have been studied in the past few decades are the Photonic Crystals (PhCs) [62]. PhCs are materials with a spatial periodicity in their dielectric constant and are composed of a periodic array of macroscopic dielectric and/or metallic unit cells. The interaction of photonic crystals with light is analogous to that in which crystal lattices interact with electrons [62,63]. An electron passing through a semiconductor experiences a periodic potential due to the ordered atomic lattice and both the crystal and the geometry of the lattice dictate the conduction properties of the crystal [61,62,63]. Similarly, in photonic crystals, photons experience periodic dielectric functions (or periodic dielectric constant). For light to interact with the photonic crystal, the periodicity of the photonic crystal should becomparable with the wavelength of light.

If a photonic crystal prohibits the propagation of electromagnetic waves, for certain frequencies, of any polarization traveling in any direction, then we say that the crystal has a **complete photonic band gap (PBG)**. If light is prohibited in just specific directions of for specific wavelengths, then we call it **partial PBG** [13]. Figure 12 is a schematic diagram of a PhC with incident light, transmitted light which propagates through the PhC and reflected light which is prohibited in the PhC. The bandgaps gives rise to distinct optical phenomena and can be used in inhibition of spontaneous emission, high-reflecting omni-directional mirrors and low-threshold PC lasers, low loss waveguides, cavity resonators, and nanolasers, etc. [13, 64, 65,66].

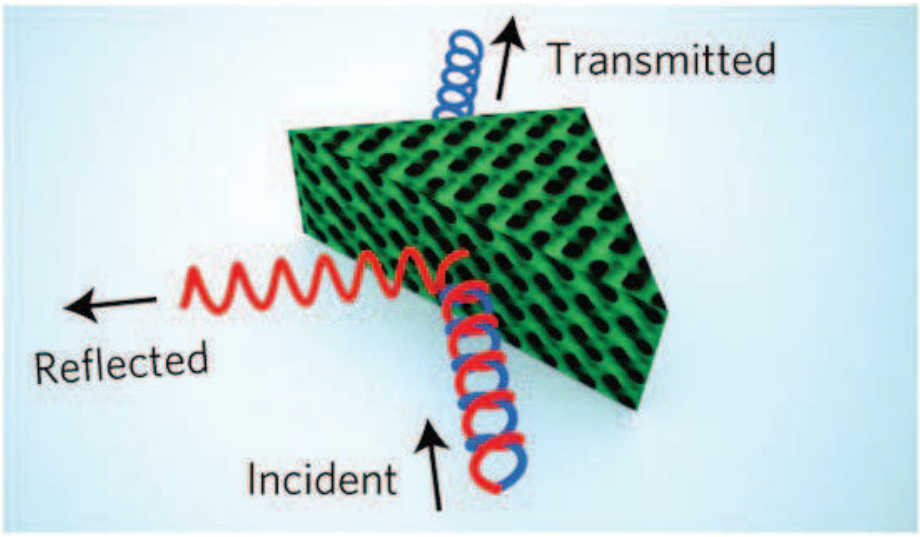

Figure 12: Incident beam with red and blue wavelengths on a PhC: blue light is transmitted and red light is reflected [66].

1.4.2 History of photonic crystals

In 1888 Lord Rayleigh studied electromagnetic wave propagation in periodic media. The periodic media consisted in periodic variation of planar refractive indices. Rayleigh understood that infinitesimal periodic variation in the structure would produce a bandgap, and that it would make a "total reflection mirror". After Rayleigh's time there have been many great achievements in extending the ideas of 1D laminated mirrors for applications in optical interference filters and lasers cavities. But the name "photonic crystals" came along a century after one dimensional bandgaps were studied, when Yablonovitch and John published two milestone papers on PCs in 1987 [13,67,68]. In 1987, Yablonovitch and John have proposed

higher dimensional periodic structures which have a periodic variation in two dimensions and three dimensions. The periodic dielectric structures should exhibit sufficiently large difference in refractive index so that photonic band gap would exist. After 1987, the number of research papers concerning photonic crystals grew in large numbers. But due to the difficulty in fabricating actual photonic crystals, most of the studies have been theoretical or experimental in microwave regime, using structures at millimeter or centimeter scale, as in the experimental study of 3D face center cubic structure by Yablonovitch in 1989 [69]. In 1991 and 1992 microwave propagation and band structure measurements in two dimensional periodic structures was studied [70,71]. In 1993 fabrication of 2D photonic crystal operating in the mid infrared was demonstrated [72]. In 1995 interferometric measurement in opals colloidal crystals was demonstrated [73]. In 1996, Thomas Krauss made the first demonstration of a two dimensional photonic crystal at optical wavelengths [74]. This opened up the way for photonic crystals to be fabricated in semiconductor materials. At the same year, laser incorporating 2D photonic ban gap mirrors was demonstrated [75]. And in 1999 2D defect mode band gap laser were demonstrated [76]. The next years the fabrication and the characterization of photonic crystals and devices based on 2D periodic structures and colloidal crystals has been reported [77].

1.4.3 Types of photonic crystals

The simplest example of a photonic crystal is in 1D and consists of a multilayer stack of two dielectric materials, in which the periodic variation is in one direction and homogenous in the other two directions (figure 13(a)). PhC structure(s) that are periodic in two different directions and homogeneous in third direction are called two – dimensional (2D) photonic crystals (figure 13(b)). Usually 2D PhCs consist of dielectric rods in air host (high dielectric pillars embedded in a low dielectric medium) or air holes in a dielectric region (low dielectric rods in a connected higher dielectric lattice). While if the periodicity is in three dimensions, the photonic crystals is called three dimensional (3D) photonic crystal (figure 13(c)). If sufficiently high dielectric contrast and suitable periodicity are met, a photonic band gap (PBG) appears in all directions and light can be reflected from any directions.

Photonic crystal slab structures consist of a 2D photonic crystal (core) surrounded by two layers of lower effective refractive index (claddings) that provide an index guiding by total

internal reflection in the direction normal to the plane of the crystal. PhC slabs can be considered 2.5D type PhCs. Indeed if there is a periodicity in two dimension, the finite height of the slab made for example of parallel cylinders of holes or pillars or single-layer of ordered nanospheres prevent it to be fully 3 dimensional .

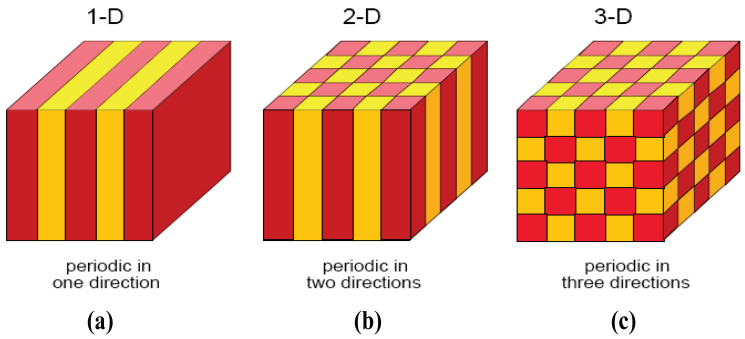

Figure 13: Photonic crystals (a) 1D photonic crystal. (b) 2D photonic crystal (c) 3D photonic crystal. [61]

In reality photonic crystals can't be made to infinite, but can be approximated to be infinite, in respective directions, after certain number of periodicities. The figure 14 shows real artificial photonic crystals slabs which are made from dielectric pillars, air holes, single-layer of spherical nanoparticles and a 3D photonic crystal based on microspheres.

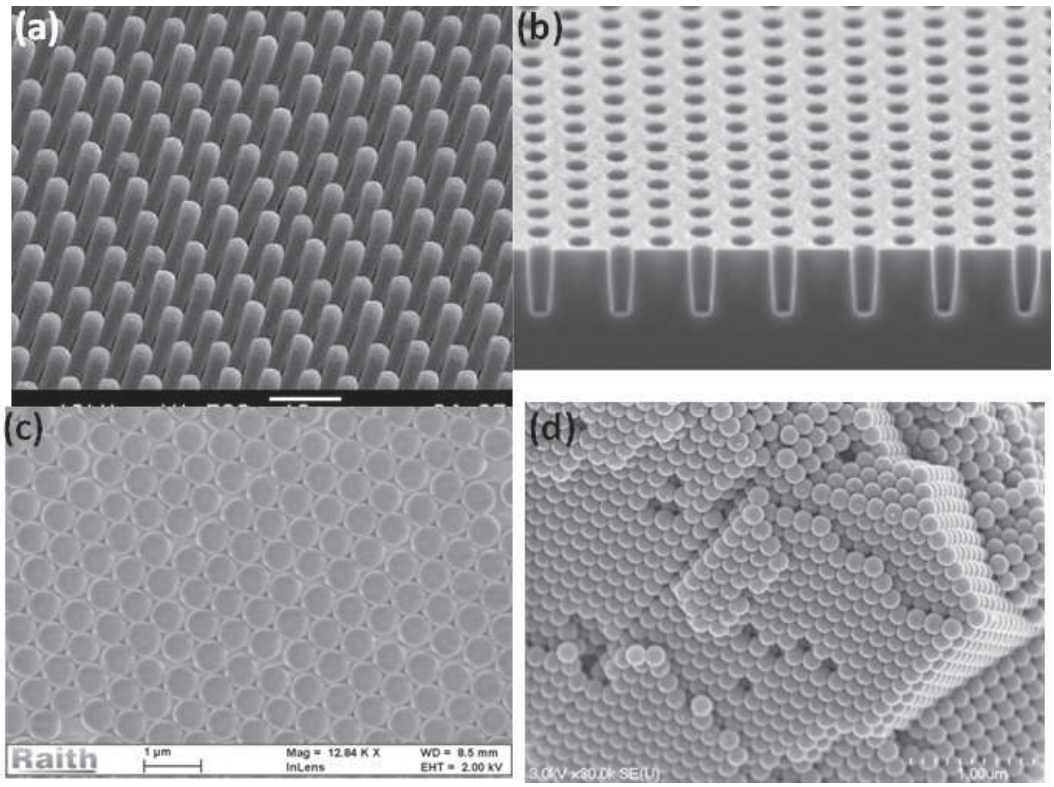

Figure 14: Real photonic crystals (a) Dielectric pillars PhC slab. (b) air holes PhC slab. (c) single-layer of spheres PhC slab. (d) 3D photonic crystal made from dielectric spheres.

A description of the photonic crystals uses Bravais Lattice. A Bravais lattice is an infinite array of discrete points that stay invariant by any translation of a vector **R** as expressed below [78,79,80]. Photonic crystals like other crystal structures consist of a pattern repeated periodically, and have discrete translational lattice. Therefore Bravais lattices constitute an interesting formalism for the description of the photonic crystal as discussed below.

1.4.3.1 One dimensional lattices

The basic step in the one dimensional lattice shown on figure 15(a) is related to the lattice constant ***a***, and to the basic step vector x also called the primitive lattice vector :

$$a\vec{x} \tag{1}$$

The lattice can be constructed by translating the unit cell of length ***a*** by the amount R and by repeating this translation over an over which defines a set of translation vectors R defined by:

$$\vec{R} = n.\, a\vec{x} \qquad (2)$$

Where ***n*** range over the integers.

The dielectric constant in the x-direction can be expressed as:

$$\varepsilon(x) = \varepsilon(x + R) \qquad \textbf{Eq. (3)}$$

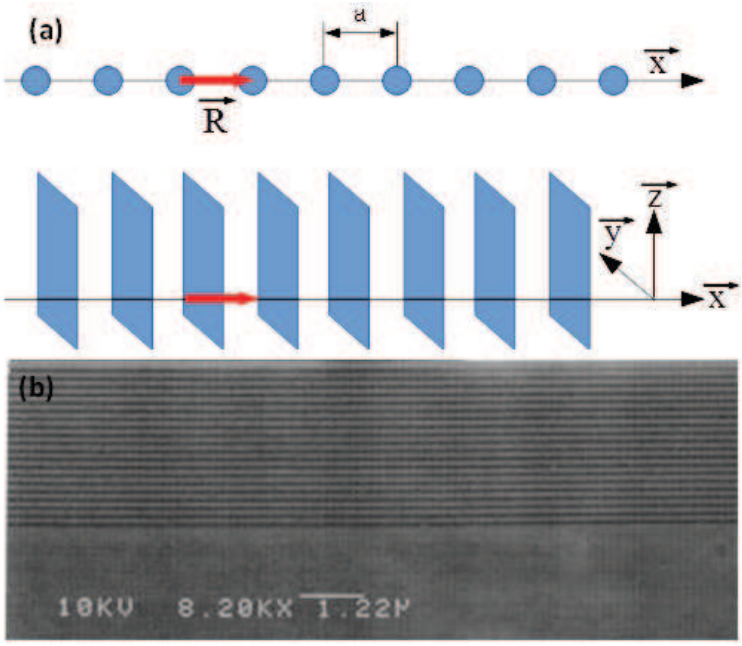

Figure 15: (a) One dimensional Bravais lattice. (b) One dimensional photonic crystal consisting of a multilayer stack of dielectric materials.

In a real system, a multilayer stack with alternative changes in the dielectric constant in one direction as shown in figure 15 (b) can be considered as a 1D PhC.

1.4.3.2 Two dimensional photonic crystal lattices

With two-dimensional photonic crystals periodic along two of its axes and homogeneous along the third axis, the lattice vectors **R** writes :

$$\vec{\mathbf{R}} = n_1 \mathbf{a_1} \vec{x} + n_2 \mathbf{a_2} \vec{y} \qquad \text{Eq. (4)}$$

where, a_1, a_2 are the primitive vectors of the 2D lattice, and n_1, n_2 range through all integers.

The vectors a1, a2 are the primitive vectors. It is important to notice that the set of vectors a1, a2 is not unique but all primitive unit cells shown on the figure have the same area S.

Thus the dielectric constant in the 2D photonic crystal plane can be expressed as :

$$\varepsilon(x,y) = \varepsilon(x+n_1a_1,\ y+n_2a_2) \qquad \textit{Eq. (5)}$$

Figure 16(b) shows a 2D square lattice PhC slab.

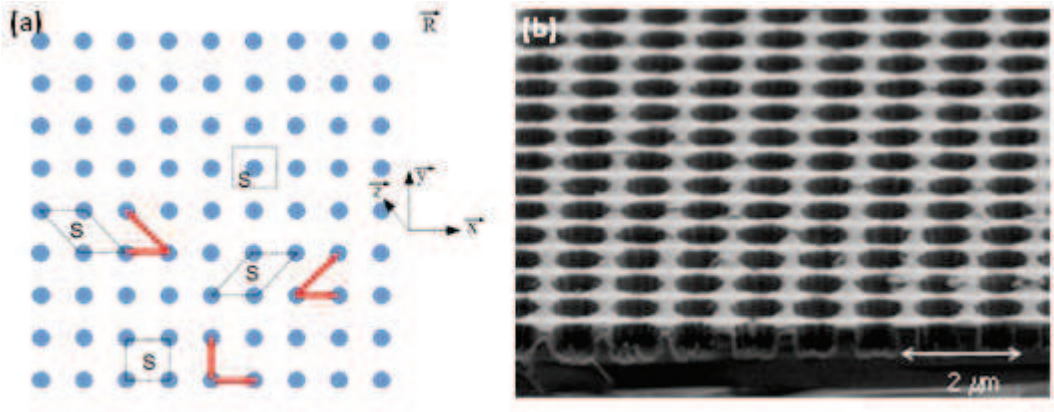

Figure 16: (a) A 2D crystal lattice. (b) SEM image of a 2D square lattice photonic crystal.

The Wigner-Seitz cell is a special type of primitive unit cell of a lattice. For a lattice point P, the Wigner-Seitz cell is the region in space that is the closest to that lattice point than to any other lattice point. Wigner-Seitz cell for 2D lattice is constructed by first drawing lines to connect the lattice point P to all nearby lattice points, and then drawing perpendicular bisector lines to the first lines. The Wigner-Seitz cell is the smallest area, innermost region,

enclosed by the lattice lines. Each step of the procedure to construct the Wigner-Seitz cell is shown in figure 17. This procedure can easily be extended to three dimensional lattices. The primary difference is that the perpendicular bisector lines will now be planes. The Wigner-Seitz cell is important to understand the Brillouin zone in the reciprocal space as will be discussed below [81].

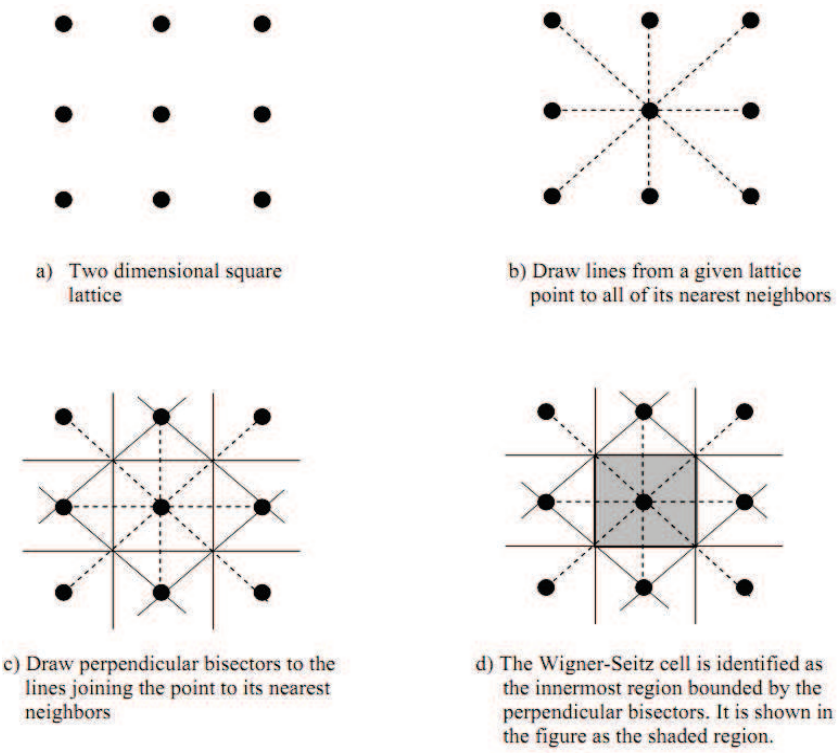

Figure 17: The steps to identify the Wigner-Seitz cell about a lattice point in a two dimensional square lattice. [82]

A common 2D photonic crystal lattice is the hexagonal lattice with equal length of lattice vectors a_1 and a_2 with angle $\theta=120°$ between them . The hexagonal lattice has the highest rotation symmetry, under the rotation of $2\pi/6$ (figure 18(a)). The Wigner-Seitz cell of a hexagonal lattice is shown in figure 18(b) bounded by red lines. The self-assembled monolayer of dielectric spheres has a 2D hexagonal lattice as shown in the figure 18(c) below. Thus, the hexagonal lattice type will be our focus of study.

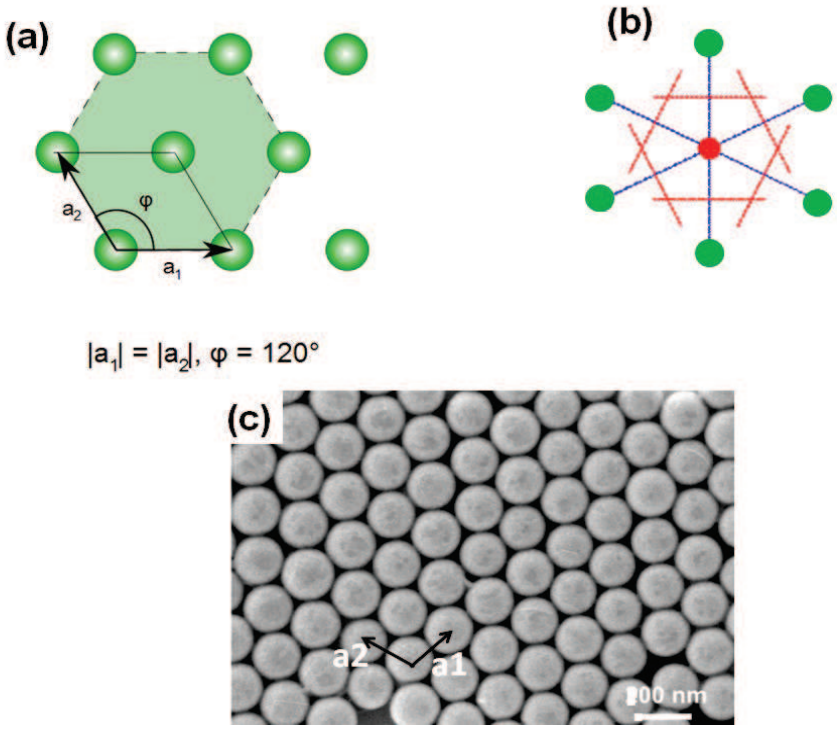

Figure 18: 2D hexagonal lattice. (a) a 2D hexagonal lattice with primitive lattice vectors a_1 and a_2.The lattice has a 60° rotational symmetry. (b) Wigner-Seitz cell of a 2D hexagonal lattice. (c) SEM image of a monolayer of dielectric spheres PhC, with a 2D hexagonal lattice.

1.4.3.3 Three dimensional photonic crystal lattices

The basic pattern also called the unit cell of a 3D Bravais lattive has the dimensions (a_1, a_2, a_3) respectively in the x, y, and z direction. The primitive lattice vectors is :

$$a_1\vec{x}+a_2\vec{y}+a_3\vec{z} \tag{6}$$

The periodic pattern of the material is obtained by any discrete translation R :

$$\vec{R}=n_1 a_1\vec{x}+n_2 a_2\vec{y}+n_3 a_3\vec{z} \tag{7}$$

where a_1, a_2 and a_3 are three non-coplanar primitive translation vectors, and n_1, n_2 and n_3 are arbitrary integers.

There are 14 different Bravais lattices which can be constructed in 3D lattices, by varying the magnitude of the primitive lattice vectors a_1, a_2, a_3 and the angle α_1, α_2 and α_3 between them, as shown in the figure below.

But for our purpose we will consider the cubic lattice with $a_1 = a_2 = a_3$, and $\alpha_1 = \alpha_2 = \alpha_3 = 90°$, where α_1 is the angle between a_1 and a_2, α_2 is the angle between a_1 and a_3 and α_3 is the angle between a_2 and a_3 as in figure 19(a). The cubic lattice can be primitive, in which there is one lattice point at each corner of a cube. The body center cubic lattice has one lattice point in the center of the unit cell in addition to the eight corner points and the face center cubic lattice has one lattice point at each face of a cube, in addition to the lattice points at the corners. The face center cubic (fcc) lattice is of main interests to us, as this type of lattice is the one usually obtained when nanoparticles self-assemble to make 3D photonic crustal structure.

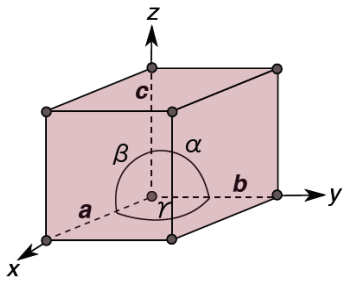

(a)

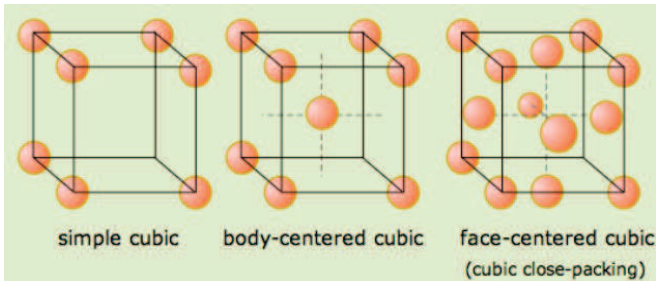

(b)

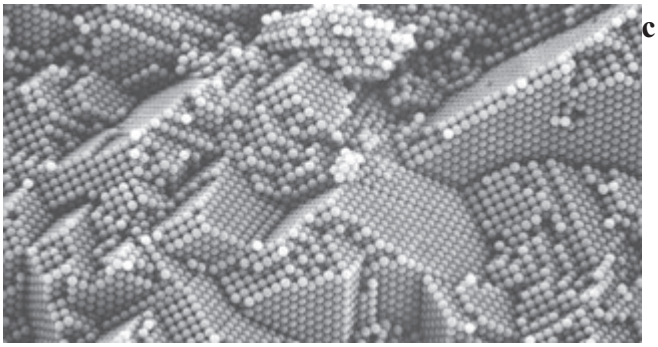

c

(c)

Figure 19: (a) a unit cell of a 3D lattice. (b) the cubic lattice (primitive, body centered, and face centered lattices). (c) A 3D photonic crystal lattice from dielectric microspheres. [83]

1.4.3.3.1 Representation of crystal planes (Miller indices)

The orientation of a crystal plane may be defined by considering how the plane or parallel planes intersects the main crystallographic axes. A family of lattice planes is represented by three numbers, h, k, l called, Miller indices. A family of parallel planes is written as (hkℓ). A family of planes which are equivalent to the (hkℓ) plane by symmetry are represented by {hkl}. [hkℓ], with square instead of round brackets, denotes a direction in the basis of the *direct* lattice vectors. For cubic lattice the [hkℓ] is perpendiculat to the (hkl). <hkl> denotes the set of all directions that are equivalent to [hkℓ] by symmetry.

The procedures to calculate the miller indices are shown as follows:

1. Identify the plane intercepts on the x, y and z-axes.

2. Take the reciprocals of the intercepts

3. Remove fractions by multiplying least common multiple of the denominators.

4. Replace negative integers with bar over the number as $\hbar$

5. Enclose the whole-number set in curvilinear brackets

6. If the plane is parallel to an axis, we say it cuts the axis at ∞ and $\frac{1}{\infty} = 0$

For the plane shown the figure 20a, the intercepts are 1, 2, 2, in terms of the primitive lattice vectors in each direction. The reciprocals of the intercepts are 1, ½, ½. Multiplying by 2 to remove the fractions, we will have the miller index (2 1 1).

The face center cubic lattice is one of the lattice types of the cubic lattice. There is one lattice point at the face of the cubic, in addition to the lattice points at corners of the cubic, as shown in the figure 19b. Figure 20b shows the (111) planes of fcc lattice. Figure 20c shows different crystal planes of 3D colloidal crystal , which is fcc lattice. The (111) plane of fcc lattice shown in fig 20b and 20c (i & ii) is the plane which is parallel to substrate that the multilayer of spheres has been deposited on [84].

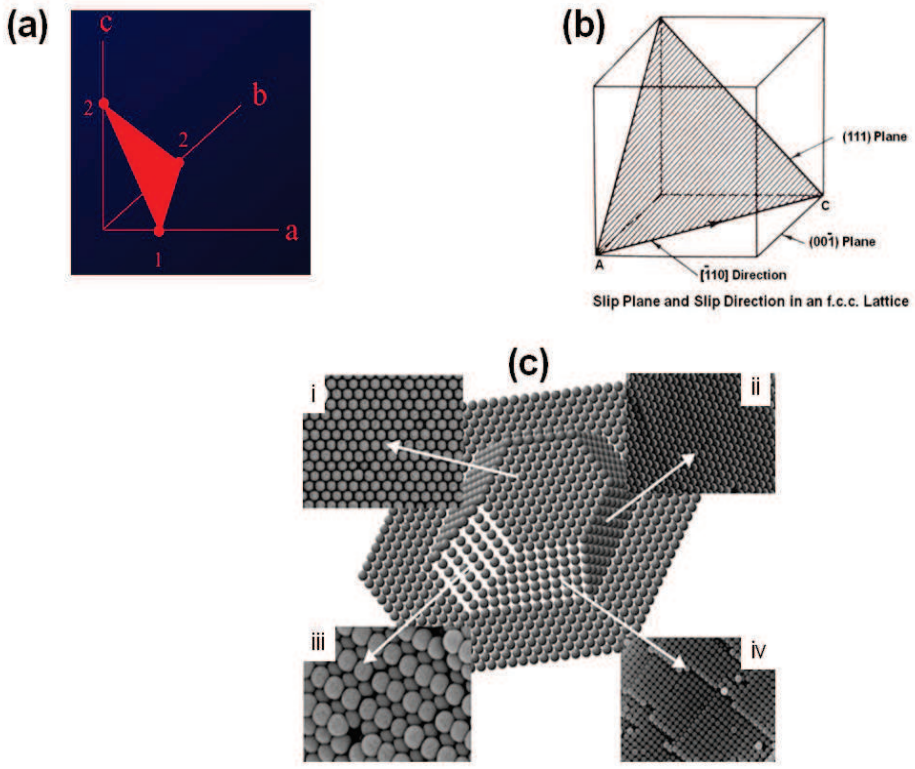

Figure 20: Crystal planes (a) (211) plane of a lattice. (b) (111) plane of an fcc alttice. (c) Scanning electron microscopy (SEM) images of four facets of an fcc structure compared with a model crystal (center) : (i) outer (111), (ii) inner (111), (iii) inner (110), (iv) inner (100) planes[12]

1.4.4 The reciprocal space and the Brillouin zone

Any quantity that varies in time can be described as a sum of Fourier components in the frequency domain. Similarly, we can describe the spatial properties of a crystal as the sum of components in Fourier space, also called reciprocal space [78]. Let's call *f* the function that define a lattice geometry. This function is periodic on the lattice which means that for any translation vector R that translate the lattice to itself:

$$f(\vec{r}) = f(\vec{r} \pm \vec{R}) \tag{8}$$

Taking the Fourier transform of f gives the function h related to f by :

$$f(\vec{r}) = \int h(q) \exp(i\vec{G}\cdot\vec{r})\, dG \tag{9}$$

From the equation 8 :

$$f(\vec{r}) = f(\vec{r}+\vec{R}) = \int h(q) \exp(i\vec{G}\cdot\vec{r})\, dG = \int h(q) \exp(i\vec{G}\cdot(r\vec{+}R))\, dG \tag{10}$$

This equality is possible if

$$\exp(i\vec{G}.\vec{R}) = 1 \tag{11}$$

From this result the reciprocal lattice vectors ***G*** are defined as

$$\vec{G}.\vec{R} = 2\pi N \tag{12}$$

N being an integer.

The distance between planes in the reciprocal lattice is inversely proportional to the distance between planes in the direct lattice, thus the notion ‘reciprocal’. The study of electromagnetic wave interaction with periodic crystals is easier with the reciprocal lattice as the units in the reciprocal lattice and the units of the wave vector are similar.

If a_1, a_2, a_3 are the primitive translation vectors of a direct lattice, then the *primitive* vectors b_1, b_2, b_3 of the reciprocal lattice can be defined as follows:

$$b_1 = 2\pi \frac{a_2 \times a_3}{a_1 \cdot (a_2 \times a_3)} \tag{13}$$

$$b_2 = 2\pi \frac{a_2 \times a_3}{a_2 \cdot (a_1 \times a_3)} \tag{14}$$

$$b_2 = 2\pi \frac{a_2 \times a_3}{a_2 \cdot (a_1 \times a_3)} \tag{15}$$

Thus, as the vectors in real space have dimension of length; the vectors in reciprocal space will have dimensions of length^{-1}. The scaling factor of, 2π, is included to make the scaling similar to the scaling of **k** space which plots λ as $2\pi/\lambda$. Thus the reciprocal space can also be referred to as the **k**-space. Thus when the direct lattice is periodic, the reciprocal lattice is periodic and infinite, being a set of points generated by an equation:

$G = h_1 b_1 + h_2 b_2 + h_3 b_3$,

where b_1, b_2 and b_3 are the primitive reciprocal vectors defined in the equation above and h_1, h_2 and h_3 are arbitrary integers.

We can see that,

$$b_1 \circ a_2 = b_1 \circ a_3 = b_2 \circ a_1 = b_2 \circ a_3 = b_3 \circ a_1 = b_3 \circ a_2 = 0 \tag{16}$$

This equation tells us that b1 is perpendicular to the vectors a2 and a3, but not necessarily parallel to a1.

$$b_1 \circ a_1 = b_2 \circ a_2 = b_3 \circ a_3 = 2 \cdot \pi \tag{17}$$

For real lattice vector **R** defined above as

$$R = n_1 a_1 + n_2 . a_2 + n_3 . a_3 \tag{18}$$

from the above equations we can have the following relation:

$$G \circ R = 2\pi (a_1 \cdot b_1 + a_2 \cdot b_2 + a_3 \cdot b_3) \tag{19}$$

And

$$e^{iG \circ R} = 1 \tag{20}$$

1.4.4.1 The Brillouin zone

The Brillouin zone is defined to be the Wigner-Seitz cell of the reciprocal lattice and is thus the primitive cell in the reciprocal space. The Brillouin zone is important to describe electromagnetic waves in periodic medium, as will be discussed later.

The Brillouin zone usually refers to the first Brillouin zone, which is simply the Wigner-Seitz cell. Although rarely used, there are also second, third, etc., Brillouin zones, corresponding to a sequence of disjoint regions (all with the same volume) at increasing distances from the origin.

The Brillouin zone can be drawn by similar procedure that we used to draw the Wigner-Seitz cell in real lattice. Draw lines to connect a given lattice point to all nearby lattice points, at the midpoint and normal to these lines, draw new lines or planes, the smallest volume enclosed in this way is the first Brillouin zone. Below we will see how we can draw the Brillouin zone for one, two and three dimensional lattices.

1.4.4.1.1 Brillouin zone in one dimensional Photonic crystals

If we consider a one dimensional lattice of period a, the corresponding reciprocal lattice vector will have a length of $2\pi/a$. Since the reciprocal lattice vectors are $2\pi/a$ in length, the Bragg planes for this reciprocal lattice occur at a length of $\frac{1}{2}*2\pi/a = \pi/a$.

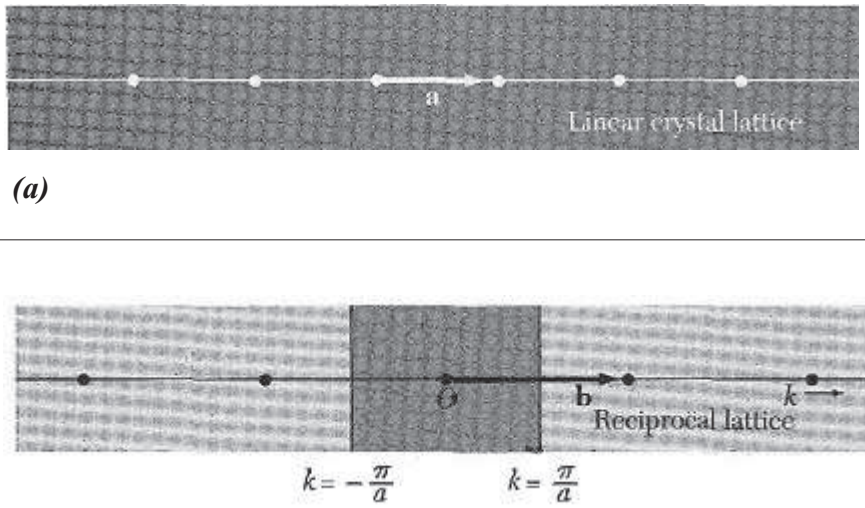

Figure 21: Crystal and reciprocal lattices in one dimension. The basis vector in the reciprocal lattice is b, of length equal to $2\pi/a$. The shortest reciprocal lattice vectors from the origin are b and -b. The perpendicular bisectors of these vectors form the boundaries of the first Brillouin zone. The boundaries are at $k = \pm \pi/a$.[78]

1.4.4.1.2 Two dimensional Brillouin zone

Here we will consider 2D hexagonal lattice as shown in figure 22(a). The primitive translation vectors of the hexagonal real space lattice may be taken as:

$$a_1 = \frac{\sqrt{3}}{2} ax + \frac{a}{2} y \tag{21}$$

$$a_2 = \frac{-\sqrt{3}}{2} a\, x + \frac{1}{2} a\, y \tag{22}$$

From the equations 21and 22 , the reciprocal lattice vectors can be calculated as,

$$b_1 = 2\pi \frac{a_2 \times a_3}{a_1 \circ (a_2 \times a_3)} = \frac{2\pi}{\sqrt{(3)}a} x + \frac{2\pi}{a} y \tag{23}$$

$$b_2 = 2\pi \frac{a_3 \times a_1}{a_1 \circ (a_2 \times a_3)} = \frac{-2\pi}{\sqrt{3}a} x + \frac{2\pi}{a} y \tag{24}$$

The lattice points based on the primitive reciprocal lattice vectors are shown on figure 22(b). Obviously, the reciprocal lattice is also a hexagonal lattice, but with a rotation about z axis by an angle of 30 degrees. Following the above mentioned procedures to draw the first Brillouin zone, we obtain the shaded region in fig. 22(b) as the first Brillouin zone.

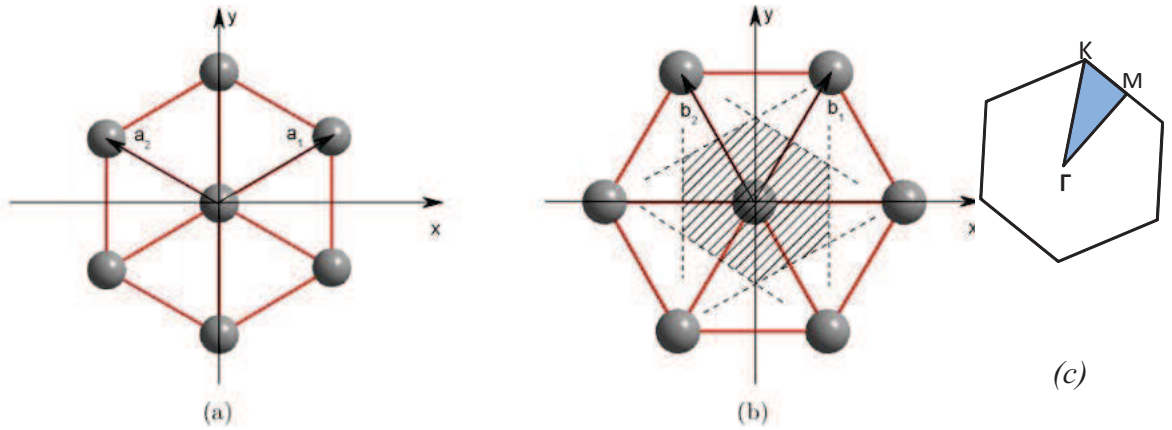

Figure 22: (a) Hexagonal lattice in real space. (b) Hexagonal lattice in the reciprocal space. Shaded area indicates the Brillouin zone. (c) The first Brillouin zone of hexagonal lattice with the irreducible Brillouin zone (shaded) inside and high symmtery points.

The high symmetry points of a Brillouin zone are important for the calculation of band diagram as will be discussed in paragraph 1.4.6. The center of the Brillouin zone is called Γ point and is the highest symmetry point. The point at the corner of the Brillouin zone is called the K point and the one at the middle of the segment is the M point.

The **irreducible Brillouin** zone (IBZ) is a small region in the first Brillouin zone and the rest of the Brillouin zone can be related by translation (rotation). For the 2D hexagonal lattice, the shaded rectangular region in figure 22(c) with points Γ, M and K, is the the irreducible Brillouin zone , and the result of the first Brillouin zone can be formed by rotation of 30°.

1.4.4.1.3 Brillouin zone of the face centered cubic lattice

By similar procedure the Brillouin zone of the fcc lattice can be constructed as in the figure 23. The coordinates of the high symmetry points are given as:

Γ	$k_x= 0, k_y= 0, k_z= 0$
X	$k_x= \pm 2\pi /a, k_y= 0, k_z= 0$
L	$k_x= \pm\pi/a, k_y= \pm\pi/a, k_z= \pm\pi/a$
W	$k_x= \pm 2\pi /a, k_y= \pm\pi /a, k_z= 0$
K	$k_x= \pm 3\pi /2a, k_y=\pm 3\pi /2a, k_z= \pm 3\pi /2a$

Similarly , the first BZ of an fcc lattice is the smallest wedge of the first Brillouin zone (BZ) (shown in the figure with solid red and dotted green lines) from which any wave-vector k in the first BZ can be obtained by performing symmetry operations of the crystal structure.

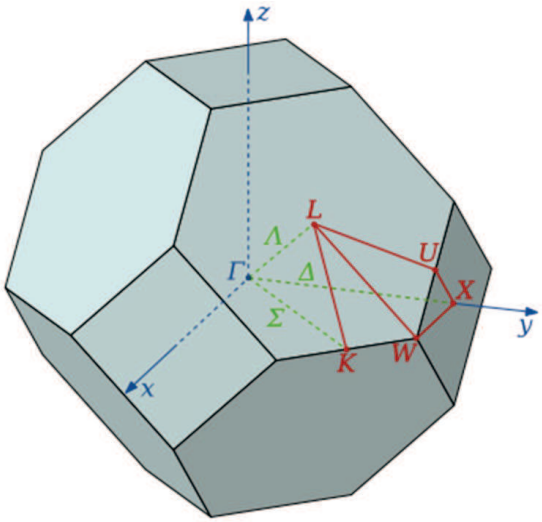

Figure 23: The Brillouin zone of the fcc lattice.

1.4.5 Maxwell equations in periodic media

The study of the propagation of electromagnetic waves in materials is based on the Maxwell's equations. Using the same notations than J. D Joannopoulos[61] for the macroscopic Maxwell equations in SI units gives :

$$\vec{\nabla}\cdot\vec{B}=0 \tag{25}$$

$$\vec{\nabla}\cdot\vec{D}=\rho \tag{26}$$

$$\vec{\nabla}\times\vec{E}+\frac{\partial\vec{B}}{\partial t}=0 \tag{27}$$

$$\vec{\nabla}\times\vec{H}-\frac{\partial\vec{D}}{\partial t}=\vec{J} \tag{28}$$

where **H** and **E** are the macroscopic electric and magnetic fields, **D** and **B** are the electric displacement and magnetic induction fields. J and ρ are free current and charge densities. This study will deal with homogenous dielectric material in which the material remains the same as time varies, and there are no charge or current sources, such that ρ = 0 and J = 0.

The constitutive relations are equations which relate the electromagnetic field to the properties of the material, in which the field exists and they relate **E** with **D** and **H** with **B**. Together with the Maxwell's equations, the constitutive relations completely describe the electromagnetic field. Considering linear regimes, isotropic materials, and ignoring frequency dependence of the dielectric constant, and considering transparent materials with purely real and positive refractive index (linear lossless materials) the constitutive relations are described as:

$$\vec{D}(r)=\epsilon_0\epsilon(r)\vec{E}(r) \tag{29}$$

$$\vec{B}(r)=\mu_0\mu(r)\vec{H}(r) \tag{30}$$

and

$$\vec{J}=\sigma\vec{E} \tag{31}$$

where $\varepsilon_o \approx 8.854 \times 10^{-12}$ Farad/m, is the vacuum permittivity, ε is relative permittivity, $\mu_o = 4\pi \times 10^{-7}$ Henry/m is the vacuum permeability, and μ is relative magnetic permeability. But for most materials of interests $\mu=1$, and hence $B = \mu_o H$. Note that the refractive index n of a material is given as

$$n = \sqrt{(\epsilon \mu)} \tag{32}$$

Taking into account eq. 29 and eq. 30, the Maxwell's equations are written as follows:

$$\nabla \circ H(r,t) = 0 \tag{33}$$

$$\nabla \times E(r,t) + \mu_0 \frac{\partial H(r,t)}{\partial t} = 0 \tag{34}$$

$$\nabla \circ [\epsilon(r).E(r,t)] = 0 \tag{35}$$

$$\nabla \times H(r,t) - \epsilon_0 \epsilon(r) \frac{\partial E(r,t)}{\partial t} \tag{36}$$

We can separate the time dependence from the special dependence of **E** and **H** by expressing the fields as harmonic modes. We will consider fields which vary sinusoidally with time.

We can express the magnetic and electric fields as:

$$H(r,t)=H(r)\mathrm{e}^{(-i\omega t)}$$
$$E(r,t)=E(r)\mathrm{e}^{(-i\omega t)} \quad (37)$$

Substituting these to equations the Maxwell's equations in eq. 34and eq. 36 gives:

$$\nabla\times E(r)-i.\omega.\mu_0 H(r)=0 \quad (38)$$

and

$$\nabla\times H(r)+i.\omega.\epsilon_0.\epsilon(r)E(r)=0 \quad (39)$$

In equation 39 E(r) can be divided by ε(r), and E(r) can be isolated :

$$E(r)=\frac{i}{\omega\epsilon_0\epsilon(r)}\nabla\times H(r) \quad (40)$$

Substituting this value of **E** (**r**) (Eq. 40) into eq. 38 and with :

$$c^2=\epsilon_0\mu_0 \quad (41)$$

where *c* is the speed of light, the coupled equations 38 and 39 writes :

$$\nabla\times[\frac{1}{\epsilon(r)}\nabla\times H(r)]=\frac{\omega^2}{c^2}H(r) \quad (42)$$

The equation 42 is called the master equation for the magnetic field and with the divergence equations 33 and 35 , it can solve the whole system. Solving this equation will let us know

H(**r**) for any dielectric structure. Once the expression for H(**r**) is known, E(**r**) can be determined as well using equation 40.

1.4.5.1 Eigenvalue approach

Solving Eq. 42 can be regarded as an eigenvalue problem. Indeed if one define the operator Θ

$$\hat{\Theta} = \nabla \times \left(\frac{1}{\epsilon(r)} \nabla \times \right) \tag{43}$$

and the eigenvalue Λ with :

$$\Lambda = \left(\frac{\omega}{c} \right)^2 \tag{44}$$

And with H(r) representing the eigen vectors the problem rewrites

$$\hat{\Theta} H(r) = \Lambda H(r) \tag{45}$$

The most used approach to solve equation 42 is the plane wave expansion (PWE) method, that is used to calculate the electronic band structures in semiconductors.

Due to translational symmetry of the dielectric constant ε(r), we expect the solution H(r) to have a translational symmetry, i.e H(r) will be a periodic function.

Bloch's theorem can be applied to express H(r) as the following:

$$H(r) = u_{kn}(r) \circ \mathrm{e}^{-ik \circ r} \tag{46}$$

where $u_{kn}(r)$ is a periodic function having a periodicity of the photonic crystal lattice, and **k** is a wave vector in the first Brillouin zone of the periodic lattice.

Note that due to this translational symmetry, it is enough to consider wave vector values just in the first Brillouin zone.

The function $u_{nk}(r)$ and the photonic potential $\frac{1}{\varepsilon(r)}$ can be expressed in Fourier series over the reciprocal lattice vector G as follows:

$$u_{nk}(r)=\sum_{G} u_{nk}^{G} e^{iG\circ r} \tag{47}$$

$$\frac{1}{\epsilon(r)}=\sum_{G} \eta_{G} e^{iG\circ r} \tag{48}$$

Inserting the equations 46 and 47 into the master equations 42, gives the equation in the frequency domain:

$$(ik+\nabla)\times\frac{1}{\epsilon(r)}(ik+\nabla)\times u_k(r)=\left(\frac{\omega}{c}\right)^2 u_k(r) \tag{49}$$

Eq. 49 is an eigenproblem with the new operator Θ_k :

$$\hat{\Theta}_k=(ik+\nabla)\times\frac{1}{\epsilon}(r)(ik+\nabla)\times \tag{50}$$

That can be rewritten as :

$$\hat{\Theta}_k u_k(r)=\left(\frac{\omega(k)}{c}\right)^2 u_k(r) \tag{51}$$

And $u_k(r)$ are the eigenvectors of the eigenproblem 51, corresponding to the mode profile. For each value of **k**, the eq. 49 has an infinite number of solutions $\omega(k)_n$ labeled by the band number *n* in order of increasing frequency.

One of the central goals in the study the optical modes of a photonic structures is to determine the dispersion relation k=k(ω) connecting the wave vector or propagation constant k of a

given mode with the frequency ω. The band structure of the PhC is the characteristic which gives the most general information about the PhC properties. It gives full information about available energy status as a function of propagation direction and allows to determine the parametric values of PhC for a design.

1.4.6 Representations of Photonic bandgaps

1.4.6.1 Band structures

For a given refractive index contrast between two dielectric materials, the frequencies for any $\omega(\mathbf{k},\mathbf{n})$ vary smoothly as the wave vector **k** varies forming a curve for 1D problem and a surface for 2D problem.

The plot in figure 24(a) represents the surface band diagram of a hexagonal lattice of 2D infinite height holes in a material of refractive index 3. The electromagnetic field has TE polarization. The radius of the holes is 0,35 times the size of the period. The horizontal plane is the 2D reciprocal lattice space (k) and the vertical axis represents the mode frequency (ωa/2πc). Each surface represents a single band (n).

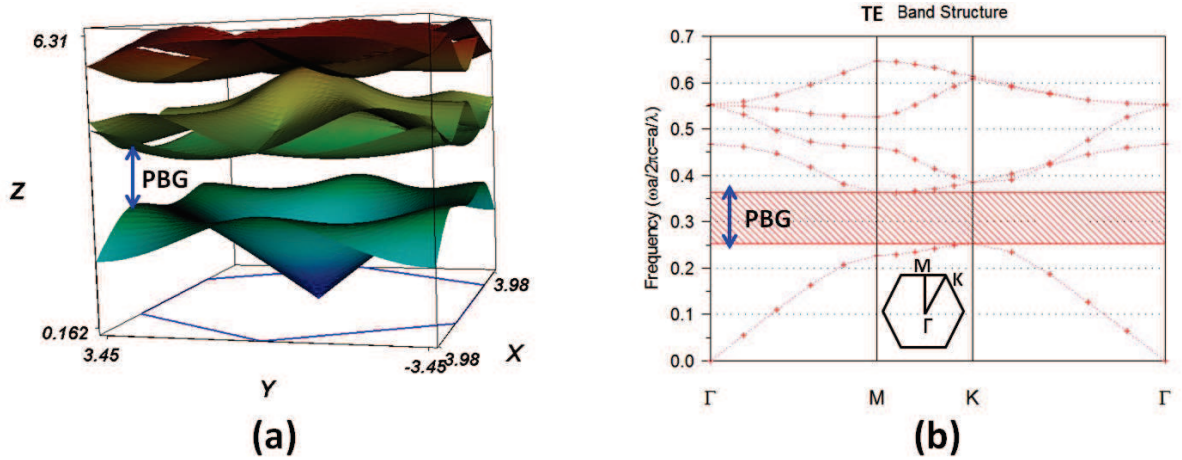

Figure 24: Photonic band structures of a hexagonal lattice of air holes with infinite height in a background refractive index of 3. (a) The band surfaces (b) Band diagram for selected K paths (ΓMKΓ) in the irreducible Brillouin zone. The inset in (b) shows the first Brillouin zone with irreducible Brillouin and high symmetry points. The radius of the holes is 0.35 times the size of the period.

In most cases, there are one or more points in k-space where the adjacent bands touch. However, if the index distribution is chosen correctly, there can be adjacent bands which do

not touch at any point. In this case, there is a range of frequencies between the two bands for which there are no solutions at all. Such a range comprises the photonic band gap (PBG) as indicated in the figure 24(a) and it is impossible for radiation of a frequency inside the gap to propagate in the crystal.

For some applications it is necessary to calculate the solution for the entire Brillouin zone, but for most of the application it is necessary to examine a small subset of points in the first Brillouin zone. Due to the symmetry of the Brillouin zone, solving this equation can be limited to some representative region in the Brillouin zone, called the irreducible Brillouin zone, as described in section 1.4.3.3 above. Thus just considering the k inside one irreducible Brillouin zone, a complete description of the band structure can be found. Group theory also tells us that the extreme points of a band occur at high symmetry points. Thus to study or calculate the size of band gaps it is only sufficient to evaluate the bands along a linear path connecting high symmetry points of the irreducible fraction of the firstBrillouin zone. This generates 2D band diagram as show in figure 24(b). The irreducible Brillouin zone and high symmetry points for a hexagonal lattice are indicated as insets in figure 24(b). The frequency and wave vector are plotted in dimensionless units $\omega a/2\pi c$ and $ka/2\pi$, respectively. The dimensionless frequency is equivalent to a/λ, where λ is the vacuum wavelength (given by $\lambda = 2\pi c/\omega$).

1.4.6.2 Transmission/ Reflection spectra

The transmission/ reflection spectra of photonic crystals in certain direction and polarization of light can indicate the presence or absence of photonic bandgaps. Minimum in transmission spectra or maximum in the reflection spectra indicate band gaps for specific crystal directions. Figure 25 shows the transmitted magnetic field component in the ΓM direction for theTE polarization for the structure studied in 1.4.6.1. The period of the lattice is 0,3μm and the radius is 0,35 times the period. The PBG, with minimum monitor value can be clearly seen for the transmitted light, indicating this part of the spectrum can't propagate in the PhC.

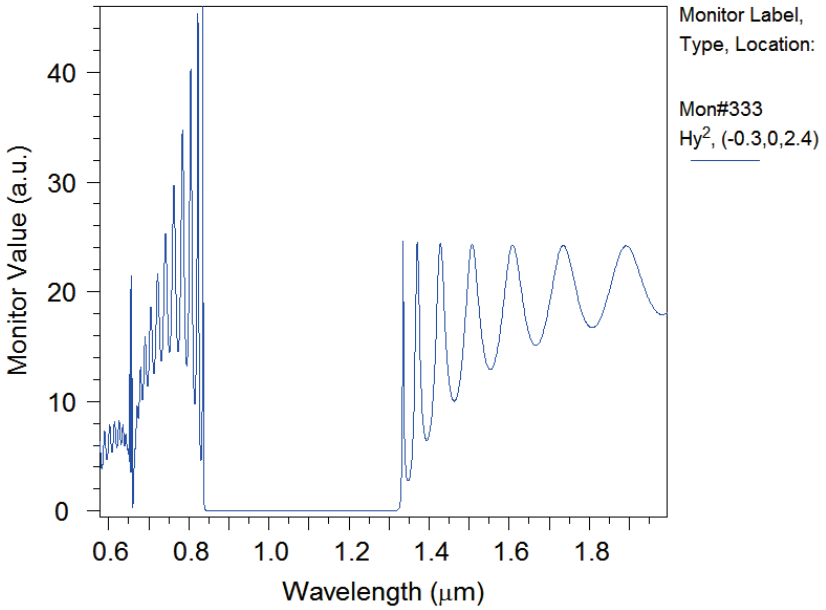

Figure 25: Magnetic field component of the transmitted wave in 2D hexagonal lattice of cylindrical holes in ΓM direction . *The period of the lattice is 0.3μm and the radius of the holes is 0.35 times the size of the period. The refractive index of the background is 3.*

1.4.6.3 Photonic crystal slab band diagram

Photonic crystal slabs are two dimensional photonic crystals with finite thickness embedded in slabs of planar waveguide, with finite height of the structure in the direction perpendicular to the plane of the PhC. Under certain conditions a PhC slab uses index-guiding to confine light in the third dimension and brag scattering in the plane of the Phc slab. Thus these slab structures have attracted considerable interest since they possess many of the features of full 3D photonic crystals, but are substantially easier to manufacture than 3D PhC [85,86].

The band structure for PhC slabs is different form that of infinite height 2D PhCs. In 2D calculations the bands correspond only to states that have no wavevector component in the direction perpendicular to the plane of periodicity (as in figure 24). But in PhC slabs, the finite height of the slab and the presence of wave vectors in the perpendicular direction create a distinct band diagram which is different from the two-dimensional calculations. The band diagram of a photonic crystal slab with a triangular lattice of holes in a dielectric slab material

is shown below [1]. The lattice constant is *a* and the radius of the holes is 0.45*a* the dielectric slab has a thickness 0.6*a*.

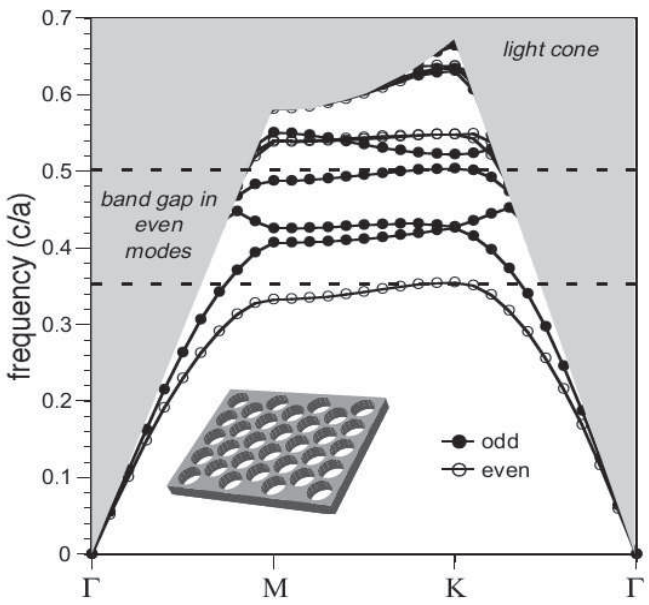

Figure 26: Band diagrams corresponding to a PhC slab indicated as inset. The lattice constant is a and the radius of the holes is 0.45a the dielectric slab has a thickness 0.6a. Whether states are even or odd with respect to the horizontal mirror plane of the slab is indicated by open or filled circles, respectively. [85]

1.4.6.3.1 The light cone :

The gray shaded region (light cone) in the band diagram above represents a continuum of states which destroys the band diagram of 2D structure. It is the most important feature of the PhC slab as compared to the 2D infinite height PhC. The light cone consists of radiation modes that are extended infinitely in the region outside the slab . Guided modes, which are states localized to the plane of the slab, can only exist in the regions of the band diagram that are below the light line(the boundary line). The primary interest in the radiation modes lies in how they interact with and constrain these guided modes [1,86]. Modes inside the gap do not propagate along the slab, thus emitted light goes directly into free space. On the other hand, modes above the light line possess large components in both the slab and free space.

1.4.7 Parameters which affect photonic crystal PBG

Several parameters affect the width of PBG and the right choice should be made to get a desired band gap or dispersion curves. Among such parameters the following are discussed.

1.4.7.1 The refractive index contrast

The refractive index contrast (RIC) in a photonic crystal is the ratio of the refractive indices of adjacent materials that compose the photonic crystals (RIC=n1/n2, where n1 is the refractive index of the high refractive index material, and n2 is the refractive index of the low index material). The RIC gives a general idea of the scattering strength of the photonic crystal. Higher RIC is important to have a wider photonic band gap

1.4.7.2 The Filling fraction

Filling fraction (ff) is the relative volume of material composing the photonic crystal. If the constitutive materials have effective dielectric constants of ε_1 and ε_2, the effective dielectric constant ε_a is give as :

$$\epsilon_a = f \cdot \epsilon_1 + (1-f) \cdot \epsilon_2 \tag{52}$$

The effective refractive index is given as :

$$n_a = \sqrt{(\epsilon_a)} \tag{53}$$

1.4.8 Scaling properties in photonic crystals

One important property of Maxwell's equations in periodic dielectric media is the scalability property. If we know the solution to one equation, it is easier to guess the solution to another equation in which the length in the periodic media or the refractive index are scaled up or down.

Considering the master equation 42, we assume that the refractive index distribution is scaled as $\varepsilon_2(x) = \varepsilon(x/\sigma)$ so that $\varepsilon_2(x)$ has the same shape as the original distribution but is expanded by a factor σ. The original master equation can be recovered for the Helmholtz equation by rescaling of the frequency to $\boldsymbol{\omega_2 = \omega/\sigma}$.

In addition, if the harmonic modes of a system with the dielectric function ε(r) are known, and if the modes of a system with a dielectric function differs by a constant factor everywhere, $\varepsilon_2(r) = \varepsilon(r)/s^2$ can be easily guessed from that of ε(r). Indeed, substituting $s^2\varepsilon_2(r)$ for ε(r) in 42 yields:

$$\nabla\times\left(\frac{1}{\epsilon_2(r)}\times H(r)\right)=\left(\frac{s\,\omega}{c}\right)^2 H(r) \tag{54}$$

The harmonic modes H(r) of the new system are unchanged, but the frequencies are all scaled by a factor s: $\boldsymbol{\omega_2 = s.\omega}$. For example, if we multiply the dielectric constant everywhere by a factor of 1/4, the mode patterns are unchanged but their frequencies double.

1.4.8.1.1 The Size of the Band Gap

Considering the transmission spectra in figure 25 the extent to which a photonic bandgap can be measured by Δω. But from the scaling property discussed above, if the crystal were expanded by a factor **σ,** the corresponding gap would have a width of $\Delta\omega/\boldsymbol{\sigma}$. Thus this definition of the bandgap would give sizes for the same structure with different scales. The gap–midgap ratio, which is the ratio of the frequency gap and the middle of the bandgap, is independent of the scale of the crystal and is the more important term to define the width of the PBG. If ω_m is the frequency at the middle of the gap, one define the gap–midgap ratio as $\Delta\omega/\omega_m$, generally expressed as a percentage. (e.g., a "15% gap" refers to a gap–midgap ratio of 0.15).

1.4.9 Computational tools

Computer based electromagnetic computations are essential to solve or at least approximate, the solutions to Maxwell's equations governing photonic crystals or other photonic structures

so as to design and model the photonic structures of our choice. With these computational tools we can calculate the allowable frequencies for light propagation and calculate the field distribution in the PhC. There are different electromagnetic computational approaches for the study of photonic crystals as plane wave expansion (PWE), finite-difference time-domain (FDTD), finite element method (FEM), finite differences frequency domain (FDFD), transfer matrix (TM) methods. Each method has its own advantages and limitations to solve a certain problem. Memory of computer, simulation time, complexity of the structure to be simulated are among the factors which makes one method more preferable than the other. PWE was used for calculating the band structure of periodic structures which extend infinitely like in the band structure in figure 24(a), and FDTD or FDFD was used for any complex structure, to calculate transmission and reflection spectra, and to solve the band structures

We will discuss two computational methods which are more applicable to this thesis. These are the plane wave expansion method and the finite–difference time-domain methods.

1.4.9.1 The plane wave expansion method

The PWE method is a highly efficient and accurate computation tool used to calculate the band structure of the photonic crystals. The frequency Eigen value equation (eq. 51) is used to solve the Eigen frequency at certain discrete wave vectors along the boundary of the first Brillouin zone. In a second step the band structures of the PhCs are obtained, in the following way. The fields themselves and the dielectric function are expanded in Fourier series along the directions in which they are periodic. This Fourier expansion will be truncated to a fixed number of terms, limiting the accuracy of the calculation.The truncated problem will yield an eigenvalue equation for the fields which will allow the calculation of the dispersion curves [87]. The presence of defects may break the translational symmetry of the crystal, however this allows localized modes to exist. To calculate the band diagram of a photonic crystal with a defect, the supercell technique is used. A periodic structure with a large primitive cell including more than one unit cell containing the defect, called a “super cell” is used for the calculation. The supercell is repeated to make the photonic crystal and minimal coupling between supercells is assumed as the supercell is large enough.

1.4.9.2 The FDTD method

The Finite-Difference Time-Domain (FDTD) method calculates rigorous solution to Maxwell's equations and is based on a spatial and temporal discretization of the equations [88]. The algorithm solve the Maxwell's equations expressed as a function of time and approximates all of the derivatives as finite-differences. The FDTD method compares the change in an electronic field in time against a change in a magnetic field across space. Conversely, it also examines the changes in magnetic field along an analogous electronic field in space. Both space and time are divided into discrete segments. Space is segmented into box-shaped cells, which are small compared to the wavelength. Time is quantized into small steps where each step represents the time required for the field to travel from one cell to the next. Many FDTD cells are combined together to form a three-dimensional volume FDTD grid or mesh.

1.4.9.2.1 *Accuracy of FDTD simulation*

The space grid size must be such that over one increment the electromagnetic field does not change significantly. This means that, to have meaningful results, the linear dimension of the grid must be only a fraction of the wavelength [89, 8]. A general rule of thumb sets the minimum resolution at ten cells per wavelength [90]. In practice the cell size will often be smaller than this in order to resolve dimensions and features of the structure to be simulated such as the thickness of a substrate or the length of a wire.

1.4.9.2.2 *Stability of FDTD simulation*

A stable FDTD simulation has less numerical errors which is desirable in FDTD calculations. For unstable simulation the simulated system will rapidly increase without bound. Instability is a spurious (nonphysical, due to numerical errors) increase of the numerical values of the field as the time-marching proceeds [91]. Often, this is observed as an exponential increase. The Courant condition is a fundamental FDTD stability condition algorithm which relates the size of time increment to the spacing of discrete nodes. The Courant condition states that the physical speed of the wave propagating in the structure should not exceed the velocity by which information can travel in the discrete grid. Said differently, the time step should be

smaller than the time for the wave to propagate from one cell to the other, i.e. a field component cannot propagate more than one cell size in the time step Δt.

For a space step of size Δx, Δy and Δz, the Courant condition in a 3D grid demands that :

$$c \cdot \Delta t = \frac{1}{\sqrt{\frac{1}{\Delta x^2} + \frac{1}{\Delta y^2} + \frac{1}{\Delta z^2}}} \tag{55}$$

, where c is the speed of light [92].

1.4.9.2.3 *Boundary conditions*

Boundary conditions are considered at the spatial edges of the computational domain. Usually absorbing boundary condition or periodic boundary conditions are considered.

The absorbing boundary condition (ABC) eliminates any outward propagating energy that impinges on the domain boundaries. One of the most effective is the perfectly matched layer (PML) [93], in which both electric and magnetic conductivities are introduced in such a way that the wave impedance remains constant, absorbing the energy without inducing reflections.

The Periodic boundary conditions (PBC) is more important to study periodic structures such as photonic crystals. In PBC, the boundary condition is chosen such that the simulation is equivalent to an infinite structure composed of the basic computational domain repeated endlessly in all dimensions.

1.5 Photonic Crystals towards low threshold Lasers

1.5.1 Introduction

A LASER stands for Light Amplification by Stimulated Emission of Radiation and works by the principle of a stimulated emission. In the process of stimulated emission, when an incident photon stimulates a transition between the excited state and ground state of the medium, it

generates additionnal photons which have the same phase as the incident photon. This leads to the distinctive coherence of the emitted light, so laser beams can have extremely well-defined frequency and very small divergence.

In general, a laser action consists of an optical pump, a medium capable of amplifying light (or the gain medium) and an optical feedback (a resonator). As light passes through the gain medium, it stimulates the emission of light, thereby gaining intensity. The resonator reflects the light backward and forward through the gain medium to build up a very intense light field [94, 95]. This is shown in figure 27(a) and figure 27(b) shows the principle of stimulated emission.

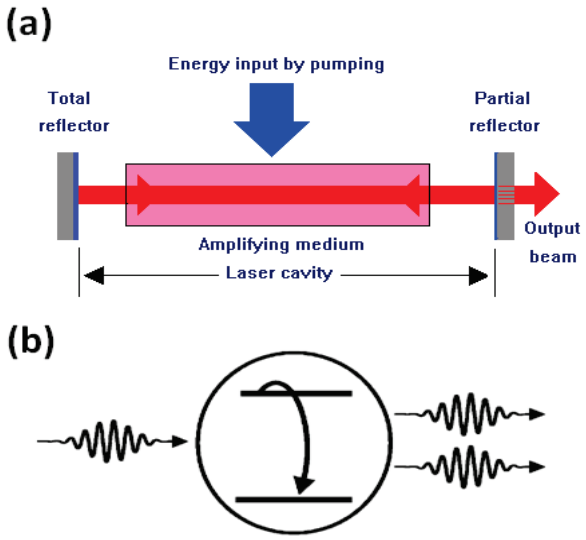

Figure 27: (a) Classical Laser architecture. (b) Schematic illustration of the stimulated emission process. In organic materials, an incoming photon interacts with a chromophore in an excited state to stimulate the emission of a second photon in phase with the first [7]

1.5.2 Feedback Mechanisms

A traditional laser has a gain medium in a physically mirrored cavity where light is temporarily trapped [96]. In conventional Fabry-Perot laser the optical feedback is provided by two parallel mirrors, and the optical cavity is larger than the emission wavelength, which results in many possible electromagnetic modes. A large fraction of photons are emitted into non-lasing modes and the lasers are characterized by the presence of threshold behavior [97, 98,99] .

However, in microcavity lasers which can be formed by 1-, 2-, or 3-D confinement, the optical cavities are comparable to the optical wavelength in size. The number of modes to which the emitters are susceptible to couple out are therefore more limited. In the case of extreme reduction of the mode volume it results in an enhancement of the fraction of spontaneous emission into the lasing mode. Ultimately suppression of all emissions into the non-lasing modes can result in a threshold-less laser with spontaneous emission only in the lasing mode. In an ideal microcavity, a single photon mode is coincident with the peak in the material gain so that zero-threshold lasing occurs. These phenomena are schematically shown in figure 28(a)and 28(b), where for a microcavity laser the emission spectrum has narrow width and the laser threshold is much less than a conventional laser.

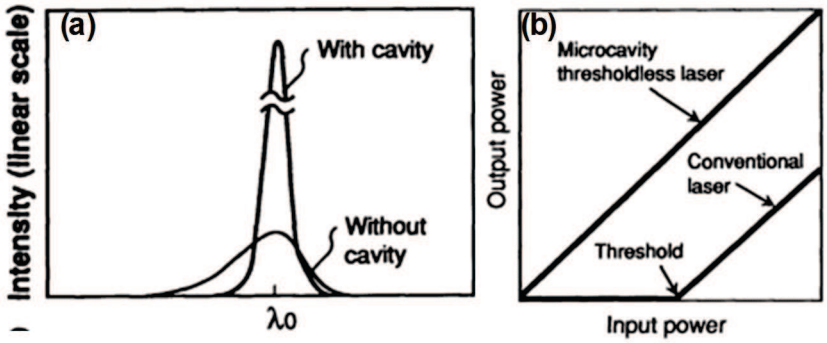

Figure 28: a) Comparision of emission spectra of emitter with and with out microcavity. With the presence of microcavity, there is narrow emmsion. (b)Schematic input / output characteristic of a conventional laser and a micro cavity laser [6]

Microcavity lasers can have *vertical Fabry–Perot* microcavity[6], microring[100], microdisc[101], Fabry-Perot waveguide[102] or diffractive structures[103] as laser resonators, as shown in figure 29. Although the lasers can have different structures, their basic function, in providing resonant feedback through the gain medium, is fundamentally the same. The different geometries of these lasers, however, lead to a rich variety of spectral, spatial, and power properties[104].

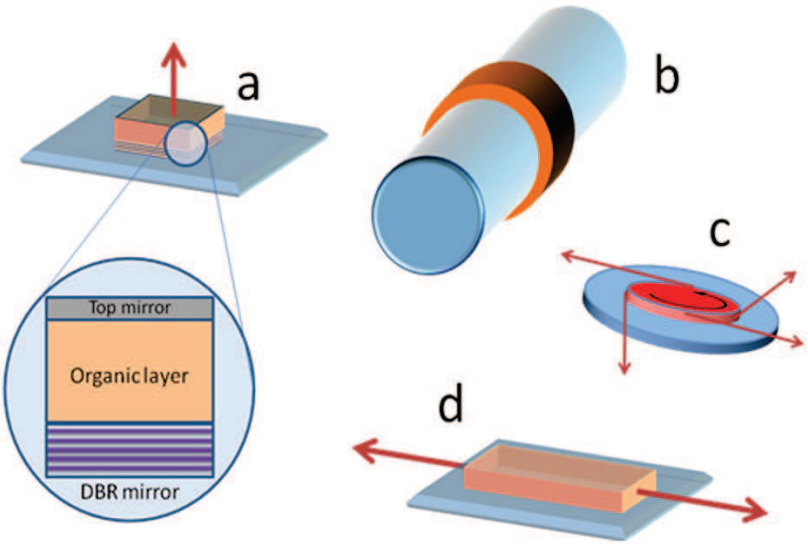

Figure 29: Various resonators used for organic lasers: (a)vertical Fabry–Perot microcavity;(b)microring resonator; (c)microdisc resonator; (d) planar Fabry–Perot waveguide.[76]

1.5.3 Microcavity lasers advantages

Microcavity lasers can be applied for optical computing and signal processing, in which compact lasers are needed. The extreme reduction in mode volume results in an enhancement of the fraction of spontaneous emission into the lasing mode. Ultimately suppression of all emission into the non-lasing modes can result in high efficiency and a very low threshold.

This is important for electrically pumped organic lasers. Organic semiconductors have very low mobilities of charges with typical current density in OLEDs being 1 to 100 mA/cm^2 [105,106]. But for laser applications higher current densities (typically 40kA/ cm^2) are required for potentially achieving population inversion. But at high injection current densities the luminescence efficiencies in organic material is reduced and charge-induced absorption increase, thus making it a problem for electrically pumped lasers. Therefore, it is necessary to have lower current threshold density to have the organic material in the good operating region.

Here, we are more interested to talk about lasers which use periodic nanostructures, like photonic crystals. There are two approaches of using photonic crystals for laser application: These are defect mode lasers and photonic crystal distributed feed back (DFB) lasers [107]. A defect mode PhC laser has a resonant cavity defined near the defect and lasing actions arise from the resonant cavity modes. While a PhC DFB laser does not have any physically defined cavity. The operation of this laser is based on zero group velocity at the photonic band edges [108, 109].

1.5.3.1 Photonic crystal defect mode Lasers

In PBG of PhCs photons with energies in the gap can not propagate through the structure due to destructive interference. But when some defects are made to break the periodicity, photons will be trapped and this creates a microcavity. The photons tend to be confined in a small region of space and a single localized mode or a set of closely spaced modes that have frequencies within the gap are created. The defects act as photonic dopants and trap and localize the light inside the material. The localization effect with a high quality factor can provide an optical feedback to achieve laser effect [110].

This kind of defect cavities are the best candidates for ultra-low threshold lasers due to their small mode volume of the order of a cubic wave-length or lower and good quality factor [60, 111, 112].

In 2D PhC slab microcavity lasers, the in-plane confinement is achieved via Bragg scattering, while the index guiding provides perpendicular confinement which results in a three-dimensionally confined optical mode. Total internal reflection (TIR) (vertically) and Bragg reflection in the plane of the PhC are generally used for light confinement (figure 30 below) [113, 114].

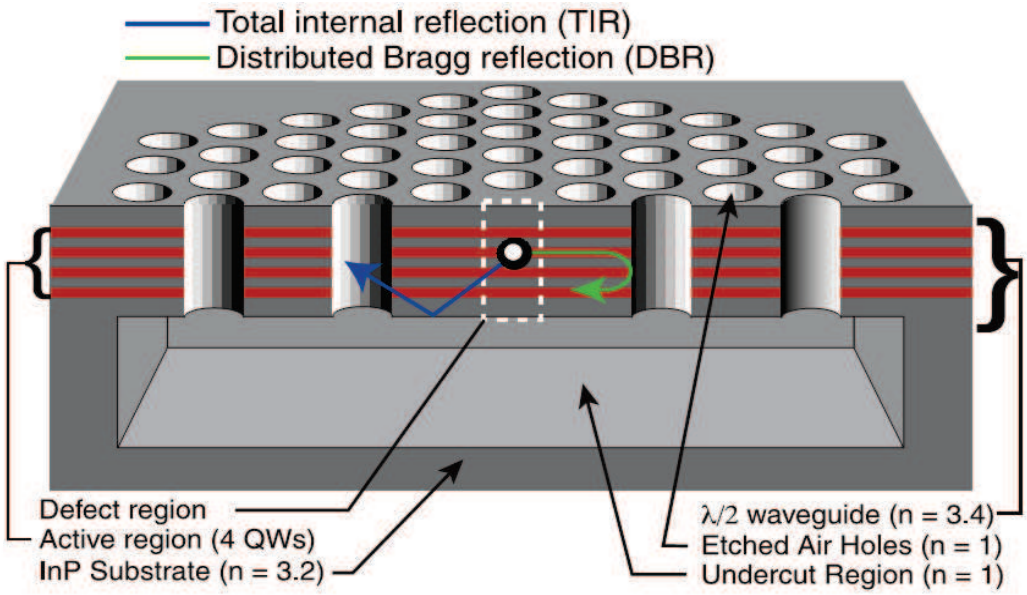

Figure 30: Cross section through the middle of the photonic crystal microcavity formed by removing a single hole in the 2D photonic crystal. Photons are also localized vertically by TIR at the air-slab interface and horizontally by Bragg reflection from the 2D photonic crystal.[60]

1.5.3.2 Photonic crystal distributed feedback (DFB) Laser

Defect-free 2D photonic crystals can also be used to provide low threshold lasers with designed emission directions [108]. These kind of lasers, called PhC distributed feedback (DFB) lasers, are band-edge lasers whose intrinsic feedback mechanism is based on Bloch waves near the PhC band edge. A DFB laser consists of a thin active layer deposited onto a corrugated substrate. Bragg reflections caused by grating reduce the group velocity of photons to zero along defined directions of crystallographic symmetry [115,116]. The period microstructures which are in the wavelength-scale diffract light to have a range of frequencies destructively cancel out while other wavelength resonates to give Bragg waves in a new direction.

The dispersion characteristics of the PhC is tailored to realize propagating Bloch modes with a very low group velocity (i.e. band edge Bloch modes) and this type of lasers doesn't require the presence of complete photonic bandgap or high refractive index contrast in the photonic crystal [117].

Figure 31(a) shows 2D DFB structure with organic layer (PBD: C490:DCMII) on a corrugated glass substrate and the corresponding photonic dispersion diagram (figure 31(b)) .The group velocity at the Γ point is nearly zero and this point was used to design the construction parameters of the PhC structure.

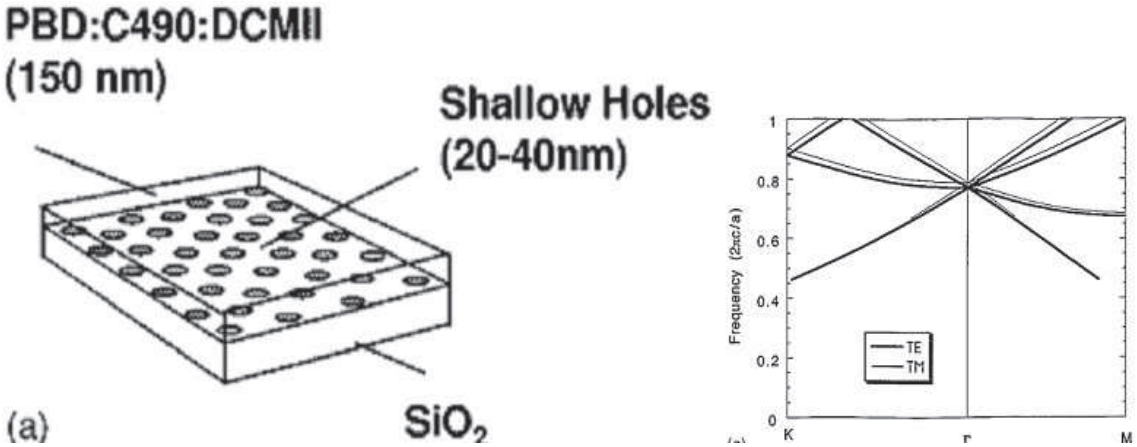

Figure 31: (a) Schematic layer structure of the lasers employed and details of the two-dimensional triangular lattice. (b) Calculated photonic band structure of the device shown for TE and TM polarizations. For TE polarization, the electric field vector is in the plane of the waveguide

1.5.4 Cavity Quality factor and cavity electrodynamics: the two-dimensional photonic crystal case

A number of key factors determine the performance of an optical cavity in a semiconductor light emitter in terms of low power and low noise device [60, 118]. The quality factor Q , the effective mode volume V_{eff}, and the spontaneous emission factor β, are to be mentioned.

According to Purcell, spontaneous emission of an emitter is governed not only by the intrinsic property of the atoms or molecules in a specific material but is also governed by the electromagnetic properties of the host or its electromagnetic surrounding, which can facilitate its suppression as well as its enhancement. In particular, if the emitter is placed in a resonant cavity, like PhC defect microcavities, the emission can be enhanced into certain modes and inhibited into other modes [119].

Purcell theoretically investigated enhancement of the spontaneous emission rate for an emitter in cavity of volume V with respect to the same emitter out of the cavity by the following factor:

$$\Gamma_{cav} = \Gamma_0 \left(3\lambda^3 / 4\pi^2 V\right) Q \qquad (56)$$

,where Γ_{cav}, is the spontaneous emission rate of an emitter in resonant cavity, Γ_0 is the spontanous emission rate of an emitter in free space, without cavity, Q is the quality factor and V is the modal volume as defined below.

Usually the value $\left(3\lambda^3 / 4\pi^2 V\right) Q$ is called the Purcell factor, ***Fp*** of the cavity:

$$F_P = \frac{3Q}{4\pi^2 V_{eff}} \left(\frac{\lambda}{n}\right)^3 \qquad (57)$$

Thus an emitter in a resonant cavity see its decay rate growing in proportion to the cavity quality factor **Q** and inversely proportional to the mode volume **V**. The advantages of using PhC microcavities is that they can combine high quality factors with small effective modal volumes that lead to enhanced values of the spontaneous emission rate through the Purcell effect [120].

The Q factor is a figure of merit used to quantify the radiation losses of an optical resonator. To calculate numerically the quality factor, the resonant frequency of the photonic crystal cavity should be calculated first. For this, a pulse source with a Gaussian frequency profile and frequency bandwidth which covers the entire PBG is excited in the vicinity of the cavity and the time evolution of the electromagnetic fields is generated. The resonant frequencies are calculated by the Fourier transform of the time varying fields at several arbitrary points in the cavity region. Then, the field is initialized by a single Gaussian pulse that excites only one resonant mode.

The quality factor is then obtained from the temporal attenuation of the electromagnetic energy after turning off the oscillation of the dipole:

$$U(t) = U(t0)\, e^{(-w(t-t0)/Q)} \qquad (58)$$

where, U(t) is the electromagnetic energy at time t and t_0 is the switch-off time of the dipole oscillation, ω is the angle frequency of the dipole oscillation.

$$Q = -w \frac{(t - t_0)}{\left(\ln\left(\frac{U_{(t)}}{U_{(t0)}}\right)\right)} \qquad (59)$$

Alternatively, placed inside a cavity featuring a resonant mode at wavelength ω and with a spectral line width of $\Delta\omega_0$, the quality factor can be calculated as follows:

$$Q = \omega / \Delta\omega_0 \qquad \textbf{(60)}$$

The effective mode volume V_{eff} is defined as the ratio of the total electric-field energy to the peak value of the electric-field energy density and is given by:

$$V_{eff} = \frac{\int \varepsilon(r)|E(r)|^2 d^3r}{\max[\varepsilon(r)|E(r)|^2]}, \qquad \textbf{(61)}$$

where, where ε(r) and E(r) are the permittivity and electric field at position r, respectively.

The advantage of reducing the mode volume is that only a few modes will interact with the atoms constituting the gain medium. One advantage of having only one or a few optical modes interacting with the gain medium is that the dissipation (i.e., coupling to the radiation mode continuum), which washes away the features of the coherent interaction between the field and the gain medium, is kept to a minimum or very little power is carried away by spontaneous emission in spurious modes and hence the threshold power of microcavity lasers can be very low [121] .

1.5.4.1 The laser threshold

In a conventional semiconductor laser a substantial part of the electron—hole inversion is lost due to spontaneous emission into the non-lasing modes, reducing the quantum efficiency. Spontaneous emission furthermore determines the threshold for laser oscillation [122]. By

inhibiting spontaneous emission into modes other than the lasing mode and funneling it to the a single cavity mode, the threshold of microcavity PhC lasers may be reduced drastically [122].

The figure of merit for this coupling is called spontaneous emission coupling factor β defined as the ratio between the rate of the spontaneous emission coupled into the laser modes divided by the total spontaneous emission rate [85].

$$\beta = \frac{spontaneous\ emission\ photons\ coupling\ into\ a\ lasing\ mode}{total\ spontaneous\ emission} \qquad \textbf{(62)}$$

Consequently, a microcavity laser designed to have larger value of $\beta \sim 1$, enables a larger fractions of photons to be emitted into a single resonant lasing mode with respect to all other modes. Such kind of cavity should have extremely low threshold (near-zero) levels and a quantum efficiency approaching unity.

Meschede et al proved that the spontaneous emission enhancement factor β is proportional to the quality factor Q and inversely proportional to the volume V at resonance. Thus, it is necessary to have high Q factor and low mode V cavities to enhance the β factor and reduce the laser threshold.

1.6 Conclusion

In summary, micro and nanoparticles of different materials can self-assemble by different techniques in a bottom-up approach to form opals and inverse-opals. These opals and inverse-opals are periodical nanostructures. In order to investigate the optical properties of these periodical structures we have recall the formalism used to study numerically the photonic crystal. We have also recall that low-threshold laser can be achieved with photonic crystal microcavity or DFB lasers.

Based on these results one may wander if opals and inverse opals may offer an interesting solution to investigate low-threshold organic lasers based on photonic crystal microcavity or 2D-DFB resonator.

A next step consist in investigating numerically the optical properties of opals and inverse opals. More specifically we would like to investigate the existence of photonic band gap in opals and inverse opals. If the existence of photonic bandgap can be predicted we would like to consider photonic crystal microcavity so as to estimate their quality factors and mode volumes that are key factors in a low-threshold laser quest.

Such numerical studies take place in the following chapter.

1.7 References

[1] Meera Ramrakhiani, “Nanostructures and their applications,” Recent Research in Science and Technology, Vol. 4, 14-19(2012).

[2] Fritz Allhoff, Patrick Lin, and Daniel Moore “What Is Nanotechnology and Why Does It Matter?,” A John Wiley & Sons, Ltd., Publication, (2010).

[3] Sujit Kumar Ghosh, and Tarasankar Pa, “Interparticle Coupling Effect on the Surface Plasmon Resonance of Gold Nanoparticles: From Theory to Applications,” Chem. Rev., Vol. 107,4797−4862 (2007).

[4] Günter Schmid and Lifeng F. Chi, “Metal Clusters and Colloids,” Adv. Mater., Vol. 10, 515–526(1998).

[5] http://www.nano.gov/nanotech-101/what/definition

[6] Manasi B Kasture, Ph.D Thesis , University of Pune

[7] http://metamodern.com/2009/12/29/theres-plenty-of-room-at-the-bottom%E2%80%9D-feynman-1959/

[8] Ian Freestone, Nigel Meeks, Margaret Sax, and Catherine Higgitt, “The Lycurgus Cup – A Roman Nanotechnology,” Gold Bulletin, 270-277(2007).

[9] http://store.nanoscience.com/store/pc/viewPrd.asp?idproduct=2412&idcategory=0

[10] M. A. Garcia, “Surface Plasmons in metallic nanoparticles: Fundamentals and applications,” Journal of Physics D: Applied Physics, Vol. 44, 283001(2011).

[11] Michael Faraday, “The Bakerian Lecture—Experimental Relations of Gold (and other Metals) to Light,” Phil. Trans. R. Soc. Lond., Vol. 147, 145-181(1857).

[12] Sujit Kumar Ghosh and Tarasankar Pal, “Interparticle Coupling Effect on the Surface Plasmon Resonance of Gold Nanoparticles: From Theory to Applications,” Chem. Rev.,Vol. 107, 4797−4862(2007).

[13] http://www.sigmaaldrich.com/materials-science/nanomaterials/gold-nanoparticles.html

[14] F. Meseguer, A. Blanco, H. Miguez, F. Garcia-Santamarı, M. Ibisatea, C. Lopez, “Synthesis of inverse opals,” Colloids and Surfaces A: Physicochemical and Engineering Aspects, Vol. 202, 281 – 290(2002).

[15] E. Reverchon, R. Adami, “Nanomaterials and supercritical fluids,” J. of Supercritical Fluids, Vol. 37, 1–22(2006).

[16] TM Blattler, A Binkert, M Zimmermann, M Textor, J Voros and E Reimhult, “From particle self-assembly to functionalized sub-micron protein patterns,” Nanotechnology, Vol.19, 075301(2008).

[17] Y. Xia1, B. Gates1, Y. Yin2 and Y. Lu2 “Monodispersed Colloidal Spheres: Old Materials with New Applications,” Advanced Materials, Vol. 12, 693–713(2000).

[18] Van Hai Le, Chi Nhan Ha Thuc, and Huy Ha Thuc, “Synthesis of silica nanoparticles from Vietnamese rice husk by sol–gel method,” Nanoscale Research Letters, Vol. 8, 1-10(2013).

[19] Werner Stober, Arthur Fink, Ernst Bohn “Controlled Growth of Monodisperse Silica Spheres in the Micron Size Range” , Journal Of Colloid And Interface Science, Vol. 26, 62-69(1968).

[20] R.B. Pettit and C.J. Brinker, “Use of sol-gel thin films in solar energy applications,” Solar energy materials, Vol. 14, 269-287(1986).

[21] Ismail Ab Rahman1 and Vejayakumaran Padavettan, “Synthesis of Silica Nanoparticles by Sol-Gel: Size-Dependent Properties, Surface Modification, and Applications in Silica-Polymer Nanocomposites—A Review,” Hindawi Publishing Corporation Journal of Nanomaterials, Vol., (2012).

[22] Varun Chaudhary, Amit K. Srivastava and Jitendra Kumar, “On the Sol-gel Synthesis and Characterization of Titanium Oxide Nanoparticles,” Mater. Res. Soc. Symp. Proc., Vol. 1, (2011).

[23] C.D. Anderson and E.S. Daniels, “Emulsion Polymerisation and Applications of Latex” ,Vol. 14, 1-85957-381-9(2003).

[24] D. Cochin and A. Laschewsky, F. Nallet “Emulsion Polymerization of Styrene Using Conventional, Polymerizable, and Polymeric Surfactants. A Comparative Study,” Macromolecules, Vol. 30, 2278-2287(1997).

[25] Chih-hung sun and peng jiang, “Photonic crystals acclaimed defects,” Nature photonics , Vol. 2 9 – 11(2008).

[26] Hiroshi Nakamura, “Colloidal Crystals -Self-Assembly of Monodispersed Colloidal Particle,”

[27] Vicki L. Colvin, “From Opals to Optics: Colloidal Photonic Crystals”, Mrs Bulletin, Vol. 26, 637-641(2001).

[28] Younan Xia, Byron Gates, Yadong Yin, and Yu Lu, “Monodispersed Colloidal Spheres:Old Materials with New Applications,” Adv. Mater., Vol. 12, 693-713(2000).

[29] Sang Kyu Kwak and David A. Kofke, “Effect of monovacancies on the relative stability of fcc and hcp hard sphere crystals,” The Journal Of Chemical Physics, Vol. 122, 176101-1-176101-2 (2005).

[30] Sang Hyuk Im, Mun Ho Kim, and O Ok Park “Thickness Control of Colloidal Crystals with a Substrate Dipped at a Tilted Angle into a Colloidal Suspension,” Chem. Mater., Vol. 15,1797-1802(2003).

[31] Brian G. Prevo and Orlin D. Velev, “Controlled, Rapid Deposition of Structured Coatings from Micro- and Nanoparticle Suspensions,” Langmuir, Vol. 20, 2099-2107(2004).

[32] N. D. denkov, O. D. velev, P. A. kralchevsky, I. B. ivanov, H. yoshimura & k. nagayama, "Two-Dimensional Crystallization", Nature, Vol. 361, 26(1993).

[33] N.D. Denkov, O.D. Velev, P.A. Kralchevsky, I.B. Ivanov, H. Yoshimura and K. Nagayama, "Mechanism of Formation of Two-Dimensional Crystals from Latex Particles on Substrata", Langmuir, Vol. 8, 3183-3190(1992).

[34] Sang Hyuk Im, Mun Ho Kim, and O Ok Park,"Thickness Control of Colloidal Crystals with a Substrate Dipped at a Tilted Angle into a Colloidal Suspension," Chem. Mater., Vol.15,1797-1802(2003).

[35] Jeffrey S. Sakamoto and Bruce Dunn “Hierarchical battery electrodes based on inverted opal structures,”J. Mater. Chem., Vol. 12, 2859–2861(2002).

[36] Miguez, H.; Meseguer, F.; Lopez, C.; Blanco, A.; Moya, J.; Requena, J.; Mifsud, A.; Fornes, V., “Control of the Photonic Crystal Properties of fcc-Packed Submicrometer SiO2 Spheres by Sintering,” Adv. Mater., Vol. 10, 480-483(1998).

[37] Dushkin, C.D., Yoshimura, H. and Nagayama, K., “Nucleation and growth of two-dimensional colloidal crystals,” Chem. Phys. Lett., Vol. 204, 455-460 (1993).

[38] Antony S. Dimitrov and Kuniaki Nagayama, “Continuous Convective Assembling of Fine Particles into Two-Dimensional Arrays on Solid Surfaces,” Langmuir, Vol. 12, 1303-1311(1996).

[39] Hulteen J C, Treichel D A, Smith M T, Duval M L, Jensen T R and Van Duyne R P, “Nanosphere Lithography: Size-Tunable Silver Nanoparticle and Surface Cluster Arrays,” J. Phys. Chem.B, Vol.103, 3854–63(1999).

[40] Raul Mayoral, Dr. Joaquin Requena, Prof. José S. Moya, Dr. Cefe López, Adelaida Cintas, Hernán Miguez, Dr. Francisco Meseguer, Dr. Luis Vázquez, Miguel Holgado and Álvaro Blanco,“3D Long-range ordering in ein SiO2 submicrometer-sphere sintered superstructure,” Advanced Materials, Vol. 9, 257–260(1997).

[41] Daniel M. Kuncicky, Brian G. Prevo and Orlin D. Velev,“Controlled assembly of SERS substrates templated by colloidal crystal films,” J. Mater. Chem., Vol. 16, 1207–1211(2006).

[42] Nagayama, K. "Fabrication of Two-Dimensional Colloidal Arrays,” Phase Transitions, Vol. 45, 185-203(1993).

[43] Zhen Yuan,D. Bruce Burckel,Plamen Atanassovand Hongyou Fan, “Convective self-assembly to deposit supported ultra-thin mesoporous silica films,” J. Mater. Chem., Vol. 16, 4637–4641(2006).

[44] C.D. Dushkin, H. Yoshimura, K. Nagayama, "Nucleation and growth of two-dimensional colloidal crystals,” Chemical Physics Letters ,Vol. 204, 455–460(1993).

[45] Peter A. Kralchevsky, Nikolai D. Denkov, “Capillary forces and structuring in layers of colloid particles,” Current Opinion in Colloid & Interface Science,Vol. 6, 383-401(2001).

[46] Kuniaki Nagayama , “Two-dimensional self-assembly of colloids in thin liquid films”, Colloids and Surfaces A: Physicochemical and Engineering Aspects, Vol. 109, 363-374(1996).

[47] Dong Hun Shin, Bo Hyun Sung, Mi Jung Im, and Ung Su Choi “Fabrication of highly qualified opal films with controlled thickness,” J. Ind. Eng. Chem. , Vol. 11,712-719(2005).

[48] Benjamin Hattona, Lidiya Mishchenkoa, Stan Davisc, Kenneth H. Sandhagec, and Joanna Aizenberg, “Assembly of large-area, highly ordered, crack-free inverse opal films,” PNAS, Vol. 107,10354–10359(2010).

[49] Beatriz H. Juárez, Pedro David García, Dolores Golmayo, Alvaro Blanco, and Cefe López, “ZnO Inverse Opals by Chemical Vapor Deposition,” Adv. Mater., Vol. 17, 2761–2765(2005).

[50] Alessandro Rugge, Jill S. Becker, Roy G. Gordon, and Sarah H. Tolbert, “Tungsten Nitride Inverse Opals by Atomic Layer Deposition,” Nano Lett., Vol. 3, 1293–1297(2003).

[51] Byron Gates, Brian Mayers, Zhi-Yuan Li, and Younan Xia, “Fabrication of Micro- and Nanostructures with Monodispersed Colloidal Spheres as the Active Components,” Mat. Res. Soc. Symp., Vol. 636, D9.15.1-5(2001).

[52] Judith E. G. J. Wijnhoven, Lydia Bechger, and Willem L. Vos,“Fabrication and Characterization of Large Macroporous Photonic Crystals in Titania,” Chem. Mater.,Vol. 13,4486-4499(2001).

[53] Judith E. G. J., Wijnhoven and Willem L. Vos,“Preparation of Photonic Crystals Made of Air Spheres in Titania,” Science, Vol. 281, 802-804(1998).

[54] Weijie Liu, Bo Zou, Jing Zhao, Haining Cui ,“Optimizing sol–gel infiltration for the fabrication of high-quality titania inverse opaland its photocatalytic activity,” Thin Solid Films, Vol. 518 , 4923–4927(2010).

[55] Qingfend Yan, Likui Wang, and X. S. Zhao,“Artificial defect engineering in three-dimensional colloidal photonic crystals,” Adv. Funct. Mater., Vol.17, 3695 - 3706(2007).

[56] Fredrik Jonsson, Clivia M. Sotomayor Torres, Jorg Seekamp, Moritz Schniedergers, Anne Tiedemann, Jianhui Ye, Rudolf Zentel, “Artificially inscribed defects in opal photonic crystals,” Microelectronic Engineering, Vol. 78–79, 429–435(2005).

[57] Younan Xia, Yadong Yin, Yu Lu, and Joe McLellan, “Template assisted self assembly of sperical colloids into complex and controllable strucutres,” Adv. Func. Mater., Vol.13, 907–918 (2003).

[58] Tobias Kraus, Laurent Malaquin,Emmanuel Delamarche, Heinz Schmid, Nicholas D. Spencer, and Heiko Wolf, “Closing the Gap Between Self-Assembly and Microsystems Using Self-Assembly, Transfer, and Integration of Particles,” Adv. Mater., Vol.17, 2438–2442(2005).

[59] Liling Yan ,Ke Wang ,Jingshen Wu, and Lin Ye , “Hydrophobicity of Model Surfaces with Loosely Packed Polystyrene Spheres after Plasma Etching,” J. Phys. Chem. B, Vol. 110 , 11241–11246(2006).

[60] Eli Yablonovitch,“Inhibited Spontaneous Emission in Solid-State Physics and Electronics,” Phys. Rev. Lett. Vol.58, 2059-2062(1987).

[61] J.D. joannopoulos, Stven G. johnson, J. N. Winn, R. D. Meade “Photonic crystals : molding the flow of light,” Princetin university Press ISBN 978-0-691-12456-8

[62] E. Yablonovitch,“Photonic band-gap structures,” J. Opt. Soc. Am. B, Vol. 10, 283-295(1993).

[63] C. Sibilia T.M. Benson and M. Marciniak T. Szoplik, “Photonic Crystals: Physics and Technology,” Springer-Verlag Italia, (2008).

[64] Susumu Noda, Masayuki Fujita and Takashi Asano,“Spontaneous-emission control by photonic crystals and nanocavities”, Nature Photon., Vol. 1, 449 - 458(2007).

[65] S. A., Garcia-Santamaria, F. and Braun, P. V., “Embedded cavities and waveguides in three-dimensional silicon photonic crystals,” Nature Photon., Vol. 2, 52-56(2007).

[66] Mark D. Turner, Matthias Saba, Qiming Zhang, Benjamin P. Cumming, Gerd E.Schröder-Turk , Min Gu,“Miniature chiral beamsplitter based on gyroid photonic crystals,” Nature Photon., Vol. 7, 801–805(2013)

[67] Sajeev John ,“Strong localization of photons in certain disordered dielectric superlattices,” Phys. Rev. Lett., Vol. 58, 2486-2489(1987).

[68] Eli Yablonovitch, “Photonic Crystals:What’s in a name?” OPN, 12-13(2007).

[69] E. Yablonovitch, T. J. Gmitter, and K. M. Leung, “Photonic band structure: The face-centered-cubic case employing nonspherical atoms,” Phys. Rev. Lett., Vol. 67, 2295-2299(1991).

[70] S. L. McCall, P. M. Platzman, R. Dalichaouch, David Smith, and S. Schultz, “Microwave propagation in two-dimensional dielectric lattices,” Phys. Rev. Lett., Vol. 67, 20172020(1991).

[71] W. M. Robertson, G. Arjavalingam, R. D. Meade, K. D. Brommer, A. M. Rappe, and J. D. Joannopoulos, “Measurement of photonic band structure in a two-dimensional periodic dielectric array,” Phys. Rev. Lett., Vol. 68, 2023-2027(1992).

[72] J. R. Wendt, G. A. Vawter1,P. L. Gourley, T. M. Brennan and B. E. Hammons, “Nanofabrication of photonic lattice structures in GaAs/AlGaAs,” J. Vac. Sci. Technol. B, Vol. 11, 2637 (1993).

[73] İ. İnanç Tarhan, Martin P. Zinkin, and George H. Watson, “Interferometric technique for the measurement of photonic band structure in colloidal crystals,” Optics Letters, Vol. 20,1571-1573(1995).

[74] Thomas F. krauss, Richard M. De La rue and Stuart brand, “Two-dimensional Photonic-Bandgap Structures Operating At Near-Infrared Wavelengths,” Nature, Vol. 383,699-702(1996).

[75] O Brien, J. D.; Painter, Oskar; Lee, R. K.; Cheng, Chuan-Cheng; Yariv, A.; Scherer, Axel, “Lasers Incorporating 2D Photonic Bandgap Mirrors,” Electronics Letters, Vol.32, 22432244(1996).

[76] O. Painter, R. K. Lee, A. Scherer, A. Yariv, J. D. O’Brien, P. D. Dapkus,I. Kim, “Two-Dimensional Photonic Band-Gap Defect Mode Laser”, Science, Vol. 284,1819-1821(1999).

[77] Dirk Englund, David Fattal, Edo Waks, Glenn Solomon, Bingyang Zhang, Toshihiro Nakaoka, Yasuhiko Arakawa, Yoshihisa Yamamoto, and Jelena Vučković, “Controlling the Spontaneous Emission Rate of Single Quantum Dots in a Two-Dimensional Photonic Crystal,” Phys. Rev. Lett., Vol. 95, 013904-1 – 013904-4(2005).

[78] Charles Kittel, “Condensed matter Physics,” 8th Edition.

[79] Neil W. Ashcroft, N. David Mermin “Solid State Physics,” (1976).

[80] J. S. Blackmore “Solid state physics,” Cambridge university press, (1985).

[81] http://reference.iucr.org/dictionary/Wigner-Seitz_cell

[82] http://nptel.ac.in/courses/113106040/Lecture30.pdf

[83] http://www.physics.nyu.edu/pine/colloidal_clusters.html

[84] Nina V. Dziomkina andG. Julius Vancso , “Colloidal crystal assembly on topologically patterned templates,”, Soft Matter, Vol. 1, 265-279(2005)

[85] Steven G. Johnson, Shanhui Fan, Pierre R. Villeneuve, and J. D. Joannopoulos, L. A. Kolodziejski, “Guided Modes In Photonic Crystal Slabs,” Physical Review B, Vol. 60, (999).

[86] BandSolve , Rsoft Design Group.

[87] http://www.ece.nus.edu.sg/stfpage/eleadj/planewave.htm

[88] K. S. Yee, “Numerical solution of initial boundary value problems involving Maxwell's equations in isotropic media,” IEEE Trans. Ant. Prop., Vol. 14, 302-307(1966).

[89] http://www.ece.nus.edu.sg/stfpage/eleadj/planewave.htm

[90] http://www.remcom.com/xf7-fdtd-method/

[91] http://www.ece.mcmaster.ca/faculty/bakr/ECE757/FDTD-I.pdf

[92] Fullwave, Rsoft Design Group

[93] P. Berenger, “A perfectly matched layer for the absorption of electronmagnetic fields,” J. of Comuptational Phys., Vol.114, 185-200(1994).

[94] Ifor D. W. Samuel, and Graham A. Turnbull, “Polymer lasers: recent advances,” Materials Today, Vol. 7, 28–35(2004).

[95] I. D. W. Samuel and G. A. Turnbull, “Organic Semiconductor Lasers,” Chem. Rev., Vol. 107, 1272−1295(2007).

[96] Heeso Noh, Jin-Kyu Yang, Seng Fatt Liew, Micheal J. Rooks, Glenn S. Solomon, and Hui Cao, “Synopsis: Bird feathers inspire mirrorless laser,” Phy. Rev. Lett., Vol. 106, 183901-1-183901-4(2011).

[97] Govind P. Agrawal and George R. Gray, "Intensity and phase noise in microcavity surface-emitting semiconductor lasers," Appl. Phys. Lett., Vol. 59 , 399-401(1991).

[98] Igor Vurgaftman and Jasprit Singh , "Steady-state performance of microcavity surface-emitting lasers with quantum confinement of electrons and photons", Appl. Phys. Lett., Vol. 64 , 1472-1474(1994).

[99] H. Yokoyama, “Physics and Device Applications of Optical Microcavities,” Science, Vol. 256, 66-70(1992).

[100] S. V. Frolov,Z. V. Vardeny and K. Yoshino, “Plastic microring lasers on fibers and wires”, Appl. Phys. Lett., Vol. 72, 1802 - 1804(1998).

[101] Wu, Xiang , Fudan Univ., Shanghai ; Hao Li ; Liu, Liying ; Xu, Lei ,“High Quality Direct Photo-Patterned Microdisk Lasers With Organic–Inorganic Hybrid Materials,” Quantum Electronics, Vol. 44 , 75 – 80(2008).

[102] Shengfei Feng, Xinping Zhang, and Peter J. Klar,“Waveguide Fabry-Pe´ rot microcavity arrays,” Applied Physics Letters, Vol. 99, 053119-1-053119-3(2011).

[103] V. G. Kozlov, G. Parthasarathy, P. E. Burrows, V. B. Khalfin, J. Wang, S. Y. Chou, and S. R. Forrest, ‘‘Structures for organic diode lasers and optical properties of organic semiconductors under intense optical and electrical excitations,’’ IEEE J. Quantum Electron., Vol. 36,18–26 (2000).

[104] Sebastien Chenais, “Habilitation à diriger de recherches,” Laboratoire de Physique des Lasers, Université Paris 13

[105] J. H. Schon, Ch. Kloc, A. Dodabalapur, B. Batlogg, “An Organic Solid State Injection Laser,” SCIENCE, Vol. 289, 599-601(2000).

[106] M. Reufer, S. Riechel, J. M. Lupton,J. Feldmann, U. Lemmer, D. Schneider, T. Benstem, T. Dobbertin, W. Kowalsky, A. Gombert, K. Forberich, V. Wittwer, U. Scherf, “Low-threshold polymeric distributed feedback lasers with metallic contacts,” Applied Physics Letters,Vol. 84, 3262-3264(2004).

[107] Nobuhiko Susa, “Threshold gain and gain-enhancement due to distributed-feedback in two-dimensional photonic-crystal lasers,” J. Appl. Phys., Vol. 89, 6959-6965(2001).

[108] Han-Youl Ryu, Soon-Hong Kwon, Yong-Jae Lee, Yong-Hee Lee, and Jeong-Soo Kim, “Very-low-threshold photonic band-edge lasers from free-standing triangular photonic crystal slabs,” Appl. Phys. Lett., Vol. 80, 3476-3478(2002).

[109] Soon-Hong Kwon,Han-Youl Ryu, Guk-Hyun Kim, and Yong-Hee Lee “Photonic bandedge lasers in two-dimensional square-lattice photonic crystal slabs,” Appl. Phys. Lett., Vol. 83, 3870-3872(2003).

[110] Francesco Di Stasio,a Luca Berti, Martin Burger, Franco Marabelli,Samuele Gardin, Tiziano Dainese, Raffaella Signorini, Renato Bozioc and Davide Comoretto, “Amplified spontaneous emission from opal photonic crystals engineered with structural defects,” Phys Chem Chem Phys., Vol. 11, 11515-11519(2009).

[111] D. V. Kuksenkova and H. Temkin, K. L. Lear and H. Q. Hou, “Spontaneous emission factor in oxide confined vertical-cavity lasers,” Appl. Phys. Lett., Vol. 70, 13-15(1997).

[112] Wei Dong Zhou, Jayshri Sabarinathan, Pallab Bhattacharya, Boaz Kochman, Erik W. Berg, Pei-Chen Yu, and Stella W. Pang, “Characteristics of a Photonic Bandgap Single Defect Microcavity Electroluminescent Device,” IEEE Journal Of Quantum Electronics, Vol. 37, 1153-1160(2001).

[113] Yoshihiro Akahane,Takashi Asano, Bong-Shik Song,Susumu Noda, “High-Qphotonic nanocavity in a two-dimensional photonic crystal Yoshihiro Akahane,” Nature,Vol. 425, 944-947(2003).

[114] Y. Akahane, T. Asano, B.-S. Song and S. Noda, "Development of High Q Photonic Nanocavity Using Two-Dimensional Photonic Crystal Slabs", Sci. Technical Review, 21-26(2005).

[115] Masahiro Nomura, Satoshi Iwamoto, Aniwat Tandaechanurat, Yasutomo Ota, Naoto
Kumagai, and Yasuhiko Arakawa, “Photonic band-edge micro lasers with quantum dot gain,” Optics Express, Vol. 17, 640-648(2009).

[116] M. Notomi, H. Suzuki, and T. Tamamura , “Directional lasing oscillation of two-dimensional organic photonic crystal lasers at several photonic band gaps,” Appl. Phys. Lett., Vol. 78, 1325-1327(2001).

[117] V. Reboud, P. Lovera, N. Kehagias, M. Zelsmann, C. Schuster, F. Reuther, G. Gruetzner, G. Redmond and C. M. Sotomayor Torres, “Two-dimensional polymer photonic crystal band-edge lasers fabricated by nanoimprint lithography”,Appl. Phys. Lett., Vol.91, 151101-1-151101-3 (2007).

[118] Han-Youl Ryu, Hong-Gyu Park, and Yong-Hee Lee, “Two-Dimensional Photonic Crystal Semiconductor Lasers: Computational Design, Fabrication, And Characterization,” IEEE Journal Of Selected Topics In Quantum Electronics, Vol. 8, 891 – 908(2002).

[119] I. Protsenko, P. Domokos, V. Lefe`Vre-Seguin, J. Hare, J. M. Raimond,And L. Davidovich, “Quantum Theory Of A Thresholdless Laser,” Physical Review A February, Vol. 59, 1667-1682 (1999).

[120] E.M. Purcell, “Spontaneous emission probabilities at radio frequencies,” Phys. Rev., Vol., Vol. 69, 681(1946).

[121] Gunnar Björk, Anders Karlsson, and Yoshihisa Yamamoto , “ Definition of laser threshold,” Phyiscal Review A , Vol. 50, 1675-1680(1994).

[122] Meschede,“Radiating Atoms In Confined Space: From Spontaneous Emission To Micromasers,” Physics Reports, Vol. 211, 201-250(1992).

Chapter 2:

Photonic properties of monolayer of periodically arrayed dielectric spheres

1.1. Introduction and motivation

In the previous chapter, it has been shown that the micro and nanoparticles are interesting objects for the nanostructuration in the context of the bottom-up approach. More over, micro and nanoparticles show specific optical properties. The purpose of this chapter is to investigate whether these optical properties include photonic bandgap and if defect microcavity in opals and inverse opals can be fabricated so as to realize organic diode laser

Indeed, it has been shown that photonic crystal microcavities offer interesting optical properties to lower the laser threshold. Based on this low-threshold or threshold-less approach, photonic crystal microcavity organic laser have been demonstrated. It has been widely studied theoretically and experimentally for PhC crystal microcavity lasers and other applications [1, 2]. Two dimensional photonic crystals "etched" into slabs are easier to fabricate compered to the 3D PhCs and they offer some 3D confinement due to the total internal reflection in the direction perpendicular to the plan of the slab. However, these PhC microcavities were realized using top-down approach and therefore are not compatible with mass production.

The monolayer of opals and inverse opals resulting from the bottom-up approach of the nanotechnology in contrast are compatible with mass-production and therefore constitute an interesting alternative approach. This type of PhC slab is an alternative from the technological point of view because their fabrication is based on the bottom-up approaches like dip-coating and drop coating, as discussed in chapter 1. The self-assembly method can be used to fabricate the artificial opal using microspheres synthesized with different dielectric materials such as PMMA, polymer, SiO_2 or TiO_2 [3]. The deposited monolayer of microspheres can be regarded as a semi-2D PhC structure and has been used to form 2D PhCs on LEDs and solar cells [4,5,6].

In this chapter we will try to answer the following question : “Can monolayers of opals and inverse opals be used to fabricate photonic crystal microcavity organic laser?” If this is possible such a

photonic crystal microcavity is to be low threshold which ideally means low mode volume and high quality factor.

To answer this question, we will first investigate the existence of photonic bandgap in monolayer of self-organized nanoparticles arranged in opals and in inverse opals. Even more precisely, we would like to identify the parameter range under which the photonic bandgap exists in opals and inverse opals. Among these parameters, the refractive index contrast plays a key role as well as the compactness.

We choose to investigate the photonic bandgap first numerically before experiments can be considered. Indeed single domain monolayer of self-organized nanoparticles are difficult to obtain experimentally. More over varying experimentally parameters like the refractive index over a large range to map the existence of the photonic band gap is almost impossible from the experimental point of view since only few materials are known to be used to inflitrate the micro nanopsheres and complete which means only few discrete values of the refractive index are attainable. This is why we choose to identify numerically the conditions under which the photonic bandgap may exist so as to define the experiments that will be able to confirm it.

Actually, the experimental characterization of in plane propagation of light in monolayer of micro nanoparticles has not been studied extensively. There have been some theoretical and experimental studies to understand the optical properties of monolayer of periodically arranged dielectric spheres, but these experimental works deal with the study of the perpendicular incident transmittance properties [7]. It deals also with the comparison of the gallery modes of individual spheres and photonic band effects from array of spheres in the monolayer in milimeterwave regime[8]. The dependence of properties of these type of PhC on compactness[9] and refractive index[10] of the spheres were studied in the microwave regime. Few theoretical studies were conducted to know the effects of the presence of a substrate[11, 12] on the optical properties. Such experiments dedicated to the demonstration of the optical properties of monolayer of opals in the optical regime require sub micrometer sphere sizes. But controlling the arrangement of the ordered array of such small spheres is difficult and much of the works were done on bigger sphere sizes of millimeter range and in the micro wave or terahertz regime. The properties studied in microwave or terahertz regime can be applied to smaller spheres at optical regime by scalability property of PhCs.

Although the monolayer of microspheres can be used in the applications mentioned above and some studies of their optical properties exist, the in-plane optical properties have not been

systematically studied well in the literature. In addition, to our best knowledge, the monolayer of *spherical voids* has not been studied yet. More over there is no theoretical study which consider the use of monolayer of dielectric/air microspheres for microcavity lasers.

1.1.1. Objective of the chapter:

The main objective of the chapter is therefore to study the in-plane propagation of light in the monolayer of opals and inverse opals. This requires two-steps : a theoretical and an experimental study. First, the existence of the photonic bandgap is to be investigated numerically so as to map them as a function of the refractive index contrast and of the compactness of spheres. In addition, the effect of the glass substrate on the optical properties is to be considered. In the second part of the theoretical study, the criteria to obtain an optical confinement in the structures will be pointed out. Preliminary results on the studies of optical microcavities made in the PhCs are discussed. Once the existence of photonic band-gaps is predicted, photonic crystal micro-cavities can be studied and their quality factor quantified. The results are used to design PhC microcavity to be used with organic semiconductor light emitter materials.

In the second step, the in-plane propagation of light in monolayer of opals and inverse opals can be investigated experimentally with the parameters identified by the numerical study.

The procedures to measure experimentally the in-plane photonic band-gap properties for monolayer of microspheres in the optical domain have to be identified and proposed. In the experimental part, systematic experimental methods for the characterization of the in-plane transmittance of monolayer of spheres in optical regime will be considered. Modified fabrication method and characterization setup will be pointed out.

1.1.2. Layout

The theoretical study will be presented in paragraph 1.2., with the mapping of the forbidden band-gaps in the section Erreur : source de la référence non trouvée and the study of the Ph.C based microcavity in section 1.2.5.. In paragraph 1.3. the experimental characterization of optical properties of monolayer of spheres is presented and the perspectives of this work is presented in paragraph 1.4..

1.2. Numerical study of the In-plane propagation of light in monolayer of opals and inverse-opals

1.2.1. Simulation conditions

1.2.1.1. The studied structures

The four structures considered in this study are;

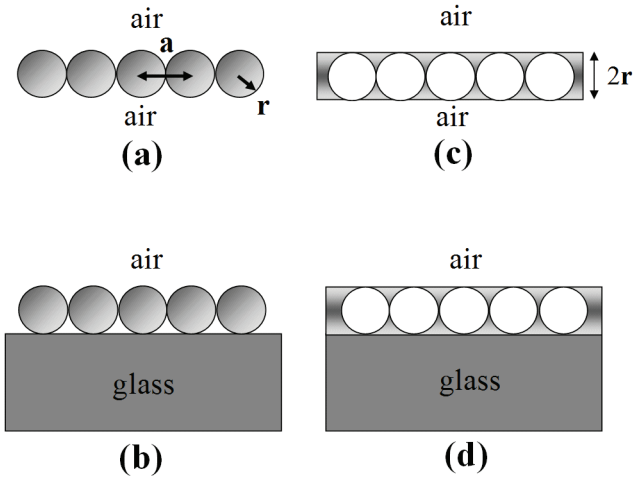

Figure 1 : Schematic drawing of the considered structures: (a) self-sustained monolayer of opals (b) monolayer of opals deposited on a glass substrate (c) self-sustained monolayer of inverse opals (d) monolayer of inverse opals deposited on a glass substrate.

- **Structure a**: The self-sustained monolayers (ML) of dielectric spheres surrounded by air (ML 'opals') (figure 1a).
- **Structure b**: The monolayers (ML) of dielectric spheres surrounded by air (ML 'opals') deposited on a semi-infinite glass substrate (figure 1b).
- **Structure c**: The self-sustained monolayer of air spheres surrounded by dielectric material (ML 'inverse opals') (figure 1c).
- **Structure d**: The monolayer of air spheres surrounded by dielectric material (ML 'inverse opals'), on semi-infinite glass substrate(figure 1d).

The monolayer of spheres are arranged in 2D triangular lattice. The thickness of the slab is equal to the diameter of the sphere. We apply the terms opal and inverse opal to the monolayer structures although these terms are usually used to refer to the 3D periodic structures. Figures 1(a)-(d) show the cross-sectional view of the opals and the inverse opals with or without glass substrate. The ***r*** and

a are defined to be the radius of the microspheres and the lattice constant of the PC structure. The thickness of the infiltrated material in inverse opals is *2r* (the diameter of microspheres) as shown in Fig. 1(c). The compactness of the spheres relates to the *r/a* ratio value. Touching spheres correspond to the ratio r/a = 0.5 and for nontouching spheres r/a < 0.5.

1.2.1.2. The varied parameters

To systematically study the photonic band gaps and transmittance of the structures, two parameters are varied; namely the refractive index ***n*** and the ***r/a*** ratio.

When the effect of the refractive index is investigated, we vary either the refractive index of the microspheres in the opals case or that of the infiltrated material in the inverse-opal case with a range from 1.5 to 3. When the refractive index is varied, compact spheres with ***r/a*** = 0.5 are considered. The refractive index of air and the glass substrate are taken to be n_0=1 and n_{glass}=1.5, respectively.

To study the effect of the compactness of spheres, the ***r/a*** ratio is varied from 0.25 to 0.5, by fixing the size of the microspheres, hence fixed height of the slab, and changing the period of the lattice. While varying the *r/a* ratio, the refractive index of the microspheres or the infiltrated material is fixed at **2.5**, which corresponds to the refractive index of the TiO_2 material which has been used for inverse opals [13].

1.2.1.3. The computation conditions

We carry out 3-D finite-difference time-domain (FDTD) simulations to study the in-plane PBG of the structures. The six boundaries of the simulation domain are illustrated in the top-view and cross-sectional view of the structure as shown in Figs. 2(a) and (b), respectively. Seventeen rows of microspheres are arranged in a triangular lattice. This was chosen in order to take into account the limited computer memory and the convergence of the results. The spatial grid was chosen to be the period/20 and the time grid was chosen to have a value of **0.00866**, the maximum time value satisfying the Courant stability condition. Smaller grid couldn't be chosen due to smaller computer memory. These parameters were sufficient to give a reasonably accurate result in a reasonable computation time. The periodic boundary is applied at the right and the left boundaries of the simulation domain, as shown in Fig. 2(a). The perfectly matched layer (PML)[14] is applied to terminate the glass substrate thus simulating an infinitely thick glass layer and the other three boundaries of the simulation domain. A light source with a Gaussian spatial profile positioned on one side of the monolayer launches a broad band signal in the plane of the periodic lattice and a monitor positioned on the other side of the structure acquires the transmitted signal. From this

transmittance, the PBGs along the Γ-M and Γ-K directions shown on in Fig. 2(c) are identified, defined. The TE and the TM modes, where the electric field is oriented predominantly along X direction and Y direction, respectively, are considered.

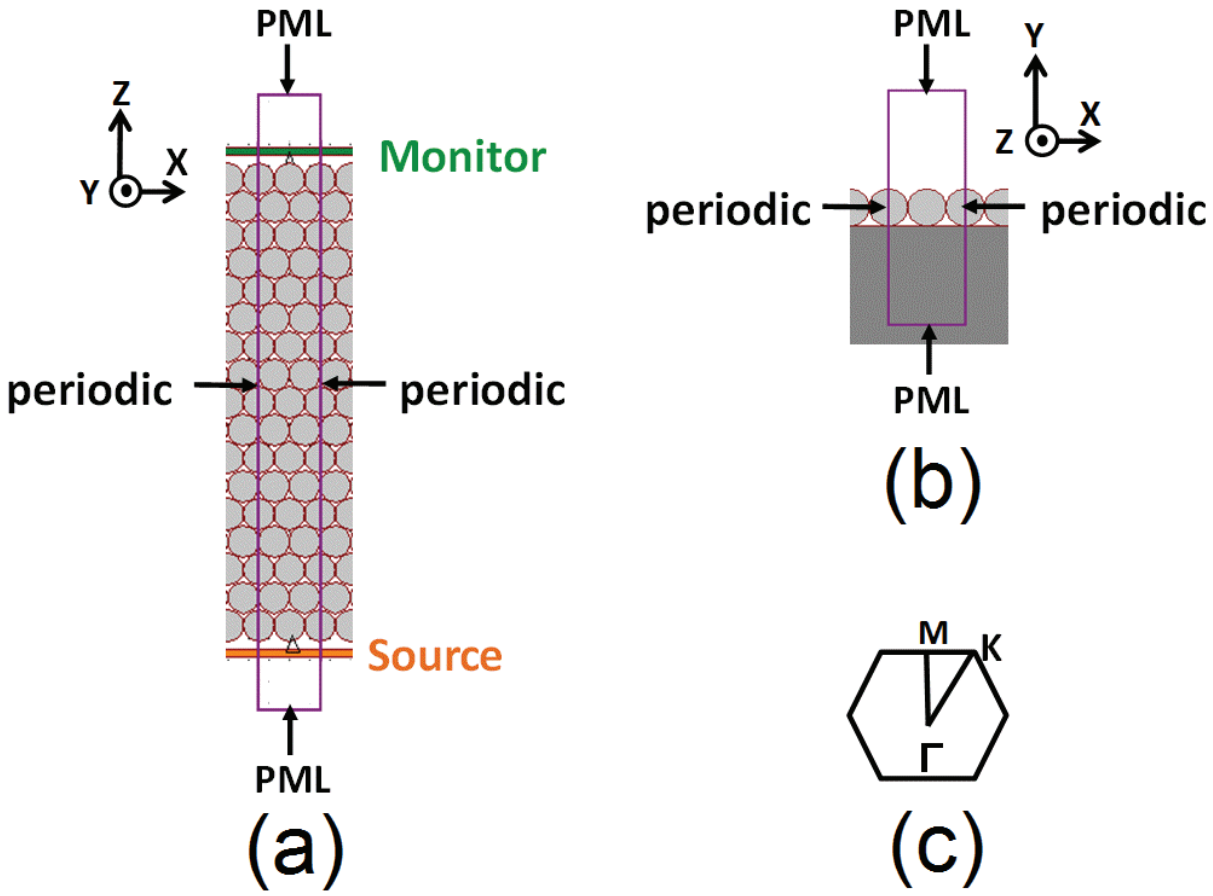

Figure 2 : Schematic drawing of the six boundaries, light source and monitor in the simulation region: (a) Simulation domain in the XZ plane. Seventeen rows of microspheres are arranged in triangular lattice. The periodical boundary is applied at the right and left side of the simulation boundaries. The perfectly matched layer is applied at the rest boundaries. The light source is launched from the edge of the monolayer along the z-direction. The monitor is positioned on the other side of the monolayer. (b) Simulation domain in XY plane (c) First Brillouin zone for the hexagonal structure

The transmittance on the whole spectrum is obtained by calculating the Fourier transform of the recorded time sequence of the field amplitudes. The cavity response is obtained by launching a broadband source in the vicinity of the cavity and transforming the time sequence acquired by the time-monitor into the frequency domain [15 16].

1.2.2. Transmittance and photonic band gaps

The figure 3 shows the simulation results of the self-sustained ML-opal (structure a) shown on

figure 1(a). Figure 3(a) is a schematic diagram of the ML-opal, with the excitation source and monitor as discussed in section 1.2.1.. In this case, the ***r/a*** ratio is 0.5 and the refractive index of the microspheres is 2.8. The excitation is a TE polarized wave propagating in the Γ-M direction. The electric field amplitude in the x-direction (**Ex**) at the transmission monitor point as a function of time steps is indicated in figure 3(b). The fast Fourier transform of the time domain signal gives the transmission spectrum for the opal structure in the frequency domain, as shown in figure 3(c). The horizontal axis represents normalized frequency in unit of ***a/λ***, where ***a*** is the period of the crystal and ***λ*** is the absolute free space wavelength. We can observe that in the normalized frequency region from 0.275 to 0.3, the transmission is relatively lower than in the rest of the spectrum indicating the PBG. The normalized frequencies 0.275 and 0.3 can be regarded as the lower and higher frequencies of the band edges of the PBG for the specific electric polarization and direction, respectively. From figure 3(c), oscillations occurring on both sides of the PBG can be observed. These oscillations are understood as Fabry-Perot free spectral range resulting from the interference produced by the reflection from the opposite edges of the photonic crystal structure.

1.2.3. Mapping the Photonic band-gaps:

In order to identify the range of existence of the PBGs, we would like to map the parameter range (region) where the PBGs exist. This '**photonic gap map**' is another representation of the PBGs obtain by the collection of different transmittances similar to the one in figure 3(c) but calculated for different values of the refractive index and plotted in a compact form. For example, the figure 3(d) shows the band edges of the PBGs for the Γ-M direction and for the TE mode calculated for the structure (a) shown in figure 3(a) as a function of the refractive index of the microspheres that ranges from 1.5 to 3. The two solid points in figure 3(d) represent the band edges of the transmission spectrum shown in figure 3(c). The dark region bounded by high and low frequency band edge points represents the PBG region as a function of the refractive index.

In the following sections, we will discuss the dependence of the transmittance and of the PBGs in the refractive index of the dielectric material in opals and in inverse-opals. In addition the PBGs will be studied for different compactnesses of the spheres that is for different **r/a** ratios as mentioned in section 1.2.1.2.. These calculations are done for both field polarizations (**TE, TM**) and for both propagation directions (**ΓM, ΓK**). The effect of glass substrate on the transmittance will be discussed. Different loss mechanisms dependent on different parameters such as effect of compactness will be pointed out.

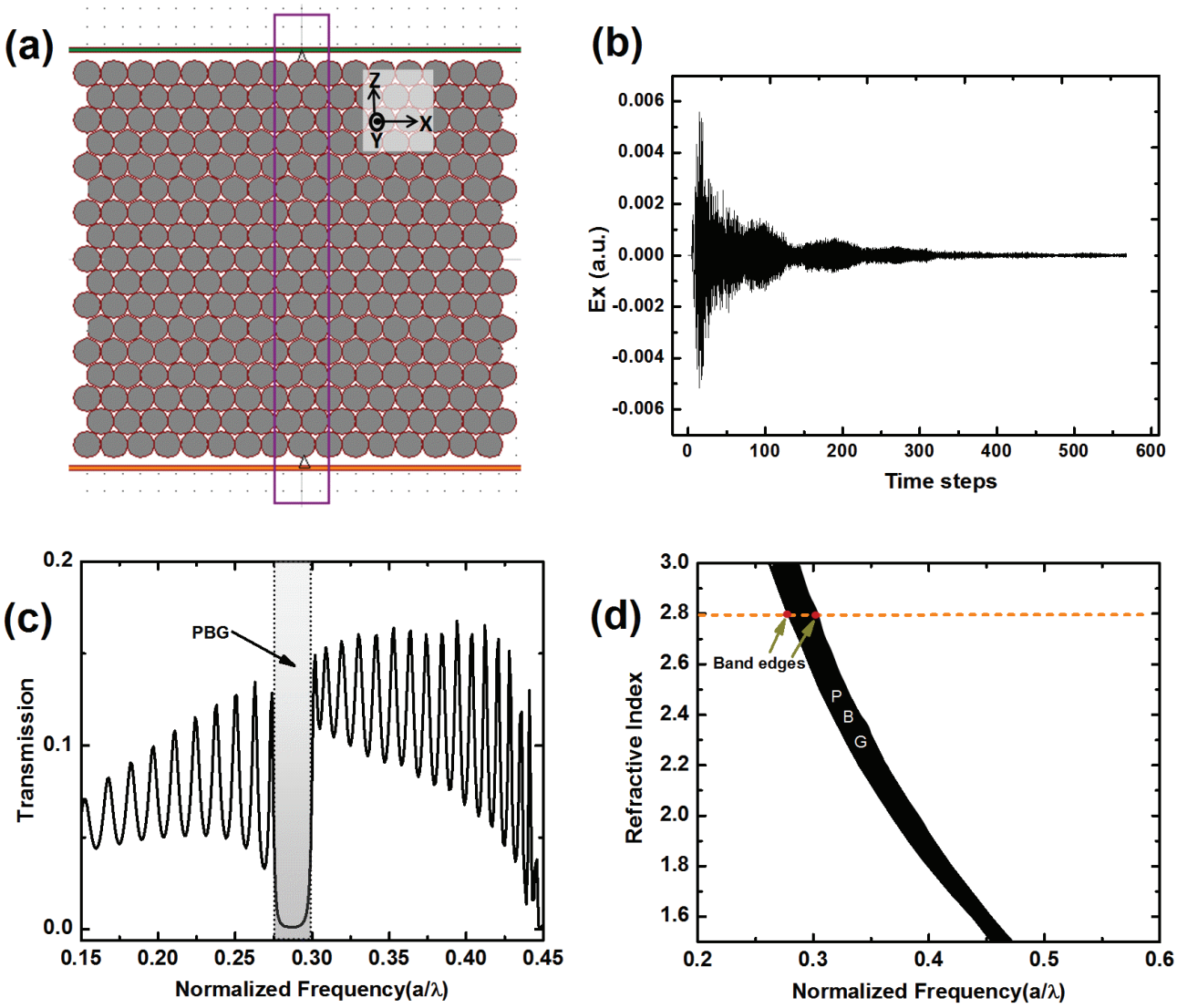

Figure 3 : (a). ML-Opal suspended in air viewed in the plane of the PhC with the source and the monitor. (b) The time-series wave form of the transmitted electric field component in the x-direction (Ex). (c) Fourier transform of the time-series showing a photonic bandgap (PBG). (d) Photonic gap map diagram showing the PBG as a function of the refractive index.

In order to identify the existence of the photonic band-gap for different available materials, the dependence of the transmittance and of the PBGs on the refractive index was studied in the case of a compact arrangement of opals and inverse-opals. Since the compact arrangement is easier to fabricate, it is worth searching for possible refractive index values maximizing the range of existence of the PBG and maximizing the optical confinement. Since the structure (a) (self sustained ML-opal) and the structure (c) (self-sustained ML-inverse opal) are simpler structures, they will be considered first before more realistic structures with glass substrate can be calculated and ultimately compared [10]. Figure 4 shows the refractive index dependence of the transmittance

for the TE and TM polarized waves in the ΓM and ΓK directions for some chosen refractive index values in the case of a self-sustained opal. As the refractive index of the spheres increases, a red shift in the PBG can be observed. This is due to the increase of the effective refractive index of the PhC slab [17]. Moreover, figures 4(a) and 4(b) show that the transmission values at the PBG frequencies decrease when the refractive index increases.

Figure 4(c) shows the photonic band gap map of the structure (a) (self-sustained ML-opal) for the Γ-M and the Γ-Kdirections of propagation and for the TE and the TM modes. As the refractive index is varied, changes are observed in the width of the PBG, and therefore in the gap-mid-gap ratio $\Delta f/f$. For the TE mode and the ΓM directions, the width of PBG is reduced from 0.083 to 0.036 as the refractive index is changed from 3.0 to 1.5. This narrowing of the PBG is due to a reduction of the refractive index contrast [18, 19]. Therefore, a larger refractive index contrast is required to obtain a wider band gap. The gray shaded region in figure 4c represents the overlap of the TM mode PBGs for different directions of propagation at higher normalized frequencies.

Figure 5 shows the confinement of the electric field intensity profile in the case of the **structure(a)** (self-sustained ML-opal) for the two different refractive index values 1.5 and 2.8. When the refractive index of the spheres is 1.5, there is more leakage of light in the vertical direction than when the refractive index of the spheres is 2.8. Thus, the transmittance will be relatively higher in the opal with monolayers of spheres of refractive index 2.8.

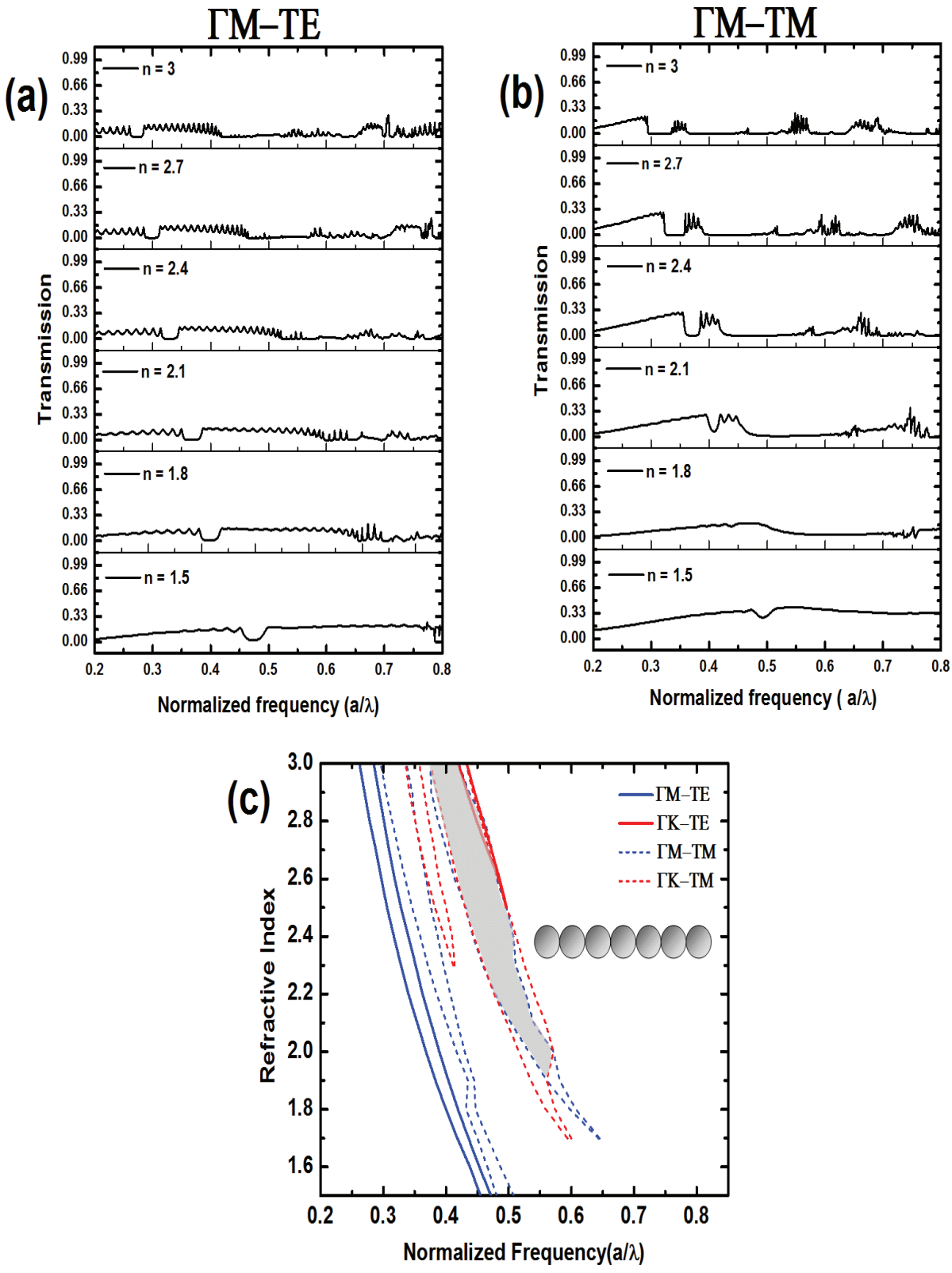

Figure 4 : Transmission spectra and photonic gap map dependence on refractive index of spheres in self sustained ML-opal photonic crystals. (a) The refractive index dependence of the calculated electric field intensity transmittance in the Γ-M direction and for the TE polarization (b) The refractive index dependence of the calculated electric field intensity transmittance in the Γ-M direction and for the TM polarization (c) Band map as a function of the refractive index. (The ML-opal is assumed to be a 2D triangular lattice of dielectric spheres. The spheres are compact with r/a=0.5.)

1.2.3.1. Refractive index dependence of the photonic band gaps

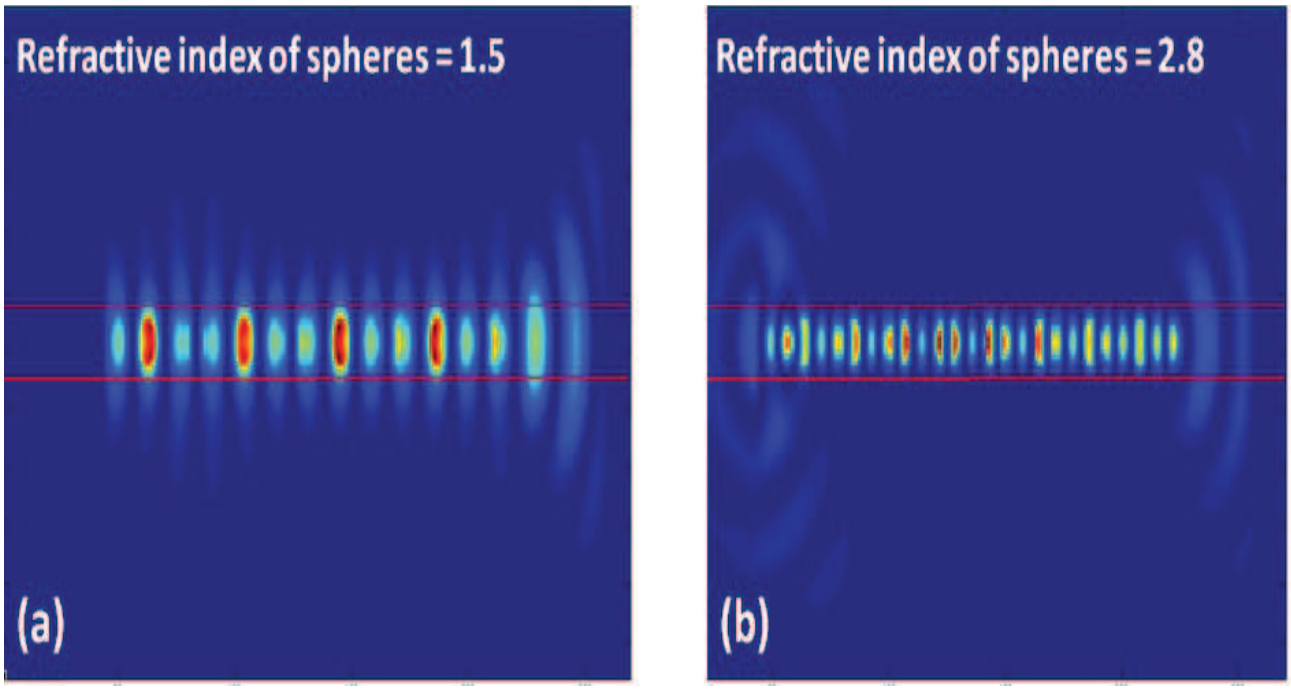

Figure 5: Electric field intensity profile in self-sustained monolayer of spheres. (a) Refractive index of spheres = 1.5. (b) Refractive index of spheres = 2.8. (The monolayer of spheres is limited by two red lines)

In the case of the structure(c) (self-sustained ML-inverse opal), the following similar transmittance can be plotted for refractive index values between 1.5 and 3.0. Figure 6(a) represents the transmittance of the **TE** mode in the G**M** direction, while figure 6(b) represents the transmittance of the **TM** mode in the G**M** direction. Note that the PBG is observed for a wide range of refractive index. Figure 6(c) shows the photonic band-gap map in the case of the structure(c) (self-sustained ML of an inverse opal structure) for TE and TM polarized waves and for the **G**M and the **G**K directions. Again, as in the self-sustained ML-opal, the PBG appears for a wide range of refractive index values and is red shifted as the refractive index is increased.

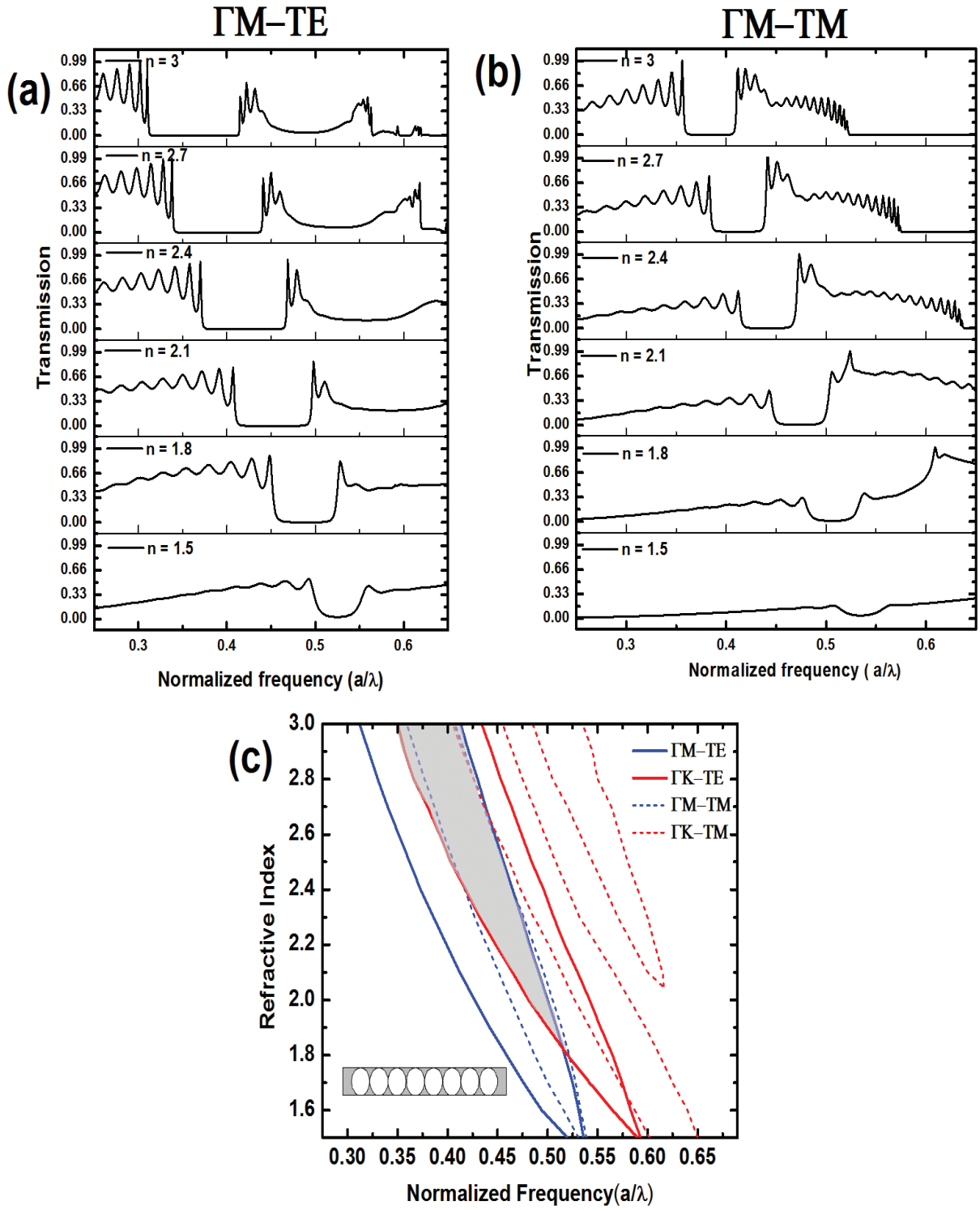

Figure 6: Transmittance and photonic gap map as a function of the refractive index in an self sustained inverse-opal photonic crystal (structure c). (a) Calculated electric field intensity transmittance in the Γ-M direction for the TE polarization (b) Transmittance of the electric field intensity in the Γ-M direction and for the TM polarization. (c) Band map diagram as a function of the refractive index. (The structure of the self-sustained inverse-opal is assumed to be a 2D triangular lattice of air spheres in a dielectric slab. The spheres are compact with r/a=0.5.)

From the figures 4(c) and 6(c), the self-sustained opals and inverse-opals exhibit a PBG for a wide range of the refractive index. The overlapp between the bandgaps calculated for the ΓM and the ΓK directions can be observed in the TM mode of the opals (figure 5(c)), and in the TE mode of the inverse-opals (figure 6(c)). These overlapps are indicated by shaded region. A first conclusion is that self-sustained opals exhibit more favorably PBG in the TM mode. Inversely self-sustained inverse-opals exhibit more favorably PBG in the TE mode. This is due to the fact that the TM band gaps are more favored in a lattice of isolated high refractive index regions (like in opals), and TE band gaps are more favored in a connected lattice (like in inverse opals) [20].

In figure 6(c) an overlap of the PBG regions is observed. This overlap of the photonic bandgap for the ΓM and the ΓK directions for the TE mode observed for the **structure(c)** appears for refractive index above 1.8. These results indicates that dielectric materials such as ZnO (refractive index at 620 nmn=2), TiO_2 (refractive index at 620 nm n =2,1), Si_3N_4 (Refractive index at 620nm=2) or diamond (refractive index at 620 nm=2.41) might be the suitable candidates to be used for the realization of self-sustained 2D inverse-opal PhC to obtain a complete confinement of the TE mode.

1.2.3.2. Effect of the compactness on the photonic properties

In addition to the refractive index studies, it is also important to study the effects of the compactness of the spheres on the PBG. Indeed, given that only few materials are compatible with the realization of opals and inverse opals, the compact arrangement might not give an optimum PBG. Actually, other values of the r/a ratio might give larger region of existence of the PBG. In order to study the effect of the compactness, the diameter of the spheres that defines the PhC thickness is fixed. To vary the compactness, constant size of spheres with diameter, **D** = 300 nm (so that **r** = 150 nm) are considered and the period, **a**, of the PhC is varied so that the ***r/a*** ratio is varied, keeping the thickness of the slab constant. The ***r/a*** ratio is varied from non-compact sphere with ***r/a*** = 0.25, to the close packed arrangement with ***r/a*** = 0.5. The refractive index is kept constant at **n = 2.5**, which corresponds to the anastase phase of TiO_2.

Figures 7 shows the transmittance and the band-gap map as a function of the ***r/a*** ratio. Figure 7 (a) and 7(c) show the transmittance in the ΓM direction and for the TE polarization in the case of self-sustained ML inverse-opals and ML opals, respectively. Figures (b) and (d) show the photonic gap maps for the different directions and for the different polarizations in the case of the ML-inverse opal and the ML-opal, respectively.

From figures 7(a) and 7(b), the center of PBG of the ML-inverse opal structure (structure c) is blue shifted as the compactness of the spheres is increased from ***r/a*** = **0.25** to ***r/a*** = **0.5**. This is due to the decrease of the average refractive index of the PhC. But for the opal structure, as the compactness is increased, the average refractive index is increased which causes the red shift of the center of the PBG, as in figures 7(c) and 7(d).

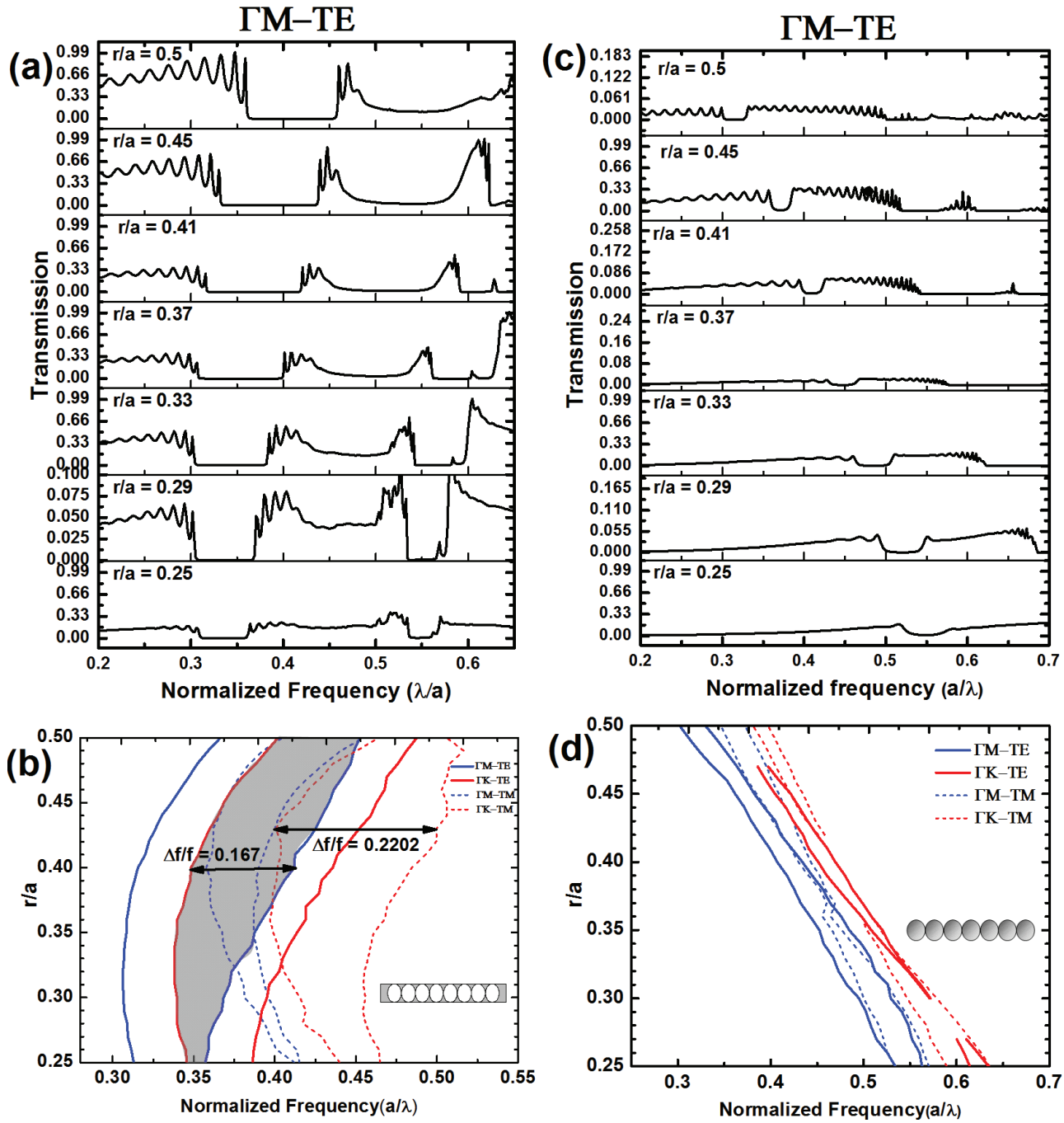

Figure 7: Effect of the compactness on the existence of the band gaps in self-sustained opals and inverse-opals (a) transmittance dependence on the r/a ratio for the self-sustained inverse-opal (b) photonic gap map of a self-sustained inverse opal (c) transmittance dependence on the r/a ratio in a self-sustained opal (d) photonic gap map of self-sustained opal.

As indicated by the shaded region in figure 7(b), in the case of the structure (c) (ML-inverse opal), the overlap of the TE modes for the ΓK and the ΓM directions is observed for a wide range of compactness values. The widest overlap of the band gap can be obtained by calculating the gap–midgap ratio. In our case, the gap-mid gap ratio is around 0.167 as the ***r/a*** ratio is around 0.40. This reveals that inverse opals might be more favorable to obtain a stronger in-plane light confinement in a microcavity.

In the case of infinite height air hole 2D hexagonal PhCs, the optimum compactness value can be chosen as the one with the larger PBG [21]. But when considering 2D PhC slabs with finite height, like monolayer of spheres, the compactness defining the larger PBG is not necessarily the optimum to achieve the strongest light confinement in microcavity applications. Indeed, the finite height of the PhC layer induces losses due to the evanescence of the field in the claddings. Thus for a given refractive index of the materials, the loss out of the PhC layer will depend on the filling ratio and therefore on the compactness of the dielectric or of the air spheres in the opals or inverse opals,cases respectively. In order to investigate in detail how the compactness affects the confinement, the electric field intensity profile has been calculated in the different structures for different compactness values.

Figure 8 shows the electric field intensity profiles for two different values of the compactness in the cases of opal and inverse-opal monolayers. The figure 8(a) shows the electric field intensity $I=|Ex|^2$ for a vertical cross section (z is the direction of propagation) for an opal slab. The incident field propagates in the ΓM direction. The source is launched from the left side of the system and the rectangular solid lines show the boundaries of the PhC slab.

Figure 8(a) and 8(b) show the field profile for a monolayer of opal in air with a compactness r/a = 0.5 and 0.31, respectively. Although the light can be seen propagating inside the PhC for both compactness values, there is relatively more evanescent field into the air cladding when the spheres are non-compact.

Figure 8(c) and figure 8(d) present the self-sustained inverse opals configuration, for com$pact air spheres (r/a = 0.5) and for non-compact air-spheres (r/a=0.31), respectively. Obviously the compact structure [figure 8(c)] induces more evanescent field and therefore is more lossy than the non-compact spheres with r/a = 0.31 [figure 8(d)]. Note that in the case of the inverse-opals, the compact spheres (r/a=0.5) configuration exhibits PBG with a gap-mid-gap ratio of $\Delta f/f$=0.117 (figure 7.b) larger than the non-compact spheres configuration (r/a=0.31) with $\Delta f/f$=0.114. In this case, the enlargement of the gap is followed by an increase of the losses. This is because in the compact configuration, the low effective refractive index resulting from the compactness increases

the limit angle of the total internal reflection as well as the evanescence of the field and produces out-of-plane radiative modes. Therefore in order to optimize the quality factor of a PhC microcavity a trade-off between a large bandgap and the reduction of the losses is required.

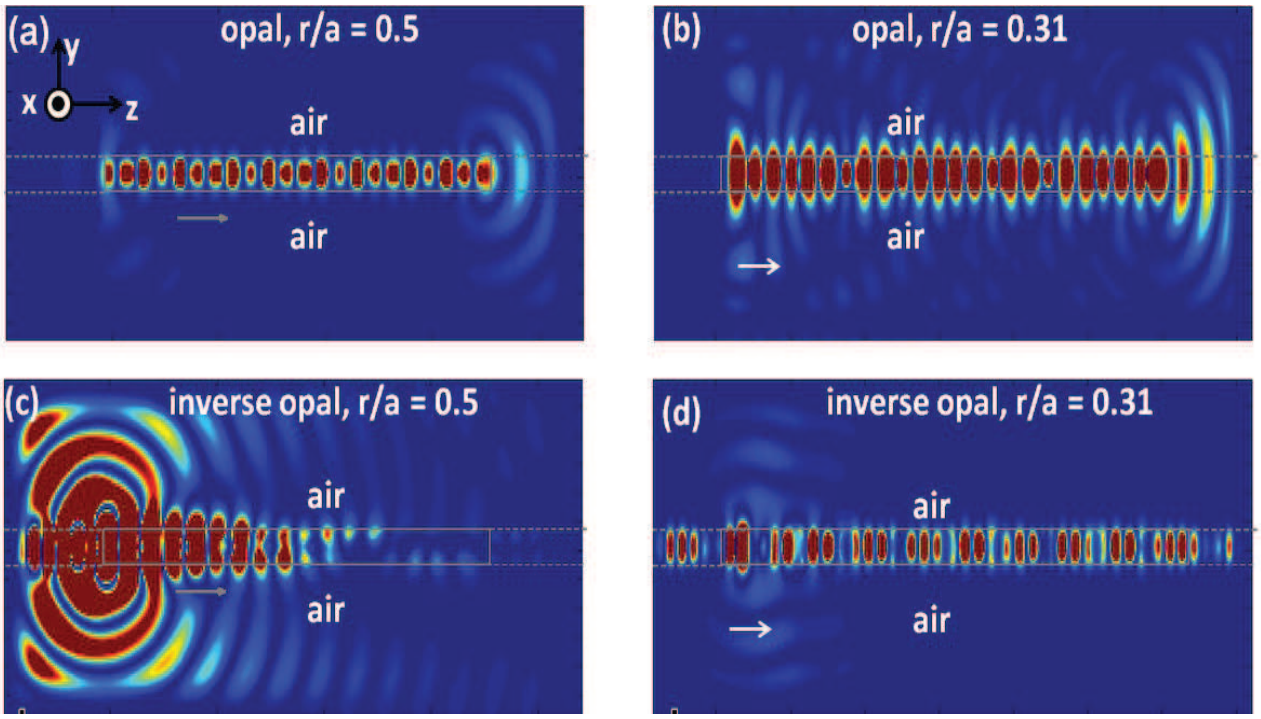

Figures 8: TE electric field propagation in self-sustained opals (structure a) and inverse-opals (structure b) for different values of the compactness. The direction of propagation is indicated by arrows. The PhC layer is limited by the rectangular solid lines. (a) Electric field intensity profile in compact arrangement (r/a = 0.5) of dielectric spheres in opals (structure a) (b) Electric field intensity profile in non-compact arrangement (r/a = 0.31) of dielectric spheres in opals (structure a) (c) Electric field intensity profile in compact arrangement (r/a = 0.5)of air spheres in inverse opals (structure c) (d) Electric field intensity profile in non-compact arrangement (r/a = 0.31) of air spheres in inverse opals (structure c) showing the propagation of the field. (The structure of the photonic crystal is assumed to be a 2D triangular lattice of dielectric or air spherical balls. The refractive index is 2.5.)

1.2.3.3. Substrate effects on monolayer of sphere array photonic crystals

The self-sustained monolayer of opal and inverse opals are air-bridge type of PhC slabs. In these cases, the index contrast between the core and the cladding is large and as a result the light is confined in the slab. However, such structures are more a school case than a real object because they are difficult to fabricate. Indeed, they aren't easy to integrate into a chip nor are they stable mechanically. In order to investigate a more realistic structures we will focus now on the optical properties of monolayer of opals and inverse opals deposited on a substrate. In these objects the lower cladding is glass and the upper cladding is air. Note that the vertical radiation loss of this-type of structures is expected to be larger than the air-bridge slab structures because of the smaller

refractive index contrast between the slab and the bottom cladding region, the substrate.

Influence of the refractive index contrast

The figure 9 shows the transmittance and the PBGs as a function of the refractive index for the opal monolayer and the inverse-opal monolayer deposited on glass substrate (**structure-b** and **structure-d**, respectively). The transmittances of the **structures-b** and **d** calculated for different values of the refractive index contrast are presented on the figures9(a) and 9(b), respectively. For the sake of comparison the transmittance of the structures without substrate are also presented (indicated by "air" in the graph). The presence of the glass substrate, suppress the existence of the PBG for lower refractive indices, as compared to self sustained structures.

Figures 9(c) and 9(d), respectively, show the photonic gap map as a function of the refractive index for the opal and the inverse-opal structures deposited on glass substrate respectively. The gray region with very low transmission (denoted by 'Lossy region') is observed as the refractive index of the microsphere or the infiltrated materials is lower than 1.8 and 2.2 respectively. This can be explained by the lower index contrast on the substrate side which results in a larger evanescence and therefore a leakage into the substrate. Note that in figure 9(c) the upper edge of this lossy region corresponds to the refractive index 1.9 at the normalized frequency 0.25 and to 1.8 at the normalized frequency 0.675. This originates from the fact that for lower normalized frequency, (longer wavelength) the mode is wider. This leads to a stronger coupling to the substrate.

This phenomenon can also be observed in the case of the structure-d [Figure 9(d)]. But in the case of an inverse-opal deposited on a glass substrate this phenomenon is even more accentuated because of the filling fraction. Indeed the filling fraction of an inverse-opal is lower than the filling fraction of an opal which results in a lower effective index of the inverse-opal. Therefore, the existence of a PBG requires a higher value of the refractive index of the infiltrated materials to compensate for the losses.

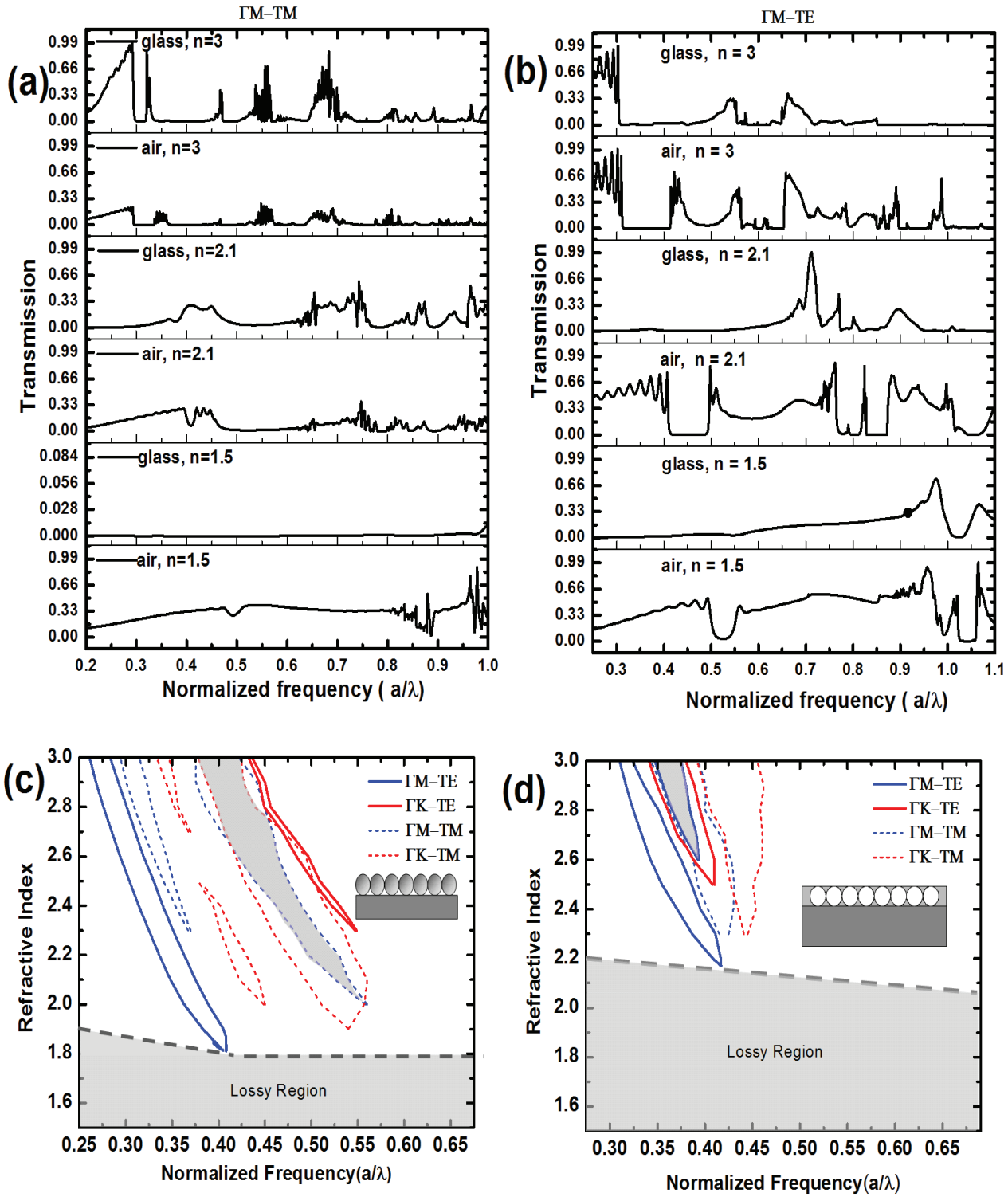

Figure 9: In-plane transmittances and photonic gap maps as a function of the refractive index in opals and inverse-opals monolayers deposited on a glass substrates. (a) In-plane transmittances of an opal monolayer on a glass substrate calculated for different refractive index values in the ΓM direction (TE polarization). (b) In-plane transmittances of an inverse-opal monolayer on glass substrate calculated for different values of the refractive index in the ΓM direction (TE polarization). (c) photonic gap map of the opal monolayer with glass substrate. (d) photonic gap map of inverse-opal monolayer on glass substrate. (Calculated with 2D triangular lattice of dielectric or air spherical balls and with a compact arrangement of spheres (r/a=0.5)).

Impact of the compactness

In this section we investigate the impact of the compactness on the existence of the PBG. This is shown in figure 10. We consider first monolayers of opal deposited on a glass substrate (structure b). When the compactness is varied, the photonic bandgap is not greatly enhanced [Fig.10(a) and (b)]. On the contrary the bandgap vanishes when the r/A factor is reduced.

Figure 10(c) shows the transmittances of monolayers of inverse-opal on glass substrate for different values of the compactness. When the **r/a** ratio varies from r/a=0.5 (compact case) to r/a = 0.33 the gap-to-midgap ratio increases. This appears clearly on the photonic gap map mainly for the ΓM and the ΓK in the TE polarization (see figure10(d)).

Intensity profile

In order to investigate further the effect of the glass substrate we map the electric field intensity profile on figure 11 and compare it with the figure 8.

The comparison of the compact opal with and without glass substrate (figure 11(a) and figure 8(a) do not emphasize strong differences. However, the comparison of the non-compact opal with and without glass substrate (figure 11(b) and figure 8(b)), respectively, shows larger differences: the presence of the glass substrate induces out-of-plane diffraction which strongly reduce the propagation.

Surprisingly in the inverse-opals configuration (figures 11(c) and 11(d)) the trend is opposite. In the compact configuration (figure 11(c)) (r/a=0.5), the light is coupled-out to the glass substrate reducing the propagation to the right side of the structure. However in the non-compact configuration 11(d), the higher effective refractive index of the PhC slab allows a better propagation of light inside the structure. A first conclusion is that when the effective refractive index contrast is reduced, the loss is higher.

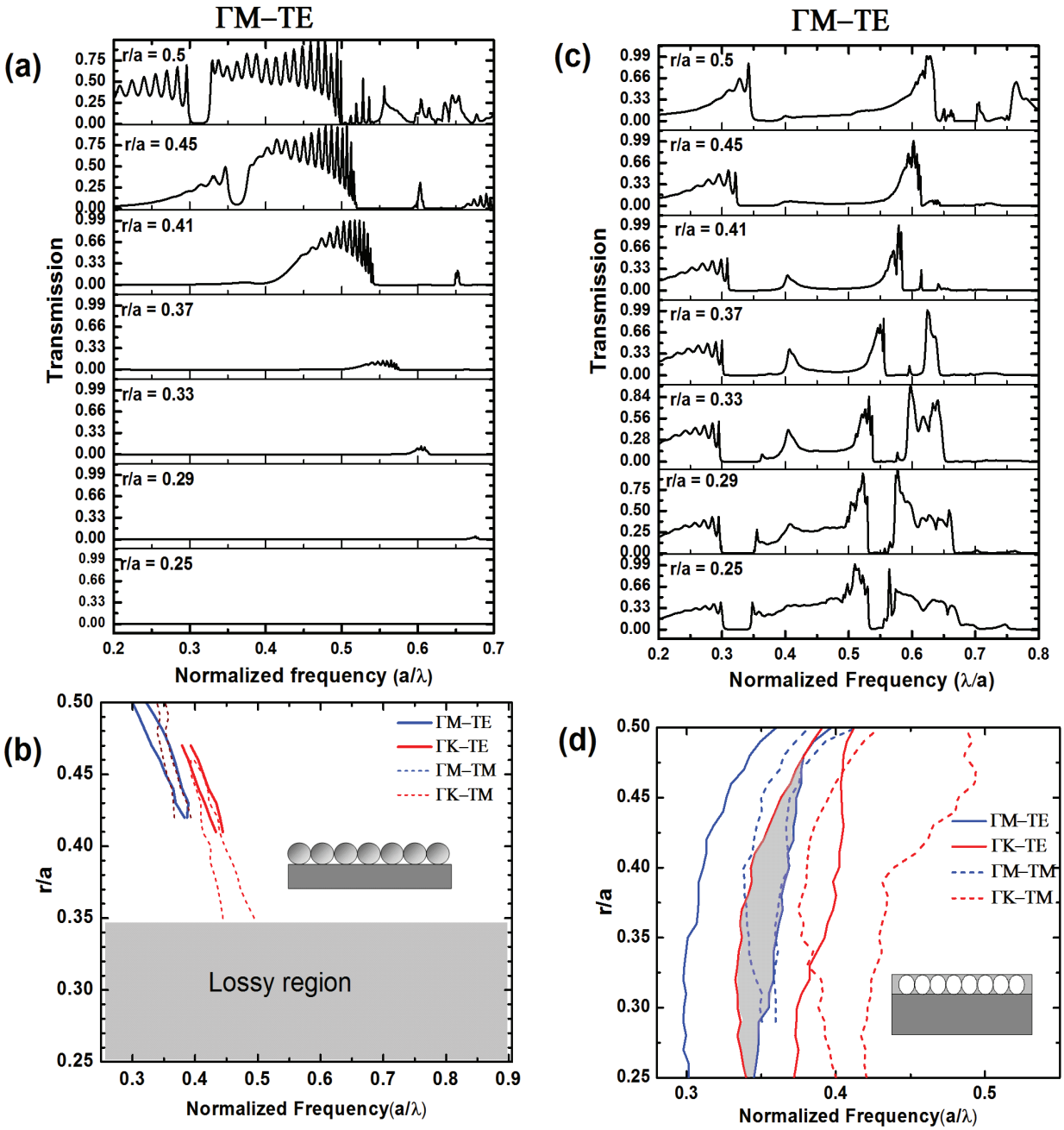

Figure 10: In-plane transmittance and photonic gap maps as a function of the compactness in opals and inverse-opals on glass substrates (a) In-plane transmittance of an opal monolayer on a glass substrate for different values of the compactness (r/a) in the ΓM direction for the TE polarization (b) Photonic gap map of an opal monolayer deposited on a glass substrate for the ΓM and Γk direction and for the TE TM polarization. (c) In-plane transmittance of an inverse-opal monolayer on a glass substrate for different compactness values (r/a) in the ΓM direction for the TE polarization. (d) photonic gap map of inverse opal monolayer on glass substrate for the ΓM and Γk direction and for the TE TM polarization. (The structure of the photonic crystal is assumed to be a 2D triangular lattice of dielectric or air spherical balls. The refractive index is 2.5.)

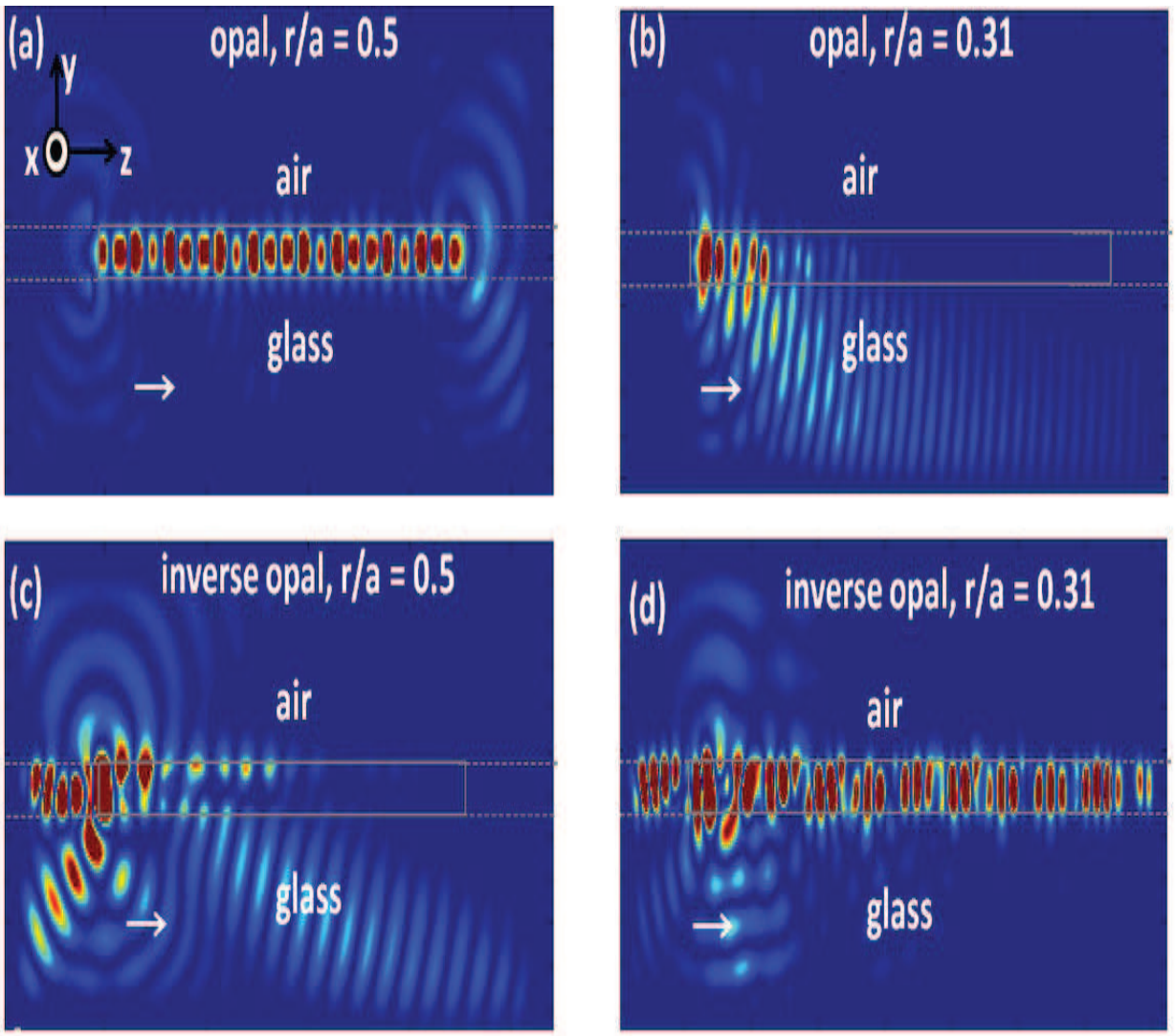

Figure 11: TE electric field propagation for opals and inverse opals on glass substrate for different values of the compactness illustrating the propagation and the losses. The direction of propagation is indicated by arrows. The PhC layer is limited by rectangular lines. (a) Electric field intensity profile in compact configuration of an opal monolayer (r/a = 0.5) (b) Electric field intensity profile in the non-compact configuration of an opal monolayer(r/a =0.31) (c) Electric field intensity profile in the compact configuration of inverse opals monolayer (r/a = 0.5) (d) Electric field intensity profile in the non-compact configuration in inverse opals (r/a = 0.31). (The structure of the photonic crystal is assumed to be a 2D triangular lattice of dielectric or air spherical balls. The refractive index is 2.5.)

1.2.4. Conclusion on the structures

In summary, we systematically study the in-plane photonic properties of monolayer of opals and inverse-opals PhC slabs formed by monolayers of microspheres with or without glass substrate. Both opals and inverse-opal structures suspended in air exhibits PBG at low refractive index contrasts. Changing the compactness can increase the gap-to-mid gap ratio and therefore the existence of the PBG.

In the presence of the glass substrate, the condition on the refractive index contrast for the PBG to exists in each configurations are more strict and the out-of-plane losses are increased.

In the non-compact configuration, the PBG is easier to obtained in the inverse-opals configuration, while in the compact configuration opals have wider PBG.

In terms of polarization, the inverse-opals favor the presence of the TE gaps as there are more overlaps of the TE PBG regions while opals favor that of TM gaps at higher frequencies.

The most relevant structures for the design of photonic crystal microcavity are therefore :

- The compact opals in the TM polarization.
- The non-compact inverse opals in the TE polarization

These results above indicate that substrates with refractive index lower than that of glass might be more favorable to support the opal or the inverse opal structure. This might be done by depositing thin films of low refractive index material like MgF2 or Cytop on the glass substrate.

An alternative is to choose different compactness of the spheres or to use higher refractive index material for dielectric spheres in opal or infiltrated material in inverse opal structures. However, as the refractive index is higher, the PBG is shifted toward lower normalized frequencies as shown in figures 4, 6 and 9. This implies that for a given wavelength, the lattice constant of the structure should be smaller. This might increase the difficulty for the fabrication and characterization of the microcavity.

1.2.5. Microcavities based on monolayer of microspheres

The existence of PBG in monolayer of opals and inverse opals, open the possibility to consider defect microcavities. Consequently we will investigate and compare different microcavity types made from monolayer of inverse opals and opals, with or without glass substrate. More precisely we will calculate and compare their quality factor.

We will consider a fixed value of the refractive index of the dielectric spheres or of the infiltrated material and vary the compactness. Note that we first conducted a study with a refractive index of 2.1 which corresponds to the amorphous phase of TiO_2 [22]. But in this configuration the cavity resonances were weak. For this reason the anastase phase of TiO_2 with a higher refractive index (n = 2.5) is considered and presented here.

The microcavities are studied as a function of the **r/a** ratios so as to optimize the quality factor. We consider H_n and L_n types of microcavities in the inverse-opal structures (shown in figure 12). H1 and H2 type microcavities have one and seven microspheres removed respectively while L3 and L5 microcavities are formed by omitting three and five microspheres along Γ-K direction, respectively.

The quality factor Q is defined as $Q = f/\Delta f$, where f is the normalized resonance frequency and Δf is the full width at half maximum (FWHM) .

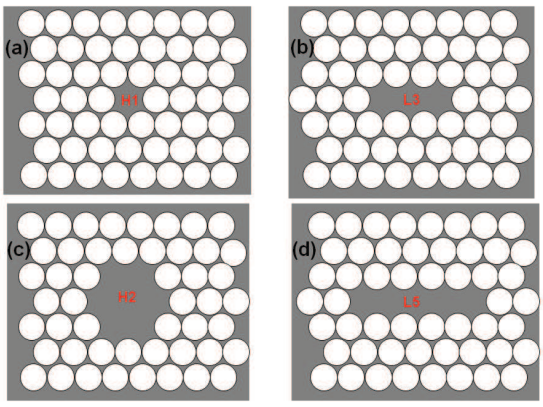

Figure 12: Different cavities studied. (a) H1 (b) L3 (c) H2 (d) L5 microcavities

1.2.5.1. Micro Cavities in Inverse opals

The ***r/a*** ratio is varied from 0.25 to 0.5 for different cavity structures in the inverse-opal configuration. The principle of the simulation is the following :A broad band TE-polarized source emits light in the cavity. The field is monitored within the defect region of the crystal at a position with low symmetry. This is used to compute the spectral response of the cavity. Unlike the energy decay method, which may also be used, the Fast Harmonic Analysis (FHA) method is able to

extract accurate complex frequencies from relatively short propagation. As pointed out in the previous sections, a higher quality factor results from a good compromise between the lateral and the vertical losses.

Figure 13(a) shows both the transmittance in the ΓM direction for an inverse-opal monolayer without substrate with an **r/a** ratio of 0.4 (solid red curve) and the cavity response (black curve), for the H1 microcavity type. The cavity peak is centered at **a/λ** = 0.38, in the middle of the PBG.

The figure 13(b) demonstrates similar results obtained for an H2-microcavity type in the case of an inverse-opal deposited on a glass substrate. It compares the cavity resonance of non-compact (r/a = 0.31) and compact (r/a = 0.5) inverse opals. Obviously a clearer and sharper resonance is obtained in the non-compact case, which confirms the results in section 1.2.3.3. Indeed less light is coupled to the glass substrate in the non-compact inverse opal configuration.

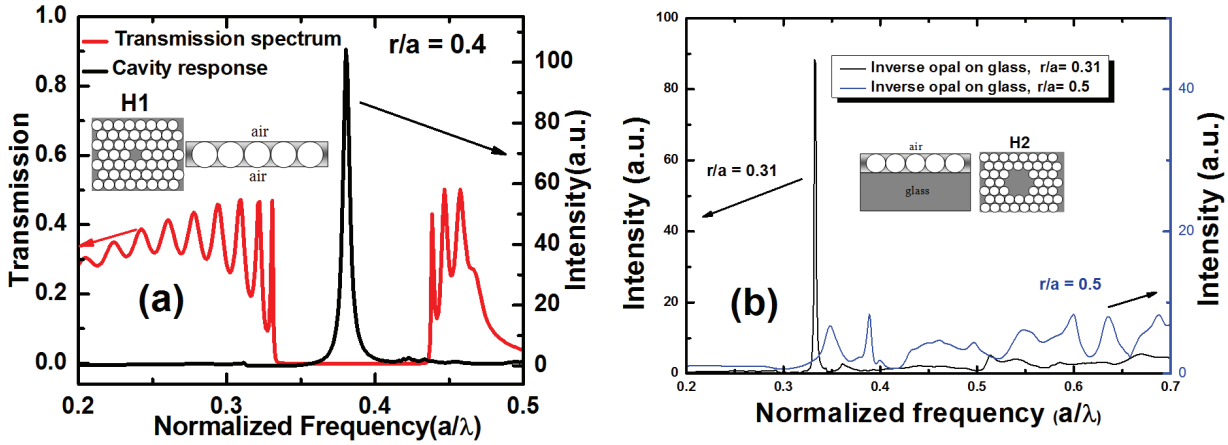

Figure 13: Cavity resonances in defect microcavities made from monolayers of inverse-opal . (a) transmittance and resonance of a H1 microcavity(r/a = 0.4) (b) Cavity resonances in H2 microcavity. for non-compact (r/a = 0.31) (black) and compact (r/a = 05) (blue)

Based on the previous method, the cavity resonances and the quality factors were calculated for the different cavity structures in the inverse opal configuration in order to find out the optimum ***r/a*** ratio providing the highest quality factor.

Finally, the resulting quality factor *Q* calculated as function of r/a ratio for the different cavity structures and in the inverse opals configuration are summarized on the figure 14. On the Figure 14(a) the quality factors is plotted as a function of the r/a ratio for an inverse-opal without substrate. The insets show the different cavity structures. Similarly the figure 14(b) shows similar results with a glass substrate. It is expected from the H1-type of microcavity to exhibit low quality factors as compared to the other cavity types. In the presence of a glass substrate the quality factor appears to

be greatly lowered compared to the structure without glass substrate. This is because a larger amount of light energy is lost from the resonator to the substrate. These results show that non compact inverse opal structures have better quality factors. More precisely, the r/a values around 0.31, 0.32, 0.33 provide better quality factors because of the interplay between a minimization of the out-of-plane scattering and a maximization of the in-plane PBG. A first clear conclusion is that in the inverse-opal configuration, compact spherical arrangement do not provide the best light confinement. As a matter of fact, the compact (r/a=0.5) inverse-opal with air claddings has lower quality factor than non-compact inverse-opal on a glass substrate. Therefore, non-compact inverse-opals appear to be the most promising route to low-threshold photonic microcavity based on micro nanoparticles although this is the most complicated route from the technological point of view. This necessitates more fabrication steps as mentioned in section 1.3.6. of chapter 1.

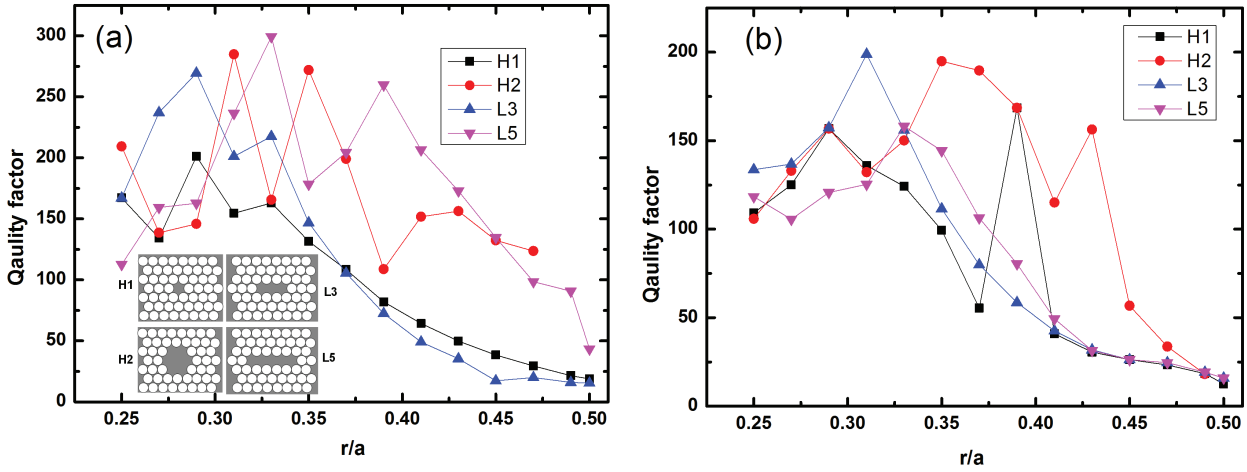

Figure 14: Dependence of the Quality factor on the r/a ratio in the case of H1, H2, L3, L5 microcavities in inverse-opal monolayer configuration (a). Quality factor for the self-sustained structure without substrate (b) Quality factor for the structure deposited on a glass substrate. The inset in (a) show different microcavity structures.

Knowing the resonant wavelength, the construction parameters of a the cavity structures can be calculated.

For instance, the H2 microcavity type presented on the figure 13b, exhibits a cavity resonance at the normalized frequency **a/λ = 0.33.** Using an organic guest-host system such as Alq3-DCM2 with an emission centered at 620 nm, the lattice is calculated to be **a**=204 nm .

1.2.5.2. Micro Cavities in opals

Having considered the inverse-opal configuration we will now focus on the microcavities

structured in a monolayer of opals. We will first study the effect of the refractive index on the resonance a H2 microcavity type. The cavity resonances were observed for refractive index contrast higher than 2.9. The transmitance of opal monolayer without substrate calculated in the ΓM direction and for the TM mode, is shown figure 15 . It appears that the resonant frequency is shifted from the PBG region of the transmittance.

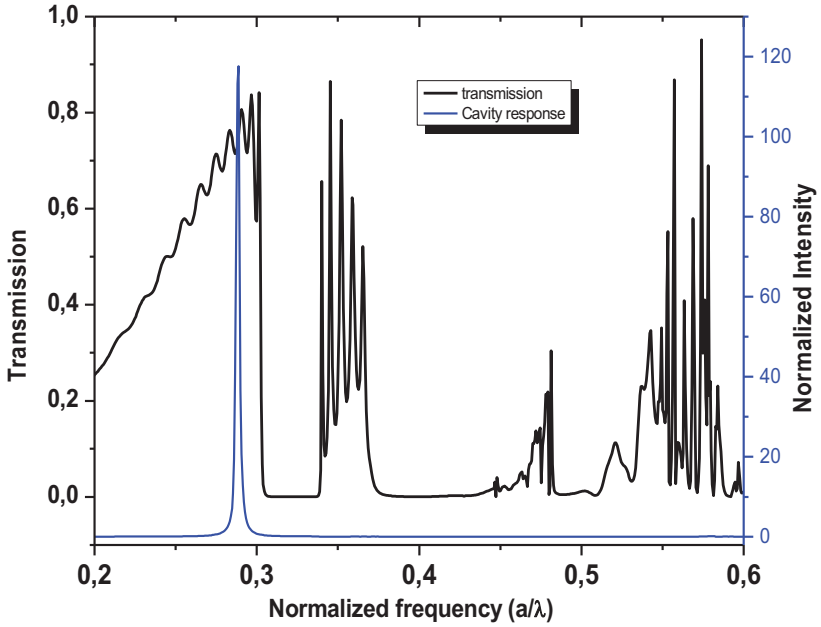

Figure 15: : Transmittance and cavity resonance of H2 microcavity type in a non-compact opal structure without substrate (r/a = 0.4)

The calculations show that up to a refractive index contrast n=3, no resonance is achieved for monolayer of opals deposited on a glass substrate. A resonance is obtained for n ≥4 as shown in figure 16. This is a clear demonstration that the inverse-opal configuration is more promising than the opal configuration in terms of resonance.

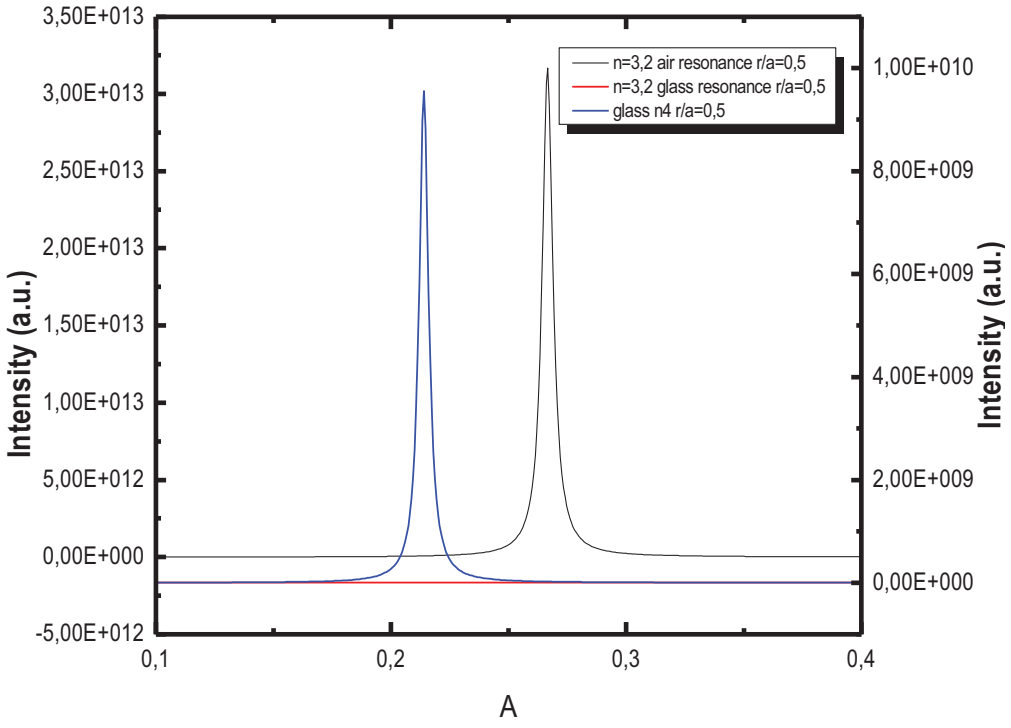

Figure 16: Cavity resonances of an H2 microcaviy type in a compact configuration of opals . When the structure is self sustained (without substrate) the resonance can be obtained for refractive index of spheres of 3.2(black curve). Resonance is not observed for the structure on glass substrate when the dielectric spheres have a refractive index of 3.2(red curve). For a structure on a glass substrate, a higher refractive index (n=4) is required to obtain a resonance (blue curve).

Now let's consider the effect of compactness on the cavity resonances for a refractive index fixed at n=2.9 . The figure 17 shows the different cavity resonances for some r/a values. It appears that the compactness is increased the cavity resonance is stronger.

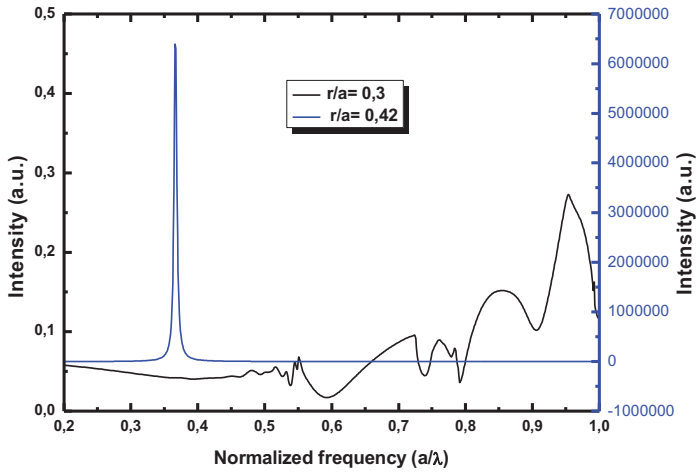

Figure 17: Cavity resonance dependence on compactness of the spheres for monolayer of opals without substrate. The refractive index of the spheres is 2.9. When the compactness of the spheres is reduced to r/a=0.3, the resonances is not observed due to an increase of the evanescent losses. For r/a = 0.42, a clearer resonance is observed.(blue)

Note that similar simulations run in the TE polarization case gave no significant resonance. This can also confirm that, TM band gaps are more favored in opal structure than TE band gaps.

1.3. Towards experimental characterization of optical properties of opals in the optical regime

1.3.1. Context

In order to confirm the validity of the simulation results an experimental demonstration is considered. Such an experiment requires the measurement of the transmittance through a monolayer of an opal or of an inverse opal. Due to the lack of technological support for the realization of inverse-opals at the time these experiments were conducted, we started with samples made with compact ML of opal structures. We aim at demonstrating the feasibility of such an experiment. Figure 18 shows the simulation result of transmittance (**ΓM** direction and **TE** polarization) for an opal monolayer made with anastase phase of TiO2 (n~2.5) nanoparticles deposited on a glass substrate. A clear deep in the transmittance is predicted which we wish to confirm experimentally as a proof of principle.

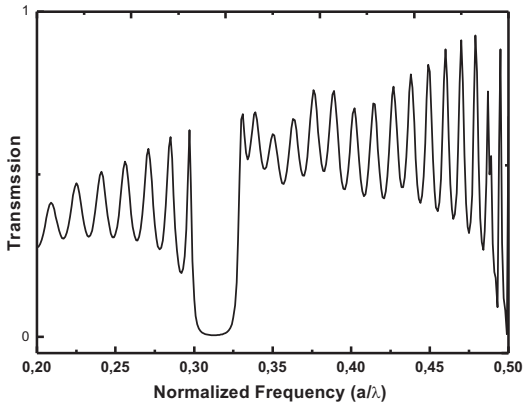

*Figure 18:Transmittance in ΓM direction and **TE** polarization of a monolayer of opal deposited on a glass substrate (n = 2.5).*

1.3.2. Objectives

Although transmittance measurement of an array of of spheres was done in the microwave or terahertz regime using millimeter size dielectric spheres [9, 10, 23] the characterization in the optical regime is difficult because it implies spheres at the scale of few hundred nanometers.

Our objectives imply therefore to characterize monolayers made of a single domain of self-organized nanoparticles. Two types of measurements are considered; first of all, a transmittance obtained from a broad spectrum light source would demonstrate the existence of a forbidden bandgap in a certain direction. Second of all, the transmittance measured for different direction of propagation allow the reconstruction of the band diagram. The latter requires an accurate control of the angle of the incident beam with respect to a well known orientation of the opal lattice. Moreover, light has to be injected into the opal monolayer with the specific crystal direction and collected after the in-plane transmission.

1.3.3. Methodology

Controlling the arrangement of sub-micrometer spheres to fabricate monolayers, sending and collecting light in a specific crystal direction is difficult as the natural self-assembly usually results in multiple crystal domain as shown in figure 19(a) below. Miyazaki et al used microrobots in electron beam microscopy to arrange microspheres mechanically and manually before measuring the transmittance [24]. But considering the equipment used, this technique is still complicated.

To have controlled deposition of the nanoparticles a special technique based on the work of

Arpiainen et al is used [25] . **Arpiainen et al** used microfluidcs channel to deposit microspheres selectively in a micro-hexagon and created multilayer of microspheres on a defined area [figure 19(b)]. The microspheres are 'forced' to self-assemble in the area defined by the hexagonal hole which results in less defects and the reduction of the number of different domains [25].

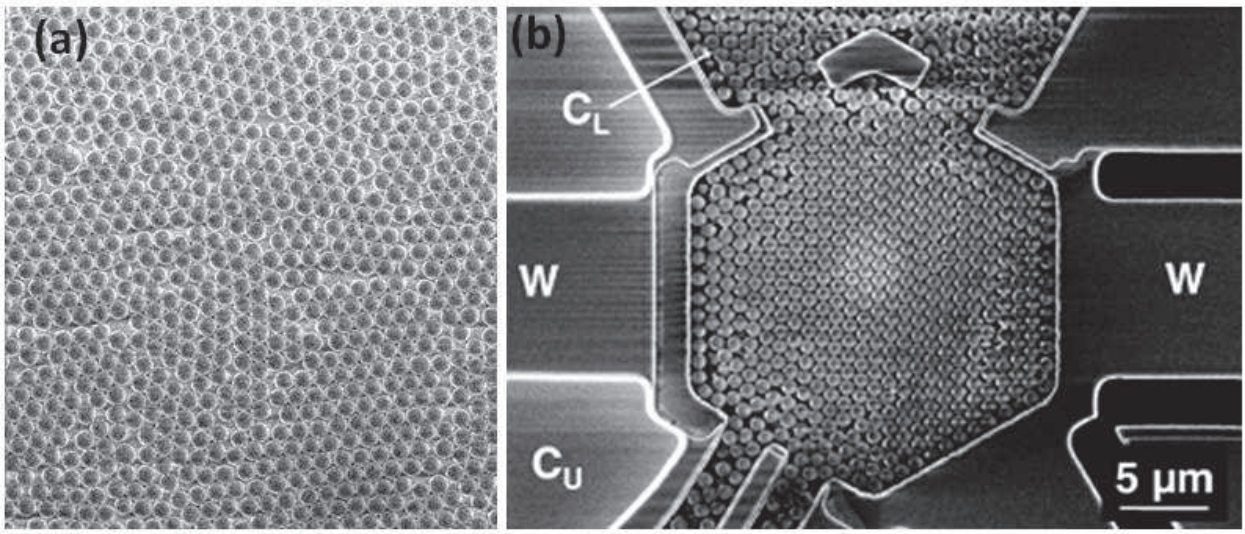

Figure 19: (a) Self assembled single layer of 550nm microspheres with multiple domain (b) Self-assembly of multilayer of microspheres in a micro hexagone with less domains [25]

In our case, we we propose a technique to selectively self-assemble nanoparticles using the drop coating method. The nanoparticles are deposited in a micro-hexagone etched in a waveguide, fabricated in precedent step by photolithography. As the hexagons are too small to be seen and manipulated manually, the experiment should be done under a microscope observation as in figure 20. The sample is placed under microscope and is adjusted until the hexagonal hole is observed. Then a microneedle tip is positioned over the hexagon by translation using a nanopositioner and a micro-droplet is dispensed to the hole by pushing the plunger of a micro-syringe with a solution containing the desired micro-spheres. It is expected that nanoparticles will be accommodated in the hexagonal hole, so that a well defined crystal directions is obtained. The waveguides on either side of the hexagonal hole are used for the input and the output coupling of light .

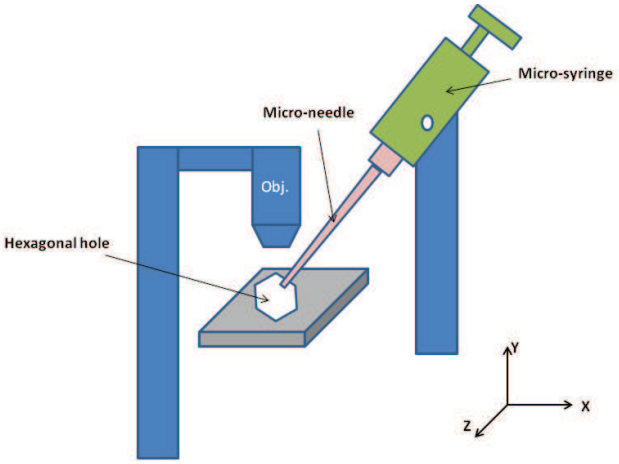

Figure 20: Set-up for self-assembly of nanoparticles under microscope. The sample and the micro needle can be translated in the 3 axes.

The transmittance is obtained by end-fire coupling using input and output waveguides to and from the the monolayer of spheres in the micro-hexagone . The characterization setup is shown in figure 21. A microscope objective attached to a CCD camera enables to observe each waveguide. Using the translation stages, different waveguides with different specific crystal direction or with different hexagon size can be chosen. The input microscope objective injects the incident light from a supercontinuum light source into the input waveguide. It is then guided to the micro-hexagon, transmitted through the opal, guided through the output waveguide and then transmitted to be collected by the output objective and focused to the fiber tip of a spectrometer.

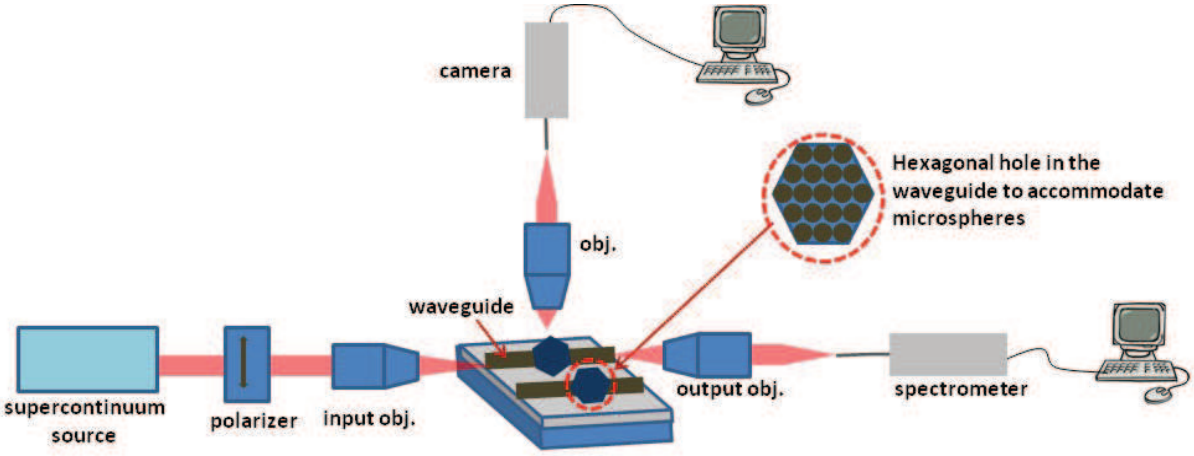

Figure 21: Characterization setup of monolayer of spheres. The spheres are confined in a hexagonal micro-hole as shown in the inset. Different hexagons have different orientation or number of spheres

1.3.4. Experimental procedures and results

In the following sections we will mention the different steps used in the fabrication of monolayer of

dielectric spheres.

1.3.4.1. The Mask design

A Photolithographic mask was designed using Clewin® software for the fabrication of the waveguide. The mask was realized by the femto Institut in Besançon. Figure 22 shows the schematic diagram of one of the mask design CAD layout.

The array of horizontal waveguides was made on glass substrate. Some of the waveguides have hexagonal holes at the center to accommodate 300 nm size TiO2 nanoparticles and the others are reference waveguides without hexagonal holes. A group of waveguides are made with similar hexagonal size, so that the same number of nanoparticles will be accommodated. To measure the transmittance at different crystal direction of the photonic crystal, the hexagons are oriented at different angles with respect to the waveguide direction.

For hexagones with similar orientation, the size of the hexagonal holes were varied so that each hexagonal hole would accommodate different number of nanospheres. The smallest hexagone can accommodate 8 nanoparticles in its side while the largest hexagone accommodates 16 nanoparticles. This would help to understand how the PhC behavior converges as the number of periods increased.

The figure below show simplified schematic diagram of waveguides for measurement of the transmittance. Three waveguides are indicated.

1. Transmission through reference waveguide (without photonic crystal)
2. Transmission through PhC in ΓK direction
3. Transmission through PhC in ΓM direction

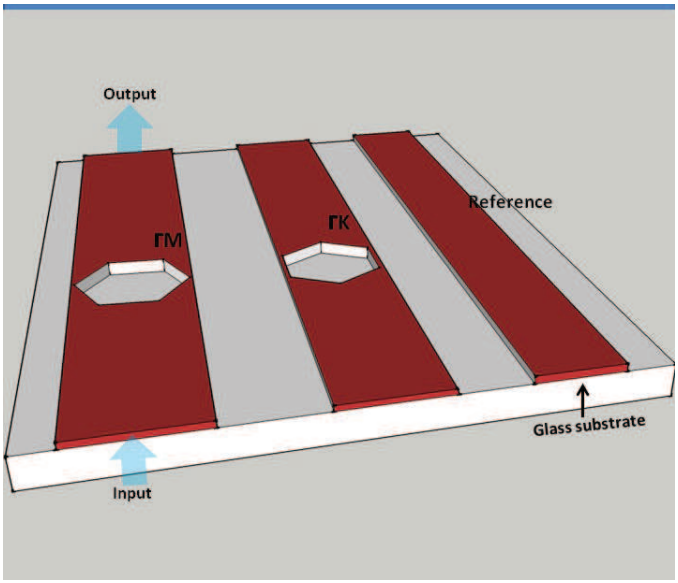

Figure 22: Schematic diagram of glass substrate with reference waveguide, and waveguides with hexagons oriented in the ΓM , ΓK directions.

1.3.4.2. Fabrication of the waveguides

The waveguides were fabricated on a glass substrate and patterned with a photoresist. Prior to use, the glass substrate was cleaned with aceton, ethanol and isopropanol for 5 minutes in each solvent, in ultrasonic bath and dried with nitrogen gas. As the size of the microspheres is 300 nm andthe thickness of the PhC slab is 300 nm,the thickness of the waveguide for light injection and out coupling is defined at 300nm.

The Az-1505 photoresist was spin coated on the glass substrate at a speed of 6000 rpm for 60 seconds. Then the sample was soft baked on a hotplate at 90°C for 1 minute and 30 seconds. Then the sample was aligned with the mask using a mask aligner and exposed to 405nm UV light for 5 seconds. After exposure the photoresist was developed using Mf 319 developer for 10 seconds and rinsed with deionized water. The quality of the fabricated waveguides was observed by confocal microscope.

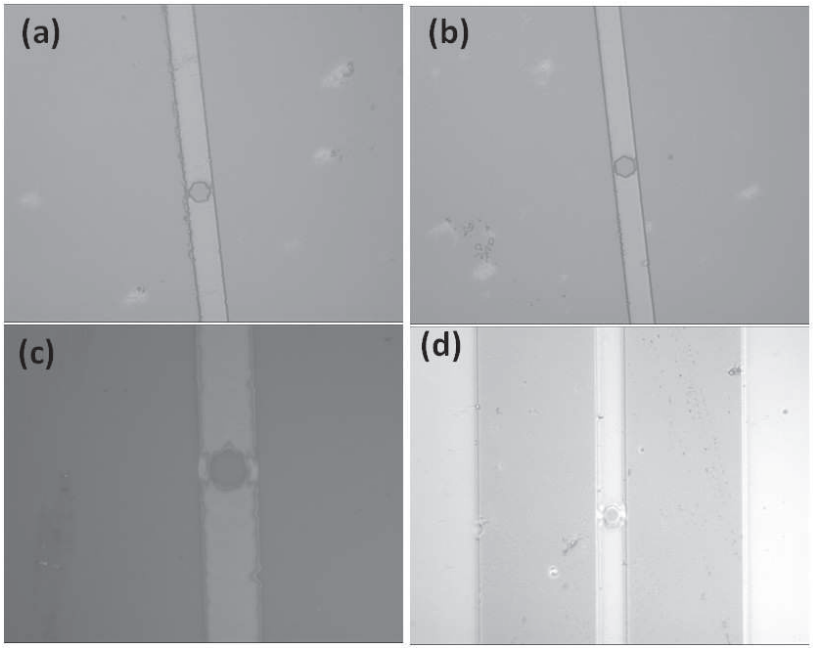

Figure 23: Waveguides made by AZ1505 photoresist on glass substrate . In the waveguides are shown hexagones oriented in different directions with respect to the waveguides.

Figure 107 below shows the optical microscope image of the fabricated waveguides on glass substrate. Hexagonal holes with different orientations with respect to the waveguides are clearly shown.

1.3.4.3. Deposition of nanoparticle:

To deposit the nanoparticles a microneedle/syring with an outer diameter of 160 μm and inner diameter of 50 μm was used. The needle was fixed to a 3-axis translation stage, and the tip of the needle was hold above the hexagonal hole under microscope [figure 24]. When there is good alignment of the tip of the syringe and the hexagonal hole, the nanoparticle solution was dispensed by pushing the plunger of the syringe. To be able to see the nanoparticles well under the microscope, the first attempts were performed with 1.5 μm polystyrene nanoparticles, although the holes were designed to accommodate 300 nm size nanoparticles.

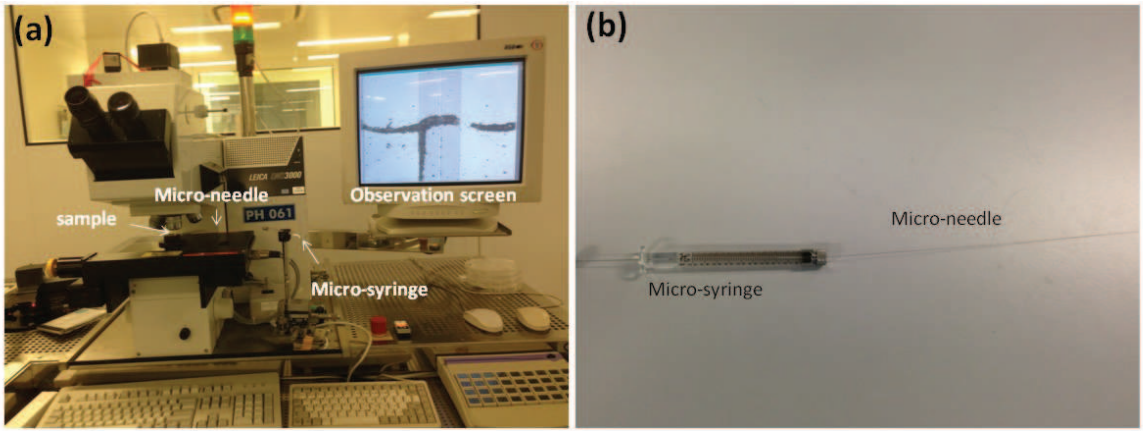

Figure 24: Microsyringe and microneedle system (a) micro needle with Microscyringe on the translation stage. The tip of the needle is positioned on the hexagonal hole. The image of the hole and the needle is observed on a screen. (b) photo of microneedle assembled in the system shown in figure (a)

Figure 25 shows the first attempts to deposit nanoparticles in the hexagonal holes. This show that the nanoparticles are not localized in the hexagonal hole but spread around the waveguide. This is partly due to the microneedle size that is larger than the hexagon holes. But if the experiment is repeated and optimizations are done with 300 nm particles, the results can be improved.

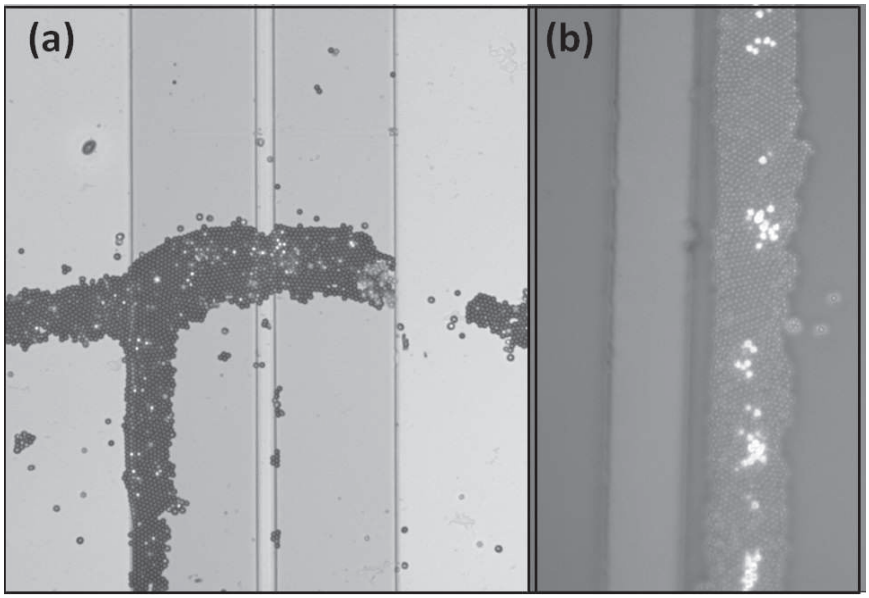

Figure 25: Monolayer of nanoparticles depostied by microneedle drop coating. The nanoaprticles assemble by the side of the wavegiude. The size of nanoparticles is 1.5µm.

Figure 26 shows the results of the deposition of the self-assembled nanoparticles as part of the optimization process for the deposition of regular arranged particles. The first attempt was done by

vertical evaporation of 300nm PMMA nanoparticles. Although different concentration by weight of the PMMA nanoparticles was used, the results predominantly gave multilayer of opals or monolayer of nanoparticle islands, with nanoparticles dispersing and not covering the surface of the substrate. As the monodispersity of the nanoparticles was low, the periodicity of the structure is disturbed [figure 26 (a)] .

Other self assembly process done was by drop coating and resulted in better monolayer regularly arranged microspheres. Figure 26 (b) shows self assembly of 1.5 μm polystyrene spheres deposited on glass substrate by drop coating technique.

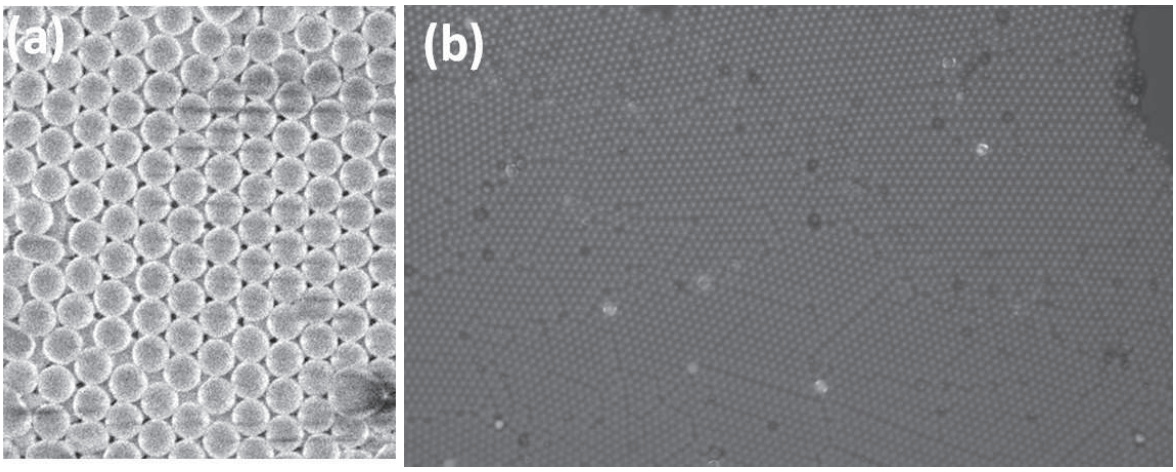

Figure 26: (a) Multilayer of 300nm PMMA nanoparticles made by vertical evaporation (b) Monolayer of 1.5μm microspheres made by drop coating technique

1.4. Perspectives

From the current results, the experiment needs to be improved. We believe the technique to self-assemble the nanoparticle in the hexagonal hole can be greatly improved. For example, a better control of the deposition on the target area can be achieved if the micro needle has a smaller diameter and if a smaller drop volume can be dispensed. Moreover, in order to obtain a better light confinement and in order to avoid the nanoparticles on the flank of the ridge waveguide, a waveguide structure with a top and bottom cladding is preferable. This way, the nanoparticles around the waveguide will be deposited on the level of the bottom cladding layer and their effect on the waveguide core will be minimized. In addition, microfluidic channels may facilitate the deposition of the nanoparticles, as in Arpiainen et al [25] .

1.5. References

[1] O. Painter, J. Vuckovic , and A. Scherer, "Defect modes of a two-dimensional photonic crystal in an optically thin dielectric slab", J. Opt. Soc. Am. B, Vol. 16, 275-285 (1999).

[2] O. Painter, R. K. Lee, A. Scherer, A. Yariv, J. D. O'brien, P. D. Dapkus, I. Kim, "Two-Dimensional Photonic Band-Gap Defect Mode Laser," Science, Vol. 284, 1819-1821(1999).

[3] Huang C K, Chan C H, Chen C Y, Tsai Y L, Chen C C, Han J L and Hsieh K H , "Rapid fabrication of 2D and 3D photonic crystals and their inversed structures," Nanotechnology, Vol. 18, 265305-12(2007).

[4] P. Kumnorkaew, Y. K. Ee, N. Tansu, and J. F. Gilchrist, "Investigation of the deposition of microsphere monolayers for fabrication of microlens arrays," Langmuir, Vol. 24, 12150–12157 (2008).

[5] Yik-Khoon Ee, Pisist Kumnorkaew, Ronald A. Arif, Hua Tong, James F. Gilchrist, and Nelson Tansu, "Light extraction efficiency enhancement of InGaN quantum wells light-emitting diodes with polydimethylsiloxane concave microstructures," Optics Express, Vol. 17, 13747-13757 (2009).

[6] C. H. Chan, C. H. Hou, S. Z. Tseng, T. J. Chen, H. T. Chien, F. L. Hsiao, C. C. Lee, Y. L. Tsai, and C. C. Chen, Improved output power of GaN-based light-emitting diodes grown on a nanopatterned sapphire substrate," Appl. Phys. Lett., Vol. 95, 011110-1-011110-3 (2009).

[7] C. Farcău, E.Vinţeler, S. Aştilean, "Experimental And Theoretical Investigation Of Optical Properties Of Colloidal Photonic Crystal Films," Journal of Optoelectronics And Advanced Materials, Vol. 10, 3165 - 3168(2008).

[8] K. Ohtaka, Y. Suda, S. Nagano, and T. Ueta, A. Imada and T. Koda, J. S. Bae and K. Mizuno, S. Yano and Y. Segawa "Photonic band effects in a two-dimensional array of dielectric spheres in the millimeter-wave region," Physical Review B, Vol. 61, 5267-5279(2000).

[9] A. Andueza, P. Morales, and J. Sevilla , "Photonic band effect in single-layers of high refractive index spheres of different compactness," J. Appl. Phys., Vol. 111, 104902 (2012).

[10] Kondo, T., S. Yamaguti, M. Hangyo, K. Yamamoto, Y. Segawa, and K. Ohtaka, "Refractive index dependence of the transmission properties for a photonic crystal array of dielectric spheres," *Phys. Rev. B*, Vol. 70, No. 23, 1-6(2004).

[11] Y. Kurokawa, H. Miyazaki, and Y. Jimba , "Light scattering from a monolayer of periodically arrayed dielectric spheres on dielectric substrates, " Phys. Rev. B, Vol. 65, 201102-1- 201102-4(2002).

[12] Y. Kurokawa, H. Miyazaki, and Y. Jimba , "Optical band structure and near-field intensity of a periodically arrayed monolayer of dielectric spheres on dielectric substrate of finite thickness", Phys. Rev. B, Vol. 69, 155117-1 - 155117-8(2004).

[13] Yanling Cao, Yanping Wang, Yongzheng Zhu, Hongbo Chen, Zhihui Li, Juan Ding, Yuanbin Chi "Fabrication of anatase titania inverse opal films using polystyrene templates," Superlattices and Microstructures, Vol. 40, 155–160(2006).

[14] Berenger,"A perfectly matched layer for the absorption of electromagnetic waves," J. of Comuptational Phys., Vol. 114, 185-200(1994).

[15] Shanhui Fan, J. D. Joannopoulos, "Analysis Of Guided Resonances In Photonic Crystal Slabs," Physical Review B, Vol.65, 235112-1 - 235112-8(2002).

[16] Yousef Nazirizadeh, Uli Lemmer, and Martina Gerken, ,"Experimental quality factor determination of guided-mode resonances in photonic crystal slabs," Appl. Phys. Lett., Vol. 93, 261110-1-261110-3(2008).

[17] Beatriz H. Juárez, Pedro David García, Dolores Golmayo, Alvaro Blanco, and Cefe López,"ZnO Inverse Opals by Chemical Vapor Deposition," Adv. Mater., Vol. 17, 2761–2765(2005).

[18] E. Yablonovitch, "Inhibited Spontaneous Emission in Solid-State Physics and Electronics," Phys. Rev. Lett., Vol. 58, 2059-2062(1987).

[19] K. Busch, and S. John, "Photonic band gap formation in certain self-organizing systems," Phys. Rev. E, 58, 3896 -3908(1998).

[20] J D. Joannopoulos, Steven G Jhonson, Joshua N. Winn, Robert D Mead, "Photonic crsytals : Molding the flow of light," Princeton University Press, (2008).

[21] M. Kafesaki, M. Agio, C. M. Soukoulis , "Waveguides in finite-height two-dimensional photonic crystals," J. Opt. Soc. Am. B, Vol. 19, 2232-2240(2002).

[22] Yu Li, François Piret, Timothée Léonard, Bao-Lian Su, “Rutile TiO2 inverse opal with photonic bandgap in the UV–visible range,” Journal of Colloid and Interface Science, Vol. 348, 43–48(2010).

[23] A. Andueza, R. Echeverría, P. Morales, And J. Sevilla , “Geometry Influence On The Of Dielectric Single Layers Of Spheres With Different Compactness ,”Journal Of Applied Physics 107, 124902-1-124902-7(2010).

[24] Hideki T. Miyazaki, Hiroshi Miyazaki, Kazuo Ohtaka and Tomomasa Sato, “Photonic band in two-dimensional lattices of micrometer-sized spheres mechanically arranged under a scanning electron microscope,” J. Appl. Phys., Vol. 87, 7152 (2000).

[25] Sanna Arpiainen, Fredrik Jonsson, James R. Dekker, Gudrun Kocher, Worawut Khunsin, Clivia M. Sotomayor Torres, and Jouni Ahopelto, “Site-Selective Self-Assembly of Colloidal Photonic Crystals”, Adv. Funct. Mater., Vol. 19, 1247–1253(2009).

Chapter 3:
Nanoparticle based two dimensional patterning of organic light emitting diodes (OLEDs)

1. Introduction

In the previous chapter we have investigated numerically the optical properties of nanoparticles. It has been shown that the fabrication of nanoparticles based photonic crystal microcavity (inverse opal microcavity) require both a high index contrast and a filling fraction different from ½. Due to technological limitations it was not possible to satisfy both conditions and therefore the inverse opal approach for organic laser cannot be studied experimentally in our laboratory, for the moment. In the current chapter, we will instead focus on the other type of organic laser cavity that can be realized and studied with nanoparticles. Indeed, single layer of nanoparticles can be used to realize two dimensional patterns. These lattice can be used both for 2D distributed feedback(DFB) laser cavity as well as for light extraction. This chapter is therefore dedicated to the theoretical study and to the experimental realization of two dimensional patterning of organic light emitting diodes.

The scientific approach chosen to address this subject consists in two steps. Firstly, the organic semiconductors and their utilization to build up organic hetero-structures and organic light emitting diodes (OLEDs) have to be presented so as to identify a patterning process compatible with the OLED fabrication. Secondly, a process based on self-organized nanoparticles is presented and studied numerically before experiments are conducted to demonstrate the feasibility of patterning large area OLEDs. The patterned OLEDs are then characterized optically and electrically.

2. Organic electroluminescent devices

This section addresses the organic semiconductors and the organic light emitting diodes. It is concerned about the possibility of using self-organized nanoparticles to pattern organic semiconducting materials, and OLEDs.

In order to establish a process compatible to the patterning of organic light emitting diodes, the electrical and optical properties of the organic semiconductors and the principle and the structure of the OLED have to be revisited. Indeed the OLED patterning requires the electric functioning of the OLED to remains unperturbed. Therefore a careful attention should be turned on the conductivity or the organic materials and on the principle of the organic heterostructure. In a similar manner, the patterning of the OLED aims at modifying its optical properties. To achieve these results, a prerequisite is to consider the optical properties of the organic materials and of the OLEDs.

Consequently, the chapter is divided into the following parts: First of all we will recall the properties of the organic materials. In order to present the electrical properties we will first presents the conductive polymers (long molecules) before considering the small molecules. We will then present the photoluminescent and electroluminescent organic materials. Finally the OLED hetrostructure and working principle will be presented.

2.1. Organic electroluminescent materials

2.1.1. Electrical properties of organic semiconductors

Organic semiconducting materials, discovered some decades ago [1], have been a promising alternative to inorganic semiconductors and have evolved to be major active materials in a new generation of optoelectronic devices as Organic Light Emitting Diodes (OLEDs), Organic Photovoltaics (OPVs), Organic Thin film transistors (OTFTs) and Organic semiconductor lasers (OSLs) [2] . The easy processing, lower cost, flexibility properties and the scope for tuning their chemical structures to give desired features make organic semiconductors superior to conventional inorganic semiconductors.

Due to their electrical properties and with room temperature conductivity of $\sigma<10^{-14}$ $\Omega^{-1}cm^{-1}$ organic compounds belong to insulators [2, 3]. But the electronic conductivity of certain

organic materials, like π-conjugated oligomers and polymers, lies between that of metals and insulators, spanning a broad range of 10^{-9} to 10^{3} Ω^{-1} cm^{-1}. Doped π-conjugated polymers have properties of metals or semi-conductors, with the advantageous processing and mechanical characteristics of polymers with low cost, versatility of chemical synthesis, ease of processing, and flexibility [2, 4, 5].

Organic semiconductors can be broadly classified into two categories: *small molecules* - (usually processed in vacuum) and *macromolecular polymers* (usually processed by wet chemical techniques). Figure 1 shows some examples of small molecule and polymeric organic semi-conductors.

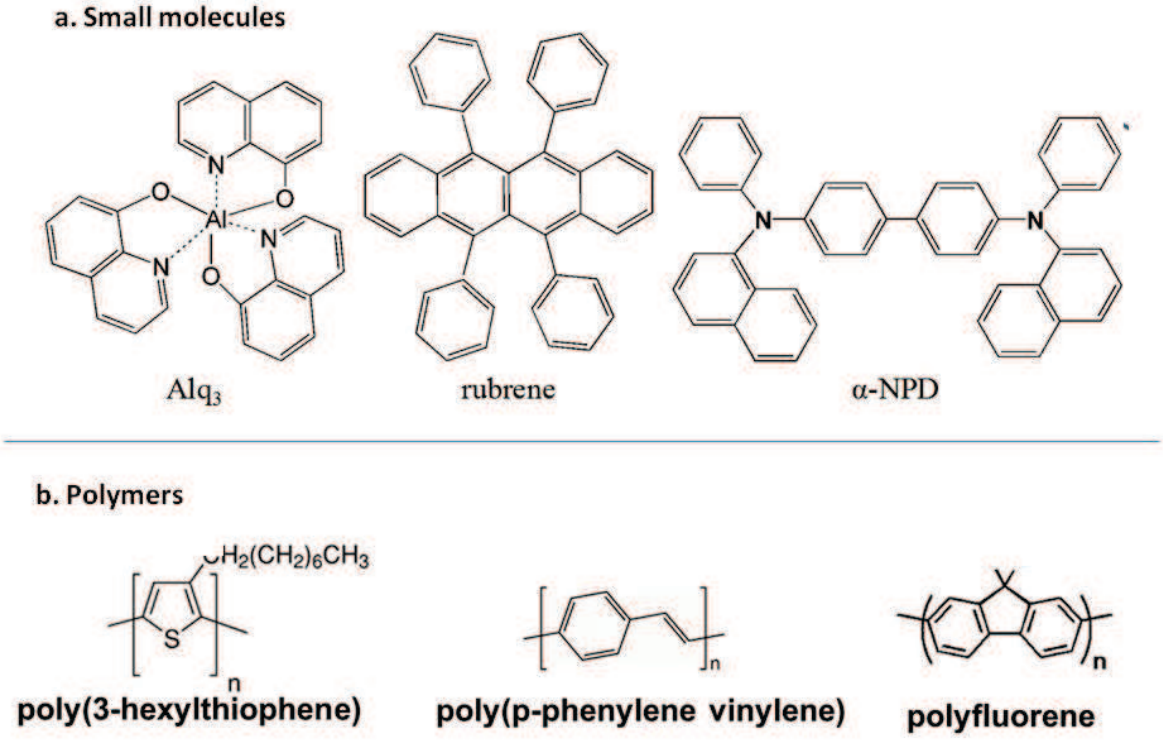

Figure 1 Organic conjugated semiconductors (a) small molecules (b) polymers

2.1.1.1. Principle of conduction in organic semiconductors

The conductivity in conducting polymers originates from the electronic configuration in the chemical structure. It relies on two key properties :

- The type of chemical bonds between the atoms

- The doping of the molecule.

2.1.1.1.1. Sigma bonding and pi bonding

Sigma bonds (σ-bonds) are the strongest type of chemical bonding related to the S atomic orbitals. When two S atomic orbitals overlap they form a covalent bond called sigma bond. Sigma bonds are the strongest type of covalent bonds due to the direct overlap of orbitals

Pi bond(π-bond) is a covalent chemical bond related to the P atomic orbitals. When two P atomic orbital overlap the resulting orbital extend sideways. As such the electrons are delocalized on the extended orbital. These type of bonds are shown in left side of figure 2 for ethane molecule.

The right part of figure 2 shows the *the energy levels of the ethane molecule.* Whenever the two atomic orbitals overlap, two molecular orbitals (MOs) form. One of the molecular orbitals (bonding) lies lower in energy from the two atomic orbitals from which it was made; the other (anti-bonding) molecular orbital lies higher in energy as shown in the energy-level diagram (also called a molecular orbital diagram) a molecular orbital diagram [6].

The highest occupied molecular orbital (HOMO) is the MO of highest energy that has electrons in it. The lowest unoccupied molecular orbital (LUMO) is the MO of lowest energy that does not have electrons in it. The energy difference between the HOMO and the LUMO — known as the HOMO–LUMO **gap**—is related to the minimum energy needed to excite an electron in the molecule.

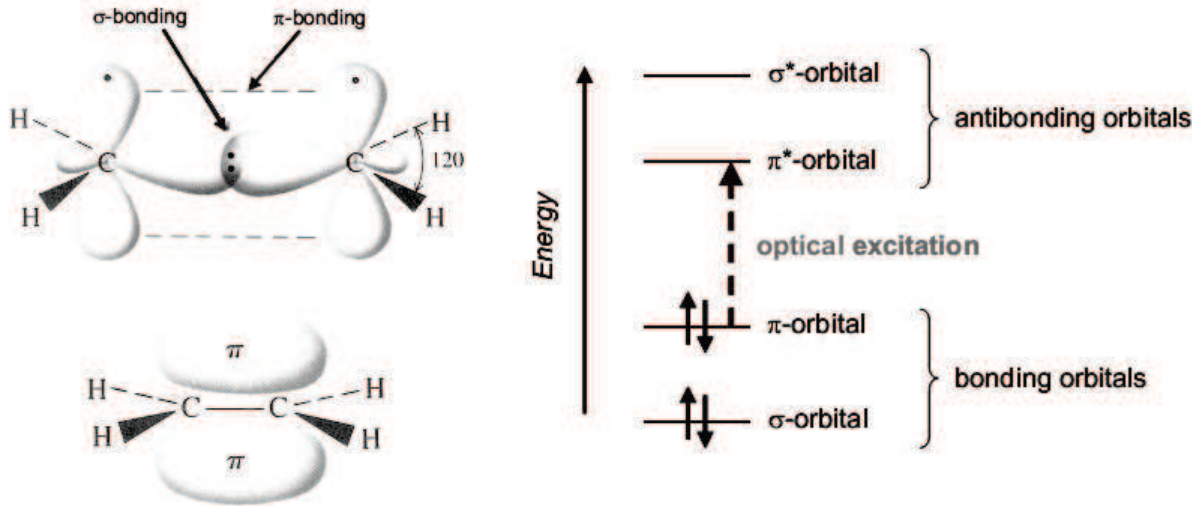

Figure 2: σ and π bonds in ethane, as an example for the simplest conjugated π electron system. The right graph shows the energy levels of a π-conjugated molecule. The lowest electronic excitation is between the bonding π orbital and the antibonding π orbital.*

2.1.1.1.2. pi conjugated polymers

A key property of a conductive polymer is the presence of conjugated double bonds along the backbone of the polymer[7]. Conjugation is the overlap of one p-orbital with another across an intervening σ-bond. In conjugation, the bonds between the carbon atoms are alternately single and double. A conjugated system has a region of overlapping p-orbitals, bridging the interjacent single bonds. They allow a delocalization of π-electrons across all the adjacent aligned p-orbitals. The pi electrons do not belong to a single bond or atom, but rather to a group of atoms.

Poly-acetylene is the simplest conjugated polymer (CH)x. In poly-acetylene, the three in-plane sigma-orbitals of the **sp^2** hybridized carbon create the "backbone"; two of them bonded to the neighboring carbons and the third sigma-orbital bonded to a hydrogen atom. The fourth electron resides in the **p_z** orbital and, because of its orthogonality to the plane defined by the other three sigma-bonds, it is independent of them. This one-electron picture of the **p_z** electron being decoupled from the backbone sigma-orbitals gives these polymers special electronic properties.

Figure 3: Polyacetelyen : conjugated polymer

2.1.1.1.3. The doping of the molecule

Doping , which is charge injection onto conjugated, semiconducting macromolecular chains, can lead to high conductivity. The role of the dopant is either to remove or to add electrons to the polymer and it was discovered that polyacetylene, which has an intrinsic conductivity much lower than $10^{-5}\ \Omega^{-1}\ cm^{-1}$, could be made highly conducting, ~ $10^{3}\ (Q.cm)^{-1}$, by exposing it to oxidizing or reducing agent. During the doping process, an organic polymer, either an insulator or semiconductor having a small conductivity is converted into a polymer which is in the metallic conducting regime. The insulating neutral polymer is converted into an ionic complex consisting of a polymeric cation (or anion) and a counterion which is the reduced form of the oxidizing agent (or the oxidized form of the reducing agent) [1,7,8].

For example,the doping agent iodine (I_2) will remove an electron under the formation of an I_3^- ion and if the electron is removed from the top of the valence band of a semiconductive polymer, like polyacetylene, the vacancy (hole) is created. If we imagine that an electron be removed locally from one carbon atom, a radical cation (called polaron) would be obtained. This radical cation is localized, partly because of Coulomb attraction to its counter ion (I_3^-), which has normally a very low mobility. The mobility of a polaron along the polyacetylene chain can be high and charge can be carried along as shown in figure 4(c)- (d) by having a high concentration of counter ions so that the polaron can move in the field of close counter ions., thus explaining why doping is necessary.

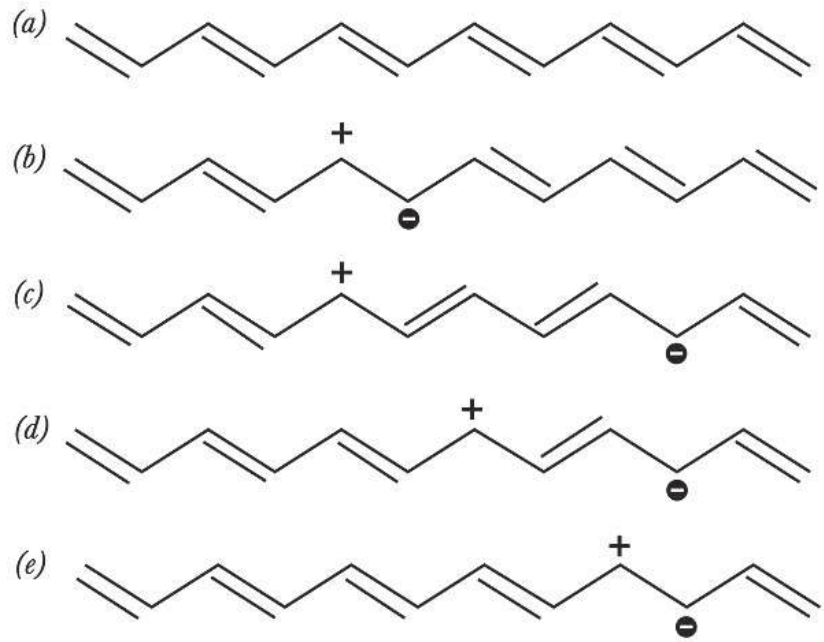

Figure 4: Radical cation ("polaron") formed by removal of one electron on the 5th carbon atom of a undecahexaene chain (a →b). The polaron migration shown in c →e.

2.1.1.2. Electronic states

For any particular molecule, several different electronic states exist depending on the total electron energy and the symmetry of various electron spin states (see figure 5 below). The ground state for most organic molecules is an electronic singlet in which all electrons are spin-paired with opposite spins and the net spin is zero. When an electron in a molecule with a singlet ground state is excited (via absorption of energy) to a higher energy level, either an excited singlet state or an excited triplet state will form. In a triplet state the excited electron

is no longer paired with the ground state electron; that is, they are parallel with the same spin and the net spin is 1.

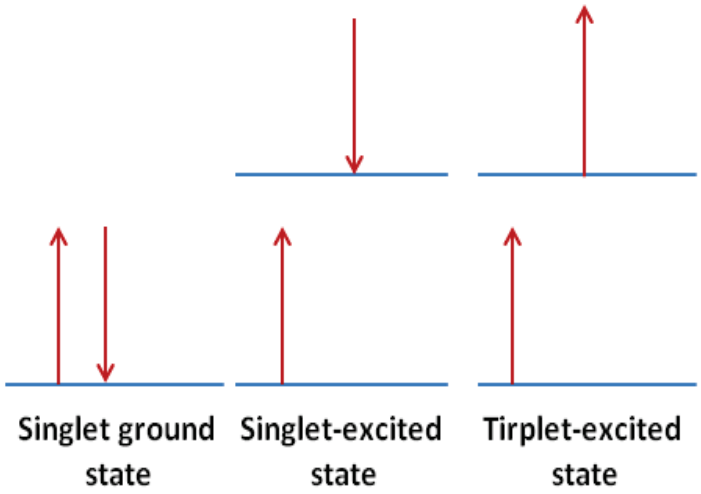

Figure 5: Singlet and triplet electronic states

2.1.2. Optical properties of organic semiconductors

Apart from conducting electricity, some organic semiconducting materials show electroluminescence- the generation of light, by electrical excitation- and photoluminscence- the generation of light, by optical excitation. Organic electroluminescence dates back to 1963 when Pope et. al. reported electroluminescence in single crystal anthracene[9, 10]. But a major breakkthrough in organics electronics was in 1987, when Tang et al demonstrated the first efficient electroluminescence in two-layer sublimed small molecular film device, i.e, the first OLED device from double-layer structure of organic thin films[11]. Friend et al. later demonstrated electroluminescence in a conjugated polymer thereby opening the way for the fabrication of polymer light-emitting diodes (PLEDs) [12, 13, 14, 15].

2.1.2.1. The Jablonski diagram

The ground and different excited electronic states of a molecule and the processes related along with absorption and emission (radiative and non-radiative) of energy are usually represented by the Jablonski diagram as shown in figure 6 below. The Jablonski diagram

describes most of the relaxation mechanisms for excited state molecules illustrating the electronic states of a molecule and the transitions between them. The electronic states are arranged vertically by energy. They are grouped horizontally by spin multiplicity. In the left part of the diagram three singlet states with anti-parallel spins are shown: the singlet ground state (**S0**) and two higher singlet excited states (**S1** and **S2**). The triplet state (**T1**) is the electronic state with parallel spins and is represented in the right part of the diagram. In each group of electronic level the numbered horizontal lines represented vibrational levels of each electronic state, numbers indicating the energy level of each vibrational state. Transitions between electronic states is indicated by arrows. The favored deactivation process is the route that is most rapid and spends less time in the excited state [16, 17, 18 , 19].

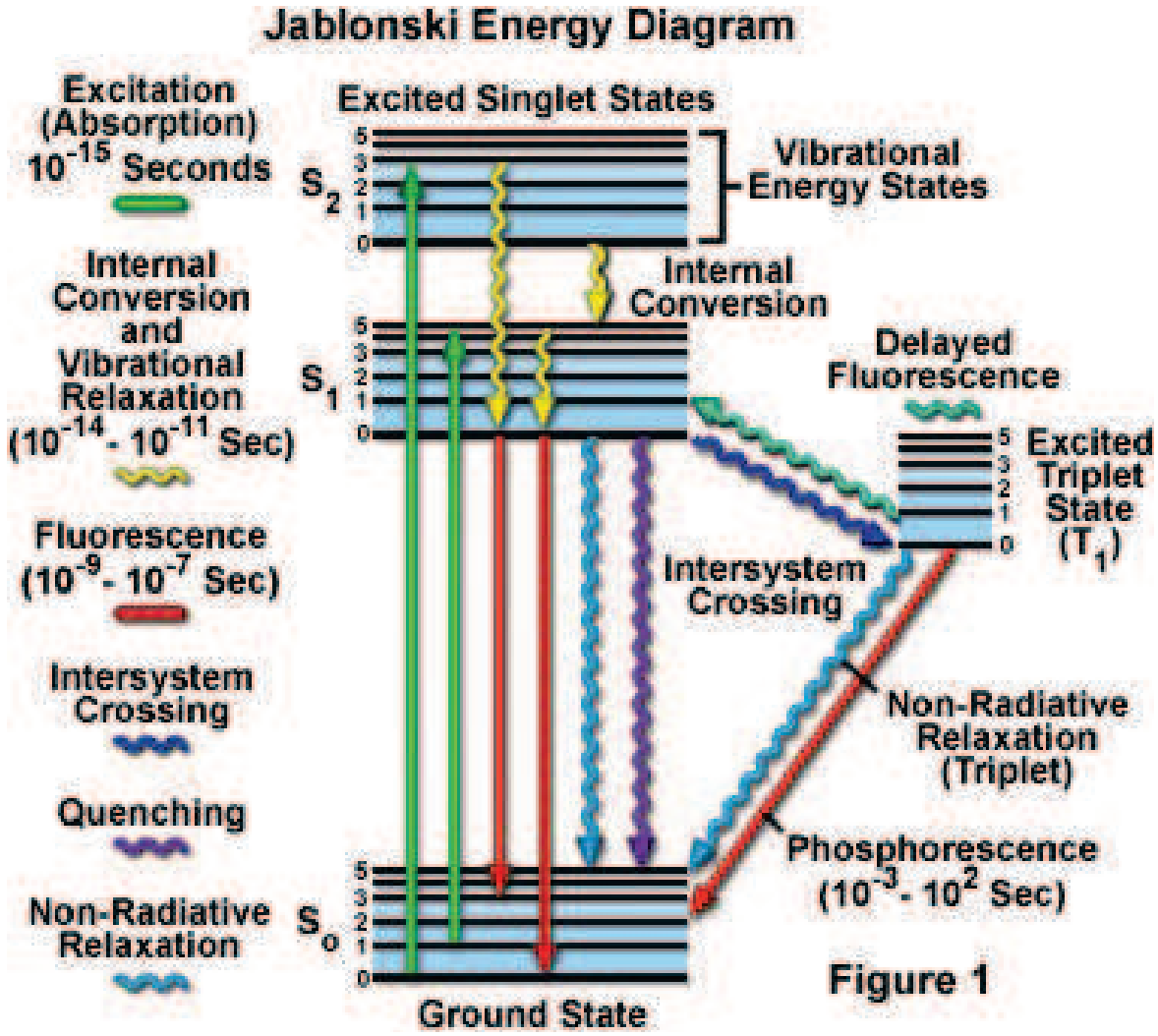

Figure 6: Jablonski energy diagram illustrating the transitions between electronic states of a molecule for the quantum mechanical processes of fluorescence and phosphorescence. Waved lines mark non-radiative transitions. IC - internal conversion, ISC- intersystem crossing [19]

2.1.2.1.1. Absorption

To understand the diagram, let's start with a molecule in the ground state, **S0**. When a molecule absorbs a photon of appropriate energy, a valence electron is promoted from the ground state to some vibrational level of unstable electronic singlet state (**S2**) (Figure 6). rapid, in the order of one femtosecond (1fs = 10-^{15}s). This excited state is rather unstable and thus has a very short lifetime. After light absorption the excited molecule ends up at the lowest vibrational level of **S1** (S1,0) via vibrational relaxation and internal conversion (**IC**) from **S2** to **S1**. This radiationless process takes place in about one picosecond (1ps = 10^{-12}s).

2.1.2.1.2. Emission

Once a molecule arrives at the lowest vibrational level of an exited singlet state S1,0, it can do a number of things, one of which is to return to the ground state by photon emission which is called **fluorescence**. The lifetime of an excited singlet state is approximately 10^{-9} to 10^{-7} sec and therefore the decay time of fluorescence is of the same order of magnitude.

2.1.2.1.3. Non radiative recombination

Several other relaxation pathways that have varying degrees of probability compete with the fluorescence emission process. The excited state energy can be dissipated non-radiatively as heat (illustrated by the cyan wavy arrow in Figure 6) or the excited fluorophore can collide with another molecule to transfer energy in a second type of non-radiative process like quenching (indicated by the indigo wavy arrow).

2.1.2.1.4. The intersystem crossing

Another phenomenon is the **intersystem crossing** (**ISC**) to the lowest excited triplet (**T1**) state which is mainly responsible for populating the triplet states from the lowest excited singlet state.

ISC ultimately results either in emission of a photon through **phosphorescence** or non radiative decay to the ground singlet state, or a transition back to the excited singlet state that yields delayed fluorescence. Fluorescence and/or phosphorescence can be also referred as **photoluminescence (PL)** when these transitions are initiated by absorption of a photon. Transitions from the triplet excited state to the singlet ground state are forbidden, which results in rate constants for triplet emission that are several orders of magnitude lower than those for fluorescence.

2.1.2.2. The Stoke shift

Even though a quantum of radiation is emitted in fluorescence this quantum will be lower in energy on the average than the quantum absorbed by the molecule, due to vibrational relaxation and internal conversion. The change in photon energy causes a shift of the fluorescence spectrum to a longer wavelength, relative to the absorption spectrum; this is referred to as the Stokes' Shift as shown in figure 7 .When the Stokes shift is increased, self-absorption by the molecule is reduced, i .e , a molecule will not absorb the light that it has emitted [[20].

$$\Delta\lambda = \lambda em - \lambda abs > 0$$

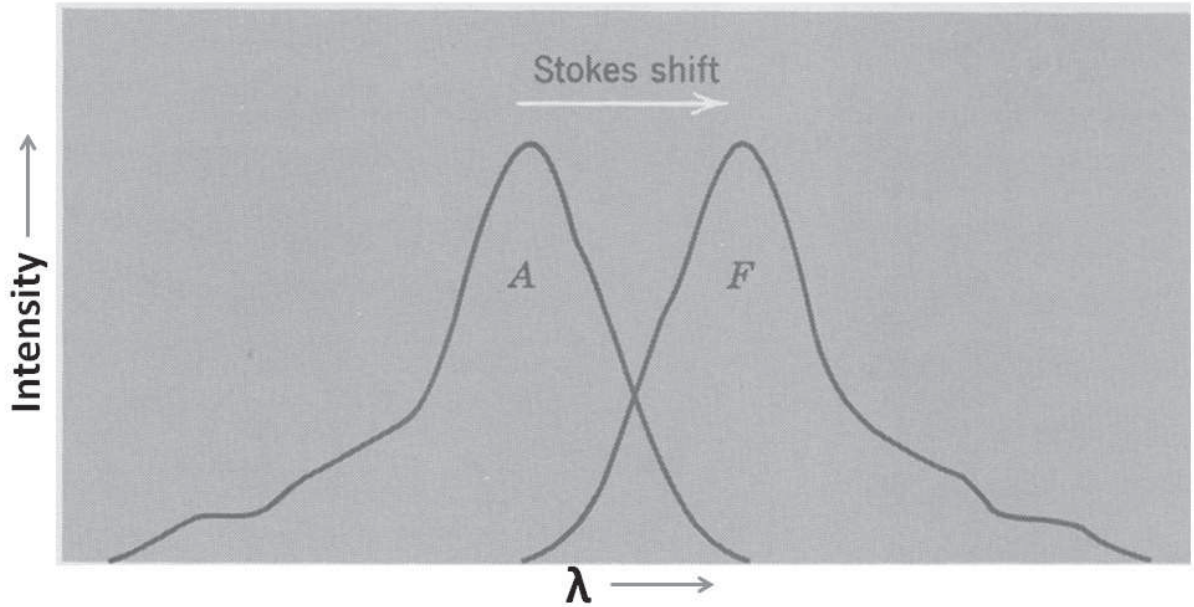

Figure 7: The Stokes' shift: displacement of the flourence band (F) with respect to the absorption band (A) of a molecule [20].

2.2. The organic heterostructure

A multilayer OLED with superior efficiency is usually made of different functional organic layers and a general architecture is shown in the figure 8 below. A positively biased anode is required in order to inject holes into the hole transport layer (HTL). Similarly, electrons are injected from the cathode into the electron transport layer (ETL). The injection of holes and electrons is facilitated by the hole injection layer (HIL) and the electron injection layer (EIL), respectively. The top electrode is usually a metallic mirror with high reflectivity and the bottom electrode is usually transparent conducting oxides (TCO) like transparent indium-tin-oxide (ITO) on a transparent substrate, like glass or plastic . The emission layer (EML) comprises one or more dyes emitting light in different regions of the visible spectrum. Additionally, these devices use air-sensitive metals or organic materials, which require rigorous encapsulation to prevent degradation [21].

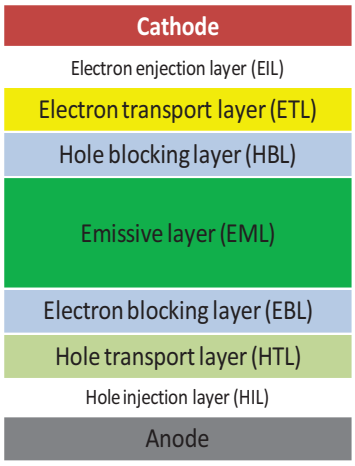

Figure 8 The OLED architecture

2.2.1. Working principles of OLED and energy level diagram

The basic processes in an OLED under operation are illustrated in figure 9 for a device with three organic layers. When a driving voltage V is applied, electrons are injected into the LUMO level of the organic layer from the cathode and holes are injected into the HOMO level of the organic layer from the anode. The electrons and holes move in the organic layers under the electric field before combining to form the exciton, which is the excited state electron-hole pair. Excitons will migrate with an average diffusion length of about 20 nm and are relaxed to the ground state emitting light [11 , 22, 23].

The whole process can be broken down into four fundamental steps:

(1) Injection of electrons and holes at the electrodes

(2) Transport of charge carriers through the organic layer

(3) Formation of bound electron–hole pairs (excitons)

(4) Migration of exciton and decay

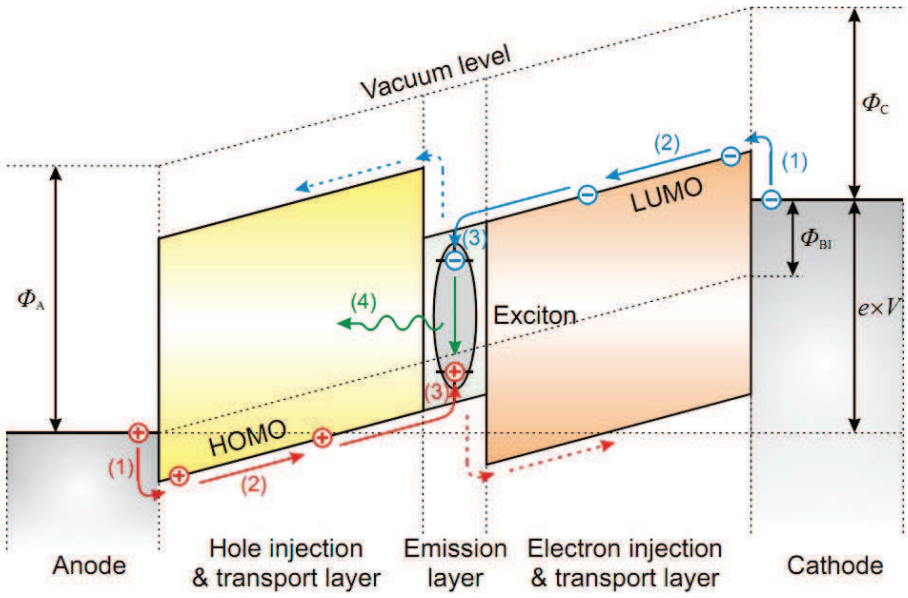

Figure 9: Schematic energy diagram of a three-layer OLED illustrating the basic processes of electroluminescence. Electrons are injected from the cathode into the lowest unoccupied molecular orbital (LUMO) of the ETL, holes from the anode into the highest occupied molecular orbital (HOMO) of the HTL (1) and are transported to the emission layer (2) where they recombine to form an exciton (3). When the exciton decays light is emitted (4) [23].

2.2.1.1. Charge injection

Electrons are injected from a low work function metal contact(cathode) into the lowest unoccupied molecular orbital (LUMO) of the ETL, holes from the anode into the highest occupied molecular orbital (HOMO) of the HTL. Since the anode and cathode have different work functions ϕ_A and ϕ_C, respectively, a built-in voltage ϕ_{BI} exists in the device,which has to be overcome by an external voltage V before current can flow through the device. The injection of holes is improved by high LUMO hole injection layer (HIL) while that of the electrons is improved by low HOMO electron injection layer (EIL)[24]. Common HIL material is NBP and common EIL material is LiF.

2.2.1.2. Charge transport

In addition, hole transport layer (HTL) or electron transporting layer (ETL) compounds with sufficient mobility have to be used to transport the charge carriers to the recombination site. [25, 26, 27] . If higher efficiency is needed, before the holes reach the EML, they pass through electron blocking layer (EBL) which prevents leakage of the electrons from the EML into the HTL. Similarly a hole blocking layers (HBL) can be inserted to improve selectively block holes from the EML to ETL. TPD, a-NPD, and S-TAD are common hole transport materials. Alq3, BCP, and BPhen are common electron transport materials [23].

2.2.1.3. Charge recombination

When two oppositely charged polarons meet, they can form bound electron–hole pairs (excitons). Energy barriers for electrons and holes to both sides of the emitter layer allow to spatially confine and improve the recombination process.

2.2.1.4. Migration of exciton and decay

Excitons will migrate with an average diffusion length of about 20 nm followed by a radiative or non-radiative decay [28]. Alq3 is often used as green fluorescent emitter material. Doping of the emitter layer with organic dye molecules allows to transfer energy from the host to the guest molecule in order to tune the emission wavelength or to increase the luminous efficiency as is discussed in the following section.

2.2.2. Organic guest-host intermolecular energy transfer process

OLEDs are multicomponent systems with various energy transfer processes which distribute the excitation to the desired emitter molecule. Introducing dopants in organic molecular films facilitates the control of a number of device properties such as electroluminescence quantum efficiency, tunning of color emission, thermal stability, durability, increasing the Stoke shift and carrier injection and transport. [29 , 30 , 31]. Thus, it is necessary to briefly review the possible energy transfers that can happen between a host (Donor) and guest (Acceptor) molecules. We

will indicate donor molecules by D, acceptor molecules by A, their multiplicities will be denoted with preceding superscripts, i.e. 1 or 3 for singlets and triplets, respectively. Furthermore, asterisks will mark excited states.

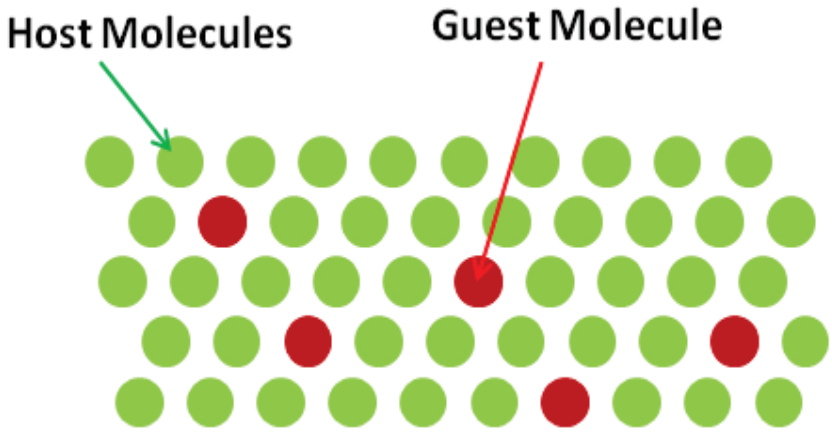

Figure 10: Organic host-guest system. In green: host molecules; In red: guest molecules

The energy loss of an exciton energy from the host to the guest can be radiative or non radiative.

Trivial way of energy transfer between molecules is when light is emitted from radiative deactivation of a donor molecular entity and is re-absorbed by an acceptor molecular entity, as shown in figure 11. The asterisk denote excited state molecule, and **D** and **A** are donor and acceptors, respectively.

$$D^* \rightarrow D + h\nu$$

$$h\nu + A \rightarrow A^*$$

Figure 11: Energy transfer by radiative diactivation

In a non-radiative energy transfer between a donor and acceptor, at the end of this process the donor molecule is in the ground state and the acceptor molecule is in the excited state and this happens without light emission. Non-radiative energy transfer can be Förster and Dexter.

2.2.2.1. Förster transfer

Förster mechanism is based on a dipole-dipole electromagnetic interaction and occurs when the emission spectrum of donor has significant overlap with the absorption spectrum of acceptor [32] and when the molecules are separated by distances considerably exceeding the sum of their van der Waals radii. In Forster energy transfer mechanism, there is no electron transfer between the two molecules. Energy transfer can be typically observed for donor-acceptor separations in the range of 2-5 nm.

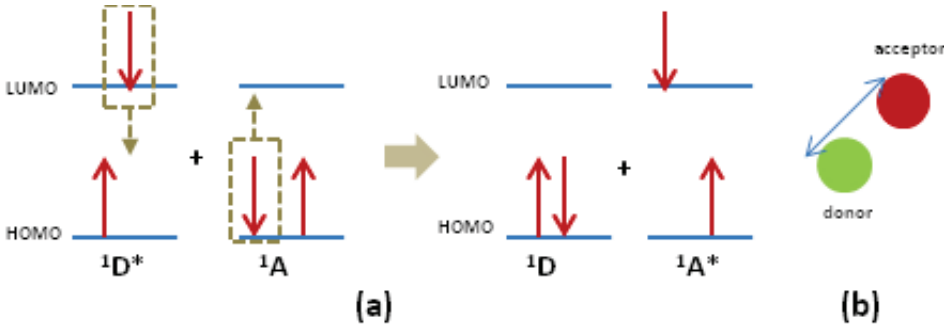

Figure 12: (a) Singlet-singlet Froster enegry transfer mechanism (b) donor and acceptor molecules with distance between them

2.2.2.2. Dexter transfer

The Dexter transfer involves excitation transfer occurring as a result of an electron exchange mechanism [33]. It requires overlap of the wave functions of the energy donor and the energy acceptor and the exchange mechanism is also called the short-range energy transfer. Dexter energy transfer involves singlet-singlet and triplet-triplet transfers and is the dominant mechanism in triplet-triplet energy transfer [34]. The exchange mechanism is based on the Wigner spin conservation rule. The spin-allow process could be singlet-singlet or triplet-triplet [35].

Singlet-singlet energy transfer:

1D* + 1A →1D +1A*, a singlet group produces another singlet group.

Triplet-triplet energy transfer:

3D*+1A →1D + 3A*, a triplet group produces another triplet group.

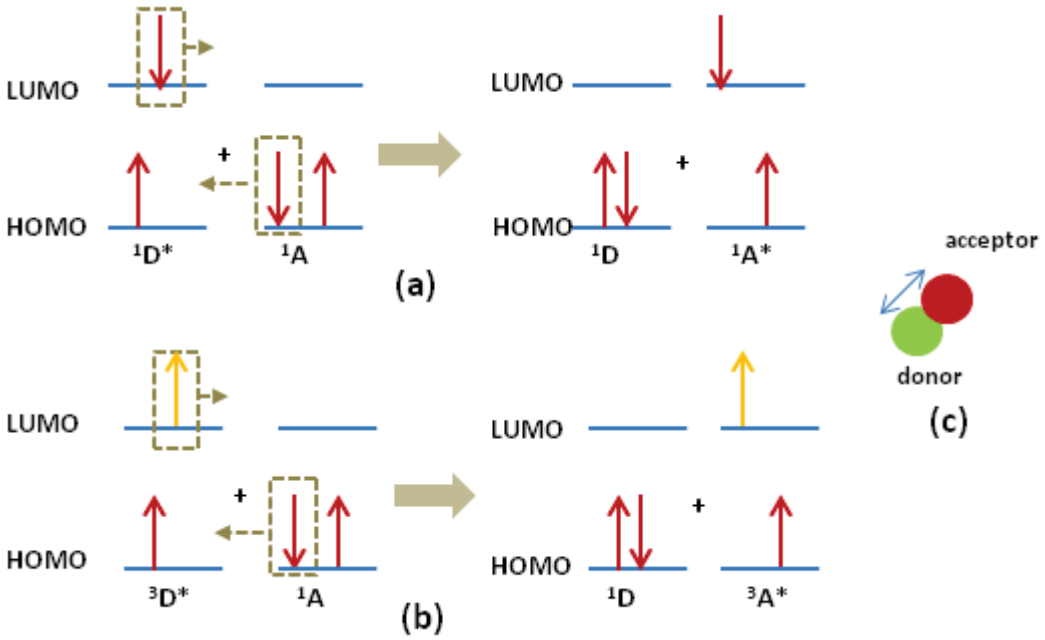

Figure 13: a.) Singlet-singlet Dexter energy transfer mechanism b) Triplet-triplet Dexter energy transfer mechanism c.) donor and acceptor molecules with shorter relative distance between them

2.3 OLEDs with Nanostructures

By integrating nanostructures with organic materials we can enhance the performance of OLEDs or make new devices with modified applications. Nanostructures can be used with conventional OLEDs or organic materials for efficiency enhancement, for spectral modification of the emission from organic materials, to make devices like lasers, or to make OLED devices as micro-OLEDs. The technique of making nanostructures makes one technique more preferable over the other in terms of cost and time of the process and large area application and quality of the desired output. In the following part we will discuss some applications obtained by using nano or microstructures with organic light emitting materials.

2.3.1. The light extraction challenge

One of he main challenges in OLEDs is the low light extraction efficiency, which is only around 20% in a conventional OLED structure. A large part of the light from OLEDs, is trapped as substrate guided mode and waveguide modes that occur due to the differences in refractive index between each OLED layer [36] .

This is shown in figure 14. The emitted light has to travel from the emissive layer (n_{org}=1.6-1.7) through the ITO contact (n_{ITO} = 1.8-2.0) and the glass substrate (n_{glass}= 1.5) and finally into air (n_{air} = 1). As the light travels through the OLED layers, it suffer from poor external efficiency that arises from Snell's law; i.e., light generated in a high-refractive-index layer tends to remain trapped in the layer due to total internal reflection[37, 38].

Total internal reflection is observed at the ITO/glass interface for light with angle of incidence larger than the limit angle $\boldsymbol{\theta lim}$. Since the organic molecules emit light in every direction, only light emitted with angle smaller than the limit angle are transmitted to the ITO layer. Another total internal reflection occurs at the glass/air interface. Again light arriving with angles larger than the limit angle are totally internally reflected and produces guided modes.

In fact, whatever the internal quantum efficiency might be, the light extraction efficiency of OLEDs with flat multi-layered structures including no additional surface modifications is typically only about 20% of the internal quantum efficiency. Therefore, if the internal quantum efficiency is 25% (singlet triplet limit), and with a transmittance of only 20%, the external quantum efficiency can be as low as to 5%.

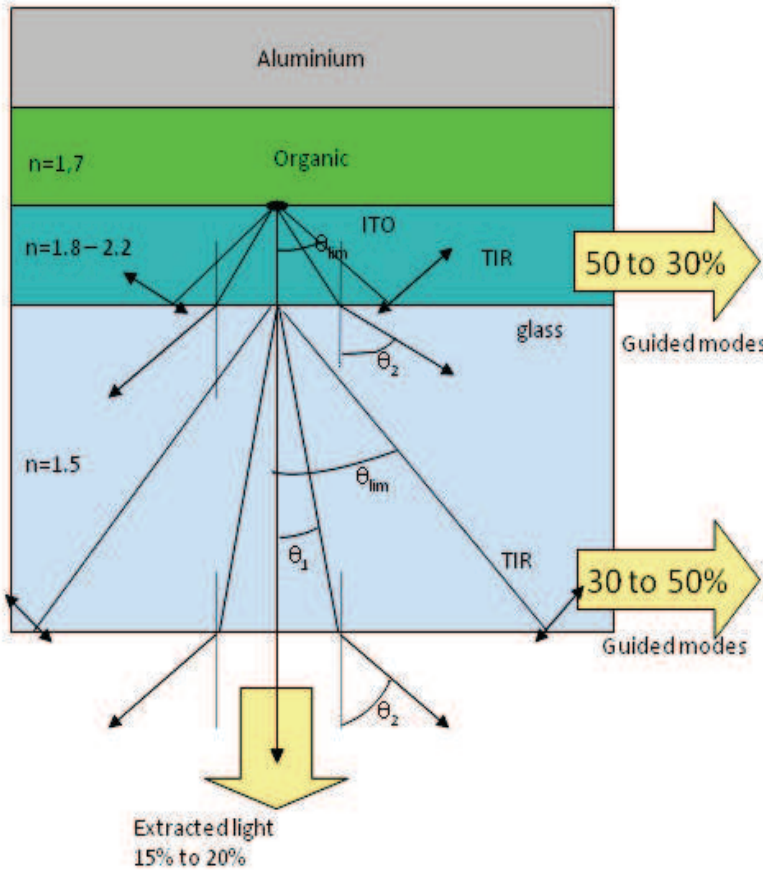

Figure 14: Index structure of an OLED featuring the light extraction issue

To improve light extraction efficiency, different device architectures are proposed. Among these are adding substrate surface roughening[39], microlenses[40,41],monolayer of spheres as a scattering medium[42] photonic-crystals structures[43] or other scattering layers.

People have used the advantage of self-organizing property of nanoparticles for light extraction applications. Moller et al used micro-lenses on the backside of the glass substrate for effective technique of extracting out substrate wave-guided modes [44, 45] Chio et al used colloidal lithography using polysterene nanospheres to pattern WO3 hole injection layer to improve light extraction efficiency (figure 15). They reported increased external quantum efficiency and the power efficiency were increased as compared with those of conventional organic light emitting diodes without WO3 layer [46] .

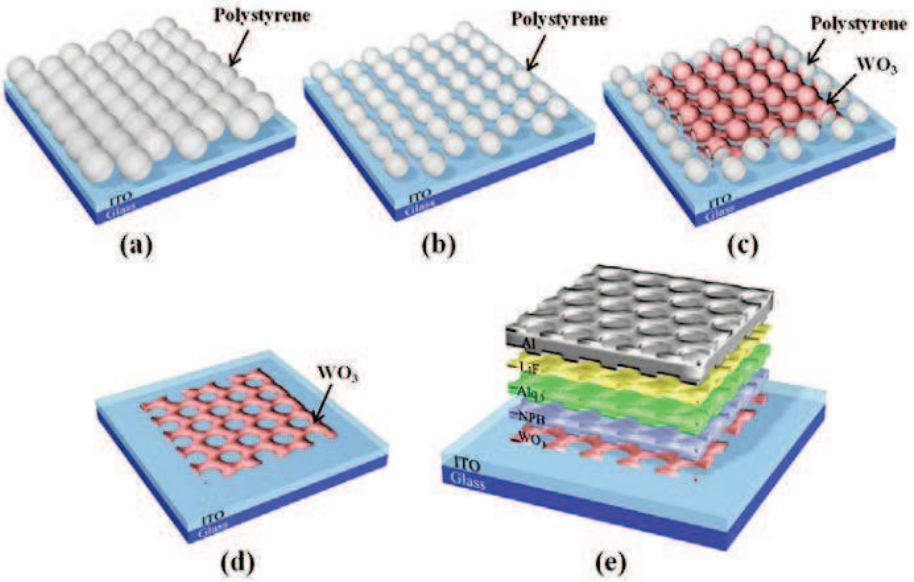

Figure 15: Graphical representation of the fabrication process of OLED with the perforated WO3 layer: (a) self-assembled polystyrene monolayer, (b) non-closely packed self-assembled polystyrene monolayer after the air-plasma etching, (c) WO3 layer deposited on the self-assembled polystyrene monolayer, (d) a perforated WO3 layer, and (e) a structure of the OLED with the perforated WO3 layer[46]

Ho et al used precisely controlled metallic nanomesh fabricated by using nanosphere lithography to pattern silver thin film. The periodical nano-hole array not only increased the transparency but also helped extracting surface plasmonic waves in organic layers. By attaching the microlens array to further extract the trapped light in substrate, the extraction efficiency enhancement of device with nano-mesh anode was 73.8% higher than 50.2% of the referenced device with ITO anode (figure 16) [47].

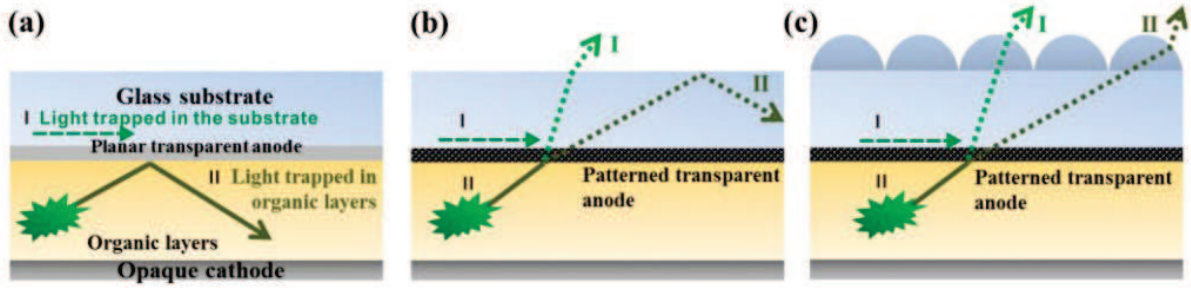

Figure 16: Light extraction of trapped photons in glass substrate (ray I) and organic layers (ray II) of bottom emission OLED. (a) Planar transparent anode, (b) patterned transparent anode, and (c) patterned transparent anode with microlens array attachment.[47]

2.3.2. Nanostructures for spectral modification and resonances: DFB lasers

Nanostructures, usually periodic, can also be used with organic light-emitting materials to make spectral modification or organic lasers. Doing this, spectral narrowing of the organic emitter material and low threshold lasing can be achieved. This is important for electrically pumped organic diode laser, which is not demonstrated yet. This is because the laser threshold is too high compared to the highest current density that an OLED can stand. Laser cavities with low threshold and ultra low cavity are therefore seeked. To compare them, the laser threshold is measured under optical pumping.

This can be achieved by 1D or 2D distributed feedback structures. In 1D periodic nanostructures, the bragg condition $\mathbf{n_{eff}\Lambda = m\,\lambda_{bragg}/2}$, where neff is the effective refractive index of the waveguide, Λ is the period of the grating, λbragg is the Bragg wavelength and m is the order of diffraction. This relation suggests that tuning of the laser wavelength can be reached by a variation of either the grating periodicity $\mathbf{\Lambda}$ or of the effective refractive index of the waveguide which can be adjusted by varying the film thickness. For first order operation (m=1) , the laser is edge emitter while for second order operation (m=2), the emission is vertical as shown in the schematic diagrams below [48].

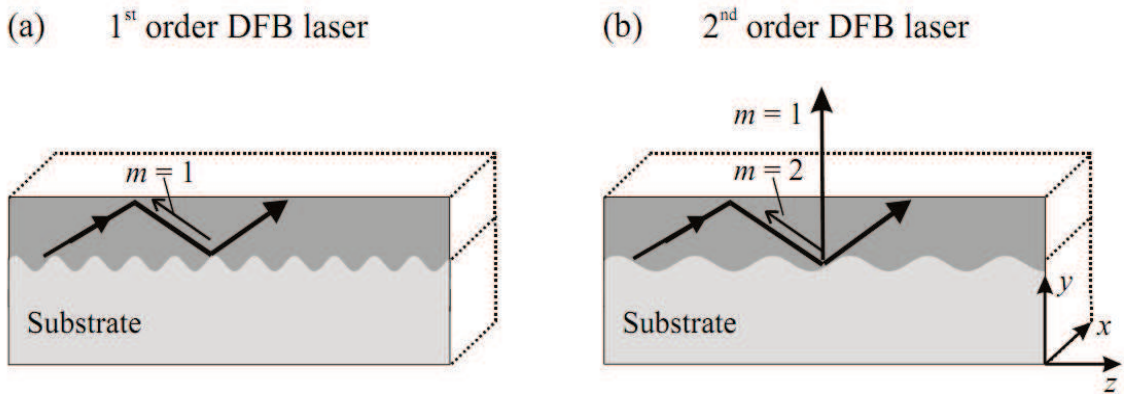

Figure 17: 1D DFB laser: (a)first order emission (b) second order emission

The concept of distributed feedback can be extended to lasers containing a two-dimensional periodic modulation, or 2D-DFB lasers. Here the photonic band-edge mode of a perfect PhC structure is utilized such that the vanishing group velocity of photons results in an optical gain enhancement [49].

Figure 18 below shows a solid-state laser composed of an Al2O3 photonic crystal and an organic gain medium. The photonic crystal is infiltrated with the polymer medium containing laser dye and a laser emission under optical excitation was obtained and the laser action was based on the band edge effect. The minimum laser threshold was about 2.4 nJ/pulse, where the linewidth of the laser emission was as narrow as 0.09 nm[50] .

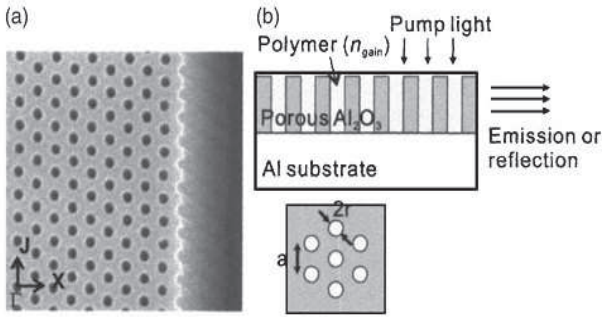

Figure 18: (a) SEM image of Al2O3 photonic crystal: lattice constant a= 200 nm, hole radius r=52 nm, r/a= 0.26. (b) Schematic of the photonic crystal laser composed of Al2O3 photonic crystal and polymer gain medium [50]

Harber et al used e-beam lithography to make 2D square lattice of TiO2 on SiO2 on Si substrate as in figure 19(a) to make 2D DFB feedback laser for organic material MeLPPP and had lasing effect due to the 2D periodicity. The periodic structure of the devices is designed to be of second order, which results in a vertical emitting component. The laser mode was identified with the calculated second-order transverse-magnetic (TM) mode at the Γ point from the band diagram (figure 19(b)). The lasing threshold of the 75μm X 75μm TiO_2 -based structures is 10 nJ per pulse [51] .

Lasing can also be realized with 2D quasi periodic restructure. Notomi et al used a Penrose lattice , in which lasing occurs through quasi-periodicity. They made a 150-nm-deep quasi-periodic hole pattern of 500-nm square in SiO_2 layer on a Si substrate by e-beam lithography and reactive ion etching as shown in figures 19(c) and 19(d) , and deposited a 300-nm-thick DCM-doped Alq3 layer on the patterned SiO_2 to have a lasing at different emission wavelength for different period of the lattice. Lasing action was observed above the pumping threshold around 100 nJ/mm^2 [52] .

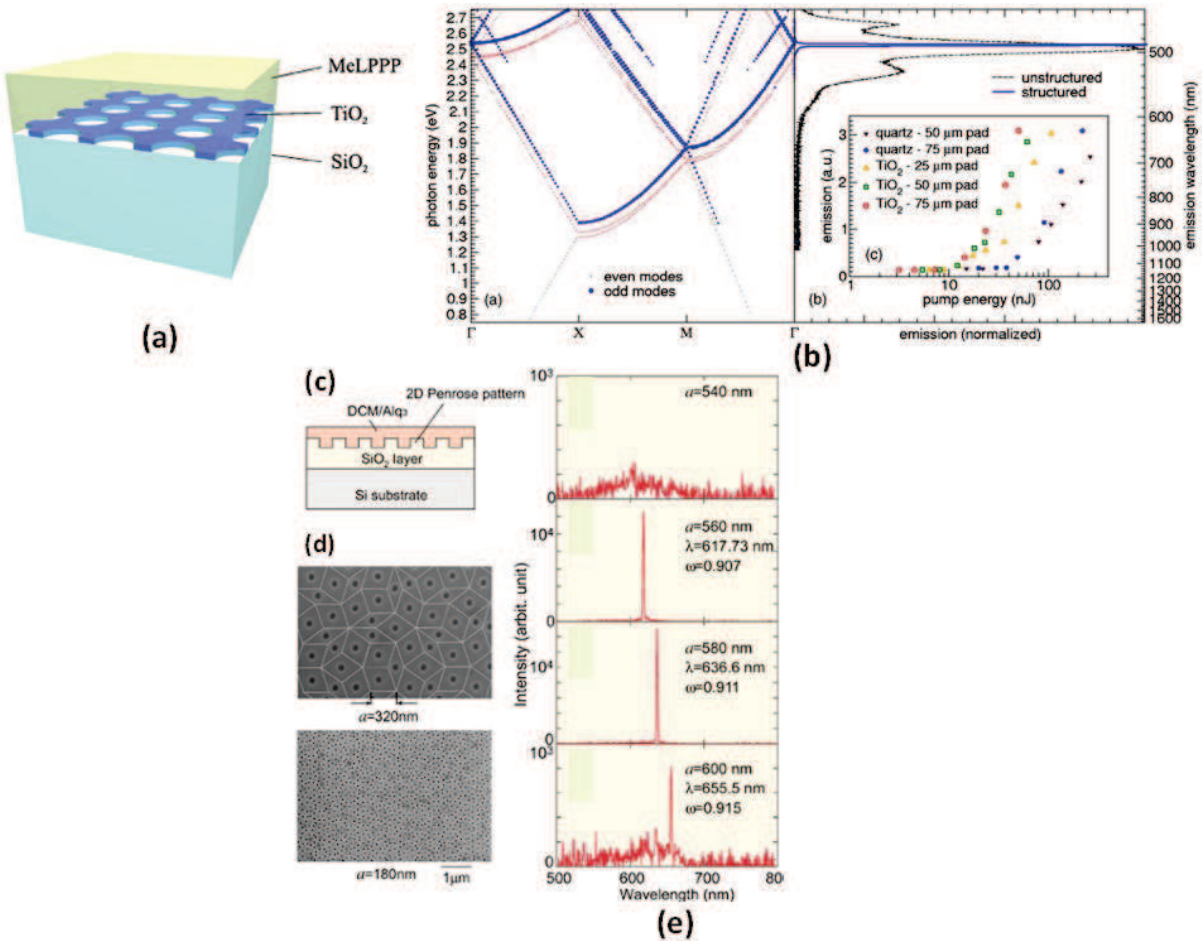

Figure 19: Nansostrcutres to make DFB lasers (a) 2D DFB laser structure with periodic nanostrcuctures: SiO2 substrate with a TiO2 photonic-crystal layer, coated with an organic light-emitting material, MeLPPP [51] (b) Band-structure calculations of the laser shown in (a) , and experimental spectra of an unstructured and a structured site of the laser sample, pumped above laser threshold,; (c) Schematic view of quasi periodic DFB laser; (d) scanning electron micrographs; (e) emission spectra of samples with period of 540, 560, 580, 600 nm.[52]

In addition to this, **nanosphere lithography (NSL)** using monolayer of self-organized spheres was used to make photonic crystals for DFB lasers with inorganic semiconductors. Ahn et al used a 2D photonic crystal PhC band-edge laser that was fabricated in an InGaAsP multiple-quantum-well structure by nanosphere lithography (NSL) to have a laser at threshold of 0.7 mw with emission at around 1550 nm [49]. Although the multi-domain nature of the self assembly was observed, as would be expected for any self-assembly process, they were able to have the lasing effect. This tells us that the multiple domains which appear due to the self-organization process can be tolerable for DFB laser applications.

2.3.3. Nanostructures to make Micro-OLEDs: displays/microscopy/small molecules emission sources

In addition, nanostructures can be used with OLEDs to make micro-OLEDs or nano-OLEDs, which are micrometer or sub-micrometer size. The micro/nano OLEDs can have applications in high resolution microdisplays and detectors, bio sensing [53] or few molecule emission sources for quantum *communication* [54]. Other potential applications include the use of these miniature light sources to achieve lithography or microscopic observations beyond the diffraction limit as in scanning near field optical microscopy [54, 55].

The fabrication of μOLEDs were demonstrated by different techniques like electron beam (ebeam) lithography [56], photolithography and soft lithography [57] techniques. Although ebeam lithography can be used to make more controlled and relatively small μOLEDs, the necessity for a simple, high throughput and low cost fabrication process makes us seek other methods of fabrication. Price *et al*. [58] fabricated arrays of 250-nm-diameter μOLEDs by nano-imprint lithography over large areas for potential application of making displays. Veinot *et al* [59] used a variant of nanosphere lithography to make sub-100 nm OLEDs using monolayer of microspheres. The OLEDs were defined in the space between the microspheres in the monolayer. However, this technique requires repeating the deposition of the self-organized microspheres for each sample. On the contrary, Bolognesi et al. used self-organized honeycomb ordered polymer films to realize the mould needed for imprint lithography. They were able to fabricate highly ordered electroluminescent spots with diameters of 1–1.5 μm. (figure 20) [60].

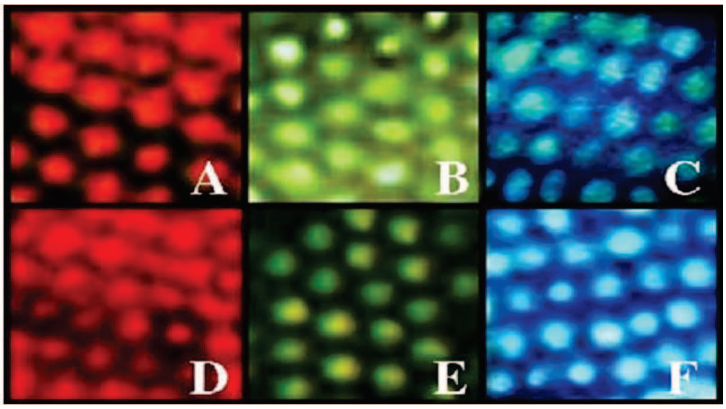

Figure 20: Electroluminescen and photoluminescence from micro-OLEDs. (A), (B), (C) Electroluminescence at 15V bias of the red, green and blue emitting spots, respectively; (D), (E), (F) Photoluminescence observed by UV illumination of the red, green and blue emitting spots, respectively.[60]

In the following sections we will discuss our technique of making nanostructures by microsphere based photolithography, which is used to make micro-OLEDs.

3. Nanoparticle mask photolithography applied to the patterning of OLEDs

3.1. Introduction

Different from the nanosphere lithography mentioned above[Erreur : source de la référence non trouvée,59], using monolayer of nanoparticles as spherical lenses in photolithography or laser ablation to make 2D periodic patterns is other novel approach to use nanoparticles to make nanostrucutres. There have been some works on using micro nanoparticles as spherical lenses to make periodic structures. For example, microspheres have been deposited in a self-organized manner on a photoresist and a UV lithography exposure has been performed through them to realize arrays of holes and pillars[61]. In this maskless process the microspheres are removed afterwards in a wet process and therefore are not reusable. However, a reusable mask made of 8µm SiO2 microspheres was reported by Claire et al. and was used for laser ablation with an excimer laser [62]. With both these techniques the microsphere lattice is reproduced as it is. Whereas, Wu et al presented in a technique using a reusable planar array of 1.5µm microspheres embedded in PDMS acting as an array of ball-lenses to projects the image of an illuminated pattern onto a photoresits [63]. The above mentioned techniques were not applied with the fabrication of organic light emitting diodes.

Here we present a new technique of two-dimensional periodic micro and nanostructuration of surfaces using monolayer of microspheres. In a subsequent step 2D array of micro and nano-OLEDs are made. The 2D array of OLEDs is a potential for spectral modification of light or may be used as DFB or random laser.

The structuration method is a based on the photolithography technique but with a mask simply made of a single layer of self-organized monodisperse nanoparticles deposited on a quartz substrate. The advantages of the technique are that the photomask is reusable, it uses conventional photoresist and moreover the light source is not a laser but a simple UV source.

It is therefore advantageous over similar techniques mentioned previously in that the process is more simple with less steps which makes it cost and time saving. The resulting pattern in the photoresist exhibits hole diameters down to 420 nm closed to the wavelength $\lambda = 405$ nm of the photolithography light source. Surprisingly, the experiments also show that the photoresist can be patterned with lattice reduced by a factor of two compared to that of the self-organized nanoparticles. This work includes an experimental systematical study of the lattice parameters as a function of the diameter of the micro-nanoparticles that range from 2.34μm down to 800 nm.

This section is organized as follow; In section 3.2. we present the theoretical and numerical studies, whereas section 3.3. contains the experimental procedures leading to the fabrication of the two dimensionally patterned OLEDs, and in section 3.4. results are presented and discussed.

3.2. Theoretical study: Reusable nanoparticle mask

When nanoparticles are used as lithographic masks, two different physical ways contribute to the kind of pattern obtained. When the concentrated UV light which is focused on a specific point on the photoresist is just from one nanoparticle, the pattern of the monolayers of spheres is replicated. In this case the the monolayer of dielectric spheres acts as an array of micro-ball lenses. Other situation is the light which passes through the nanoparticle mask and is focused on a point on the photoresist is the interaction from the spheres in the monolayer. In that case the pattern obtained on the photoresist is not replica of the monolayer of spheres and the array of microspheres collectively act a phase mask. This two conditions can be obtained by changing the distance between the monolayer of spheres and the photoresist in photolithography experiment. This corresponds the hard contact and soft contact modes of the mask aligner, as shown in the figure 21 . In hard contact mode, we obtained the period of the structured photoresist to be equal to the period of the microspheres and in soft contact mode the period of the patterned photoresist was half of the period of in th monolayer of spheres mask.

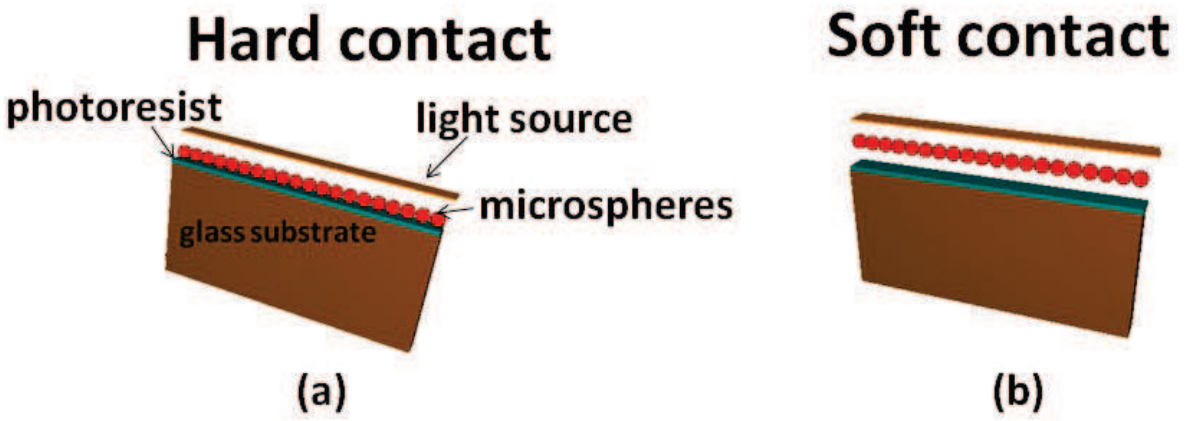

Figure 21: Soft contact and hard contact modes of a mask aligner. (a) Hard contact mode: the monolayer of spheres is in contact with the photoresist (b) Soft-contact mode: there is a spacer between the monlayer of spheres and the photoresist. The monolayer of spheres is assumed to be deposited on glass substrate (not shown).

To theoretically study these two effects effects, 3D FDTD simulation was done as in figure 22. Figure 22(a) shows the field obtained using 3D FDTD simulations with the particles in close contact with the photoresist. In this mode, that corresponds to the hard contact mode of the mask aligner, the light at the wavelength λ=405 nm originates from the Hg light source and travels downward successively through air, through the micro nano-particules (NP) characterized by a diameter **D**=1.68µm and a refractive index n_{bl}=1.4705, through the 200 nm thick photoresits (PR) with refractive index $\mathbf{n_{PR}}$=1.6905 and finally through the glass substrate (SB) $\mathbf{n_{SB}}$=1.5. The optical field calculated at the photoresist interface is obviously focused by each micro nanoparticles, which is confirmed by the period of the intensity profile that matches the lattice **D** of the micro-nanoparticules array (see figure 22(b)). In this configuration each micro-nanoparticles can be assimilated as a microsphere focusing light like a ball-lens.

The phase mask behavior of the mask made with the self-organized particles is illustrated in figure 22(c). There, a **1.5µm** spacing (**SP**) has been introduced between the micro-nanoparticles and the photoresists. This configuration corresponds to the soft contact of the mask aligner. If the intensity profile exhibits a local maximum at the plumb of each microspheres, the spacing produces a modification of the optical field distribution producing

another local maximum in the plumb of the contact point of two microspheres. The intensity profile in figure 22(d) exhibits a quasi period that corresponds to the half of the microsphere diameter D/2. . This phenomenon is linked to the phase mask properties of the mono layer of spheres. Indeed, the array of micro-nanoparticles of diameter ***D*** operates like a gratings with a pitch ***D***. If the conditions of existence of the order +1 and -1 are fulfilled, the array operates like a phase-mask and the interference between the +1 and -1 orders produces a new pattern. In that case, the period of the fringes is exactly one half of the pitch of the phase mask. Therefore, in the soft-contact mode, a nanostructuration with a period ***D/2*** at the half of the microsphere diameter ***D*** is expected.

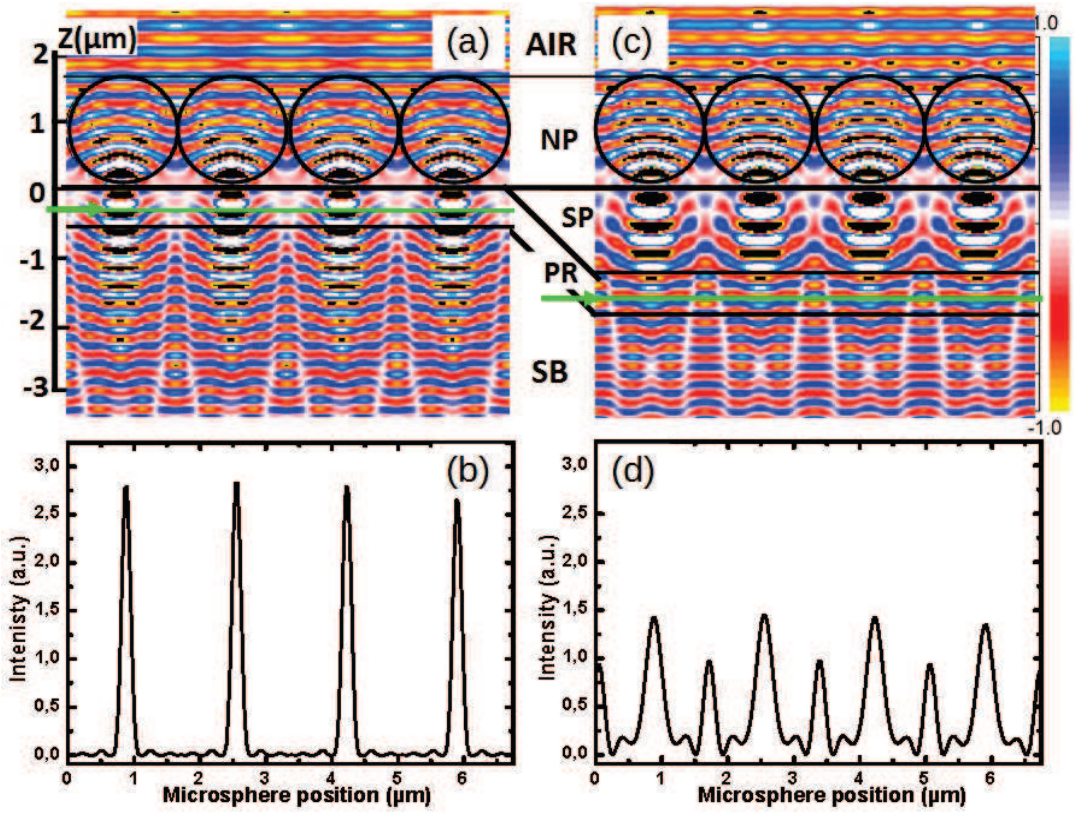

Figure 22: FDTD simulation illustrating the principle of microsphere based photolithography: NP : nanoparticles, SP : Spacing, PR : photoresist, SB : Substrate. The light is focused by the microspheres (a) Electric field distribution in the hard-contact mode. The green line indicates where the intensity profile is calculated. (b) Intensity profile in the hard contact mode. (c) Electric field distribution in the soft-contact mode. The green line indicates where the intensity profile is calculated. (d) Intensity profile in the soft-contact mode.

At this step, we would like to specify the conditions under which this behavior can be obtained. The geometry of the system is presented in figure 23(a) below. Unlike blazed gratings, and because of the symmetry of the structure, the +1 order exists together with the -1 order under normal incidence. The angle of transmission θ_1 of the order m =1 is calculated using the grating fundamental law :

$$m\lambda = (n_{air}\sin(\theta_i) + n_m\sin(\theta_1))D \qquad \text{Eq. 1}$$

Where n_m is the refractive index of the medium underneath the grating. Depending on the distance of the photoresist to the microsphere, n_m is either the refractive index of the photoresist n_{PR} (hard-contact mode) or that of the air n_{ar} (soft-contact mode). Under normal incidence θ_i =0, the orders ±1 exist if the angle θ_1 associated to the order 1 is smaller than the maximum angle θ_{max} transmitted by the microspheres and related to their numerical aperture.

The Back Focal Length (***BFL***) and the numerical aperture ***NA*** of a ball-lens writes respectively [64] :

$$BFL = EFL - \frac{D}{2} = \frac{n_{bl}D}{4(n_{bl}-1)} - \frac{D}{2} \qquad \text{Eq. 2}$$

$$NA = \frac{2a(n_{bl}-1)}{n_{bl}D} \qquad \text{Eq. 3}$$

Where a is the aperture, which in our case and for normal incidence, is the micro particles diameter $d=D$. The **NA** gives the maximum angle θ_{max} for the transmitted field:

$$\sin(\theta_{max}) = \frac{1}{n_m}\frac{2(n_{bl}-1)}{n_{bl}} \qquad \text{Eq. 4}$$

The condition of existence of the orders ±1 writes :

$$\sin(\theta_{max}) \geq \sin(\theta_1) = m\frac{\lambda}{n_m D} \qquad \text{Eq. 5}$$

The angles θ_{max} and θ_1 are plotted as a function of the diameter D on figure 23(b) with a dashed red and a solid blue lines, respectively. Under our assumptions θ_{max} is independent of D and appears as a horizontal line on figure 23(b). Figure 23(b) explains the fact that for D larger than a certain value D_0, the angle of the orders 1 is smaller than the aperture angle and the interferences may occur.

The condition on the diameter D of the nanoparticles writes:

$$D_0 \geq m \frac{n_{bl}\lambda}{2(n_{bl}-1)} \qquad \text{Eq. 6}$$

Under this assumption and with the current parameters, D_0 is 624 nm. This imposes a lower limit on the diameter D of the microspheres to achieve a lattice $D/2$. This limit D_0 is indicated with a green solid vertical line on figures 23(b) and 23(c). Above D_0, the angle $\theta_1 > \theta_{max}$ and the orders +1 and -1 exist. It imposes a theoretical lower limit $D_0/2$=312 nm on the existence of the reduced lattice period $D/2$ which remains larger than the Abbe limit. Another condition of existence of the interferences can be understood from the figure 23(a). Due to the symmetry of the problem, the front wave emitted from the microsphere 1 (MS_1 center O_1) with the angle θ_{Max}, interfere constructively in A with its symmetrical front wave issued from the microsphere 2 (MS_2 center O_2).

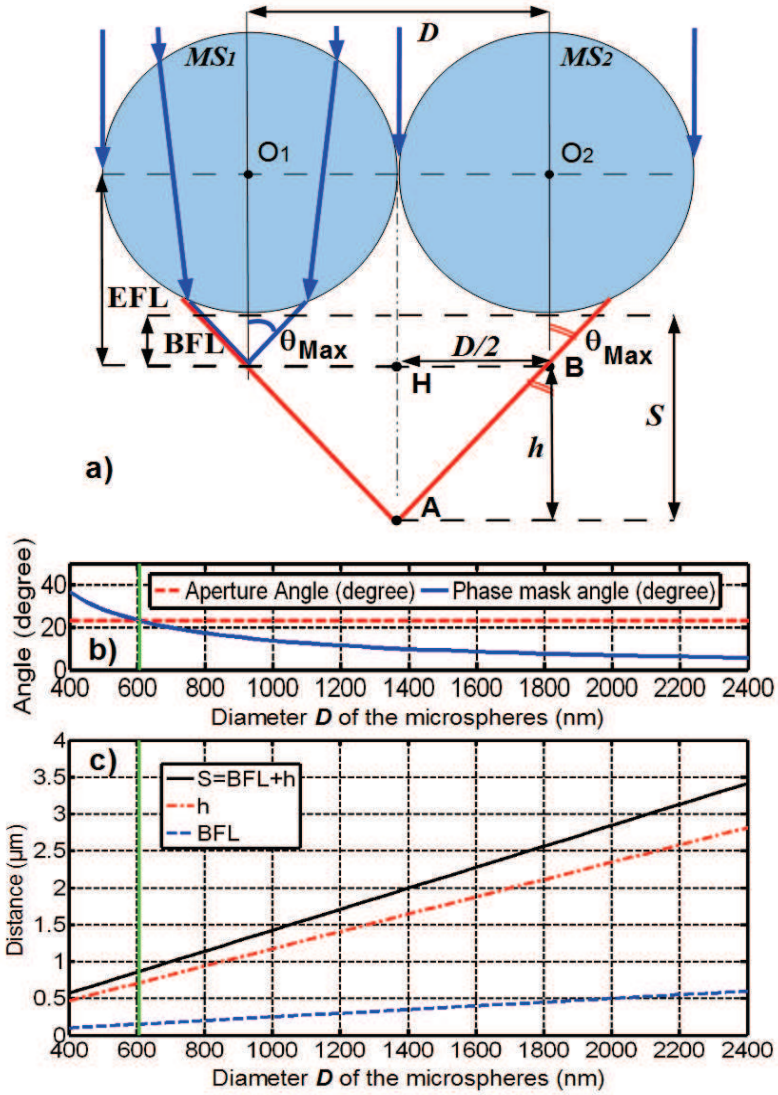

Figure 23: (a) Schematic showing the optical path and the interference conditions. ***MS1****,* ***MS2****: Microspheres (center* O_1 *and* O_2*),* ***D:*** *diameter and lattice,* ***BFL:*** *back focal length,* ***h:*** *distance from the plane of focus to the plan of interference (b) The aperture Angles* θ_{max} *and the phase-mask angle of the orders ±1* θ_1 *as a function of the diameter* ***D*** *of the microspheres. (c) Effective distance* ***S*** *for the existence of the interference between the orders +1 and -1 calculated from Eq. (8).*

Knowing the distance ***D*** between the microspheres, it is straightforward from the relations in the triangle HBA to calculate the distance ***h*** from the plane of focus to the plane of interference

$$h = \frac{D}{2.\tan(\theta_{max})} \qquad \text{Eq. 7}$$

Replacing the angle by the right term of eq. 5, the distance ***S=BFL+h*** from the plane in contact of the spheres to the plan of constructive interference containing A writes:

$$S = D\left[\frac{n_{bl}}{4(n_{bl}-1)} - \frac{1}{2} + \sqrt{\left(\frac{n_m n_{bl}}{2(n_{bl}-1)}\right)^2 - 1}\right] \qquad \text{Eq. 8}$$

Eq. 8 is plotted on figure 23(c). This curve shows that the minimum distances to achieve a phase mask behavior with a period of the fringes equal to the half of the micro nanoparticles diameter ranges from ***h***=0.8µm to ***h***=3.5µm which corresponds to the spacing induced by the soft-contact mode. By comparison the back focal length (***BFL***) of the micro nanoparticles ranges from 100 nm to 700 nm.

3.3. Experimental procedures

This section is dedicated to the experimental demonstration of the two-dimensional patterning applied to the fabrication of patterned OLEDs. The experiments is conducted in four steps: the synthesis of the nanoparticles, the fabrication of the photomask (monolayer of micro nanospheres), the processing of the patterns and the deposition of the OLED.

Figure 24 shows the schematic diagram of the fabrication process of microstructures and micro-OLEDs. We will discuss the fabrication process of the microstructure in detail as the process can be used not only to make µOLEDs, it may also be used as intermediate step to make periodic textures for performance enhancement of organic electronics devices.

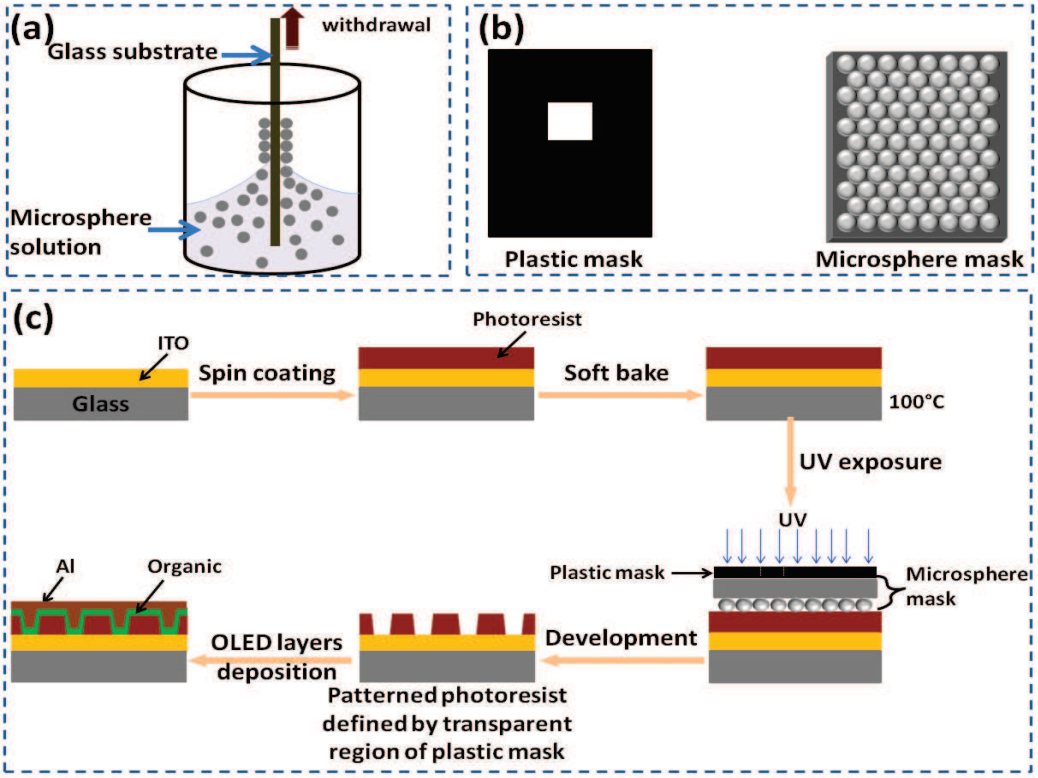

Figure 24: Schematic diagram of the fabrication process of micro-nanostructures and micro-nano OLEDs. (a) Self assembly of nanoparticles by dip-coating process. (b) General plastic mask and microsphere masks. (c) Positive photoresist is deposited on ITO coated glass substrate by spin coating. The photoresist is soft baked on a hotplate and the sample, the microsphere mask and the plastic mask are aligned as shown and the sample is exposed to UV . The photorist is developed after UV exposure and OLED layers are deposited by evaporation on the patterned photoresist.

3.3.1. Synthesis of microspheres and fabrication of monolayer of colloidal crystals

3.3.1.1. Synthesis of microspheres

The experiments were started with the synthesis of different monodisperse nanoparticles made from SiO_2 and polystyrene (PS). Different diameters were used in the different experiments; 800 nm, 1 µm, 1.25 µm, 1.53 µm, 2 µm, and 2.34 µm for SiO_2 and 1,68 µm for PS. The SiO2 microspheres are prepared by modified Stober and sol–gel processes in an alcohol-rich phase

[65]. Fresh alcohol, purified water, and ammonium hydroxide are firstly added into a sealed bottle and well mixed by a stirrer. Tetraethylorthosilicate (TEOS) is introduced into the system. The transparent solution turns into milk-like solution. After stirring for 2 h, the milk like solution is put under a centrifugal force to collect the SiO_2 microspheres and washed with fresh alcohol three times. The SiO_2 micro-nanoparticles are finally dispersed into alcohol phase and the solid content was controlled to be about 10 wt% [66]. The microspheres were synthesized by our collaborators at National central University of Taiwan.

The monodisperse PS micro-nanoparticles were synthesized via emulsion polymerization at 70°C. After heating at 70°C for 24 hours, the latex was centrifuged. The PS spheres were collected and washed with methyl alcohol six times to remove any remaining impurities. They were then dispersed into a solvent. The solid content was controlled to about 10 wt %.

3.3.1.2. Fabrication of colloidal crystals

The fabrication of the photomask is based on dip-coating. The SiO_2 micro-nanoparticles were deposited by a dip-coating method on both sides of two glass slides stacked and pressed together. The slides were held vertically and were immersed in the solution of micro nanoparticles and withdrawn. The rising speed of the glass slides was controlled at 5 mm/s and the pair of samples were separated and heated at 100^{o}C in the air for 10 min to remove the solution figure 24 (a) and discussed in chapter 1. Similarly the PS spheres were deposited in a highly ordered self-assembled structure on a quartz substrate by a dip coating method as in our previous study [67,68].

3.3.2. Patterning of photoresist and making micro-OLEDs

3.3.2.1. Patterning of photoresist

Figure 24 (c) illustrates the different steps of the fabrication process of micro nano-OLEDs. The patterning process started with the cleaning of 1.7cm by 2.5cm ITO coated glass used as a substrate for the OLEDs. AZ-1505 (MicroChemicals) was used as a positive photoresist and diluted with AZ-EBR solvent (MicroChemicals) (with volume ratio =2:1, 2 parts for AZ-1505). The photoresist was then spin coated on the ITO coated substrate at 6000 rpm for 60 seconds. The thickness of the deposited photoresist was 190 nm as measured by profilometer (Alpha-Step IQ Surface Profiler). The photoresist at the edge of the substrate was thicker as

more resist is accumulated during the spin coating process. This edge bead was removed by AZ-EBR solvent to improve the flatness of the samples and ultimately to improve the contact between the surface of the photoresist and the microsphere mask. The evolution of the geometrical parameters of the micro nanostructurations are verified by Scanning Electron Microscope (SEM), optical microscope, or Atomic Force Microscope (AFM) inspection at each step of the process.

3.3.2.2. OLED layers deposition and characterization

As an example, we have fabricated two types of OLED devices with red and green emission. The OLED layers were deposited on top of the patterned photoresist by evaporation at a vacuum pressure of 2.10^{-7} Torr in an evaporation chamber. The schematic diagram of the evaporation chamber with substrate holder and different material heaters is shown in figure 25. The energy diagrams of the green and red organic hetero-structures are shown in figures 26(a) and 26(b), respectively. The green emitting device consists of a 40 nm thick 4,4',4'',tris-(3-methylphenylphenylamino) triphenylamine (m-MTDATA) layer as hole injection layer (HIL), a 15 nm of N,N'-diphenyl-N,N'-bis(1-naphthyl)-1,1'-biphenyl-4,4-diami (NPD) as a hole transport layer, a 50 nm of Tris(8-hydroxyquinolinato) aluminum (AlQ_3) host material as the emissive layer (EML) with an intrinsic peak emission centered at 520 nm. The organic layers were followed by a 1 nm of lithium fluoride (LiF) and a 150 nm thick aluminum (Al) layers as a cathode that was vapor deposited at the same background pressure.

The red OLED is structured as follows: a 40 nm thick m-MTDATA layer, a 15 nm thick NPD layer, a 30 nm of AlQ_3 doped DCM2 (4-(dicyanomethylene) -2–methyl -6-(p-dimethylaminostyrl) -4H-pyran) as the red emitting layer. The heterostructure was completed with a 10 nm thick BCP (bathocuproine: 2,9-Dimethyl-4,7-diphenyl-1,10-phenanthroline)hole blocking layer, and a 10 nm thick Alq3 layer as an electron emitting layer. Finally a 1 nm thick lithium fluoride (LiF) and a 150 nm thick aluminum layers form the cathode. In total, the OLED hetero-structure thickness (without the aluminum layer) is 105 nm with an active area of 4 x 5 mm.

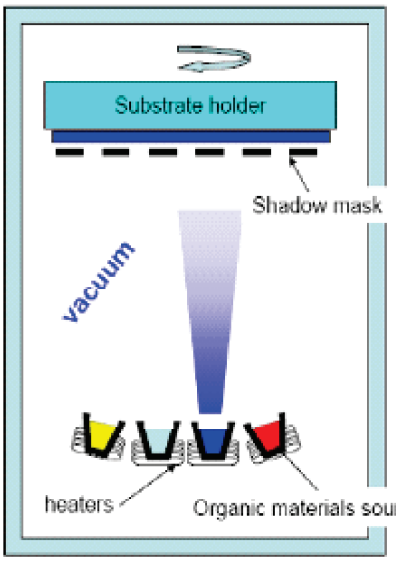

Figure 25: Schematic diagram of OLED evaporation chamber.

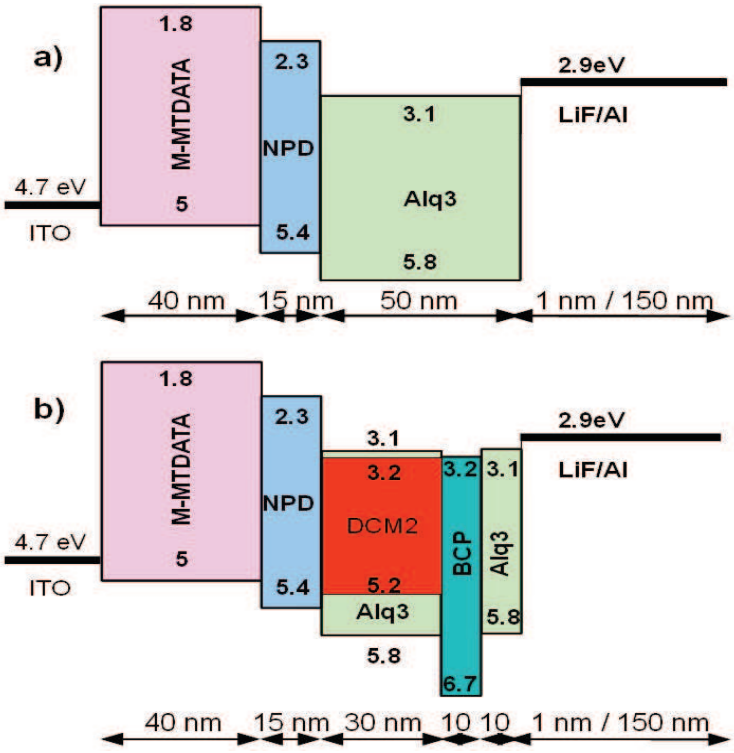

Figure 26: Band diagram of the organic heterostructures (a) organic heterostructure for green emission (b) organic heterostructure for red emission.

The characterization of micro-OLEDs involves optical microscopy observation and spectral characterization of the micro-OLEDs and was done in glove box system on a probe station. The schematic diagram of the characterisation system and the figure of the mounted setup is shown in the figures 27(a) and 27(b) below.

For the observation of the micro-OLEDs, a CCD camera mounted on a high working distance microscope objective was used. For spectral characterization, a beam splitter sends the emission from the OLEDs to optical fiber tip of a spectrometer via another microscope objective. The spectrum of the emission from the micro-OLEDs was compared with the emission from large area reference OLEDs.

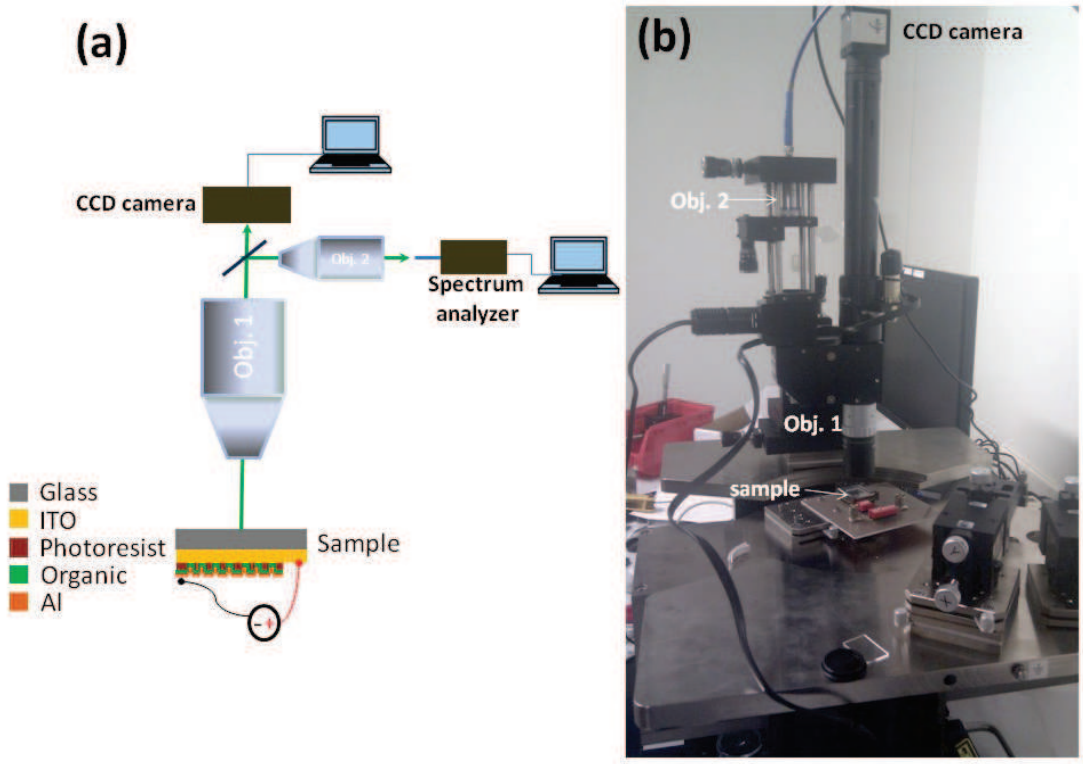

Figure 27: Experimental characterization setup of micro OLEDs (a) Schematic diagram of the experimental setup (b) Figure of prob station used

3.4. Experimental results and discussion

The experimental results on the patterning of photoresist and micro-OLEDs will be discussed in detail in the following sections.

3.4.1. Patterning of Photoresist

Figure 28(a) represents the global view of the mask made with a single layer of 2.34 μm SiO_2 nanoparticles self organized on a 17x25 mm quartz substrate. The monolayer of nanoparticles covers the whole glass substrate and is uniform without significant aggregates as seen by eye. When observed at different angles the substrate diffracts different colors of light, which is a manifestation that the self-assembly has made periodical structure. A closer view of the self-assembly by SEM is shown in figure 28(b). The image is a single layer of 2.34μm size microparticles showing the regularity of the self-assembled organization, with some defects.

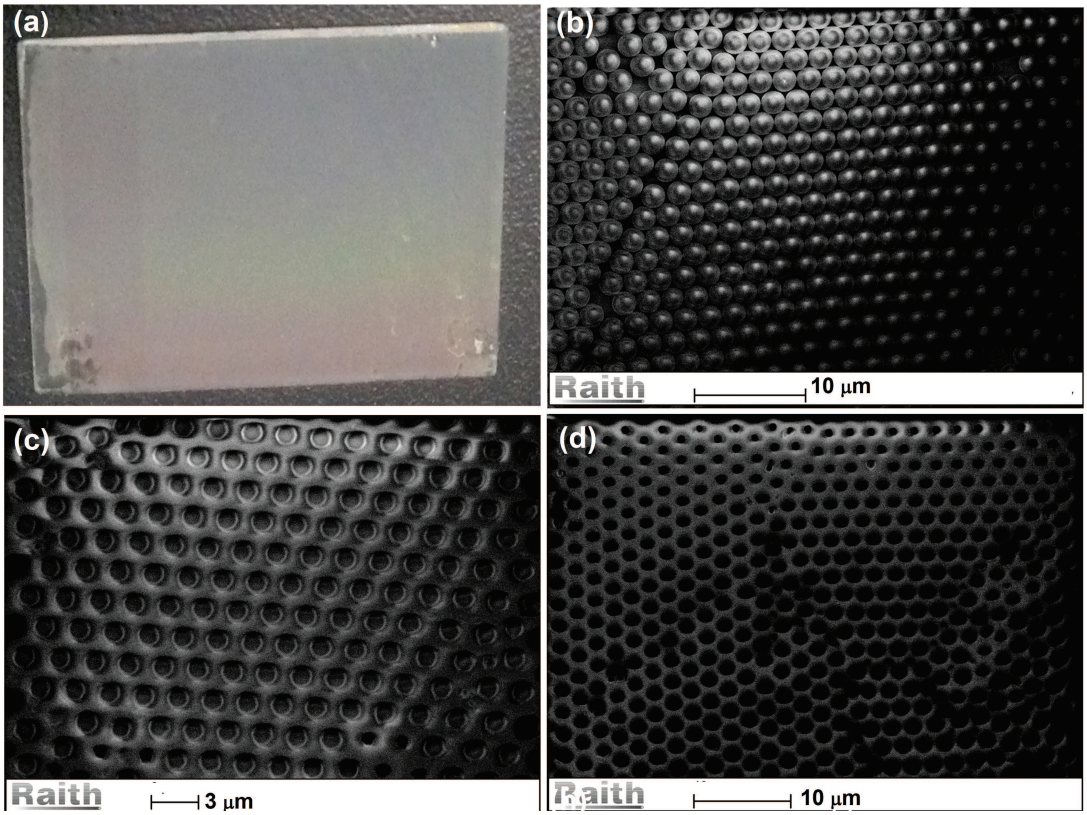

Figure 28: (a) Image of 17mm x 25mm quartz substrate with 2.34 μm microspheres deposited on it. (b) SEM image of the self-assembled microspheres (size of a sphere = 2.34 μm) (c) and (d) SEM image of the patterned photoresist

Figure 28(c) and 28(d) show SEM images of a patterned photoresist made using 2.34μm microspheres mask. We can note that eventually the multiple domains which usaully appear in self-assembled monolayer of microspheres are clearly reproduced in figure 28(d) of the patterned photoresist.

In the figure 29 below we present the result of microstructure made by using 1.68µm microsphere mask. The diameter of the resulting hole diameter was measured to be 1.27 µm which is smaller than the nanoparticles diameter which confirms the focusing properties of the micro nanoparticles as ball lenses. To measure the depth of the holes and make sure that the exposed photoresist is etched down to the ITO layer, the surface morphology of the mictrostructured photoresist was observed with an atomic force microscope in contact mode (AFM Nanosurf) as shown figure 29(b). The depth of the holes measured by AFM microscope was comparable to the thickness of photoresist measured by the profilometer, before the structuration was performed. This confirmed that the photoresist is etched down to the ITO layer which ensures that an electrical contact between the ITO and the organic layers exists and the structure we made will be compatible with the OLED deposition process.

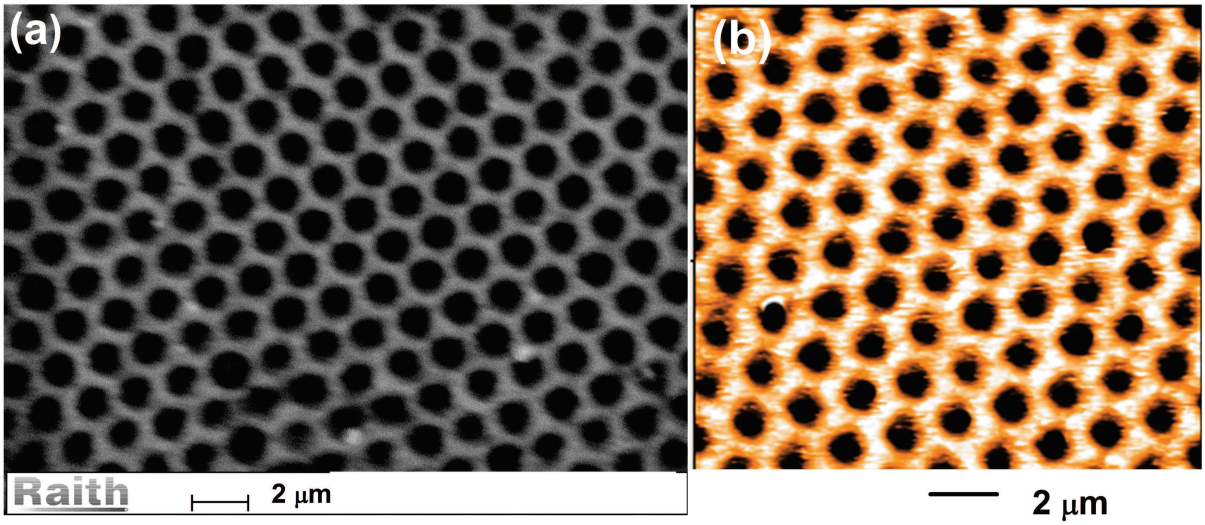

Figure 29: Pattern made by using 1.68 µm mask in hard contact mode. (a) SEM image of the patterned photoresist (1.68 µm lattice). (b) Atomic force microscope image of a patterned photoresist (1.68 µm lattice).

Note that contrary to unpatterned substrate (figure 30(a)), processed substrates exhibit different colors of iridescence when vied at different angles (see figures 30(b)-(d)) which is an evidence of the existence of the pattern on the whole ITO covered glass.

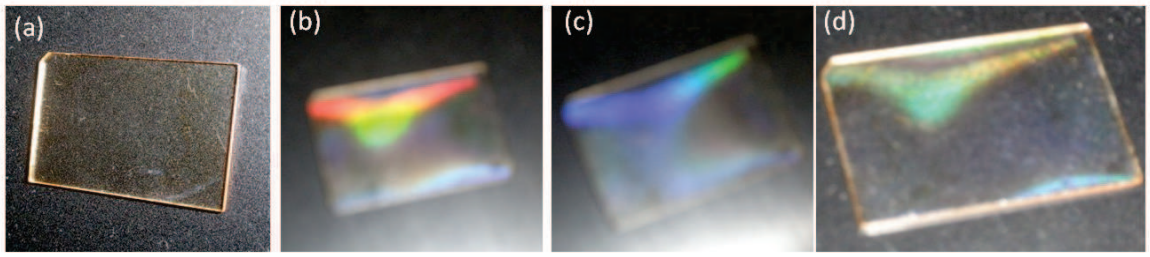

Figure 30: Diffraction of light by micro nanostrucutred photoresisit on glass substrate. (a) Unstractured photrosist. (b), (c) and (d) structured photoresist viewed at different angles. We can see different diffracted colors of the patterned photoresist for different viewing angles.

In order to apply this process to the realization of two dimensional distributed feedback organic lasers in optical regime, smaller period of the lattice in the structured photoresist is desired. For this we have investigated the lattice parameters of the structuration as a function of the *diameter of the nanoparticles* and *different mask alignment conditions*. In this context, it appears interesting to demonstrate the possibility to apply the phase mask properties of the micro-nanoparticles array to nanostructure in two-dimension with a pattern period equal to the half of the particle diameter D.

For this reason, and as an intermediate step, the photolithography process was repeated with 1.68 µm micro-nanoparticles on a photoresist layer which presents thickness fluctuations of few micrometers. This induces variations of the spacing between the photoresist and the photomask. As a results, unreduced (***D***) and reduced (***D/2***) lattice periods clearly appear on the same sample (see figure 31). Despite a lack of control in the positioning of the different patterns, we present the figure 31 for the sake of the demonstration. This is indeed a clear experimental demonstration that two patterning configurations exist and may coexist with the same photolithography mask made with the same diameter ***D*** of self-organized micro nanoparticles:

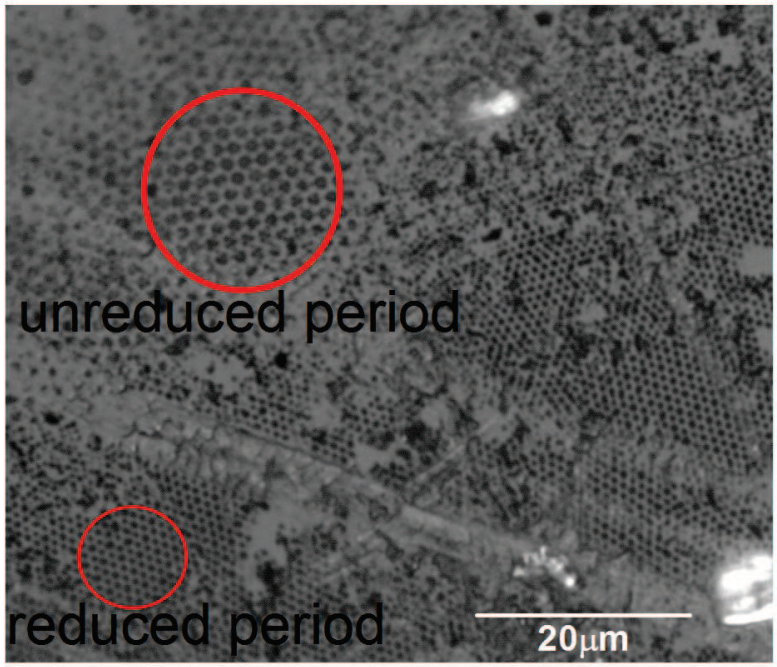

Figure 31: Optical microscope image showing a patterned photoresist with an irregular thickness. The pattern exhibits two lattice periods. D =1.68 μm (unreduced) and D/2 =840 nm (reduced) periods created on the same sample with the same photomask. (size of spheres is 1.68 μm).

Similarly, using the same microsphere mask and two different photoresisit samples, one in the soft contact mode and the other in hard contact mode, resulted in two different periodicities. The AFM images shown in figures 32(a) and 32(b) correspond to microstrucutres made by using microsphere mask of 1.68 μm in hard contact and soft contact modes, respectively. The number of periods spanned by a length of around 17.2 μm is twice for the pattern made by soft contact mode(figure 32(b)) as compared to the number of periods of the pattern made by hard contact mode(figure 32(a)).

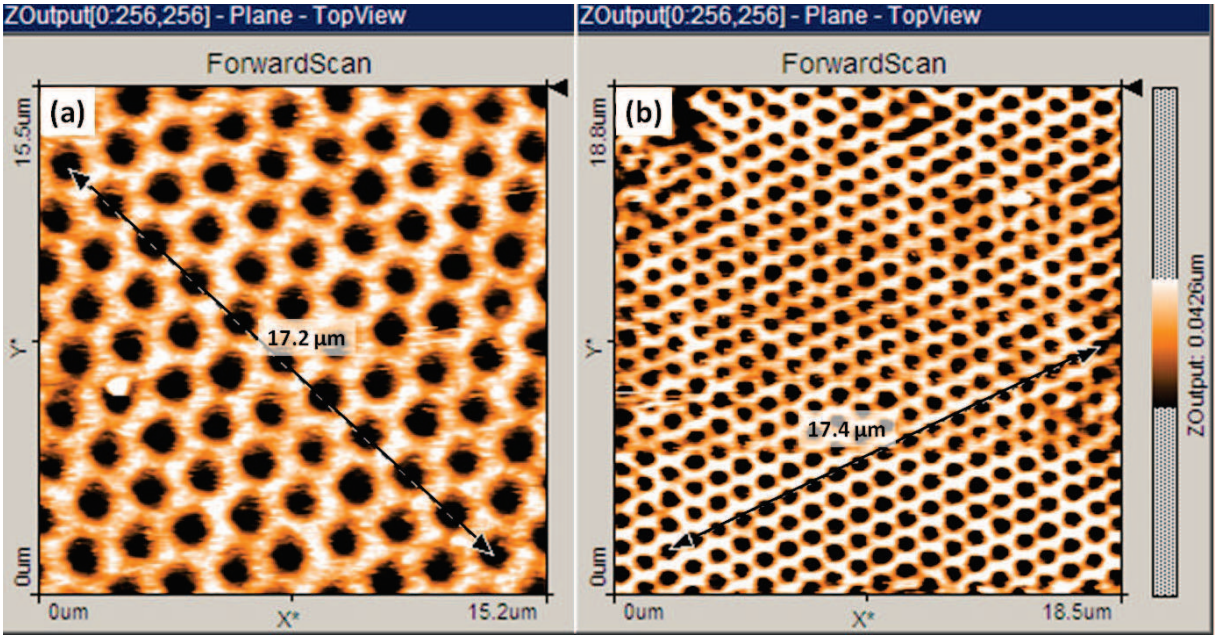

Figure 32: AFM images of two different samples patterned with 1.68µm size microsphere mask and obtained by different mask alignment conditions. (a)pattern made by hard-contact mode of the mask aligner(unreduced period) (b) pattern made by soft contact mode of mask aligner (reduced period)

In order to investigate the diameter dependence of the micro-ball lens and phase mask properties, the process was repeated systematically in the hard contact mode and in the soft contact mode for different sizes of the micro-nanoparticles. We have used microspheres of size 800 nm, 1 µm, 1.25 µm, 1.53µm, 1.68µm, 2µm and 2.34µm. For the different particle sizes, the hole diameters and the lattice periods were measured both in hard contact and in soft contact modes.

Figure 33 summarizes the dependence of hole diameter and period of the patterned photoresist on the period of the monolayer of spheres for hard contact and soft contact modes. To clearly understand the graph, we put optical microscope images of 6 different patterned photoresist samples (**S1, S2, S3, S4, S5, S6**) under different conditions on the top of the graph.

The blue dots in the graph correspond to the period of the nanostructures fabricated with the hard contact mode and are perfectly aligned and exhibits a slope 1±0.1 which confirms that the self-organized micro-nanoparticles lattice is exactly reproduced in the photoresists with a period **D** equal to the particles size (the periods are unreduced). The hole diameters (white

circle) of this unreduced periods exhibit a lower alignment with an averaged slope obtained by linear regression of 0.69 indicating the proportion of the hole diameters to the particles size. We believe the small variations are due to uncontrolled process parameters like the aging of the chemicals and time exposure, or developement fluctuations.

But when soft contact mode is used, clearly the same mask allows to have an unreduced period patterns. (See (samples S3&S5) in hard-contact mode and the corresponding reduced period pattern (samples S4&S6) in the soft-contact mode). The black squared line in figure 33 clearly indicates a reduction of the pattern periods by a factor 2 compared to the particles diameter used for the photomask. Indeed, a linear regression gives a slope of 0.51±0.1 indicating that the reduced pattern period is ***D/2*** as expected from the interference between the orders +1 and -1 in a phase-mask with a pitch D.

The hole diameters obtained in the soft-contact mode (empty quares in figure 33) exhibit a linear regression with the diameter ***D*** giving a slope of 0.35±0.1 which corresponds to the half of the hole diameters obtained in the hard-contact mode. Note that the smaller hole diameter obtained with 1.25 μm microparticles (sample S4) is 420 nm which is close to the diffraction limit with a light source at λ = 405 nm. (white squares in figure 33)

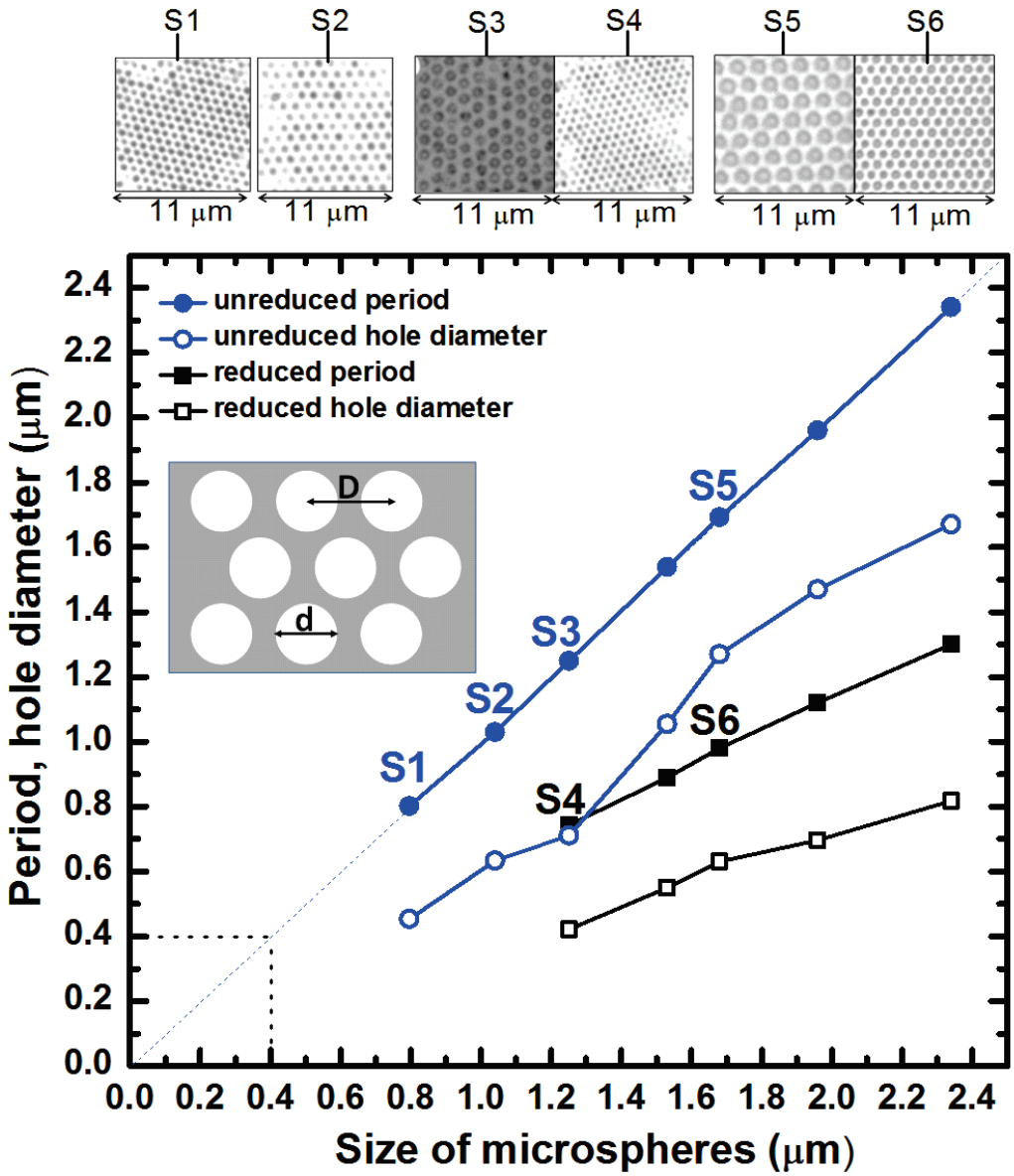

Figure 33: The dependence of the period and the size of holes in the microstructures as a function of the size of particules: ● The period of the pattern in the hard contact mode (unreduced period), ○ Diameter of the holes corresponding to the unreduced period, ■ Reduced period of the pattern in the soft contact mode, □ The diameter of holes corresponding to reduced period.

In addition to that, the fabrication of nanostructures with reduced period ***D/2*** were not observed with the particle diameter smaller than 1.25 μm (see samples **S1** &**S2** corresponding to the pattern made by 800nm and 1μm particle masks, respectively). However, the theory predicted a lower limit on the particle size for reduced period at D_0=624 nm which was not achieved here. We believe that the difference is due to the fact that the soft-contact mode

introduces a too large spacing for particle sizes below 1.25 μm and further experiments with a better control of the spacing are required.

3.4.2. Micro-OLED characterisation

For the fabrication of micro-OLEDs, the photoresist was patterned using microsphere masks of 1.68μm in hard contact mode corresponding to sample **S5** in figure 33. The period of the lattice is 1.68 μm and the size of the holes was 1.27μm. Figure 34 presents the image of micro-OLEDs captured by CCD camera. The first type of micro-OLEDs is a red OLED(figure 34(a)) fabriated according to the organic heterostructure presented in Fig. 26(b) and the maximum of emission is at λ = 620 nm. The photography taken under a x50 objective was obtained for a turn on voltage of 12 V (threshold voltage is 10V) and a driving curent of 15mA. The second type of micro OLEDs is shown on the figures 34(b) and 34(c) taken with x50 and x20 objectives, respectively. It corresponds to the green organic heterostructure shown on fig 26(a) structured with 1.68 μm microparticles and resulting in hole diameter of 1.27 μm. The OLED was driven with 16 mA at 8.5 V and shows under normal incidence a luminance of 2142 cd/m2 and 2.35 lm/W of power efficiency.

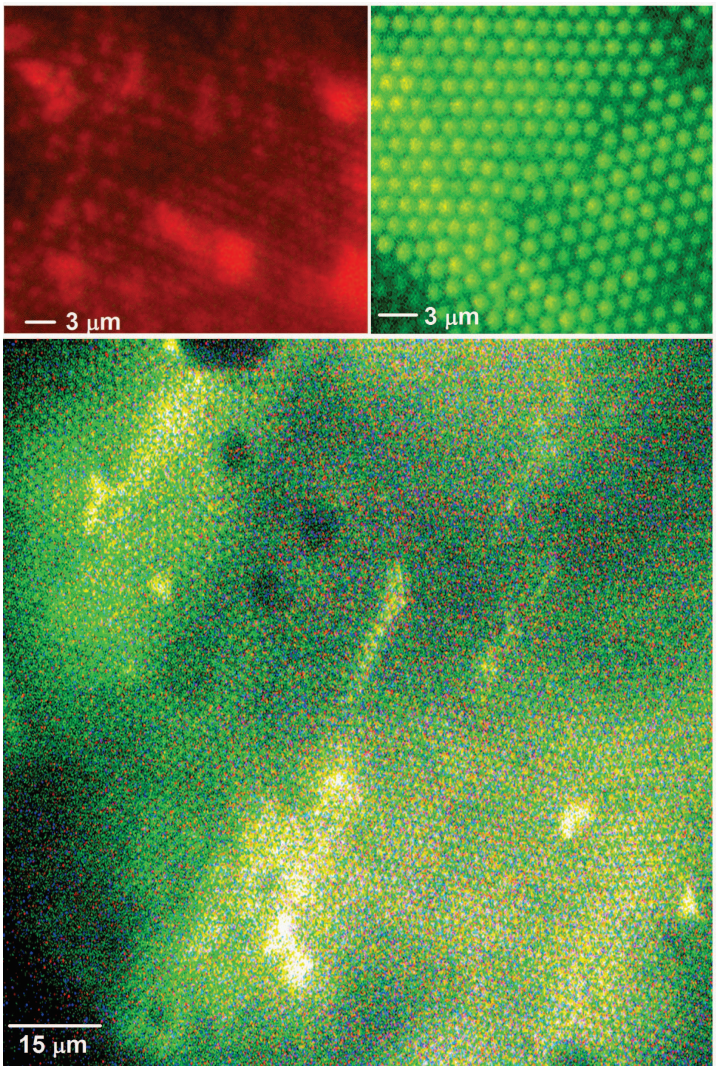

Figure 34: Micro nanoOLEDs observation. (a) Optical microscope image of an array of red OLEDs (λ= 620 nm, diameter is 1.27 µm, size of micro-nanoparticles is 1.68 µm). (b) Optical microscope image of an array green OLEDs (λ=520m OLED diameter is 1.27 µm, size of micro nanoparticle is 1.68 µm). (c) Optical microscope image of large area of a green OLED (OLED diameter is 1.27 µm, size of micro nanoparticles is 1.68 µm).

By comparison the unpatterned green reference OLED shows for 8.5V a current density of 30 mA, a luminance of 5355 cd/m2 and an efficiency of 3.28 lm/W. The patterned active area obtained with 1.68 µm microparticles and a hole diameter of 1.270 µm represents 46% of the unpatterned OLED. Taking into account the uncertainties on the monodispersity of the microparticles (5%) and on the defect in the self-organization, the reduction by 46% of the active area explains the 40% decrease of the luminance. This is a clear demonstration that this

patterning method based on the nanoparticles photolithography remains compatibles with the OLED deposition process.

3.4.2.1. Spectrum

Finally, figure 35 shows perpendicular to substrate emission spectra of the reference large area OLED (black curve) and the green micro-OLEDs (green curve). The spectral difference is indicated by the blue curve. No significant difference in the emission spectra was observed, apart from the a small shift as indicated by the blue curve, which is a spectral difference btween the spectra of the micro-OLED and the reference OLED. This small insignificant difference might be because of the absorption or diffraction of light by the photoresist in the micro-OLEDs. To have a spectral narrowing of the micro-OLEDs, the period of the lattice should be smaller, as demonistrated for 2D DFB lasers in the literature.

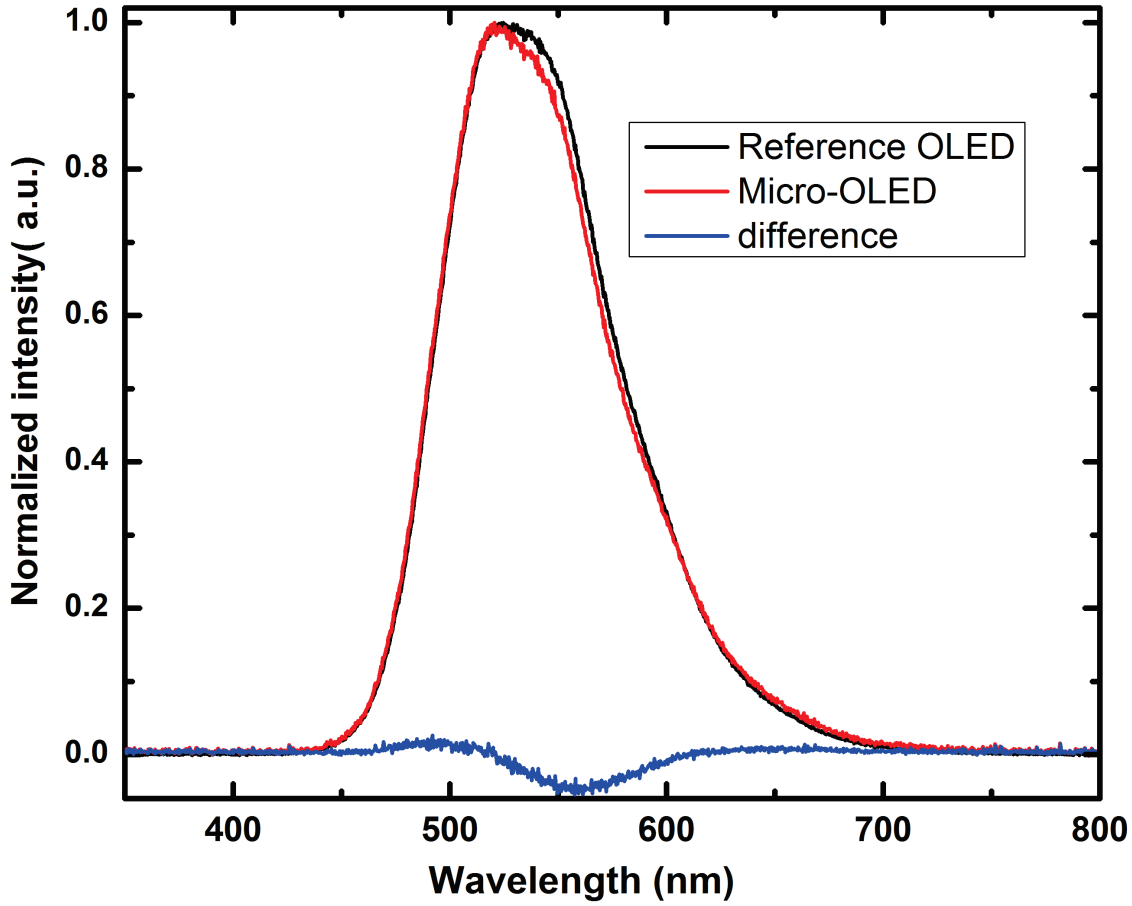

Figure 35: Perpendicular emission spectra from micro-OLED(black curve) and reference large area OLED(red curve). The blue curve is the sepctral difference between the spectra of the micro OLED and the reference OLED.

4. Conclusion and perspectives

As a conclusion, we study numerically and experimentally the 2D nanostructuration of a photoresist deposited on the ITO electrode of an OLED. The nanostructuration process is based on photolithography and a reusable mask made with a self-organized monolayer of SiO_2 and polystyrene micro nanoparticles. This work includes a study of the lattice parameters (period and hole diameter) of the patterned photoresist as a function of the diameter ***D*** of the micro nanoparticles ranging from 800 nm to 2.4 µm. Depending on the

spacing between the photomask and the photoresist, two different configurations can be distinguished; the hard-contact mode and the soft-contact mode.

In the hard-contact mode (i.e. the mask is in close contact with the photoresist) each micro nanoparticle behaves like a ball-lens that focuses the UV light on part of the photoresist which is in direct contact with it. This creates a periodic variation of the energy absorbed by the photoresist, which results in a periodic arrangement of holes once the photoresist is developed. In this case the period of the two-dimensional pattern is equal to the particles diameter D.

The soft-contact mode corresponds to a distance of few micrometers between the photomask and the photoresist. This allows interferences to occur in a similar manner as in a 2D phase-mask. The interferences of the orders +1 and -1 produce a pattern with a lattice period equal to the half (***D/2***) of the micro nanoparticles diameter. Period as low as 740 nm with holes diameters down to 420 nm were achieved with a simple photolithography process at the wavelength of 405 nm.

Two different organic hetero-structures were then evaporated on the patterned photoresist deposited on an ITO electrode. to fabricated red and green micro-nano OLEDs. We believe this process can still be applicable for smaller size of micro nanoparticles (range 400 nm – 800 nm).

As a perspective, we will extend this process with shorter wavelength light sources (365 nm, 193 nm) so as to produce 2D-DFB laser resonators compatible with the visible emission of organic heterostructures. This requires deep-UV lithography and UV-sensitive photoresists. Although there are unavoidable natural defects and mutiple-domains in the self-assembly process, DFB lasing was observed in quasi periodic photonic crystals and 2D patterns by nanosphere lithography[49,52]. Thus periodic nanostrucutres made by our technique can be well applied to making DFB lasers.

Moreover, the ITO layer can be patterned in subsequent step of ICP etching or by wet chemical etching. This may lead to better light extraction efficiency or spectral modification. The positive or negative photoresist can also be deposited on the glass side of the substrate to make holes and pillars, respectively. Subsequent etching of the glass substrate can give periodic patterns of holes or pillars on the glass substrate which may be important for light extraction, as in microlenses deposited on glass substrate.

5. References

[1] Hideki Shirakawa, Edwin J. Louis, Alan G. Macdiarmid, Chwan K. Chiang, And Alan J. Heeger, "Synthesis Of Electrically Conducting Organic Polymers: Halogen Derivatives Of Polyacetylene, (CH)x," J.C.S. Chem. Comm., Vol. 474, 578-580(1977).

[2] I. D. W. Samuel and G. A. Turnbull, "Organic Semiconductor Lasers," Chem. Rev., Vol. 107,1272−1295(2007).

[3] C. Hamann,"Organic Semiconductors," National Aeronautics And Space Admltlistration Washington, (1966).

[4] Focus Article, "Twenty-five years of conducting polymers," Chem. Commun., 1-4(2003)

[5] Jean-Luc Bredas, David Beljonne, Veaceslav Coropceanu,and Jerome Cornil, "Charge-Transfer and Energy-Transfer Processes inð-Conjugated Oligomers and Polymers: A Molecular Picture," Chem. Rev., Vol. 104,4971−5003(2004).

[6] http://photonicswiki.org/index.php?title=The_Polyene_Series

[7] "The Nobel Prize in Chemistry, 2000: Conductive polymers", The royal Sweedish Academy of Science.

[8] J. L. Brdas, And G. B. Stree,"Polarons, Bipolarons, And Solitons In Conducting Polymers," Acc. Chem. Res., Vol. 18, 309-315(1985).

[9] http://www.organicsemiconductors.com/

[10] http://www.iue.tuwien.ac.at/phd/li/node9.html

[11] Tang, C. W. and VanSlyke, S. A., "Organic electroluminescent diodes," Appl. Phys. Lett., Vol. 51, 913-915 (1987).

[12] M. Pope, H. P. Kallmann, and P. Magnant ,"Electroluminescence in Organic Crystals", J. Chem. Phys., Vol. **38**, 2042(1963).

[13] J. H. Burroughes, D. D. C. Bradley, A. R. Brown, R. N. Marks, K. Mackay, R. H. Friend, P. L. Burn & A. B. Holmes, "Light-emitting diodes based on conjugated polymers," *Nature,Vol.* **347,** 539–541 (1990).

[14] R. H. Friend, R. W. Gymer, A. B. Holmes, J. H. Burroughes, R. N. Marks, C. Taliani, D. D. C. Bradley, D. A. Dos Santos, J. L. Breâdas, M. Loègdlund & W. R. Salaneck, "Electroluminescence In Conjugated Polymers," Nature, Vol. 397, (1999).

[15] Richard Friend, Jeremy Burroughes And Tatsuya Shimoda, "Polymer Diodes", Physics World, (1999).

[16] http://www.uni-leipzig.de/~pwm/web/?section=introduction&page=fluorescence

[17] http://chemwiki.ucdavis.edu/Physical_Chemistry/Spectroscopy/Electronic_Spectroscopy/Electronic_Spectroscopy%3A_Theory

[18] _http://www.photobiology.info/Visser-Rolinski.html

[19] __http://www.olympusmicro.com/primer/techniques/confocal/fluoroexciteemit.html

[20] Eugene Rabinowitch "Photosynthesis" John Wiley Sons, Inc., New York

[21] L. S. Hung, C.W. Tang, andM. G.Mason, Appl. Phys. Lett. 70(2), 152–154 (1997).

[22] Jorge Morgado, Nunzio Barbagallo, Ana Charas, Manuel Matos, Luís Alcácer and Franco Cacialli,"Self-assembly surface modified indium–tin oxide anodes for single-layer light-emitting diodes,"J. Phys. D: Appl. Phys, Vol., 36, 434–438(2003).

[23] Wolfgang Bru¨tting, Jo¨ rg Frischeisen, Tobias D. Schmidt, Bert J. Scholz, and Christian Mayr "Device efficiency of organic light-emitting diodes: Progress by improved light outcoupling", Phys. Status Solidi A, Vol. 210, 44–65 (2013).

[24] Dirk Ammermann, Achim , Wolfgang Kowalsky ",Multilayer Organic Light Emitting Diodes for Flat Panel Displays", Annual report, Institut Hochfrequenztechnik, TU Braunschweig, (2009).

[25] Sebastian Reineke, Michael Thomschke, Bj$_{DEL}$orn L$_{DEL}$ussem and Karl Leo, "White organic light-emitting diodes: Status and perspective," Reviews Of Modern Physics, Vol. 85, 1245-1293(2003).

[26] Norbert Koch "Electronic structure of interfaces with conjugated organic materials," Phys. Status Solidi RRL, Vol. 6, 277–293 (2012).

[27] I.G. Hill, D. Milliron, J. Schwartz, A. Kahn "Organic semiconductor interfaces: electronic structure and transport properties," Applied Surface Science, Vol.166, 354–362(2000).

[28] C.W. Tang, S. A. VanSlyke, C. H. Chen: "Electroluminescence of doped organic thin films," J. Appl.Phys., Vol. 65, 3610–3616(1989).

[29] Tatsuo Mori and Teruyoshi Mizutani, "Application of Energy Transfer Model to Partially DCM-doped Alq3 Light-emitting Diode," Polymers for Advanced Technologies, Vol. 8, 471–476 (1997).

[30] A. J. Ma¨Kinen, I. G. Hill, Z. H. Kafafi "Vacuum Level Alignment In Organic Guest-Host Systems," Journal Of Applied Physics, Vol. 92, 1598 (2002).

[31] Shidong Kan, Xiaodong Lui , Fangzhong Shen, Jingying Zhang, Yuguand Ma, Guo zhang, Yue Wang ,and Jiacong Shen, "Improved efficiency of single-layer polymer light-emitting devices with poly (vinylcarbazole) doubly doped with phosphorescent and flourescent dyes as the emmiting layer" Adv. Funct. Mat., Vol. 13, 603- 608(2003).

[32] Von Th. Forster, "Zwischenmolekulare Energiewanderung und Fluoreszenz" Aitiaalen cler Physik. 6. Folgc. Batid 2. (1948)

[33] D. L. Dexter, "A theory of sensitized luminescence in solids," J. Chem. Phys., Vol. 21, 836-850 (1953).

[34] IUPAC

[35] http://chemwiki.ucdavis.edu/Theoretical_Chemistry/Fundamentals/Dexter_Energy_Transfer#ref_1

[36] K. Saxena, V.K. Jain, D.S. Mehta, "A review on the light extraction techniques in organic electroluminescent devices", Optical Materials, Vol. 32, 221–233(2009).

[37] Klaus Meerholz and David C. Müller,"Outsmarting Waveguide Losses in Thin-Film Light-Emitting Diodes", Adv. Funct. Mater., Vol. 11, 251-253(2001).

[38] Tetsuo Tsutsui, Masayuki Yahiro, Hiroshi Yokogawa, Kenji Kawano, and Masaru Yokoyama ,"Doubling Coupling-Out Efficiency in Organic Light-Emitting Devices Using a Thin Silica Aerogel Layer," Adv. Mater. Vol. 13, 1149–1152 (2001).

[39] Windisch R., Heremans P., Knobloch A., Kiesel P., Dohler G. H., Dutta B., Borghs G., "Light-emitting Diodes with 31% External Quantum Efficiency by Outcoupling of Lateral Waveguide Modes." Appl. Phys. Lett., Vol. 74, 2256-2258(1999).

[40] Sun J, Forrest S. R., "Organic Light Emitting Devices with Enhanced Outcoupling via Microlenses Fabricated by Imprint Lithography," J. Appl. Phys.,Vol. 100, 073106(2006).

[41] Moller S, Forrest S. R., "Improved Light Out-coupling in Organic Light Emitting Diodes Employing Ordered Microlens Arrays," J. Appl. Phys.,Vol. 91, 3324-3327(2002).

[42] Yamasaki T., Sumioka K., and Tsutsui T. "Organic Light-emitting Device with an Ordered Monolayer of Silica Microspheres as a Scattering Medium," Appl. Phys. Lett., Vol. 76: 1243-1245(2000).

[43] Lupton J. M., Matterson B. J., Samuel I. D. W., Jory M. J., Barnes W. L., " Bragg Scattering from Periodically Microstructured Light Emitting Diodes," Appl. Phys. Lett.; Vol. 77, 3340-3342(2000).

[44] S. Moller, S.R. Forrest, "Improved light out-coupling in organic light emitting diodes employing ordered microlens arrays, " J. Appl. Phys., Vol. 9, 3324-3327(2002).

[45] F. Li, X. Li, J. Z. and B. Yang, "Enhanced light extraction from organic light-emitting devices by using microcontact printed silica colloidal crystals," Organic Electronics, Vol. 8, 635–639(2007).

[46] Chung Sock Choi, Sung-Min Lee, Myung Sub Lim, Kyung Cheol Choi, Donghyuk Kim, Duk Young Jeon, Youngjo Yang, and O Ok Park "Improved light extraction efficiency in organic light emitting diodes with a perforated WO3 hole injection layer fabricated by use of colloidal lithography, " Optics Express ,Vol. 20, A309-A317 (2012).

[47] Yu-Hsuan Ho, Kuan-YuChen, Kai-YuPeng, Ming-Chih Tsai, Wei-Cheng Tian, and Pei-Kuen Wei, "Enhanced light out-coupling of organic light-emitting diode using metallic nanomesh electrodes and microlens array," Optics Express, Vol. 21, 8535-8543(2013).

[48] Stefan Riechel "Organic semiconductor lasers with two-dimensional distributed feedback," Dissertation der Fakulat fur phsik, Munchen, (2002).

[49] Sungmo Ahn, Hanbit Kim, Heonsu Jeon, , Jeong Rok Oh, Young Rag Do, and Hyo Jin Kim,"Two-Dimensional Hexagonal Lattice Photonic Crystal Band-Edge Laser Patterned by Nanosphere Lithography," Applied Physics Express, Vol. 5, 042102-1-042102-3(2012).

[50] Shiyoshi Yokoyama, Tatsuo Nakahama, And Shinro Mashiko, Masashi Nakao "Motohiro Yamada, Kazuyuki Nishio, And Hideki Masuda, "Photonic Crystal Templates For Organic Solid-State Lasers," Applied Physics Letters, Vol. 87, 191101-1- 191101-3(2005).

[51] Rik Harbers, Patric Strasser, Daniele Caimi, Rainer F. Mahrt, Nikolaj Moll, Bert Jan Offrein, Daniel Erni, Werne Bächtold, And Ullrich Scherf "Enhanced Feedback In Organic Photonic-Crystal Lasers," Applied Physics Letters, Vol. 87, 151121-1- 151121-3(2005).

[52] M. Notomi, H. Suzuki,T. Tamamura, And K. Edagawa, "Lasing Action Due To The Two-Dimensional Quasiperiodicity Of Photonic Quasicrystals With A Penrose Lattice," Physical REV. Letts. , Vol. 92, 123906-1-123906-4(2004).

[53] M. Vasilopoulou , D. G. Georgiadou, L. C. Palilis, A. Botsialas, P. S. Petrou, S. E. Kakabakos and P. Argitis, "Photopatterned PLED arrays for biosensing applications," Microelectronic Engineering, Vol. 86, 1511-1514 (2009).

[54] H. Yamamoto, J. Wilkinson, J. P. Long, K. Bussman, J. A. Christodoulides and Z. H. Kafafi, "Nanoscale Organic Light-EmittingDiodes," Nano Letters, Vol. 5, 2485-2488(2005).

[55] J. Lu, H. W. Lin, H. Y. Chen, Y. C. Yang and S. Gwo, "Single InGaN nanodisk light emitting diodes as full-color subwavelength light sources", Applied Physics Letters, Vol. 98, 233101-1-233101-3((2011).

[56] F. A. Boroumand, P. W. Fry and D. G. Lidzey, "Nanoscale Conjugated-Polymer Light-Emitting Diodes,", Nano Letters, Vol. 5, 67-71(2005).

[57] C. Piliego, M. Mazzeo, B. Cortese, R. Cingolani and G. Gigli, "Organic light emitting diodes with highly conductive micropatterned polymer anodes", Microelectronic Engineering Organic Electronics , Vol. 9, 401–406(2008).

[58] S. P. Price, J. Henzie, T. W. Odom, "Addressable, Large-Area Nanoscale Organic Light-Emitting Diodes", Small Vol. 3, 372–374(2007).

[59] J. G. C. Veinot, H. Yan, M. S. Stephen, J. Cui, Q. Huang and T. J. Marks, "Fabrication and Properties of Organic Light-Emitting "Nanodiode" Arrays", Nano Letters, Vol. 2, 333-335(2002).

[60] A. Bolognesi, C. Botta, S. Yunus, "Micro-patterning of organic light emitting diodes using self-organised honeycomb ordered polymer films", Thin Solid Films, Vol. 492, 307–312(2005).

[61] W.Wu, D. Dey, O. G. Memis, A. Katsnelson, H . Mohseni, "A Novel Self-aligned and Maskless Process for Formation of Highly Uniform Arrays of Nanoholes and Nanopillars," Nanoscale Res Lett., Vol. 3, 123–127(2008).

[62] C. O'Connell, R. Sherlock, T. J. Glynn, "Fabrication of a reusable microlens array for laser-based structuring", *Opt. Eng*. Vol. 49, 014201(2010).

[63] M.H. Wu G. M. Whitesides,"Fabrication of arrays of two-dimensional micropatterns using microspheres as lenses for projection photolithography," Appl. Phys. Lett., Vol. 78, 2273-2275(2001).

[64] Fundamentals of micro-optics, H. Zappe, Cambridge University Press (November 15, 2010), ISBN-10: 0521895421

[65] W. Stöber, A. Fink, E.J. Bohn, "Controlled growth of monodisperse silica spheres in the micron size range," J. Colloid Interface Sci., Vol. 26, 62-69(1968).

[66] C.-H. Chan · A. Fischer · A. Martinez-Gil · P. Taillepierre · C.-C. Lee · S.-L. Yang · C.-H. Hou · H.-T. Chien · D.-P. Cai · K.-C. Hsu · C.-C. Chen, "Anti-reflection layer formed by monolayer of microspheres," Applied Physics B,Vol. 100, 547–551 (2010).

[67] C-H Chan, C-H Hou, C-K Huang, T-J Chen, S-Z Tseng, H-T Chien, C-H Kuo, K-H Hsieh, Y-L Tsai, K-C H and C-C Chen, "Patterning periodical motif on substrates by monolayer of microspheres: Application on GaN LEDs," Jpn. J. Appl. Phys., Vol. 48, 020212-1-020212-3 (2009).

[68] C-H Hou , S-Z Tseng , C-H Chan, T-J Chen , H-T Chien , F-L Hsiao , H-K Chiu , C-C Lee , Y-L Tsai , C-C Chen, "Output power enhancement of light-emitting diodes via two-dimensional hole arrays generated by a monolayer of microspheres," Applied Physics Letters, Vol 95, 133105-1-, 133105-3(2009).

Chapter 4:

Conclusion and Perspective

1. General conclusion:

To conclude, we studied monolayer of dielectric spheres which can potentially be used with organic luminescent materials to make organic lasers, to enhance the efficiency of OLEDs, or to make periodic textures for other applications. Our study was made in two axes. In the first axis, the photonic properties of monolayer of nanoparticles were numerically studied. In the second axis, the monolayer of nanoparticles was used as photolithographic masks to pattern insulating photoresist deposited on ITO coated glass substrate. This was used to make 2D patterning of OLEDs.

In the first axis of this study, photonic bandgaps and cavity resonances of monolayer of opals and inverse opals with and without glass substrate were investigated. The photonic bandgaps were studied for changes of refractive index of dielectric materials (for touching spheres) and of the compactness of the spheres (when the refractive index of the materials is kept at 2.5). This study was done for different crystal directions and for different polarizations of the field.

FDTD simulations show that PBGs are observed for refractive indices as low as 1.5 for monolayers of inverse opals and opals without substrate. In inverse opals, overlap of the TE mode bandgap is observed for both directions of propagation, which tells that inverse opals favour TE bandgaps. The presence of glass substrate results in the absence of PBG for low refractive index values. However, decreasing the compactness of the spheres in inverse opals recovers the PBGs, though compact configuration of monolayer of opals has a wider PBG than the non-compact configuration.

Mircocavities in inverse opal configuration show higher quality factors when non-compact spheres are used with r/a values around **0.31, 0.32**, and **0.33** (when refractive index of infiltrated material is 2.5, corresponding to anatase phase of TiO2). For this reason an

optimized inverse opal microcavity needs another step of fabrication to make non-compact spheres, like the reactive ion etching of the spheres before the sol-gel process. This makes the fabrication more difficult than the proposed simplicity of the process. However, still using this method, we can avoid the electron beam lithography writing. On the other hand, the opal arrangement needs higher refractive index of spheres in air (n = 3) to have significance resonance of the TM mode. If glass substrate is used, a higher refractive index of the spheres (n = 4) is needed to have the resonances. This makes the realization more difficult as available materials to make micro- and nano- spheres don't have such a high refractive index. Thus, the non-compact arrangement of inverse opal on glass substrate can be more feasible in achieving defect mode microcavities.

Our modified experimental approach for the characterization of the in-plane transmission spectra of monolayer of spheres in the optical regime is possible and promising if the deposition of nanoparticles in the pre-fabricated hexagonal templates is optimized.

In the second axis of this study, the monolayer of spheres was used as photolithographic mask to pattern insulating photoresist deposited on ITO coated glass substrate. There are two different physical effects of the monolayer of micro-nanoparticle mask: The first is micro-ball lens effect, in which the periodicity of the monolayer of spheres is replicated in the patterned photoresist; and the second is the phase-mask effect, in which the periodicity of the structured photoresist is half of the periodicity of the monolayer of spheres. We were able to obtain the period of the pattern of the structured photoresist down to 740 nm with corresponding size of holes of 420 nm. The organic hetero-structure deposition on the patterned photoresist resulted in an array of micro-OLEDs with a diameter of 1.27 μm. This method of fabrication is promising to make patterns with periodicity less than 500 nm. This may have applications to realize DFB lasers in the optical regime.

2. Perspective

As continuation of this PhD thesis, the two different axes of the research should be investigated in more depth. In the first axis, experimental characterization of transmission spectra in monolayer of dielectric spheres deposited on glass substrate can be novel result (continuation of the work of chapter 1). In the second axis, nanoparticles can be used to

pattern photoresist to be used for spectral modification of the emission from organic luminescent materials (continuation of chapter 2). This has an ultimate goal of realizing 2D DFB lasing. In the following sections we will discuss the two axes of the work in more detail.

2.1 Experimental characterization of monolayer of nanoparticles deposited in a waveguide

The first axis consists in the characterization of transmission spectra of monolayer of spheres in optical regime. The simulation results show that the monolayer of nanoparticles on glass substrate shows PBG in ΓM direction and for TE polarization of the field. Thus, experimentally demonstrating the simulation results is important and is a first step for further realization of the micro-cavity lasers.

As discussed in chapter 2, the problem with self assembly process is the presence of multiple domains in the crystal. This means, for transmission spectra characterization, the incident beam will encounter different crystal directions (for example ΓM and ΓK) as it propagates through the crystal. In addition, the nanoparticles are too small to manipulate manually and it is difficult to identify a specific crystal direction for the injection of light. Thus, a more controlled self-assembly with single crystal domain is necessary. We propose to use micro-hexagons for the deposition of the nanoparticles as was done by Arpiainen et. al. to have more controlled homogeneity and waveguides for the light injection and collection which made identifying the crystal direction simpler.

Although we have started this work by drop coating technique, the deposition of nanoparticles in the micro-hexagon requires very small volume of drop than what we got by experiment. In addition, a very thin micro-needle with diameter smaller than the size of the micro-hexagon is needed, in principle.

As we didn't have very promising results using the drop coating technique, it is more advisable to use micro-fluidic channels to deliver the colloidal solution to the micro-hexagon, similar to what was done by Arpiainen et. al., who made homogeneous monolayer of nanoparticles [[1]]. In addition, using simple waveguides as in our experimental results is not advisable as the nanoparticles overflowing from the micro-hexagon can be deposited in the exterior of the core of the waveguide, which can cause light coupling to the nanoparticles outside the waveguide and results in distortion of the direction of propagation of the incident beam.

- **Buried waveguides with polymer micro-hexagon**

As mentioned in chapter 2, the first step is to realize polymer waveguides for light injection and collection. Some of waveguides have micro-hexagons for the deposition of nanoparticles, while other waveguides are reference. Making different orientation of the micro-hexagons with respect to the direction of the waveguides helps the incident beam to meet the PhC in different crystal directions and it will enable to construct the 2D dispersion diagram of the monolayer of spheres. Figure 1 below shows schematic diagram of the different waveguides and a group of similar size micro-hexagons with different orientations, as indicated by the angles. As the photoresist layer might not be uniform throughout substrate, having reference waveguides close to waveguides with micro-hexagons enables to have more accurate comparison of the transmitted light through the nanoparticles and the reference waveguides. Thus we have two reference waveguides for similar size of hexagons.

To study how the transmission spectra converge when the number of periods in the monolayer is increased, a similar design can be made for different size of hexagons, which can accommodate the required number of nanoparticles. In our case, we have designed different set of micro-hexagons which can accommodate eight to sixteen 300nm-size nanoparticles by the side of the hexagon.

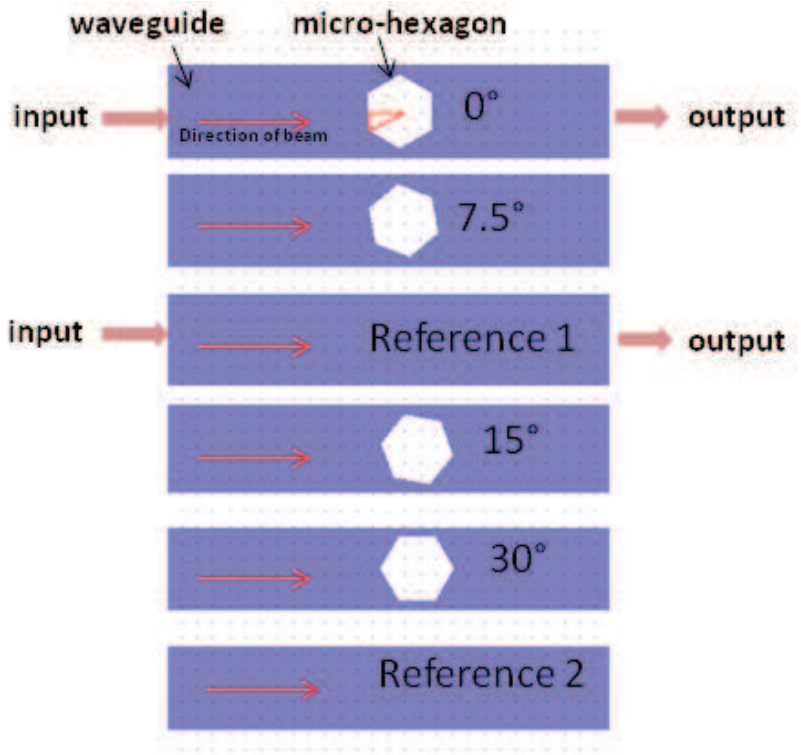

Figure 1 Schematic diagram of waveguides and micro-hexagons for the characterization monolayer of spheres. These set of hexagons are design to accommodate N number of nanoparticles and they are oriented at different angles with respect to the waveguides, or the direction of the incident beam.

The figure 2 below shows the schematic diagram of top view of the waveguides on the substrate, with two micro hexagons oriented in two different directions. The points 1 and 2 in the waveguides of figure 2a, respectively show the light injection point and the middle of the hexagon. This is shown by the cross-sectional views in figure 2b and 2c, where we have nanoparticles in the middle of the hexagon (corresponding to position 2 of figure 2a).

The cross-sectional view of the *simple waveguide* is shown in figure 2b, which is a waveguide whose core is made of polymer and has air and glass as claddings. From preliminary experiment discussed in chapter 2, the simple waveguide is not advisable as the nanoparticles overflowing from the micro-hexagon can be deposited in the exterior of the core of the waveguide, which can cause light coupling to the nanoparticles outside the waveguide and leads to a distortion of the direction of propagation of the incident beam. Thus we propose the buried waveguide approach.

The cross-sectional view of the buried waveguide is shown in figure 2c and it has a polymer core and claddings which have lower refractive index. In this configuration, the overflowing nanoparticles will have less contact with the guiding portion and we expect to have better propagation of the light.

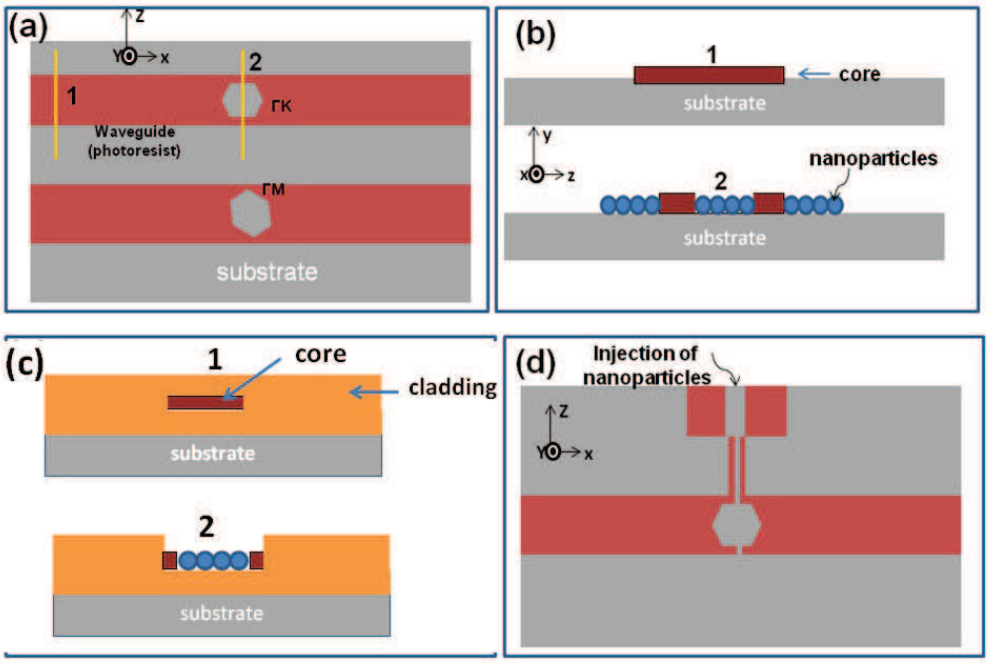

Figure 2. Schematic diagram of the waveguides for the characterization of nanoparticles. (a) Top view of guides on the substrate. Point 1: injection point; Point 2: middle of hexagone (b) Cross-sectional view of a simple waveguide at the point of injection and middle of the hexagon. (c) Cross-sectional view of a buried waveguide at the point of injection and middle of the hexagon (d) Method of delivering the nanoparticles to the micro-hexagon using micro-channels

- ***Microchannels for delivering nanoparticles.***

For better control, the nanoparticles will be guided to the micro-hexagon by a microchannel. This is shown in the figure 2d where a canal is drawn to deliver the hexagon with nanoparticles. Nanoparticles can be injected at the other end of the canal.

2.2 Realization of 2D DFB structure to order N by structuring using self-organized nanoparticles

The second axis of this work is to use a monolayer of micro nanoparticles to pattern a periodic two-dimensional arrays on a photosensitive resin layer by a photolithography method. We will then make a film of organic luminescent material on the structured photoresist whose parameters are appropriately designed. Due to the 2D periodicity some specific wavelength can be resonated in the structure resulting from a 2D DFB action. Normally this requires the period of the lattice to be in the order of 300-400nm, which we were not able to fabricate due to limit of the wavelength of our exposure light source (which is at 405nm). Thus to have a periodic pattern with period below 740 nm, which we achieved already, it is necessary to use other light source which can provide lower wavelength. Thus, the future work includes realizing periodic patterns with smaller period of the patterns (using excimer laser) and subsequent application with organic luminescent materials.

- ***Photolithography with excimer laser at 193 nm***

To make periodic structures with period smaller than 400 nm, we have to use a source with lower wavelength, like an excimer laser with emission at 193 nm. This needs the use of a photosensitive resin at 193 nm, which is commonly called Deep UV (DUV) photoresist.

- ***Characterization by optical pumping / electric DFB structures with an organic layer as the gain medium***

Figure 3 below shows different patterns which can be made by microsphere based photolithography.

Organic luminescent layers can be deposited on the structured photoresist to complete the DFB structure, as in figure 3a. This can give the required resonance by optical pumping. In addition, by making the periodic structure on ITO, and by completing the OLED layers, it is possible to have spectral modification in OLED emission by electrical excitation (figure 3b). This can be achieved by having angle resolved detection of the emitted light.

This patterning technique can also be used for making nanostructures on the ITO layer (as in figure 3b) by subsequent steps. This can result in spectral modification or enhance light extraction from OLEDs. It is also possible to make the photoresist pattern on the outer face of

the glass substrate of the OLED and then transfer the periodic grating on the glass by etching. By using positive or negative photoresist, periodic holes or semi-spheres can be realized on the glass substrate. This will provide greater out coupling of light and enhance the efficiency in OLEDs with a simple and cheaper process (Fig. 2c & 2d) [2].

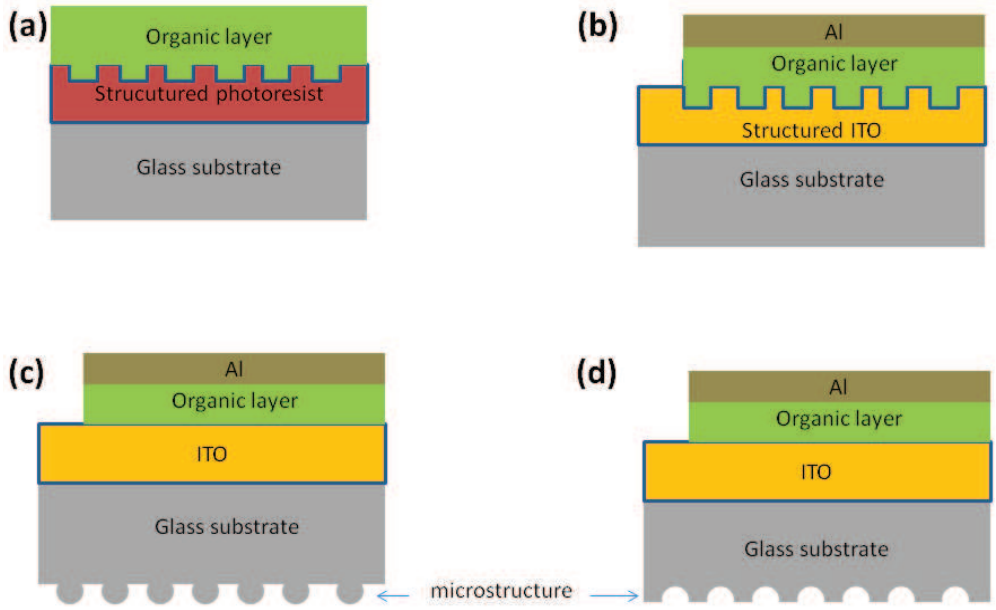

Figure 3. Microstructures which can be made using two-dimensional self-organized micro nanoparticles. (a) An organic gain medium deposited above a layer of structured resin as a base structure for the DFB laser. (b) Organic hetero structure deposited on structured ITO for spectrum modifications or improved light extraction. (c) & (d) OLEDs with structured glass substrate for improving light extraction.

3. References

[1] Sanna Arpiainen, Fredrik Jonsson, James R. Dekker, Gudrun Kocher, Worawut Khunsin, Clivia M. Sotomayor Torres, and Jouni Ahopelto, “Site-Selective Self-Assembly of Colloidal Photonic Crystals”, Adv. Funct. Mater., Vol. 19, 1247–1253(2009).

[2] Yu Luo 2013, “High light-extracting efficiency for OLED directly fabricated on double-side nanotextured silica substrate”, Optics Letters, Vol. 38, No. 14, (2013)

Abstract :

We investigate the in-plane photonic properties of monolayer of self-organized nanostructures. We aim at investigating the contribution of photonic self-organized nanostructures to organic photonic crystal (PhC) cavities, and novel organic light sources.

The first chapter presents bulk opals and inverse-opals made of self-organized nanoparticles and their optical properties. In a second part, photonic crystals are introduced as well as the physics and the numerical tools to quantify them.

The second chapter deals with the study of photonic properties of two-dimensional periodic array of monolayer of self-organized dielectric nanoparticles. The in-plane optical transmission and the existence of photonic bandgap are systematically studied by using the 3D finite-difference time-domain (3D FDTD) method. The structures studied are monolayer of dielectric spheres surrounded by air ('opals') and air spheres infiltrated with dielectric material ('inverse opals') in triangular lattice, with and without glass substrate. The dependence of photonic band gaps (PBGs) on the refractive index and on the compactness of spheres is studied. For self-sustained structures, PBG is observed for relatively low refractive indices of materials. However, the presence of a glass substrate reduces the PBGs. Defect microcavity designed in opals and in inverse opals are then considered. The best quality factor are obtained with inverse-opals when the compactness (**r/a** ratio) is around 0.32. An experiment to measure the in-plane propagation in monolayers of opals is presented.

In the third chapter of this study, we present a new approach of two-dimensional patterning based on self-organized nanoparticle photolithography for nanostructuration of organic light emitting diodes. This technique uses conventional photolithography, a reusable photomask made of self-organized micro nanoparticles, and a conventional photoresist. The mask consists of micro and sub-micron sized SiO_2 or Polystyrene mono-dispersed spheres deposited in a self-organized manner on a quartz substrate. The principle of operation is similar to the one of conventional photolithography except that two configurations can be distinguished : The hard-contact mode and the soft-contact mode. In the first configuration, each microsphere acts as a micro ball-lens that focuses the light and expose the part of the photoresist underneath the spheres. The resulting pattern reproduce the triangular lattice arrangement of the spheres with the same period. In the soft contact mode a phase mask behavior is obtained which results in lattice periods being the half of the sphere diameters. Lattice periods and hole diameter as small as 750 nm and 420 nm respectively are demonstrated with a 405 nm light source. Eventually, this new two-dimensional patterning technique is applied to the nanostructuration of OLEDs. As an example, green and red patterned OLEDs are demonstrated.